

Doctoral Thesis

Development of functional coherent X-ray  
nanoimaging with deep-learning methods

Sung Yun Lee (성 윤)

Department of Physics

Pohang University of Science and Technology

2025



# 기능성 결맞는 엑스선 나노이미징과 딥러닝 방법론 개발

Development of functional coherent X-ray  
nanoimaging with deep-learning methods

# Development of functional coherent X-ray nanoimaging with deep-learning methods

by

Sung Yun Lee

Department of Physics

Pohang University of Science and Technology

This thesis was submitted to the faculty of  
Pohang University of Science and Technology in partial fulfillment of  
the requirements for the degree of Doctor of Philosophy in Physics

Pohang, Republic of Korea

05. 27. 2025.

Approved by

Changyong Song (Signature) 

Academic advisor

# Development of functional coherent X-ray nanoimaging with deep-learning methods

Sung Yun Lee

The undersigned have examined this thesis  
and hereby certify that it is worthy of acceptance for a doctoral degree  
from Pohang University of Science and Technology

05. 27. 2025.

Committee Chair	Changyong Song	(Seal)
Member	Bumjoon Kim	(Seal)
Member	Daewoong Nam	(Seal)
Member	Hyon Chol Kang	(Seal)
Member	Tae-Hwan Kim	(Seal)

DPH

이 성 윤 Sung Yun Lee

20202818

Development of functional coherent X-ray  
nanoimaging with deep-learning methods

기능성 결맞는 엑스선 나노이미징과  
딥러닝 방법론 개발

Department of Physics, 2025, 149 pages

Advisor: Changyong Song

Text in English.

## ABSTRACT

Coherent diffraction imaging has enabled high-resolution noninvasive imaging of various specimens in nanoscale resolution regardless of optical performance of imaging optics, fully utilizing advantages of short-wavelength sources, especially for X-rays. In addition, development of X-ray free-electron lasers has realized time-resolved imaging for tracking ultrafast dynamics and phase transitions of diverse systems in outstanding spatiotemporal resolution. Despite its superiority, rising of emerging materials with complicated properties demands for enhancements on performance and functionality of diffraction imaging methods.

In this thesis, we introduce theoretical backgrounds for coherent diffraction imaging and dedicated improvement methods by employing new experimental techniques and deep-learning methods. The proposed experimental techniques include multidistance measurements to overcome a trade-off between resolution and reciprocal-space sampling and a use of vortex beams, which exhibit topological wavefront structures and inherent orbital angular momenta, to reinforce sensitivities on complex or chiral structures. On the other hand, the developed deep-learning methods enable denoising and real-time phase retrieval of noise-buried, partially damaged diffraction patterns captured by single-pulse measurements using the X-ray free electron lasers. Advancements of coherent diffraction imaging by these methodological developments will assist future scientific research to investigate a wide range of advanced materials with characteristic properties.



# Contents

I. Introduction .....	1
II. Background .....	2
1. Diffraction of electromagnetic waves .....	2
1.1. Introduction .....	2
1.2. Electromagnetic wave equation .....	2
1.3. Quantized radiation field .....	6
1.4. Light–matter interaction .....	8
1.5. The Lippmann–Schwinger equation .....	10
1.6. The Born approximation .....	14
1.7. Fresnel–Kirchoff diffraction formula .....	16
1.8. Bragg’s law and Ewald sphere .....	19
1.9. Coherence .....	25
1.10. Plane-wave coherent diffraction imaging (CDI) and ptychography .....	27
2. Phase retrieval .....	30
2.1. Introduction .....	30
2.2. Iterative projection algorithms .....	31
2.3. Resolution estimation for phase retrieval .....	35
2.4. Lagrange dual problem .....	36
2.5. Primal-dual algorithms .....	38
2.6. Generalized proximal smoothing .....	40
3. Vortex beam .....	44
3.1. Introduction .....	44
3.2. Vector potential of vortex beam .....	45
3.3. Light–matter interaction with vortex beams and helical dichroism .....	48
3.4. Linear response theory with vortex beams and helical dichroism .....	52
3.5. Spiral zone plate (SZP) .....	56

<b>III. Development of Experimental Techniques for CDI</b>	60
4. Multidistance CDI	60
4.1. Introduction	60
4.2. Multidistance CDI and adaptive phase retrieval algorithm	61
4.3. Multidistance coherent X-ray tomography of mesoporous SiO <sub>2</sub> nanoparticle	65
4.4. Quantitative analyses on porous structures	68
4.5. Conclusion	74
5. Off-axis vortex beam ptychography	74
5.1. Introduction	74
5.2. Numerical simulation of vortex beam generation by off-axis SZPs	75
5.3. Numerical experiments on off-axis vortex beam ptychography	77
5.4. Synchrotron experiments on off-axis X-ray vortex beam ptychography	79
5.5. Conclusion	84
6. Helical dichroism on ferroelectric topological defects	85
6.1. Introduction	85
6.2. Helical dichroism on ferroelectric structures of BiFeO <sub>3</sub>	86
6.3. Synchrotron experiments on helical dichroism with BiFeO <sub>3</sub>	89
6.4. Conclusion	94
<b>IV. Development of Deep-Learning Models for CDI</b>	95
7. Diffraction pattern denoiser	95
7.1. Introduction	95
7.2. <i>k</i> -space convolutional neural network for denoising diffraction data	95
7.3. Phase retrieval of simulated diffraction patterns with deep denoising	99
7.4. Phase retrieval of experimental data with deep denoising	101
7.5. Application of deep denoising on preconditioning the phase problem	104
7.6. Conclusion	107
8. Real-time phase retrieval	107
8.1. Introduction	107
8.2. Deep neural network for phase retrieval of diffraction data	108

8.3. Deep phase retrieval on simulated diffraction patterns .....	115
8.4. Deep phase retrieval on experimental data .....	117
8.5. Conclusion .....	123
<b>V. Summary .....</b>	<b>124</b>
<b>Summary in Korean .....</b>	<b>128</b>
<b>References .....</b>	<b>131</b>
<b>Acknowledgements .....</b>	<b>138</b>
<b>Curriculum Vitae .....</b>	<b>139</b>

## List of Figures

1.1.	Schematic diagram for the scattering of a particle by a scatterer .....	12
1.2.	Schematic diagram for the derivation of the Kirchhoff's integral theorem .....	16
1.3.	Schematic diagram for the derivation of the Fresnel–Kirchhoff diffraction formula .....	17
1.4.	Schematic diagram for the derivation of the Bragg's law .....	19
1.5.	Schematic diagram of the Ewald sphere .....	20
1.6.	Schematic diagram of $\phi$ -scan .....	22
1.7.	Reciprocal-space regions spanned by the $\phi$ -scans for different $\theta$ s .....	23
1.8.	Schematic diagram of $\theta$ -rocking .....	24
1.9.	Schematic diagram for the transverse coherence length .....	26
1.10.	Schematic diagram of plane-wave CDI and ptychography .....	28
3.1.	Example images of on-axis and off-axis SZPs for $l = 1$ .....	58
4.1.	Schematic diagram of coherent X-ray tomography using multidistance CDI .....	61
4.2.	Schematic diagram of adaptive phase retrieval algorithm for multidistance CDI .....	62
4.3.	Numerical simulation for a comparison of direct merging method and non-merging method with the adaptive algorithm .....	64
4.4.	Multidistance coherent X-ray tomography of mesoporous SiO <sub>2</sub> nanoparticle .....	66
4.5.	PRTF and line profile for the resolution estimation of 2D and 3D reconstructions .....	67
4.6.	Pore structure extracted from the 3D image .....	68
4.7.	Network-based analysis of the highly interconnected porous structure .....	69
4.8.	Quantitative analyses of the porous structure based on fractal theory and its skeletons .....	71
5.1.	Schematic diagram of ptychography experiments using the off-axis SZP and example of off-axis SZP patterns .....	75
5.2.	Numerical simulation of vortex beam generation by the partial illumination of off-	

axis SZPs .....	76
5.3. Numerical experiments on ptychography of a weakly scattering object using off-axis vortex beams .....	78
5.4. Edge gradient profiles of the phase of the reconstructed object .....	79
5.5. SEM images of fabricated off-axis SZP patterns.....	80
5.6. SEM image of the off-axis SZP patterns in the actual experimental geometry .....	80
5.7. Recovered beam profile generated by the off-axis SZPs from ptychography experiments on the test target.....	81
5.8. SEM image of the bar-shaped multilayer film .....	82
5.9. Reconstruction results of off-axis vortex beam ptychography on the bar-shaped multilayer film .....	82
5.10. Final results of off-axis vortex beam ptychography on the bar-shaped multilayer film .....	83
5.11. Resolution estimation of off-axis vortex beam ptychography by FRC with the 0.5-bit information threshold curve.....	83
 6.1. PFM images of BiFeO <sub>3</sub> thin film .....	89
6.2. Contrast changes of satellite peaks from ferroelectric domains with respect to a specular peak during $\theta$ -rocking at a photon energy of 7.130 keV .....	90
6.3. Diffraction patterns measured near the pseudocubic (0 0 1) Bragg peak of BiFeO <sub>3</sub> with the $\theta$ -offset of $-0.062^\circ$ at a photon energy of 7.124 keV .....	91
6.4. X-ray fluorescence signals and their asymmetry ratios for helical dichroism measured with different sample orientations.....	92
6.5. Asymmetry ratios of X-ray fluorescence signals for linear dichroism .....	93
 7.1. Schematic diagram of the $k$ -space CNN for denoising noisy, partially damaged diffraction patterns .....	96
7.2. Schematic diagram of dataset generation for the $k$ -space CNN.....	97
7.3. Phase retrieval of the simulated diffraction pattern with deep denoising .....	100
7.4. Box and whisker plots to compare deep denoising and the Gaussian smoothing on	

phase retrieval .....	101
7.5. Phase retrieval of the single-pulse diffraction pattern from the core–shell nanoparticle with deep denoising .....	102
7.6. Denoising and phase retrieval of the single-pulse diffraction pattern from the core–shell nanoparticle by various denoising methods .....	103
7.7. Denoising results near the zeroth speckle by various denoising methods .....	104
7.8. Reconstruction results by HIO, GPS, and dpGPS .....	106
 8.1. Schematic diagrams of dataset generation and architecture of the DNN for phase retrieval of imperfect, photon-limited diffraction patterns .....	109
8.2. Ablation studies on loss function components .....	112
8.3. Training results of DPR with different conditions .....	113
8.4. Phase retrieval of the simulated diffraction patterns by DPR .....	115
8.5. Phase retrieval of single-pulse diffraction patterns from actual experiments at PAL-XFEL by DPR .....	118
8.6. Radial distributions of local <i>R</i> -factors from reconstructions of experimental data measured at PAL-XFEL .....	119
8.7. Phase retrieval of experimental data measured at PAL-XFEL by DPR without centrosymmetric filling .....	120
8.8. Phase retrieval of single-pulse diffraction patterns from CXIDB by DPR .....	121
8.9. Radial distributions of local <i>R</i> -factors from reconstructions of experimental data from CXIDB .....	122

## List of Tables

7.1. Full description of layers composing the <i>k</i> -space CNN .....	96
 8.1. Full description of layers composing the DNN for phase retrieval .....	110

## I. Introduction

X-ray microscopy has been widely used for high-resolution imaging of various specimens including both crystalline and non-crystalline samples [1]. Utilizing short wavelength and high penetration power of the X-rays, it offers much higher resolution compared to optical microscopy while dealing with micron-sized specimens, which cannot be treated by electron microscopy. However, its resolution is limited by the performance of image-forming optics, restricting high potential of the X-rays. In this regard, lensless imaging methods have been requested strongly in the X-ray regime with their aberration-free diffraction-limited imaging performance.

Coherent diffraction imaging (CDI) is a lensless imaging method measuring diffraction patterns rather than object images formed by the optics. CDI offers diffraction-limited resolution without any aberrations in principle. However, a main problem of CDI is that diffraction signals lost their phase information during measurements, so-called the phase problem; therefore, a direct inversion from the Fourier space, or equivalently reciprocal space, to the real space is not possible, requiring an additional phase recovery process. Such procedure is called phase retrieval and is required to solve phase problems typically suffered in crystallography and optics [2]. Starting from Gerchberg and Saxton in 1972, various iterative algorithms have been suggested to solve phase problems [3,4].

The first experimental realization of CDI for a nonperiodic object was accomplished by Miao *et al.* in 1999 [5]. After this success, CDI has been widely used in multidisciplinary sciences, that require high-resolution imaging, together with its variants, such as Bragg CDI, Fresnel CDI, ptychography, etc., and is also possible to be applied to electron diffractions, facilitating atomic-resolution imaging for several specimens [6,7]. Moreover, development of X-ray free-electron lasers (XFELs) has enabled time-resolved studies with superior spatiotemporal resolutions in few-nanometer, sub-picosecond scales [8–11].

Despite the excellence of CDI, its performance has been limited by several constraints that are suffered in actual experimental situations. In this circumstance, we developed dedicated methods to enhance performance and functionality of CDI in two main branches of introducing

new experimental techniques or employing deep-learning (DL) models, overcoming such limitations.

The methods in the first branch includes multidistance CDI, off-axis vortex beam ptychography, and helical dichroism on ferroelectric topological defects [12,13]. First, the multidistance CDI overcomes a trade-off between resolution and reciprocal-space sampling for large specimens with finite-size detectors by measuring diffraction patterns at different distances. Next, the off-axis vortex beam ptychography offers edge-enhanced, phase-sensitive images of weakly scattering specimens by using off-axis vortex beams. Last, helical dichroism on ferroelectric topological defects experimentally demonstrated, and further application on Bragg ptychography is suggested for functional imaging of ferroelectric systems.

The methods in the second branch consists of DL models for denoising and real-time phase retrieval of noisy, imperfect diffraction patterns measured using XFELs [14,15]. When using XFELs, each diffraction pattern is measured by a single ultrashort pulse in diffraction-before-destruction scheme due to their intense X-ray pulses that instantly destroy specimens [16,17]. In this regard, the measurements undergo strong noises and partial omissions from limited photon counts in a single pulse and use of beam stops to occlude intense direct transmission. Conventional methods are hard to handle such obstacles, and this becomes more severe for high-repetition-rate XFELs that generate huge amounts of data. In this circumstance, the proposed DL models offer working solutions, facilitating denoising and real-time phase retrieval of noise-buried, partially damaged diffraction patterns.

This thesis aims to introduce the abovementioned newly proposed methodologies with their basic theoretical backgrounds. It covers the background knowledges including diffraction, phase retrieval, and vortex beam in Part II and introductions of newly proposed methodologies to improve performance and functionality of current diffraction imaging methods in Part III and IV. Through this thesis, it is expected to have better understanding and further insights on diffraction imaging and its application.

## II. Background

### 1. Diffraction of electromagnetic waves

#### 1.1. Introduction

Diffraction is a phenomenon that waves deviate when passing obstacles, and it is one of the important properties of the waves. Diffracted waves are forming certain patterns by constructive and destructive interferences, and obviously, such patterns also appear in a case of light, an electromagnetic wave. The interference of light was first experimentally demonstrated by Thomas Young in early 1800s through his well-known double-slit experiment [18]. Since his experimental efforts, a wave nature of the light has been generally accepted.

In a quantum-mechanical perspective, the light can be described as photons, which are quanta of the electromagnetic field. Accordingly, the diffraction of the light can be understood as a collective behavior of the photons scattered by the obstacles, where the interference of their wave functions leads to characteristic diffraction patterns. In modern condensed matter physics, this point of view is necessary to interpret diffractions with various materials such as strongly correlated, exotic, and quantum materials. Thus, understanding both concepts is important to comprehend basic background of diffraction imaging methods and further applications. In this chapter, an overall review on diffraction of electromagnetic waves and a brief introduction of CDI and ptychography would be covered.

#### 1.2. Electromagnetic wave equation

Electromagnetic beams, which are generated by various kinds of resonators, can be described by the inhomogeneous electromagnetic wave equation [19]. Starting from the Maxwell's equations, the curl of the magnetic field satisfy the following relation.

$$\nabla \times \mathbf{B} = \mu_0 \mathbf{J} + \frac{1}{c^2} \frac{\partial \mathbf{E}}{\partial t} \quad (1.1)$$

, where  $\mathbf{E}$  is the electric field,  $\mathbf{B}$  is the magnetic field, and  $\mathbf{J}$  is the current density. Here, the scalar potential and vector potential are introduced for further derivation of the electromagnetic

wave equation, defined as follows.

$$\begin{cases} \mathbf{E} = -\nabla\Phi - \frac{\partial\mathbf{A}}{\partial t} \\ \mathbf{B} = \nabla \times \mathbf{A} \end{cases} \quad (1.2)$$

, where  $\Phi$  is the scalar potential and  $\mathbf{A}$  is the vector potential. When the vector potential follows the Lorenz gauge, it satisfies the following condition.

$$\nabla \cdot \mathbf{A}^L + \frac{1}{c^2} \frac{\partial \Phi^L}{\partial t} = 0 \quad (1.3)$$

, where the superscript L denotes the Lorenz gauge. As the electromagnetic fields are varied by  $e^{-i\omega t}$  with the angular frequency,  $\omega = ck$ , where  $k$  is the wavenumber, the scalar potential becomes  $\Phi^L = -(ic/k)\nabla \cdot \mathbf{A}^L$ . Thus, the electric field of the electromagnetic beam can be expressed only with the vector potential as follows.

$$\mathbf{E} = -\nabla\Phi^L - \frac{\partial\mathbf{A}^L}{\partial t} = \frac{ic}{k}\nabla(\nabla \cdot \mathbf{A}^L) + ick\mathbf{A}^L \quad (1.4)$$

Substituting the electric and magnetic fields with the vector potential, Eq. (1.1) becomes as follows.

$$\nabla \times (\nabla \times \mathbf{A}^L) - \nabla(\nabla \cdot \mathbf{A}^L) - k^2\mathbf{A}^L = \mu_0\mathbf{J} \quad (1.5)$$

Using the curl of the curl identity,  $\nabla \times (\nabla \times \mathbf{A}^L) = \nabla(\nabla \cdot \mathbf{A}^L) - \nabla^2\mathbf{A}^L$ , Eq. (1.4) finally simplified as follows.

$$(\nabla^2 + k^2)\mathbf{A}^L = -\mu_0\mathbf{J} \quad (1.6)$$

This equation is the inhomogeneous electromagnetic wave equation.

Considering the electromagnetic beam under the transversality condition (i.e.,  $\nabla \cdot \mathbf{A} = 0$  or  $\mathbf{k} \cdot \mathbf{A} = 0$  with the wavevector,  $\mathbf{k}$ ), that is usually assumed for paraxial beams, Eq. (1.6) becomes equivalent with the Helmholtz equation defined as follows.

$$(\nabla^2 + k^2)\mathbf{A}^L = 0 \quad (1.7)$$

When the beam is propagating along z-axis, the vector potential of the beam can be simply

defined as  $\mathbf{A}^L(\mathbf{r}) = \boldsymbol{\varepsilon} u(\mathbf{r}) e^{ikz}$ , where  $\boldsymbol{\varepsilon}$  is the polarization vector, that is orthogonal to the  $z$ -axis. Substituting the vector potential with the above equation, Eq. (1.7) becomes as follows [19].

$$\nabla^2 u + 2ik \frac{\partial u}{\partial z} = 0 \quad (1.8)$$

For the paraxial beams, the paraxial approximation is frequently used for the simplicity. Such approximation is valid under the following conditions that  $u(\mathbf{r})$  is a slowly varying function along  $z$ -axis.

$$\left| \frac{\partial^2 u}{\partial z^2} \right| \ll \left| 2k \frac{\partial u}{\partial z} \right|, \quad \left| \frac{\partial^2 u}{\partial z^2} \right| \ll |\nabla_{\perp}^2 u| \quad (1.9)$$

, where  $\perp$  denotes the transverse directions. Then, Eq. (1.7) becomes the paraxial wave equation as follows.

$$\nabla_{\perp}^2 u + 2ik \frac{\partial u}{\partial z} = 0 \quad (1.10)$$

A solution of Eq. (1.10) includes various Gaussian modes, which would be discussed in Chapter 3.

When the polarization vector of the beam is not perpendicular to its wavevector, the divergence of the vector potential becomes nonzero, not satisfying the transversality condition. The Lorenz gauge becomes no longer convenient because of the nonvanishing scalar potential. In this circumstance, the Coulomb gauge might be preferred, in which the scalar potential vanishes and the vector potential is transverse [20]. When the vector potential follows the Coulomb gauge, it satisfies the following condition.

$$\nabla \cdot \mathbf{A}^C = 0 \quad (1.11)$$

, where the superscript  $C$  denotes the Coulomb gauge. Ignoring the scalar potential, the electric field of the electromagnetic beam can be expressed with the vector potential as follows.

$$\mathbf{E} = i c k \mathbf{A}^C \quad (1.12)$$

Thus, comparing Eqs. (1.4) and (1.12), the vector potentials in the Lorenz and Coulomb gauge have the following relationship.

$$\mathbf{A}^C = \frac{\nabla(\nabla \cdot \mathbf{A}^L)}{k^2} + \mathbf{A}^L \quad (1.13)$$

### 1.3. Quantized radiation field

In quantum mechanics, photons can be treated as the excitations of the radiation field, replacing the Fourier coefficients by annihilation and creation operators if the radiation oscillator has canonical variables composed of noncanonical operators [21]. Starting from the classical radiation field, which satisfies the transversality condition, the vector potential can be decomposed by Fourier series at the instant ( $t = 0$ ) with an assumption of the periodic boundary condition as follows.

$$\mathbf{A}(\mathbf{r}, t)|_{t=0} = \frac{1}{\sqrt{V}} \sum_{\mathbf{k}} \sum_{\alpha=1,2} [c_{\mathbf{k},\alpha}(0) \mathbf{u}_{\mathbf{k},\alpha}(\mathbf{r}) + c_{\mathbf{k},\alpha}^*(0) \mathbf{u}_{\mathbf{k},\alpha}^*(\mathbf{r})] \quad (1.14)$$

with the Fourier component,  $\mathbf{u}_{\mathbf{k},\alpha}(\mathbf{r}) = \boldsymbol{\varepsilon}^{(\alpha)} e^{i\mathbf{k}\cdot\mathbf{r}}$ , where  $\alpha$  is an index for orthonormal vectors, which are perpendicular to the wavevector under the transversality condition. Here, the Fourier components satisfy following conditions.

$$\begin{aligned} \int d^3\mathbf{r} \mathbf{u}_{\mathbf{k},\alpha} \cdot \mathbf{u}_{\mathbf{k}',\alpha'}^* &= V \delta_{\mathbf{k},\mathbf{k}'} \delta_{\alpha,\alpha'} \\ \int d^3\mathbf{r} \left\{ \mathbf{u}_{\mathbf{k},\alpha} \cdot \mathbf{u}_{\mathbf{k}',\alpha'}^* \right\} &= V \delta_{\mathbf{k},-\mathbf{k}'} \delta_{\alpha\alpha'} \end{aligned} \quad (1.15)$$

Simply assigning time-dependent terms,  $e^{-i\omega t}$ , to the Fourier coefficients, the vector potential becomes as follows.

$$\begin{aligned} \mathbf{A}(\mathbf{r}, t) &= \frac{1}{\sqrt{V}} \sum_{\mathbf{k}} \sum_{\alpha} [c_{\mathbf{k},\alpha}(t) \boldsymbol{\varepsilon}^{(\alpha)} e^{i\mathbf{k}\cdot\mathbf{r}} + c_{\mathbf{k},\alpha}^*(t) \boldsymbol{\varepsilon}^{(\alpha)} e^{-i\mathbf{k}\cdot\mathbf{r}}] \\ &= \frac{1}{\sqrt{V}} \sum_{\mathbf{k}} \sum_{\alpha} [c_{\mathbf{k},\alpha}(0) \boldsymbol{\varepsilon}^{(\alpha)} e^{i(\mathbf{k}\cdot\mathbf{r}-\omega t)} + c_{\mathbf{k},\alpha}^*(0) \boldsymbol{\varepsilon}^{(\alpha)} e^{-i(\mathbf{k}\cdot\mathbf{r}-\omega t)}] \end{aligned} \quad (1.16)$$

For the quantized radiation field, the Fourier coefficients should be substituted by  $c_{\mathbf{k},\alpha}(t) \rightarrow \sqrt{\hbar/2\omega\epsilon_0} a_{\mathbf{k},\alpha}(t)$  and  $c_{\mathbf{k},\alpha}^*(t) \rightarrow \sqrt{\hbar/2\omega\epsilon_0} a_{\mathbf{k},\alpha}^\dagger(t)$ , where  $a_{\mathbf{k},\alpha}(t)$  and  $a_{\mathbf{k},\alpha}^\dagger(t)$  are annihilation and creation operators, respectively. Then, Eq. (1.16) becomes as follows.

$$\mathbf{A}(\mathbf{r}, t) = \frac{1}{\sqrt{V}} \sum_{\mathbf{k}} \sum_{\alpha} \sqrt{\hbar/2\omega\epsilon_0} [a_{\mathbf{k},\alpha}(t) \boldsymbol{\epsilon}^{(\alpha)} e^{i\mathbf{k}\cdot\mathbf{r}} + a_{\mathbf{k},\alpha}^\dagger(t) \boldsymbol{\epsilon}^{(\alpha)} e^{-i\mathbf{k}\cdot\mathbf{r}}] \quad (1.17)$$

The Hamiltonian operator of the quantized radiation field is defined as follows.

$$H = \frac{1}{2} \int d^3\mathbf{r} \left( \epsilon_0 |\mathbf{E}|^2 + \frac{1}{\mu_0} |\mathbf{B}|^2 \right) \quad (1.18)$$

Using Eq. (1.15), the first part of Eq. (1.18) is calculated as follows.

$$\begin{aligned} H^{(1)} &= \frac{\epsilon_0}{2} \int d^3\mathbf{r} \left| \frac{\partial \mathbf{A}}{\partial t} \right|^2 \\ &= \frac{\hbar\omega}{4V} \sum_{\mathbf{k}, \mathbf{k}'} \sum_{\alpha, \alpha'} \int d^3\mathbf{r} (a_{\mathbf{k},\alpha} \mathbf{u}_{\mathbf{k},\alpha} + a_{\mathbf{k},\alpha}^\dagger \mathbf{u}_{\mathbf{k},\alpha}^*) \cdot (a_{\mathbf{k}',\alpha'} \mathbf{u}_{\mathbf{k}',\alpha'} + a_{\mathbf{k}',\alpha'}^\dagger \mathbf{u}_{\mathbf{k}',\alpha'}^*) \\ &= \frac{\hbar\omega}{4} \sum_{\mathbf{k}, \mathbf{k}'} \sum_{\alpha, \alpha'} \left[ (a_{\mathbf{k},\alpha} a_{\mathbf{k}',\alpha'} + a_{\mathbf{k},\alpha}^\dagger a_{\mathbf{k}',\alpha'}^\dagger) \delta_{\mathbf{k}, -\mathbf{k}'} \delta_{\alpha, \alpha'} \right. \\ &\quad \left. + (a_{\mathbf{k},\alpha} a_{\mathbf{k}',\alpha'}^\dagger + a_{\mathbf{k},\alpha}^\dagger a_{\mathbf{k}',\alpha'}) \delta_{\mathbf{k}, \mathbf{k}'} \delta_{\alpha, \alpha'} \right] \\ &= \frac{\hbar\omega}{4} \sum_{\mathbf{k}} \sum_{\alpha} (a_{\mathbf{k},\alpha} a_{\mathbf{k},\alpha}^\dagger + a_{\mathbf{k},\alpha}^\dagger a_{\mathbf{k},\alpha}) \end{aligned} \quad (1.19)$$

Next, the second part of Eq. (1.18) becomes as follows.

$$\begin{aligned} H^{(2)} &= \frac{1}{2\mu_0} \int d^3\mathbf{r} |\nabla \times \mathbf{A}|^2 \\ &= \frac{\hbar c^2}{4\omega V} \sum_{\mathbf{k}, \mathbf{k}'} \sum_{\alpha, \alpha'} \int d^3\mathbf{r} (a_{\mathbf{k},\alpha} \nabla \times \mathbf{u}_{\mathbf{k},\alpha} + a_{\mathbf{k},\alpha}^\dagger \nabla \times \mathbf{u}_{\mathbf{k},\alpha}^*) \\ &\quad \cdot (a_{\mathbf{k}',\alpha'} \nabla \times \mathbf{u}_{\mathbf{k}',\alpha'} + a_{\mathbf{k}',\alpha'}^\dagger \nabla \times \mathbf{u}_{\mathbf{k}',\alpha'}^*) \end{aligned} \quad (1.20)$$

Using the vector calculus identities with the transversality and periodic boundary conditions, the dot product of the curls in Eq. (1.20) is simplified as follows.

$$\begin{aligned}
\int d^3r (\nabla \times \mathbf{u}_{k,\alpha}) \cdot (\nabla \times \mathbf{u}_{k',\alpha'}^*) &= \int d^3r [\nabla \cdot \{\mathbf{u}_{k,\alpha} \times (\nabla \times \mathbf{u}_{k',\alpha'}^*)\} \\
&\quad + \mathbf{u}_{k,\alpha} \cdot \{\nabla \times (\nabla \times \mathbf{u}_{k',\alpha'}^*)\}] \\
&= \int d^3r [\nabla \cdot \{\mathbf{u}_{k,\alpha} \times (\nabla \times \mathbf{u}_{k',\alpha'}^*)\} \\
&\quad + \mathbf{u}_{k,\alpha} \cdot \{\nabla(\nabla \cdot \mathbf{u}_{k',\alpha'}^*) - \nabla^2 \mathbf{u}_{k',\alpha'}^*\}] \\
&= - \int d^3r \mathbf{u}_{k,\alpha} \cdot \nabla^2 \mathbf{u}_{k',\alpha'}^* \\
&= \left(\frac{\omega}{c}\right)^2 \int d^3r \mathbf{u}_{k,\alpha} \cdot \mathbf{u}_{k',\alpha'}^*
\end{aligned} \tag{1.21}$$

Substituting the above results with Eq. (1.15), Eq. (1.20) becomes as follows.

$$\begin{aligned}
H^{(2)} &= \frac{\hbar\omega}{4} \sum_{\mathbf{k}, \mathbf{k}'} \sum_{\alpha, \alpha'} \left[ \left( a_{\mathbf{k},\alpha} a_{\mathbf{k}',\alpha'} + a_{\mathbf{k},\alpha}^\dagger a_{\mathbf{k}',\alpha'}^\dagger \right) \delta_{\mathbf{k},-\mathbf{k}'} \delta_{\alpha\alpha'} \right. \\
&\quad \left. + \left( a_{\mathbf{k},\alpha} a_{\mathbf{k}',\alpha'}^\dagger + a_{\mathbf{k},\alpha}^\dagger a_{\mathbf{k}',\alpha'} \right) \delta_{\mathbf{k},\mathbf{k}'} \delta_{\alpha,\alpha'} \right] \\
&= \frac{\hbar\omega}{4} \sum_{\mathbf{k}} \sum_{\alpha} (a_{\mathbf{k},\alpha} a_{\mathbf{k},\alpha}^\dagger + a_{\mathbf{k},\alpha}^\dagger a_{\mathbf{k},\alpha})
\end{aligned} \tag{1.22}$$

As  $a_{\mathbf{k},\alpha}^\dagger a_{\mathbf{k},\alpha} = N_{\mathbf{k},\alpha}$  and  $a_{\mathbf{k},\alpha} a_{\mathbf{k},\alpha}^\dagger = N_{\mathbf{k},\alpha} + 1$ , where  $N_{\mathbf{k},\alpha}$  is the number operator, the Hamiltonian operator finally summarized into the following equation.

$$\begin{aligned}
H &= \frac{\hbar\omega}{2} \sum_{\mathbf{k}} \sum_{\alpha} (a_{\mathbf{k},\alpha} a_{\mathbf{k},\alpha}^\dagger + a_{\mathbf{k},\alpha}^\dagger a_{\mathbf{k},\alpha}) \\
&= \sum_{\mathbf{k}} \sum_{\alpha} \left( N_{\mathbf{k},\alpha} + \frac{1}{2} \right) \hbar\omega
\end{aligned} \tag{1.23}$$

## 1.4. Light–matter interaction

The interaction between the quantized radiation field and nonrelativistic electrons of an atom can be expressed based on the interaction Hamiltonian defined as follows [21].

$$H_{\text{int}} = \sum_i \left[ -\frac{e}{2mc} \{ \mathbf{p}_i \cdot \mathbf{A}(\mathbf{r}_i, t) + \mathbf{A}(\mathbf{r}_i, t) \cdot \mathbf{p}_i \} + \frac{e^2}{2mc^2} \mathbf{A}(\mathbf{r}_i, t) \cdot \mathbf{A}(\mathbf{r}_i, t) \right] \tag{1.24}$$

, where  $\mathbf{p}$  is the momentum operator and  $i$  is an index for each atomic electron. If the spins

of the atomic electrons become significant, they interact with the magnetic field; therefore, the interaction Hamiltonian additionally has the following term.

$$H_{\text{int}}^{(\text{spin})} = - \sum_i \frac{e\hbar}{2mc} \boldsymbol{\sigma}_i \cdot [\nabla \times \mathbf{A}(\mathbf{r}, t)]_{\mathbf{r}=\mathbf{r}_i} \quad (1.25)$$

, where  $\boldsymbol{\sigma}$  is a tensor describing the spin interaction.

For the calculation of the absorption and emission of a photon by the atom, the following relations associated with the momentum operator are used. First, the momentum operator,  $\mathbf{p} = -i\hbar\nabla$ , satisfies the following relation under the transversality condition.

$$\mathbf{p} \cdot (\mathbf{A}\psi) = -i\hbar(\nabla \cdot \mathbf{A})\psi - i\hbar\mathbf{A} \cdot (\nabla\psi) = -i\hbar\mathbf{A} \cdot (\nabla\psi) \equiv \mathbf{A} \cdot (\mathbf{p}\psi) \quad (1.26)$$

The momentum operator is applied to the everything on the right, and this relation makes the calculation easier by replacing  $\mathbf{p} \cdot \mathbf{A}$  with  $\mathbf{A} \cdot \mathbf{p}$ . Next, the square of the momentum operator has the following commutation relation.

$$\begin{aligned} [\mathbf{p}^2, \mathbf{r}]\psi &= \mathbf{p}[\mathbf{p}(\mathbf{r}\psi)] - \mathbf{r}[\mathbf{p}(\mathbf{p}\psi)] \\ &= [\mathbf{p}(\mathbf{pr})]\psi + 2(\mathbf{pr})(\mathbf{p}\psi) + \mathbf{r}[\mathbf{p}(\mathbf{p}\psi)] - \mathbf{r}[\mathbf{p}(\mathbf{p}\psi)] \\ &= -\hbar^2(\nabla\mathbb{I})\psi - 2\hbar^2\mathbb{I}\nabla\psi \\ &= -2\hbar^2\nabla\psi \\ &\equiv -2i\hbar\mathbf{p}\psi \end{aligned} \quad (1.27)$$

Considering the Hamiltonian operator,  $H_0 = \mathbf{p}^2/2m$ , the momentum operator can be replaced as follows.

$$\mathbf{p} = \frac{i}{2\hbar}[\mathbf{p}^2, \mathbf{r}] = \frac{im}{\hbar}[H_0, \mathbf{r}] \quad (1.28)$$

As mentioned in Section 1.3, the vector potential is formed by a linear combination of the annihilation and creation operators, leading to the quantization of the radiation field. In the case that an atom absorbs a single photon,  $n_{k,\alpha} \rightarrow n_{k,\alpha} - 1$ , and its state changes from the initial state to the final state,  $g \rightarrow f$ , the radiative transition can be described as follows.

$$\langle f; n_{k,\alpha} - 1 | H_{\text{int}} | g; n_{k,\alpha} \rangle \quad (1.29)$$

Using the Eqs. (1.17) and (1.26), Eq. (1.29) becomes as follows. Here, only components with

the single annihilation operator did not vanish for the single-photon absorption.

$$\begin{aligned} & -\frac{e}{mc} \sqrt{\frac{\hbar}{2\omega V \epsilon_0}} \langle f; n_{k,\alpha} - 1 | \sum_i [a_{k,\alpha}(0) \boldsymbol{\epsilon}^{(\alpha)} e^{i(\mathbf{k} \cdot \mathbf{r}_i - \omega t)}] \cdot \mathbf{p}_i | g; n_{k,\alpha} \rangle \quad (1.30) \\ & = -\frac{e}{mc} \sqrt{\frac{n_{k,\alpha} \hbar}{2\omega V \epsilon_0}} \sum_i \langle f; n_{k,\alpha} - 1 | e^{i\mathbf{k} \cdot \mathbf{r}_i} \boldsymbol{\epsilon}^{(\alpha)} \cdot \mathbf{p}_i | g; n_{k,\alpha} - 1 \rangle e^{-i\omega t} \end{aligned}$$

Similarly, in the case of the radiative transition from  $|g; n_{k,\alpha}\rangle$  to  $|f; n_{k,\alpha} + 1\rangle$  by the single-photon emission, it can be described as follows.

$$\begin{aligned} & -\frac{e}{mc} \sqrt{\frac{\hbar}{2\omega V \epsilon_0}} \langle f; n_{k,\alpha} + 1 | \sum_i [a_{k,\alpha}^\dagger(0) \boldsymbol{\epsilon}^{(\alpha)} e^{-i(\mathbf{k} \cdot \mathbf{r}_i - \omega t)}] \cdot \mathbf{p}_i | g; n_{k,\alpha} \rangle \quad (1.31) \\ & = -\frac{e}{mc} \sqrt{\frac{(n_{k,\alpha} + 1) \hbar}{2\omega V \epsilon_0}} \sum_i \langle f; n_{k,\alpha} + 1 | e^{-i\mathbf{k} \cdot \mathbf{r}_i} \boldsymbol{\epsilon}^{(\alpha)} \cdot \mathbf{p}_i | g; n_{k,\alpha} + 1 \rangle e^{i\omega t} \end{aligned}$$

Typically, as the wavelength is typically much larger than the atomic radius,  $\lambda = 2\pi/|\mathbf{k}| \gg |\mathbf{r}|$ , we can approximate  $e^{-i\mathbf{k} \cdot \mathbf{r}_i}$  as  $e^{-i\mathbf{k} \cdot \mathbf{r}_i} = 1 - i\mathbf{k} \cdot \mathbf{r}_i + (\mathbf{k} \cdot \mathbf{r}_i)^2/2 + \dots$ . When only the leading term does not vanish as  $e^{-i\mathbf{k} \cdot \mathbf{r}_i} \approx 1$ , such approximation is called electric dipole (E1) approximation.

## 1.5. The Lippmann–Schwinger equation

To describe the scattering process of a particle by a scatterer, which has a nonzero potential energy,  $V$ , the Hamiltonian can be simply defined as  $H = H_0 + V$  [22]. If the particle does not lose the energy during the scattering process, this process is called elastic scattering. For the elastic scattering, the time-independent Schrödinger equation is defined as follows.

$$H_0 |\phi\rangle = E |\phi\rangle, \quad (H_0 + V) |\psi\rangle = E |\psi\rangle \quad (1.32)$$

, where  $|\phi\rangle$  and  $|\psi\rangle$  are the solution for free and scattered particles, respectively. As  $|\psi\rangle$  becomes equivalent with  $|\phi\rangle$  when  $V \rightarrow 0$ , the solution is desired to have the following form.

$$|\psi\rangle = |\phi\rangle + \frac{1}{E - H_0} V |\psi\rangle \quad (1.33)$$

However, a complication arises by the singularity of  $1/(E - H_0)$ . To resolve such issue, the small imaginary component,  $\pm i\varepsilon$ , is added to the energy eigenvalue.

$$|\psi^{(\pm)}\rangle = |\phi\rangle + \frac{1}{E - H_0 \pm i\varepsilon} V |\psi^{(\pm)}\rangle \quad (1.34)$$

This equation is called the Lippmann–Schwinger equation. Note that it is a ket equation regardless of its representations.

Using the position basis, the Lippman–Schwinger equation becomes as follows.

$$\langle \mathbf{r} | \psi^{(\pm)} \rangle = \langle \mathbf{r} | \phi \rangle + \int d^3 \mathbf{r}' \left\langle \mathbf{r} \left| \frac{1}{E - H_0 \pm i\varepsilon} \right| \mathbf{r}' \right\rangle \langle \mathbf{r}' | V | \psi^{(\pm)} \rangle \quad (1.35)$$

First, the first part in the integral term can be expanded with the momentum operator as follows.

$$\begin{aligned} \left\langle \mathbf{r} \left| \frac{1}{E - H_0 \pm i\varepsilon} \right| \mathbf{r}' \right\rangle &= \int d^3 \mathbf{p}' \int d^3 \mathbf{p}'' \langle \mathbf{r} | \mathbf{p}' \rangle \\ &\quad \times \left\langle \mathbf{p}' \left| \frac{1}{E - H_0 \pm i\varepsilon} \right| \mathbf{p}'' \right\rangle \langle \mathbf{p}'' | \mathbf{r}' \rangle \end{aligned} \quad (1.36)$$

As  $\langle \mathbf{r} | \mathbf{p}' \rangle = e^{i\mathbf{p}' \cdot \mathbf{r}/\hbar} / (2\pi\hbar)^{3/2}$  and  $\langle \mathbf{p}'' | \mathbf{r}' \rangle = e^{-i\mathbf{p}'' \cdot \mathbf{r}'/\hbar} / (2\pi\hbar)^{3/2}$ , Eq. (1.36) becomes as follows.

$$\begin{aligned} &\frac{1}{(2\pi\hbar)^3} \int d^3 \mathbf{p}' e^{i\mathbf{p}' \cdot \mathbf{r}/\hbar} \int d^3 \mathbf{p}'' \frac{\delta^{(3)}(\mathbf{p}' - \mathbf{p}'')}{E - \mathbf{p}'^2/2m \pm i\varepsilon} e^{-i\mathbf{p}'' \cdot \mathbf{r}'/\hbar} \\ &= \frac{1}{(2\pi\hbar)^3} \int d^3 \mathbf{p}' \frac{e^{i\mathbf{p}' \cdot (\mathbf{r} - \mathbf{r}')/\hbar}}{E - \mathbf{p}'^2/2m \pm i\varepsilon} \end{aligned} \quad (1.37)$$

Substituting by  $E = \hbar^2 k^2 / 2m$ ,  $\mathbf{p}' = \hbar \mathbf{q}$ , and  $\varepsilon' = 2m\varepsilon/\hbar^2$ , Eq. (1.37) becomes as follows.

$$\begin{aligned} &\frac{2m}{\hbar^2} \frac{1}{(2\pi)^3} \int_0^\infty dq \int_0^{2\pi} d\phi \int_{-1}^1 d(\cos\theta) \frac{q^2 e^{iq|\mathbf{r} - \mathbf{r}'| \cos\theta}}{k^2 - q^2 \pm i\varepsilon'} \\ &= \frac{2m}{\hbar^2} \frac{i}{4\pi^2 |\mathbf{r} - \mathbf{r}'|} \int_0^\infty dq \frac{q(e^{iq|\mathbf{r} - \mathbf{r}'|} - e^{-iq|\mathbf{r} - \mathbf{r}'|})}{q^2 - k^2 \mp i\varepsilon'} \end{aligned} \quad (1.38)$$

As the integrand is an even function, the integral term in Eq. (1.38) can be calculated using the

residue theorem for the contour enclosing the singularity. Note that the singularity for each term has an opposite sign, considering the sign of the coefficients in the exponents.

$$\begin{aligned} & \frac{1}{2} \int_{-\infty}^{\infty} dq \frac{q(e^{iq|r-r'|} - e^{-iq|r-r'|})}{q^2 - k^2 \mp i\varepsilon'} \\ &= \pi i \cdot \left[ \text{Res}_{q=\pm\sqrt{k^2\pm i\varepsilon'}} \left\{ \frac{qe^{iq|r-r'|}}{q^2 - k^2 \mp i\varepsilon'} \right\} - \text{Res}_{q=\mp\sqrt{k^2+i\varepsilon'}} \left\{ \frac{qe^{-iq|r-r'|}}{q^2 - k^2 \mp i\varepsilon'} \right\} \right] \\ &= \pi i e^{\pm i\sqrt{k^2\pm i\varepsilon'}|r-r'|} \approx \pi i e^{\pm ik|r-r'|} \end{aligned} \quad (1.39)$$

Thus, Eq. (1.36) finally becomes as follows.

$$\langle \mathbf{r} | \frac{1}{E - H_0 \pm i\varepsilon} | \mathbf{r}' \rangle = -\frac{2m}{\hbar^2} \frac{e^{\pm ik|r-r'|}}{4\pi|\mathbf{r} - \mathbf{r}'|} \quad (1.40)$$

Using the above result, Eq. (1.35) becomes as follows.

$$\langle \mathbf{r} | \psi^{(\pm)} \rangle = \langle \mathbf{r} | \phi \rangle - \frac{2m}{\hbar^2} \int d^3 \mathbf{r}' \frac{e^{\pm ik|r-r'|}}{4\pi|\mathbf{r} - \mathbf{r}'|} \langle \mathbf{r}' | V | \psi^{(\pm)} \rangle \quad (1.41)$$

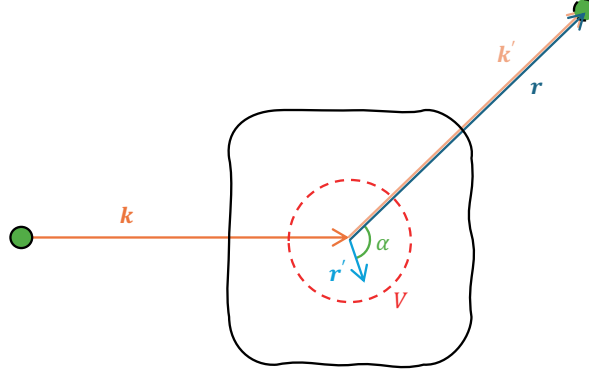


**Figure 1.1** · Schematic diagram for the scattering of a particle by a scatterer.

For an explicit calculation of the wave function, a potential, which is local, satisfying  $\langle \mathbf{r}' | V | \mathbf{r}'' \rangle = V(\mathbf{r}') \delta^{(3)}(\mathbf{r}' - \mathbf{r}'')$ , is considered. This local potential is reasonable in practical scattering schemes, where scatterers are mostly electrons, which have finite-range potentials. Then, Eq. (1.41) becomes as follows.

$$\langle \mathbf{r} | \psi^{(\pm)} \rangle = \langle \mathbf{r} | \phi \rangle - \frac{2m}{\hbar^2} \int d^3 \mathbf{r}' \frac{e^{\pm ik|r-r'|}}{4\pi|\mathbf{r} - \mathbf{r}'|} V(\mathbf{r}') \langle \mathbf{r}' | \psi^{(\pm)} \rangle \quad (1.42)$$

In the practical circumstances, the observation is conducted much far from the scatterers,  $|\mathbf{r}| \gg |\mathbf{r}'|$ . The distance between the scatterer and the observation point is simply written as follows.

$$\begin{aligned} |\mathbf{r} - \mathbf{r}'| &= \sqrt{r^2 - 2rr' \cos \alpha + r'^2} \\ &= r \left( 1 - \frac{2r'}{r} \cos \alpha + \frac{r'^2}{r^2} \right)^{1/2} \\ &\approx r - \hat{\mathbf{r}} \cdot \mathbf{r}' \end{aligned} \quad (1.43)$$

, where  $\alpha$  is an angle between two position vectors,  $\mathbf{r}$  and  $\mathbf{r}'$ . This approximation gives  $1/|\mathbf{r} - \mathbf{r}'| \approx 1/r$  and  $e^{\pm ik|\mathbf{r}-\mathbf{r}'|} \approx e^{\pm ikr} e^{\mp ik' \cdot \mathbf{r}'}$  with the outgoing wavevector,  $\mathbf{k}' = k\hat{\mathbf{r}}$ . Note that the free-particle wave function,  $|\phi\rangle$ , with the wavevector,  $\mathbf{k}$ , is defined as  $\langle \mathbf{r} | \phi \rangle = e^{i\mathbf{k} \cdot \mathbf{r}} / (2\pi)^{3/2}$ . Then, the wave function with the positive sign becomes as follows.

$$\begin{aligned} \langle \mathbf{r} | \psi^{(+)} \rangle &\approx \langle \mathbf{r} | \phi \rangle - \frac{2m}{\hbar^2} \frac{e^{ikr}}{4\pi r} \int d^3 \mathbf{r}' e^{-i\mathbf{k}' \cdot \mathbf{r}'} V(\mathbf{r}') \langle \mathbf{r}' | \psi^{(+)} \rangle \\ &= \frac{1}{(2\pi)^{3/2}} \left[ e^{i\mathbf{k} \cdot \mathbf{r}} + \frac{e^{ikr}}{r} f(\mathbf{k}', \mathbf{k}) \right] \end{aligned} \quad (1.44)$$

Here, the scattering amplitude,  $f(\mathbf{k}', \mathbf{k})$ , is defined as follows.

$$\begin{aligned} f(\mathbf{k}', \mathbf{k}) &\equiv -\frac{(2\pi)^3}{4\pi} \frac{2m}{\hbar^2} \int d^3 \mathbf{r}' \frac{e^{-i\mathbf{k}' \cdot \mathbf{r}'}}{(2\pi)^{3/2}} V(\mathbf{r}') \langle \mathbf{r}' | \psi^{(+)} \rangle \\ &= -\frac{(2\pi)^3}{4\pi} \frac{2m}{\hbar^2} \int d^3 \mathbf{r}' \langle \mathbf{k}' | \mathbf{r}' \rangle V(\mathbf{r}') \langle \mathbf{r}' | \psi^{(+)} \rangle \\ &= -\frac{(2\pi)^3}{4\pi} \frac{2m}{\hbar^2} \langle \mathbf{k}' | V | \psi^{(+)} \rangle \end{aligned} \quad (1.45)$$

Similarly, for the scattered-particle wave function with the negative sign, the coefficient of the scattering amplitude in Eq. (1.44) and the bra-ket term in Eq. (1.45) are replaced by  $e^{-ikr}/r$  and  $\langle -\mathbf{k}' | V | \psi^{(-)} \rangle$ , respectively.

The differential cross section,  $d\sigma/d\Omega$ , which is the probability of particles scattered to a specific differential solid angle element, satisfies the following relation, using the terms in Eq. (1.44).

$$\begin{aligned}\frac{d\sigma}{d\Omega} d\Omega &= \frac{|\mathbf{j}_{\text{scat}}|}{|\mathbf{j}_{\text{inci}}|} r^2 d\Omega = \frac{|(e^{ikr}/r)f(\mathbf{k}', \mathbf{k})|^2}{|e^{ik\cdot r}|^2} r^2 d\Omega \\ &= |f(\mathbf{k}', \mathbf{k})|^2 d\Omega\end{aligned}\quad (1.46)$$

, where  $\mathbf{j}_{\text{inci}}$  and  $\mathbf{j}_{\text{scat}}$  are the fluxes of incident and scattered particles, respectively. Thus, the differential cross section is defined as follows.

$$\frac{d\sigma}{d\Omega} = |f(\mathbf{k}', \mathbf{k})|^2 \quad (1.47)$$

## 1.6. The Born approximation

For a calculation of the differential cross section, Eq. (1.45) is yet difficult to compute due to the unknown scattered-particle wave function,  $|\psi^{(+)}\rangle$  [22]. When the scattering by the scatterer is not strong, the wave function  $\langle \mathbf{r}' | \psi^{(+)} \rangle$  can be approximated by  $\langle \mathbf{r}' | \phi \rangle$ . Such approximation is called the first-order Born approximation. Under this approximation, the scattering amplitude becomes as follows.

$$f^{(1)}(\mathbf{k}', \mathbf{k}) = -\frac{1}{4\pi} \frac{2m}{\hbar^2} \int d^3 \mathbf{r}' e^{i\mathbf{Q}\cdot\mathbf{r}'} V(\mathbf{r}') \quad (1.48)$$

, where  $\mathbf{Q}$  is the momentum transfer, which is defined as  $\mathbf{Q} = \mathbf{k} - \mathbf{k}'$ . The integral term in Eq. (1.48) is equivalent with the 3D Fourier transform of the potential of the scatterer,  $V$ , with respect to the momentum transfer,  $\mathbf{Q}$ .

For the validity of the first-order Born approximation,  $\langle \mathbf{r}' | \psi^{(+)} \rangle$  is not far from  $\langle \mathbf{r}' | \phi \rangle$  inside the range of the finite-range potential. Considering the exact expression in Eq. (1.42), the second term should be negligible, especially at the center of the scatterer,  $\mathbf{r} \approx 0$ , giving the following condition.

$$\left| \frac{1}{4\pi} \frac{2m}{\hbar^2} \int d^3 \mathbf{r}' \frac{e^{i\mathbf{k}\cdot\mathbf{r}'}}{r'} V(\mathbf{r}') e^{i\mathbf{k}\cdot\mathbf{r}'} \right| \ll 1 \quad (1.49)$$

For the medium with a complex refractive index,  $n$ , the scattering potential is defined as follows [23].

$$V(\mathbf{r}', k) = V_0[n^2(\mathbf{r}', k) - 1] \quad (1.50)$$

, where  $V_0 = \hbar^2 k^2 / 2m$ . In the X-ray regime, where the complex refractive index is typically represented as  $n = 1 - \delta - i\beta$  with very small  $\delta$  and  $\beta$ , the scattering potential becomes as follows.

$$V(\mathbf{r}', k) \approx -2V_0(1 - n) \quad (1.51)$$

Substituting the scattering potential, Eq. (1.49) becomes as follows.

$$\begin{aligned} & \left| \frac{k^2}{2\pi}(1-n) \int dr' \int d\theta \int d\phi r' \sin \theta e^{ikr'(1+\cos \theta)} \right| \\ &= |2k(1-n)e^{ik\rho} \sin k\rho| \\ &\leq 2k|1-n| \ll 1 \end{aligned} \quad (1.52)$$

, where  $\rho$  is the outer boundary of the finite-range potential. As the first-order Born approximation represents single scattering across the medium, the thickness of the medium must be considered for a practical calculation. In this regard, Eq. (1.52) becomes as follows [24,25].

$$t < \frac{2\pi\lambda\eta}{|1-n|} \quad (1.53)$$

, where  $t$  is the thickness of the medium and  $\eta$  is a small coefficient, roughly 0.2 for the X-ray regime. When the above condition is not met, the multiple scattering effect should be considered. In this circumstance, the multislice method is generally used to reflect the multiple scattering from the medium [26].

## 1.7. Fresnel–Kirchoff diffraction formula

Previous sections have described the scattering quantum-mechanically. In the optical point of view, the scattering events have occurred during the waves propagating in the medium, and these events resultantly lead to a macroscopic interference of the waves, which is called diffraction. The diffraction has been classically described by the Huygens–Fresnel principle, treating each point of the wavefront as a spherical wave source. Kirchhoff mathematically

showed that the Huygens–Fresnel principle is an approximate form of a particular integral theorem for the homogeneous wave equation [23]. Considering a strictly monochromatic scalar wave,  $V(\mathbf{r}, t) = U(\mathbf{r})e^{-i\omega t}$ , satisfying the Helmholtz equation,  $(\nabla^2 + k^2)U = 0$ , the Green's second identity gives the following relation with an arbitrary function,  $U'$ , if both  $U$  and  $U'$  are twice continuously differentiable in the integrating region.

$$\iiint_v d\nu (U \nabla^2 U' - U' \nabla^2 U) = - \iint_S dS \left( U \frac{\partial U'}{\partial \mathbf{n}} - U' \frac{\partial U}{\partial \mathbf{n}} \right) \quad (1.54)$$

, where  $v$  is a volume enclosed by  $S$  and  $\partial/\partial \mathbf{n}$  is a directional derivative along the inward normal direction of  $dS$ . When  $U'$  also satisfies the Helmholtz equation,  $(\nabla^2 + k^2)U' = 0$ , the integrand in the left side of Eq. (1.54) vanished, giving a result as follows.

$$\iint_S dS \left( U \frac{\partial U'}{\partial \mathbf{n}} - U' \frac{\partial U}{\partial \mathbf{n}} \right) = 0 \quad (1.55)$$

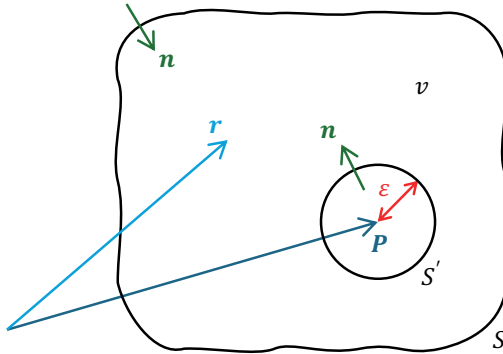


**Figure 1.2** · Schematic diagram for the derivation of the Kirchhoff's integral theorem.

For an explicit calculation,  $U'(\mathbf{r}) = e^{iks}/s$ , where  $s$  is the distance between  $\mathbf{r}$  and a certain position,  $\mathbf{P}$ , is assigned. As  $U'$  has a singularity at  $s = 0$ , the integrating region must exclude a small sphere with a radius of  $\varepsilon$ , giving the following equation.

$$\left( \iint_S + \iint_{S'} \right) dS \left[ U \frac{\partial}{\partial \mathbf{n}} \left( \frac{e^{iks}}{s} \right) - \frac{e^{iks}}{s} \frac{\partial U}{\partial \mathbf{n}} \right] = 0 \quad (1.56)$$

As  $S'$  is known, the second term becomes as follows.

$$\begin{aligned} \iint_{S'} dS \left[ U \frac{\partial}{\partial \mathbf{n}} \left( \frac{e^{iks}}{s} \right) - \frac{e^{iks}}{s} \frac{\partial U}{\partial \mathbf{n}} \right] &= \iint_{\Omega'} d\Omega \varepsilon^2 \left[ U \frac{e^{ik\varepsilon}}{\varepsilon} \left( ik - \frac{1}{\varepsilon} \right) - \frac{e^{ik\varepsilon}}{\varepsilon} \frac{\partial U}{\partial \mathbf{n}} \right] \\ &= \iint_{\Omega'} d\Omega \left[ (ik\varepsilon - 1)U - \varepsilon \frac{\partial U}{\partial \mathbf{n}} \right] e^{ik\varepsilon} \end{aligned} \quad (1.57)$$

, where  $\Omega'$  is a solid angle spanning  $S'$ . Limiting  $\varepsilon$  to zero, Eq. (1.55) finally becomes as follows.

$$U(\mathbf{P}) = \frac{1}{4\pi} \iint_S dS \left[ U \frac{\partial}{\partial \mathbf{n}} \left( \frac{e^{iks}}{s} \right) - \frac{e^{iks}}{s} \frac{\partial U}{\partial \mathbf{n}} \right] \quad (1.58)$$

This equation is called the Kirchhoff's integral theorem.

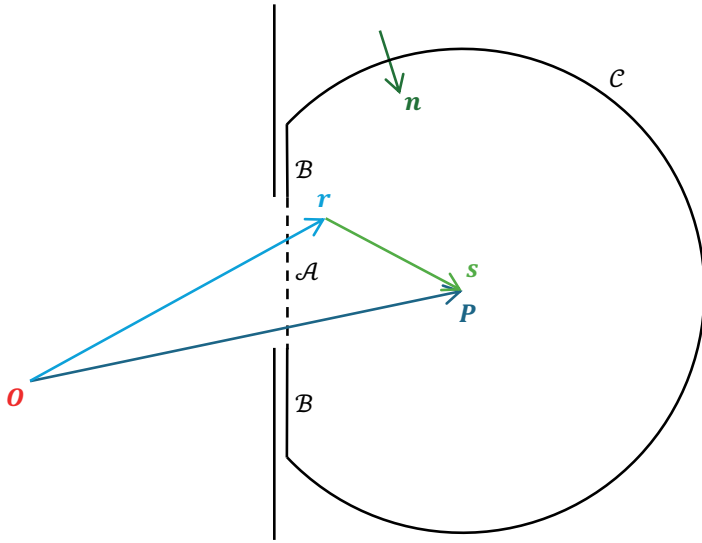


**Figure 1.3** · Schematic diagram for the derivation of the Fresnel–Kirchhoff diffraction formula.

When a monochromatic scalar wave from a point source at  $\mathbf{O}$  propagates through an aperture, the Kirchhoff's integral theorem gives the following relation.

$$U(\mathbf{P}) = \frac{1}{4\pi} \left( \iint_{\mathcal{A}} + \iint_{\mathcal{B}} + \iint_{\mathcal{C}} \right) dS \left[ U \frac{\partial}{\partial \mathbf{n}} \left( \frac{e^{iks}}{s} \right) - \frac{e^{iks}}{s} \frac{\partial U}{\partial \mathbf{n}} \right] \quad (1.59)$$

, where  $\mathcal{A}$ ,  $\mathcal{B}$ , and  $\mathcal{C}$  denote the opening, obstructing, and remaining parts of the spherical integrating surface centered at  $\mathbf{P}$ , respectively. As  $\mathcal{A}$  and  $\mathcal{B}$  is identical to the cases with the waves not affected by the aperture and the waves completely blocked, respectively, it is

reasonable to set following conditions for these regions.

$$\begin{cases} U = \frac{Ae^{ikr}}{r}, & \frac{\partial U}{\partial \mathbf{n}} = \frac{Ae^{ikr}}{r} \left( ik - \frac{1}{r} \right) \cos(\mathbf{n}, \mathbf{r}), \quad \text{on } \mathcal{A} \\ U = 0, & \frac{\partial U}{\partial \mathbf{n}} = 0, \quad \text{on } \mathcal{B} \end{cases} \quad (1.60)$$

, where  $A$  is a constant. Meanwhile, if the radius of the spherical integrating surface is so large that the disturbance at  $\mathbf{P}$  does not affect from its contribution, the integral term on  $\mathcal{C}$  vanished. Thus, Eq. (1.59) finally becomes as follows.

$$\begin{aligned} U(\mathbf{P}) &= \frac{1}{4\pi} \iint_{\mathcal{A}} dS \left[ \frac{Ae^{ikr}}{r} \frac{\partial}{\partial \mathbf{n}} \left( \frac{e^{iks}}{s} \right) - \frac{e^{iks}}{s} \frac{Ae^{ikr}}{r} \left( ik - \frac{1}{r} \right) \cos(\mathbf{n}, \mathbf{r}) \right] \\ &= \frac{A}{4\pi} \iint_{\mathcal{A}} dS \frac{e^{ik(r+s)}}{rs} \left[ \left( ik - \frac{1}{s} \right) \cos(\mathbf{n}, \mathbf{s}) - \left( ik - \frac{1}{r} \right) \cos(\mathbf{n}, \mathbf{r}) \right] \\ &= -\frac{iA}{2\lambda} \iint_{\mathcal{A}} dS \frac{e^{ik(r+s)}}{rs} [\cos(\mathbf{n}, \mathbf{r}) - \cos(\mathbf{n}, \mathbf{s})] \end{aligned} \quad (1.61)$$

This equation is called the Fresnel–Kirchhoff diffraction formula.

When  $\mathbf{r}$  and  $\mathbf{s}$  deviate by  $(\xi, \eta)$  on the aperture plane, giving  $r^2 = (x_0 - \xi)^2 + (y_0 - \eta)^2 + z_0^2$  and  $s^2 = (x - \xi)^2 + (y - \eta)^2 + z^2$  in the Cartesian coordinate,  $r$  and  $s$  can be expanded with power series as follows.

$$\begin{cases} r \approx r' - \frac{x_0\xi + y_0\eta}{r'} + \frac{\xi^2 + \eta^2}{2r'} - \frac{(x_0\xi + y_0\eta)^2}{2r'^3} \\ s \approx s' - \frac{x\xi + y\eta}{s'} + \frac{\xi^2 + \eta^2}{2s'} - \frac{(x\xi + y\eta)^2}{2s'^3} \end{cases} \quad (1.62)$$

, where  $r'^2 = x_0^2 + y_0^2 + z_0^2$  and  $s'^2 = x^2 + y^2 + z^2$ . Then, Eq. (1.61) becomes as follows.

$$U(\mathbf{P}) \approx -\frac{i \cos \delta}{\lambda} \frac{Ae^{ik(r'+s')}}{r's'} \iint_{\mathcal{A}} d\xi d\eta e^{ikf(\xi, \eta)} \quad (1.63)$$

, where  $\delta$  is an angle between  $\mathbf{P}$  and  $\mathbf{n}$  on  $\mathcal{A}$ , giving  $\cos(\mathbf{n}, \mathbf{r}) - \cos(\mathbf{n}, \mathbf{s}) \approx 2 \cos \delta$ . The function of  $\xi$  and  $\eta$  in the exponent of the integrand is defined as follows.

$$f(\xi, \eta) = \left( -\frac{x_0}{r'} - \frac{x}{s'} \right) \xi + \left( -\frac{y_0}{r'} - \frac{y}{s'} \right) \eta + \frac{1}{2} \left[ \left( \frac{1}{r'} + \frac{1}{s'} \right) (\xi^2 + \eta^2) - \frac{1}{r'} \left( \frac{x_0}{r'} \xi + \frac{y_0}{r'} \eta \right)^2 - \frac{1}{s'} \left( \frac{x}{s'} \xi + \frac{y}{s'} \eta \right)^2 \right] \quad (1.64)$$

If the quadratic terms in  $\xi$  and  $\eta$  are negligible, this is called Fraunhofer diffraction. Otherwise, if the quadratic terms cannot be neglected, this is called Fresnel diffraction. Note that the quadratic terms can be ignored if the following condition satisfies.

$$\frac{1}{2} \left[ \left( \frac{1}{r'} + \frac{1}{s'} \right) (\xi^2 + \eta^2) - \frac{1}{r'} \left( \frac{x_0}{r'} \xi + \frac{y_0}{r'} \eta \right)^2 - \frac{1}{s'} \left( \frac{x}{s'} \xi + \frac{y}{s'} \eta \right)^2 \right] \ll \lambda \quad (1.65)$$

## 1.8. Bragg's law and Ewald sphere

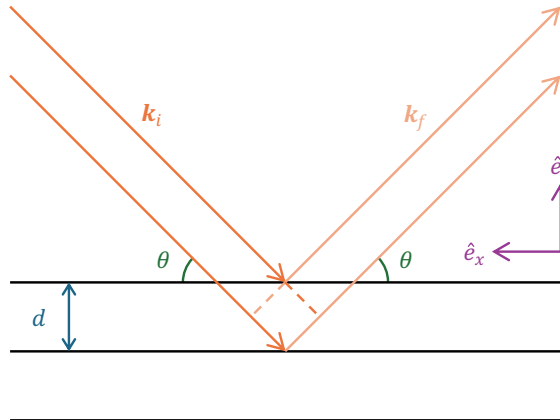


**Figure 1.4** Schematic diagram for the derivation of the Bragg's law.

Considering a periodic partially reflecting layers with a regular interval of  $d$ , the incident lights are reflected at each layer, and two neighboring lights have a different optical path length, giving the following relation for a constructive interference [27].

$$2d \sin \theta = m\lambda \quad (1.66)$$

, where  $m$  is a positive integer. This is called the Bragg's law. In the point of the reciprocal space, the momentum transfer corresponding to the Bragg's law is defined as  $\mathbf{Q} = \mathbf{k}_f - \mathbf{k}_i = (4\pi/\lambda) \sin \theta \hat{e}_z$  if  $|\mathbf{k}_i| = |\mathbf{k}_f| = k$ . This gives the constructive interference position at

$2k \sin \theta$  in the reciprocal space correspond to  $d$  in the real space along the same direction.

As the size of the incoming and outgoing wavevectors,  $\mathbf{k}_i$  and  $\mathbf{k}_f$ , is conserved in the elastic scattering scheme, it is convenient to construct a sphere with a radius of  $k = 2\pi/\lambda$ . This configuration is called the Ewald sphere. When the measurement is accomplished by a detector pixelated by  $N$ -by- $N$ , of which the plane is perpendicular to and centered at the incoming wavevector,  $\mathbf{k}_i$ , the momentum transfer,  $\mathbf{Q}$ , which varies across the detector plane, is defined as follows.

$$\mathbf{Q} = \frac{2\pi}{\lambda} \sin 2\theta \hat{\mathbf{q}}_1' - \frac{2\pi}{\lambda} (1 - \cos 2\theta) \hat{\mathbf{q}}_3' \quad (1.67)$$

, where  $\hat{\mathbf{q}}_1'$ ,  $\hat{\mathbf{q}}_2'$  and  $\hat{\mathbf{q}}_3'$  are two in-plane and one out-of-plane bases with respect to the detector plane, respectively.

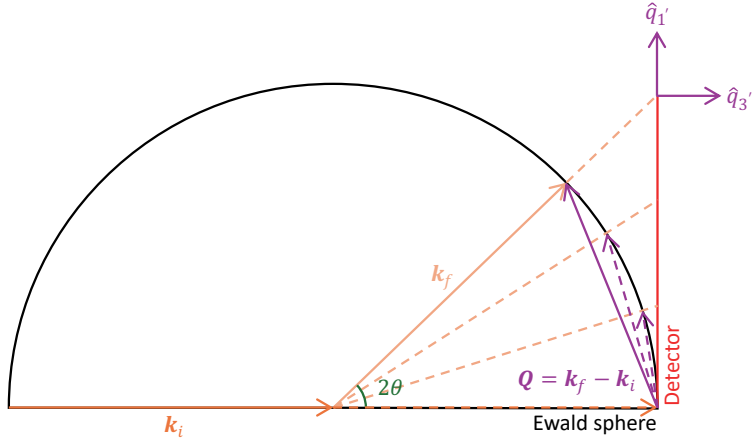


**Figure 1.5** · Schematic diagram of the Ewald sphere.

In the practical situation, the maximum scattered angle spanned by the detector plane is defined as  $2\theta_{\max} = \tan^{-1}(Np/2z)$ , where  $p$  is the pixel size of the detector and  $z$  is the sample-to-detector distance. Using this quantity, the maximum momentum transfer along  $\hat{\mathbf{q}}_1'$  is defined as follows.

$$\begin{aligned} \mathbf{Q}_{\max} &= \frac{2\pi}{\lambda} \frac{Np/2}{\sqrt{z^2 + (Np/2)^2}} \hat{q}_{1'} - \frac{2\pi}{\lambda} \left( 1 - \frac{z}{\sqrt{z^2 + (Np/2)^2}} \right) \hat{q}_{3'} \\ &= \frac{\pi Np}{\lambda z} \left[ 1 - \frac{1}{2} \left( \frac{Np}{2z} \right)^2 + \dots \right] \hat{q}_{1'} - \frac{\pi}{\lambda} \left[ \left( \frac{Np}{2z} \right)^2 + \dots \right] \hat{q}_{3'} \end{aligned} \quad (1.68)$$

When the detector is far from the sample,  $(Np/2z)^2 \ll 1$ , Eq. (1.68) becomes as follows.

$$\mathbf{Q}_{\max} \approx \frac{\pi Np}{\lambda z} \hat{q}_{1'} \quad (1.69)$$

This gives the real-space equivalent as  $d = 2\lambda z / Np$ . This is the full-period resolution for the finite measurement of the diffraction pattern. In the point of diffraction imaging, the pixel resolution is a half-period resolution, given as  $d_{px} = \lambda z / Np$ .

Unfortunately, the curvature of the Ewald sphere causes the nonlinearity of the momentum transfer corresponding to each pixel that is arranged regularly. Considering up to quadratic terms,  $(Np/2z)^2$ , in the series expansion of Eq. (1.68), the error along  $\hat{q}_{1'}$  is calculated as follows.

$$|\delta Q_{1'}| \leq \frac{\pi p}{\lambda z} \left[ 1 - \frac{1}{2} \left( \frac{p}{2z} \right)^2 \right] - \frac{1}{N} \frac{\pi Np}{\lambda z} \left[ 1 - \frac{1}{2} \left( \frac{Np}{2z} \right)^2 \right] = \frac{\pi(N^2 - 1)p^3}{8\lambda z^3} \quad (1.70)$$

In addition, except for the in-plane components, the out-of-plane components also arise from the Ewald sphere curvature. Similarly, the maximum error along  $\hat{q}_{3'}$  is calculated as follows.

$$|\delta Q_{3'}| \leq \frac{1}{2} \frac{\pi}{\lambda} \left( \frac{Np}{2z} \right)^2 - \frac{\pi}{\lambda} \left( \frac{Np}{4z} \right)^2 = \frac{\pi N^2 p^2}{16\lambda z^2} \quad (1.71)$$

Thus, the effect of the Ewald sphere curvature should be considered carefully for diffraction imaging measuring high-angle signals, which is required for the higher resolution.

Reminding the result of the first-order Born approximation in Section 1.6, Eq. (1.48) implies the scattering signals represent 3D Fourier transform of the real-space distribution of scattering potentials, mostly by electrons. However, the detector only measures the cross section of the 3D diffraction pattern, which correspond to the 2D projected distribution; therefore, an additional angle scan is required to obtain a full 3D diffraction pattern.

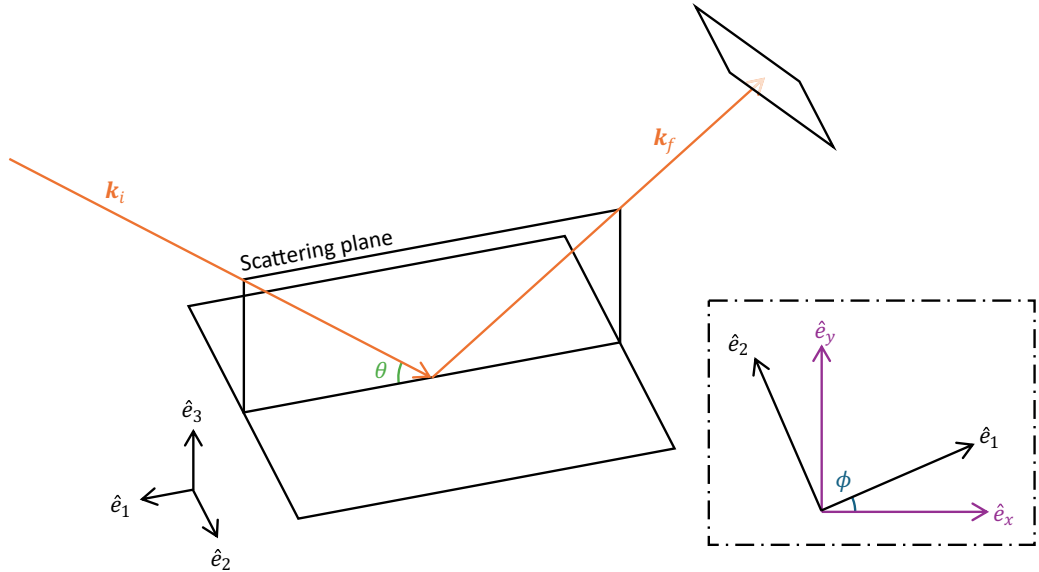


**Figure 1.6** · Schematic diagram of  $\phi$ -scan.

In this circumstance, the azimuthal scan,  $\phi$ -scan, is typically used for 3D diffraction imaging. For the sake of simplicity, the calculation is under the reflection geometry, but the result would be identical. When the sample is rotated along  $\hat{e}_3 = \hat{e}_z$  with an amount of  $\phi$ , the in-plane bases,  $\hat{e}_1$  and  $\hat{e}_2$ , are simply derived by the rotation matrix as  $\hat{e}_1 = \cos \phi \hat{e}_x + \sin \phi \hat{e}_y$  and  $\hat{e}_2 = -\sin \phi \hat{e}_x + \cos \phi \hat{e}_y$ . As the Fourier transform satisfies  $\mathcal{F}[f(\mathbf{A}\mathbf{r})] = F(\mathbf{A}\mathbf{Q})$ , where  $\mathcal{F}$  represents the Fourier transform,  $F(\mathbf{Q}) = \mathcal{F}[f(\mathbf{r})]$ , and  $\mathbf{A}$  is an orthogonal matrix, including the rotation matrix. Thus, the in-plane components of the reciprocal space on the detector plane become as follows.

$$\begin{cases} \hat{q}_1' = \sin \theta \hat{q}_1 + \cos \theta \hat{q}_3 = \sin \theta \cos \phi \hat{q}_x + \sin \theta \sin \phi \hat{q}_y + \cos \theta \hat{q}_z \\ \hat{q}_2' = \hat{q}_2 = -\sin \phi \hat{q}_x + \cos \phi \hat{q}_y \end{cases} \quad (1.72)$$

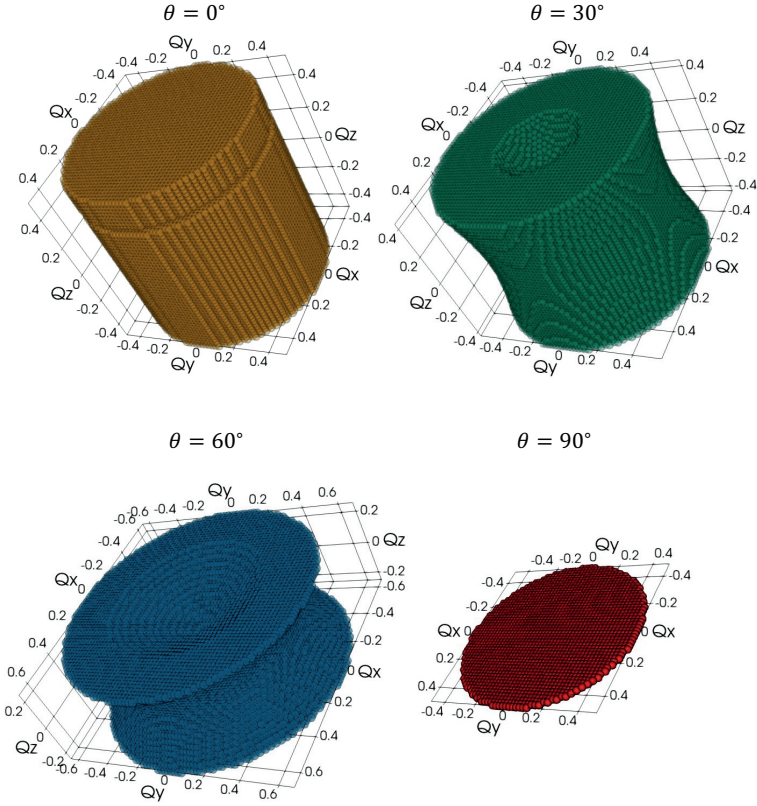


**Figure 1.7** · Reciprocal-space regions spanned by the  $\phi$ -scans for different  $\theta$ s.

When  $\theta = 0^\circ$  and  $\mathbf{Q}_{\text{cen}} = 0$ , where  $\mathbf{Q}_{\text{cen}}$  is the momentum transfer at the center of detector plane, this case is equivalent with the angle scan of conventional tomography [28]. When the rotation axis is tilted,  $\theta > 0^\circ$ , this case is equivalent with the angle scan of laminography, which is a kind of tomography specialized to flat objects. Unlike the case of  $\theta = 0^\circ$ , missing cones along  $\hat{\mathbf{q}}_z$  appeared in the reciprocal space, excluding a certain portion of the 3D reciprocal-space information. However, when the target object is flat, the angle scan of the conventional tomography causes missing wedges by the limited angles from the sample morphology, and laminography becomes advantageous. Otherwise, when the rotation axis is parallel to the incident beam,  $\theta = 90^\circ$ , this case does not give the 3D reciprocal-space information. Note that there is a special method named ankylography, which reconstructs 3D real-space distribution from a single diffraction measurement spanning a large portion of the Ewald sphere surface with very high angles [29].

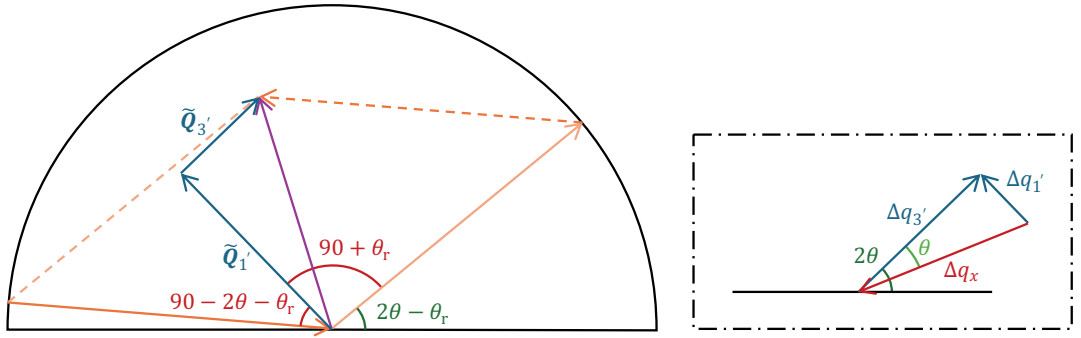


**Figure 1.8** · Schematic diagram of  $\theta$ -rocking.

In the reflection geometry, especially the Bragg reflection geometry,  $\mathbf{Q}_{\text{cen}} = 2\pi/d$ , where  $d$  is an interatomic spacing of a crystal structure,  $\theta$ -rocking, which is an angle scan of a small step angle of  $\theta_r$  with a fixed detector position,  $2\theta$ , also gives the 3D reciprocal-space information. Starting from the initial momentum transfer,  $\mathbf{Q}_{\text{cen}} = (2\pi/\lambda) \sin 2\theta \hat{q}_1' + (2\pi/\lambda)(1 - \cos 2\theta)\hat{q}_3'$ , the momentum transfer after  $\theta$ -rocking defined as follows.

$$\mathbf{Q}'_{\text{cen}} = \frac{2\pi}{\lambda} [\sin(2\theta + \theta_r) - \sin \theta_r] \hat{q}_1' + \frac{2\pi}{\lambda} [-\cos(2\theta + \theta_r) + \cos \theta_r] \hat{q}_3' \quad (1.73)$$

Assuming  $\theta_r \ll 1$ , the above equation becomes as follows.

$$\begin{aligned} \mathbf{Q}'_{\text{cen}} &= \frac{2\pi}{\lambda} [\sin 2\theta \cos \theta_r + \cos 2\theta \sin \theta_r - \sin \theta_r] \hat{q}_1' \\ &\quad + \frac{2\pi}{\lambda} [-\cos 2\theta \cos \theta_r + \sin 2\theta \sin \theta_r + \cos \theta_r] \hat{q}_3' \\ &\approx \frac{2\pi}{\lambda} [\sin 2\theta - \theta_r(1 - \cos 2\theta)] \hat{q}_1' + \frac{2\pi}{\lambda} [1 - \cos 2\theta + \theta_r \sin 2\theta] \hat{q}_3' \end{aligned} \quad (1.74)$$

Using the above result, the deviation of the momentum transfer is calculated as follows.

$$\begin{aligned} \Delta \mathbf{Q}_{\text{cen}} &= \mathbf{Q}'_{\text{cen}} - \mathbf{Q}_{\text{cen}} \approx -\frac{2\pi}{\lambda} \theta_r (1 - \cos 2\theta) \hat{q}_1' + \frac{2\pi}{\lambda} \theta_r \sin 2\theta \hat{q}_3' \\ &= -\frac{4\pi}{\lambda} \theta_r \sin^2 \theta \hat{q}_1' + \frac{4\pi}{\lambda} \theta_r \sin \theta \cos \theta \hat{q}_3' \\ &= -\frac{4\pi}{\lambda} \theta_r \sin \theta \hat{q}_x \end{aligned} \quad (1.75)$$

Thus,  $\theta$ -rocking is a translational scanning of the detector plane along  $\hat{q}_x$  in the reciprocal space.

In the point of the reciprocal-space sampling,  $dQ$ ,  $\phi$ -scan and  $\theta$ -rocking give different out-of-plane reciprocal-space samplings along  $\hat{q}_3'$ , giving the following relations.

$$\begin{cases} dQ_{3'} = Q_{2'}[\sin(\phi + \phi_r) - \sin \phi] \approx Q_{2'}\phi_r \cos \phi, & \text{for } \phi\text{-scan} \\ dQ_{3'} \approx \frac{2\pi}{\lambda}\theta_r \sin 2\theta, & \text{for } \theta\text{-rocking} \end{cases} \quad (1.76)$$

, where  $Q_{2'} = 2\pi mp/\lambda z$  with a positive integer,  $m$ , smaller than  $N/2$ . When the sampling of out-of-plane components,  $dQ_{3'}$ , is matched with the sampling of in-plane components,  $dQ_{1'}$  and  $dQ_{2'}$ , which are  $2\pi p/\lambda z$ , the required step angle is calculated as follows for each scan. Note that the calculation for  $\phi$ -scan uses  $Q_{2',\max} = \pi N p / \lambda z$ .

$$\begin{cases} \phi_r = \frac{2}{N \cos \phi}, & \text{for } \phi\text{-scan} \\ \theta_r = \frac{2}{N}, & \text{for } \theta\text{-rocking} \end{cases} \quad (1.77)$$

However, both scanning methods cause additional shifts of in-plane components, so the step angles cannot be simply defined. For  $\phi$ -scan, the step angles can be corrected by  $1/\cos \phi$  or  $1/\sin \phi$  depending on the range of  $\phi$ , assigning equally sloped angles, not equally angled, for tomography [30]. For  $\theta$ -rocking,  $dQ_{3'}$  cannot be matched to the sampling of in-plane components because the additional shift of  $-(2\pi/\lambda)\theta_r(1 - \cos 2\theta)$  also exists along  $\hat{q}_1'$ . Thus, the shifts along both axes should be considered and they are preferred to have integer ratios with respect to the in-plane sampling that is defined by detector pixels. Also, the object size should be considered for the oversampling along  $\hat{q}_3'$ , and this would be discussed in Chapter 2.

## 1.9. Coherence

Coherence is the degree of correlation for the phase across the wavefield [27]. It is generally expressed in the form of lengths, longitudinal and transverse coherence lengths, that imply the spatial boundaries assuring certain degrees of the coherence along the directions. Considering typical quasi-monochromatic plane waves,  $\Delta\lambda/\lambda \ll 1$ , the longitudinal coherence length,  $\xi_l$ ,

is defined as a longitudinal distance showing a half-period difference between the waves with wavelengths of  $\lambda$  and  $\lambda + \Delta\lambda$ , where they are completely canceled out. Thus, it satisfies the following equation.

$$\frac{\xi_l}{\lambda} - \frac{\xi_l}{\lambda + \Delta\lambda} = \frac{1}{2} \Leftrightarrow \xi_l = \frac{\lambda(\lambda + \Delta\lambda)}{2\Delta\lambda} \approx \frac{\lambda^2}{2\Delta\lambda} \quad (1.78)$$

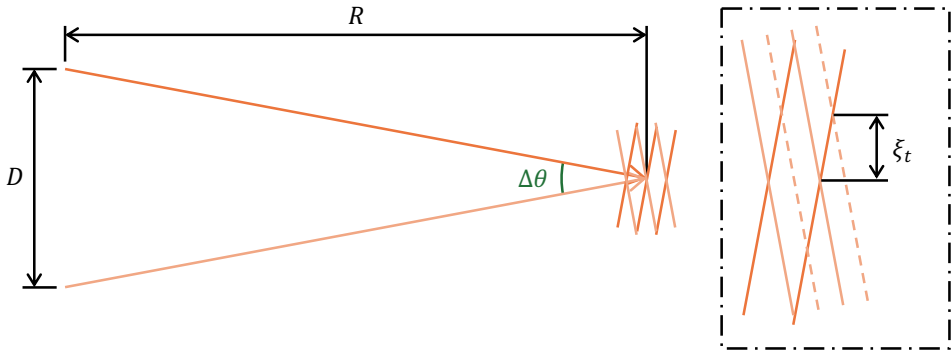


**Figure 1.9** Schematic diagram for the transverse coherence length

Similarly, the transverse coherence length,  $\xi_t$ , is defined as a transverse distance with the same condition, but instead the waves are assumed to be originated from different position with a lateral deviation of  $D$  and have a same wavelength of  $\lambda$ . At the converging point  $R$  away from the origins, the angle deviation is defined as  $\Delta\theta = 2 \tan^{-1}(D/2R)$ . Then, the transverse coherence length is defined as follows with an assumption that  $(1/2)(D/2R)^2 \ll 1$ .

$$\xi_t = \frac{\lambda \cos(\Delta\theta/2)}{2 \sin \Delta\theta} = \frac{\lambda}{4 \sin(\Delta\theta/2)} = \frac{\lambda \sqrt{R^2 + (D/2)^2}}{2D} \approx \frac{\lambda R}{2D} \quad (1.79)$$

When using a pixelated detector for measurement, two types of coherence give different effects to measured diffraction patterns. For the longitudinal coherence, a spectral deviation leads to a deviation of the momentum transfer for each detector pixel, giving the following relation.

$$\delta Q = \frac{2\pi mp}{\lambda z} - \frac{2\pi mp}{(\lambda + \Delta\lambda)z} = \frac{2\pi mp}{z} \frac{\Delta\lambda}{\lambda(\lambda + \Delta\lambda)} = \frac{\pi mp}{z\xi_l} \quad (1.80)$$

, where  $m$  is a positive integer smaller than  $N/2$ . Thus, when the deviation,  $\delta Q_{\max} =$

$\pi N p / 2z \xi_l$ , is smaller than the half of the sampling,  $dQ/2 = \pi p / \lambda z$ , giving  $\xi_l > N\lambda/2$ , this effect can be safely ignored as the error is within 1 pixel. Meanwhile, the influence of the transverse coherence is usually described by the Gaussian Schell model defined as follows [31].

$$\mu(\Delta\mathbf{r}) = e^{-|\Delta\mathbf{r}|^2/(2\sigma_\mu)^2} \quad (1.81)$$

, where  $\Delta\mathbf{r}$  is a transverse displacement vector and  $\sigma_\mu$  is a transverse coherence length in the root mean square value. This model is applied to the 2D real-space density distribution,  $\rho$ , as follows.

$$\begin{aligned} I'(\mathbf{Q}) &= |\mathcal{F}[\text{AC}\{\rho(\mathbf{r})\}\mu(\Delta\mathbf{r})]| \\ &= \left| \mathcal{F} \left[ \mathcal{F}^{-1}\{I(\mathbf{Q})\} e^{-|\Delta\mathbf{r}|^2/(2\sigma_\mu)^2} \right] \right| \end{aligned} \quad (1.82)$$

, where AC represents the autocorrelation, which can be calculated by  $\text{AC}\{f(\mathbf{r})\} = \mathcal{F}^{-1}[|\mathcal{F}\{f(\mathbf{r})\}|^2]$ ,  $I$  and  $I'$  is diffraction patterns before and after applying the model, respectively.  $|\Delta\mathbf{r}|$  is given by the radial distance from the center.

Coherence is an important keyword for diffraction imaging. As the measurement is conducted by counting the scattered photons to the certain solid angle elements, only the intensity of the signals can be obtained. Although the Fourier transform is a linear operation, the measured signals are the absolute square of the Fourier transform of real-space information, thereby lost the linearity. Thus, it is important to use the probe beam with a well-defined single-mode wavefront for high-resolution imaging.

## 1.10. Plane-wave coherent diffraction imaging (CDI) and ptychography

After the experimental verification of plane-wave CDI for a nonperiodic object by Miao *et al.* in 1999, CDI has been widely used for high-resolution imaging surpassing the performance of optical microscopy by using X-ray and electron beams [5]. Although conventional microscopy also performed well with X-ray and electron beams, CDI does not need image-forming lenses, thereby its resolution is not restricted by optical performance and intrinsic aberrations of the lens system. In addition, as the ideal resolution of the X-ray lenses, such as zone plates or

multilayer Laue lenses, is determined as  $1.22\Delta r_N$  by the Rayleigh criterion, where  $\Delta r_N$  is the minimum width of grating components, the technical limitation of nanofabrication strongly hinders the resolution below 10 nm, and this problem becomes severe for hard X-rays, which demand an extremely high aspect ratio process [27,32]. Note that the diffractive optics is typically used as a refractive index of materials is very close to 1 in the X-ray regime.

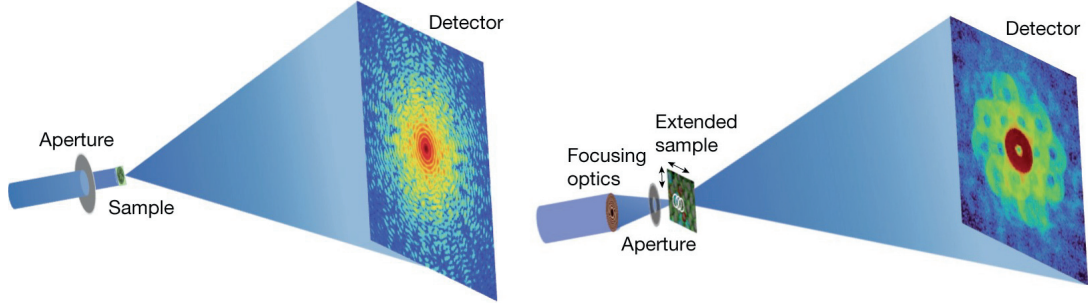


**Figure 1.10** · Schematic diagram of plane-wave CDI (left) and ptychography (right). Adapted from Ref. [7], Springer Nature Limited.

Based on the conventional plane-wave CDI, there are many variants including Fresnel CDI, reflection CDI, Bragg CDI, holographic CDI, ptychography, and Fourier ptychography [7]. Here, two representative types, plane-wave CDI and ptychography, would be covered. Plane-wave CDI assumes the plane-wave incidence, which gives the uniform wavefront across an object, assigning a constant probe field as follows.

$$z(\mathbf{Q}) = \mathcal{F}[u(\mathbf{r})v(\mathbf{r})] \approx \mathcal{F}[u(\mathbf{r})] \quad (1.83)$$

, where  $z$ ,  $u$ , and  $v$  are functions corresponding to far-field diffraction, object, and probe, respectively. Even if the incident beam is not a well-defined plane wave, the wavefront deviation across the object is negligible when the object size is much smaller than the beam size. Under this condition,  $u$  can be simply obtained by the inverse Fourier transform of  $z$ , and phase retrieval, which reconstructs the phase-preserved diffraction function,  $z$ , can be numerically accomplished by iterative algorithms [4]. However, the object must be localized and have positive real values for the uniqueness of a solution in practice [33]. If the object contains negative real or complex values, positions with nonzero values should be precisely given for the uniqueness. Detailed discussion about phase retrieval would be presented in Chapter 2.

Meanwhile, ptychography is first proposed by Hoppe in 1969 to solve the phase problem for electron diffractions from crystalline samples [34]. The word ptychography is derived from the Greek words *ptycho* and *graphein*, meaning to fold and to write, respectively. Ptychography does not assume plane-wave incidence; instead, it adopts a 2D scan with partial overlaps across the object as follows.

$$z_i(\mathbf{Q}) = \mathcal{F}[u(\mathbf{r})v(\mathbf{r} - \mathbf{r}_i)] \quad (1.84)$$

, where  $i$  is an index of each scan position. In early days, phase retrieval for ptychography is achieved by noniterative methods like Wigner-distribution decomposition [35]. Nowadays, modern ptychography adopts iterative phase retrieval methods, like as plane-wave CDI, and its first experimental demonstration was achieved by Rodenburg *et al.* in 2007 [36]. After the successful demonstration, ptychography has been widely used to capture images of both object and probe in nanoscale resolution [37]. Phase retrieval of ptychography is like that of plane-wave CDI, but both object and probe are simultaneously updated as follows [38,39].

$$u(\mathbf{r}) = \frac{\sum_i v^*(\mathbf{r} - \mathbf{r}_i)\psi_i(\mathbf{r})}{\sum_i |v(\mathbf{r} - \mathbf{r}_i)|^2}, \quad v(\mathbf{r}) = \frac{\sum_i u^*(\mathbf{r} + \mathbf{r}_i)\psi_i(\mathbf{r} + \mathbf{r}_i)}{\sum_i |u(\mathbf{r} + \mathbf{r}_i)|^2} \quad (1.85)$$

, where  $\psi_i$  is an exit wave function defined as  $\psi_i = u(\mathbf{r})v(\mathbf{r} - \mathbf{r}_i)$ . Unlike CDI, ptychography does not require real-valued functions for both object and probe.

Besides such details, definitions of oversampling ratios, which are important factors in a possibility of phase retrieval, are fundamentally different for CDI and ptychography. In a case of CDI, the oversampling ratio along each dimension is simply defined as a ratio of a window size with respect to an object width [40]. However, as ptychography employs a probe scanning across the extended object, additional parameters are added to the oversampling ratio [41]. Note that object and probe are assumed to have rectangular shapes for the sake of simplicity.

$$\sigma_{\text{ptycho},i} = \frac{\sigma_{\text{CDI},i}}{1 - \varsigma_i} \quad (1.86)$$

, where  $i$  is an index of each dimension and  $\varsigma_i$  is a ratio of an overlapped length of a scanning probe with respect to the probe width along each dimension. Here,  $\sigma_{\text{CDI},i}$  uses the probe width instead of the object width for a calculation of  $\sigma_{\text{ptycho},i}$  as an illumination of the extended

object by the probe is effectively the object at each scan point of ptychographic measurements. Thus, the oversampling ratio along each dimension is determined by a ratio of the window size with respect to a step size for the scanning probe, being more conveniently adjustable compared to CDI.

Both plane-wave CDI and ptychography have advantages and disadvantages on different circumstances. Plane-wave CDI enables imaging from a sing-shot measurement, facilitating time-resolved studies. In addition, as diffraction patterns are invariant for translational vibration if the object is within the incident beam, it provides the maximal resolving power. However, it only handles isolated objects and has difficulty managing complex-valued objects. Otherwise, ptychography enables imaging of a complex-valued extended object, facilitating imaging of various materials without the constraints of plane-wave CDI, such as size and resonant behaviors like magnetic signals. In addition, it is possible to obtain a wavefront image of the incident beam, thereby it can be utilized for beam diagnosis. However, time-resolved imaging is not possible, and phase retrieval is computationally more expensive. It also requires a dedicated experimental setup for a stable 2D scan across the object. Thus, it is important to choose the appropriate method in consideration of target systems.

## 2. Phase retrieval

### 2.1. Introduction

The phase problem is a well-known problem in crystallography, diffraction, astronomy, and remote sensing [42]. As only the intensity, which is proportional to the number of photons, can be measured by detectors, phase information is lost, and this is called the phase problem. In a typical case, where a measured signal is the Fourier transform of a certain illumination or density function related to a target system, the phase problem hinders the inverse transform of the Fourier transform to obtain real-space information of the target system and requires additional procedures to recover the lost phase of the measured signals. This process is called phase retrieval, and iterative algorithms have been suggested for the phase recovery [4].

The first widely accepted phase retrieval algorithm was proposed by Gerchberg and

Saxton in 1971 [3]. The Gerchberg–Saxton algorithm iteratively projects amplitude components of both real- and Fourier-space variables onto measured ones; therefore, it requires two-intensity measurement, which investigates not only diffraction pattern but also density of an object. However, considering the purpose of diffraction imaging, the object density cannot be given, and Fienup proposed two algorithms, error reduction (ER) and input-output, in 1978 by using a finite support with positive real constraint instead of the object density for the real-space projections [43]. Then, Bates proposed the oversampling method in 1982, showing that the phase problem is uniquely solvable for a positive real-valued object more than one dimension when the spatial sampling is more than 2 along each dimension [44]. He also claimed that the uniqueness for the object having negative real or complex values is only valid for the most compact object corresponding to the Fourier intensity [45]. In this regard, Fienup showed some examples for successful reconstructions of complex-valued objects with tight supports by numerical experiments [46]. In addition, Miao *et al.* showed that the successful reconstruction of complex-valued objects can be achieved with loose real-space supports and positivity constraints on both real and imaginary components by numerical experiments [42]. They also showed that the oversampling ratios of 2.60 and 2.57 are enough for 2D and 3D, respectively, instead of 2 along each dimension. Based on these efforts, the phase problem becomes no longer a difficult problem to solve. In this chapter, brief introduction of representative iterative projection algorithms followed by advanced approaches by means of the convex optimization would be covered.

## 2.2. Iterative projection algorithms

The problem, which is aimed to be solved by phase retrieval, is defined as follows. Note that the variables,  $u$  and  $z$ , are in a form of a matrix, strictly a column vector, for the sake of simplicity.

$$\min_{u,z \in \mathbb{C}^{N \times M}} [\mathcal{J}_S(u) + \mathcal{J}_T(z)], \quad \text{subject to } \mathcal{F}^{-1}z = u \quad (2.1)$$

, where  $\mathcal{J}_S$  and  $\mathcal{J}_T$  are indicator functions for real-space support and Fourier-space amplitude constraints,  $S$  and  $T$ , respectively. Each constraint is a set of matrices defined as follows.

$$\begin{aligned}\mathcal{S} &= \{u \in \mathbb{R}^{N \times M} | u_i, \text{ if } i \in S \wedge u_i \geq 0; \quad u_i = 0, \text{ otherwise}\} \\ \mathcal{T} &= \{z \in \mathbb{C}^{N \times M} | |z| = b\}\end{aligned}\quad (2.2)$$

, where  $i$  is a position index of the matrix elements,  $S$  is a set of position indices, at which an object is located, and  $b$  is the Fourier amplitude defined as  $b = \sqrt{I}$ . The indicator functions can be substituted by arbitrary convex functions of which the minima are corresponding to the constraints.

The simplest way to solve Eq. (2.1) is iteratively project onto both constraints as follows.

$$u^{(j+1)} = \text{proj}_{\mathcal{J}_S} [\mathcal{F}^{-1} \text{proj}_{\mathcal{J}_T} \{\mathcal{F}u^{(j)}\}] \quad (2.3)$$

, where  $j$  is an index of iterations and  $\text{proj}_f$  is a projection operator, producing the closest variable from the input that gives the minimum value of the target function,  $f$ . This algorithm is called the error-reduction (ER), which is virtually equivalent with the Gerchberg–Saxton algorithm [43]. The projection operators in Eq. (2.3) can be operated as follows.

$$\begin{aligned}(\text{proj}_{\mathcal{J}_S} u)_i &= \begin{cases} u_i, & \text{if } i \in S \\ 0, & \text{otherwise} \end{cases} \\ \text{proj}_{\mathcal{J}_T} z &= b \odot e^{i \arg z}\end{aligned}\quad (2.4)$$

Considering a nonlinear system with an input,  $u^{(j)}$ , and output, which is defined as  $\tilde{u}^{(j)} = \mathcal{F}^{-1} \text{proj}_{\mathcal{J}_T} [\mathcal{F}u^{(j)}]$ , an additional gradient outside the object support can be given as follows based on the nonlinear feedback control theory [47].

$$u^{(j+1)} = \text{proj}_{\mathcal{J}_S} \tilde{u}^{(j)} + \text{proj}_{\mathcal{J}_{S^c}} [u^{(j)} - \beta \tilde{u}^{(j)}] \quad (2.5)$$

, where  $\beta$  is a real parameter, which is typically given as 0.9, and  $S'$  is the complement of the real-space support constraint defined as follows.

$$\mathcal{S}^c = \{u \in \mathbb{R}^{N \times M} | u_i, \text{ if } i \in S^c \vee u_i < 0; \quad u_i = 0, \text{ otherwise}\} \quad (2.6)$$

This algorithm is called the hybrid input-output (HIO) [4]. HIO is typically used with several iterations of ER.

Some iterative projection algorithms are generalized by an algorithm called the

difference map (DM) defined as follows [47,48]. Note that the Fourier-space projection operator for a real-space matrix,  $\mathcal{F}^{-1} \text{proj}_{\mathcal{J}_T} \mathcal{F}$ , is expressed as  $\text{proj}_{\mathcal{J}_T}^{(\text{real})}$  for convenience.

$$u^{(j+1)} = u^{(j)} + \beta \text{proj}_{\mathcal{J}_S} \left[ (1 + \gamma_s) \text{proj}_{\mathcal{J}_T}^{(\text{real})} u^{(j)} - \gamma_s u^{(j)} \right] - \beta \text{proj}_{\mathcal{J}_T}^{(\text{real})} \left[ (1 + \gamma_t) \text{proj}_{\mathcal{J}_S} u^{(j)} - \gamma_t u^{(j)} \right] \quad (2.7)$$

, where  $\gamma_s$  and  $\gamma_t$  are real parameters. It is recommended to use  $\gamma_s = -1/\beta$  and  $\gamma_t = 1/\beta$ . If the positivity constraint is not enforced, DM is equivalent with HIO when  $\gamma_s = 1/\beta$  and  $\gamma_t = -1$ .

The last algorithm to be introduced is the relaxed averaged alternating reflection (RAAR) defined as below [47,49].

$$u^{(j+1)} = \frac{1}{2} \beta \left[ \text{refl}_{\mathcal{J}_S} \left\{ \text{refl}_{\mathcal{J}_T}^{(\text{real})} u^{(j)} \right\} + u^{(j)} \right] + (1 - \beta) \text{proj}_{\mathcal{J}_T}^{(\text{real})} u^{(j)} \quad (2.8)$$

, where  $\text{refl}_f = 2\text{proj}_f - \mathbb{I}$ . RAAR utilizes reflection operators, which make the variable moving exactly twice of that from the projection operator, being designed for stable and fast phase retrieval. If the positivity constraint is not enforced, RAAR coincides with HIO when  $\beta = 1$ .

Using these kinds of iterative projection algorithms, phase retrieval is conducted from a random phase,  $\phi_{\text{rand}} \in [0, 2\pi)^{N \times M}$ , giving an initial object,  $u^{(0)} = \mathcal{F}[be^{i\phi_{\text{rand}}}]$ , and multiple runs, of which each run starts from a randomly generated initial object, called seeds, are parallelly executed to verify stability and convergence of the reconstruction. After enough iterations, the best  $u$  is typically selected based on  $R$ -factor, which is a normalized mean absolute error of the Fourier amplitude, defined as follows [50]. Note that mean squared error and root mean squared error of the Fourier amplitude are also used occasionally.

$$R_F^{(j)} = \frac{\sum_i \left| |\mathcal{F}u^{(j)}|_i - b_i \right|}{\sum_i b_i} \quad (2.9)$$

An increase of the noise in a measured diffraction pattern hinders the phase recovery and the reconstructed image becomes sensitive to the phase retrieval conditions including object

support and initial objects. Thus, determination of such conditions is important when dealing with noisy diffraction signals, and various approaches are suggested for the successful reconstruction. In this regard, three add-on methods would be introduced representatively.

The first method is the shrink-wrap algorithm [51]. Although a tight boundary of the object cannot be obtained from the measured diffraction pattern without any prior knowledges, autocorrelation of the object can be acquired by the inverse Fourier transform of the Fourier intensity if a sufficient portion of the zeroth speckle is not occluded by a beam stop, providing an upper boundary of the object. In this manner, the shrink-wrap algorithm sets the initial support by a contour at a certain intensity level of the autocorrelation. Then, while the object is gradually forming its shape along with the iterations of the phase retrieval algorithm, it updates the support by thresholding the temporary object after the Gaussian convolution for every few iterations, and the Gaussian kernel is also updated by slowly reducing its width. Note that the algorithm is failed when the real-space noise becomes larger than the threshold for updating the support.

The second method is the guided hybrid input-output (GHIO) [52]. Instead of searching a tight object support, GHIO repeats the whole HIO iterations with assigning the initial objects based on results of the previous generation defined as follows.

$$u_{g+1,m}^{(0)} = \sqrt{u_{g,\text{best}}^{(f)} \odot u_{g,m}^{(f)}} \quad (2.10)$$

, where  $g$  and  $m$  stand for the indices of generations and seeds, respectively, and  $u^{(f)}$  denotes the final object after several iterations of the following additional operation on the result of each seed with the minimum  $R$ -factors.

$$u^{(j+1)} = \text{proj}_{\mathcal{J}_S} \tilde{u}^{(j)} + \text{proj}_{\mathcal{J}_{S^c}} [\alpha \tilde{u}^{(j)}] \quad (2.11)$$

, where  $\alpha$  is a real parameter, linearly decreasing from 1 to 0. For the zeroth generation, assuming real-valued objects, the initial phase is generated randomly, but the phase value at  $-Q$  is assigned to be conjugated with the value at  $Q$ . Consequently, GHIO guides the initial objects from the previous generations, enforcing HIO to search near the previous minimum points in the error landscape for global minima.

The last method to be introduced is the oversampling smoothness (OSS) [53]. OSS additionally applies the Gaussian function in the Fourier space after each iteration of HIO to reduce an effect of the noise as follows.

$$u_i^{(j+1)} = \begin{cases} u_i^{(j+1)}, & \text{if } i \in S \\ (\mathcal{F}^{-1}[W \odot \mathcal{F}u^{(j+1)}])_i, & \text{otherwise} \end{cases} \quad (2.12)$$

, where  $W$  is a normalized Gaussian kernel defined as  $W(\mathbf{Q}) = e^{-Q^2/2\alpha^2}$  with a linearly decreasing  $\alpha$  typically in 10 steps from  $2NdQ$  to  $(2N/10)dQ$  during iterations. This operation gradually suppresses high- $Q$  signals, which show lower signal-to-noise ratios (SNRs) compared to low- $Q$  signals, offering noise-robust reconstructions. These methods help bypassing strong local minima by the noises to obtain optimal solutions.

### 2.3. Resolution estimation for phase retrieval

Resolution estimation of reconstructed real-space images after phase retrieval is conducted based on the convergence of individual reconstructions from initial random phases. In this regard, phase retrieval transfer function (PRTF), which is a normalized mean Fourier amplitude of all reconstructed images from initial random phases, is generally used and defined as follows [25,54].

$$\text{PRTF} = \frac{|\overline{\mathcal{F}u}|}{\sqrt{I}} \quad (2.13)$$

, where  $\overline{\mathcal{F}u}$  denotes an element-wise average of  $\mathcal{F}u$  over all images. The typical threshold criteria on the radial distribution of PRTF are 0.5 and  $1/e$  [25,55]. Based on these criteria, image resolution can be simply obtained by  $2\pi/Q_{\text{cut}}$  with the cut-off momentum transfer,  $Q_{\text{cut}}$ , for the full-period resolution. However, as PRTF and its criteria are not strictly defined, they often cause discussion [56].

In case of the resolution estimation for scanning methods like angle scans for tomography, Fourier shell correlation (FSC) is generally used [57]. Note that Fourier ring correlation (FRC) is identical with FSC but for 2D images. FSC calculates radial correlations

in the Fourier space defined as follows.

$$\text{FSC}_{A,B} = \frac{\mathcal{F}u_A \odot (\mathcal{F}u_B)^*}{|\mathcal{F}u_A| \odot |\mathcal{F}u_B|} \quad (2.14)$$

, where  $A$  and  $B$  denote two independent datasets splitting from whole measured data and  $u_A$  and  $u_B$  are reconstruction results from each dataset. These datasets are usually assigned by even- and odd-order data from ordered scans. Similarly, FSC also uses threshold criteria on their radial distribution, and typical criteria for the resolution estimation are a constant threshold of 1/7 and 0.5-bit information threshold curve [57,58]. The constant threshold of 1/7 is from  $\sqrt{2\text{FSC}/(1 + \text{FSC})} = 0.5$ , considering SNR when signal and noise are uncorrelated [58]. Meanwhile, the radial distribution of FSC approximately has the following relation with SNR when  $\mathcal{F}u_A$  and  $\mathcal{F}u_B$  share same signals with different noises of similar SNRs [57].

$$\text{FSC}(Q_i) \approx \frac{\text{SNR}(Q_i) + 2\sqrt{\text{SNR}(Q_i)}/\sqrt{n_{\text{voxel}}(Q_i)} + 1/\sqrt{n_{\text{voxel}}(Q_i)}}{\text{SNR}(Q_i) + 2\sqrt{\text{SNR}(Q_i)}/\sqrt{n_{\text{voxel}}(Q_i)} + 1} \quad (2.15)$$

, where  $\text{SNR}(Q_i)$  and  $n_{\text{voxel}}(Q_i)$  are SNR and voxel number of the data in a spherical shell with a radius of  $Q_i$ . Note that the thickness of the shell is mostly assigned the Fourier-space sampling,  $dQ$ . Thus, considering that the half dataset gives SNR half of that for the full dataset, the 0.5-bit information threshold curve is defined as follows for  $0.5 \text{ bit} = \log_2(1 + \text{SNR}_{\text{full}}) \Rightarrow \text{SNR} = (\sqrt{2} - 1)/2$  with the SNR for the full dataset,  $\text{SNR}_{\text{full}}$ .

$$T_{0.5\text{-bit}}(Q_i) = \frac{(\sqrt{2} - 1)/2 + \left(\sqrt{2(\sqrt{2} - 1)} + 1\right)/\sqrt{n_{\text{voxel}}(Q_i)}}{(\sqrt{2} + 1)/2 + \sqrt{2(\sqrt{2} - 1)}/\sqrt{n_{\text{voxel}}(Q_i)}} \quad (2.16)$$

Based on these criteria, the resolution can be estimated by the cut-off momentum transfer like as PRTF.

## 2.4. Lagrange dual problem

As the phase problem is an optimization problem, it would have duality and equivalent dual

problem can be constructed [59]. Starting from the primal problem in Eq. (2.1), corresponding Lagrangian is simply defined as follows.

$$\mathcal{L}(u, z, y) = \mathcal{J}_S(u) + \mathcal{J}_F(z) + \operatorname{Re}\langle y, \mathcal{F}^{-1}z - u \rangle \quad (2.17)$$

, where  $y$  is a Lagrange multiplier and  $\langle \cdot, \cdot \rangle$  is the Hermitian inner product. Then, the Lagrange dual function is defined as follows.

$$\max_{y \in \mathbb{C}^{N \times M}} \min_{u, z \in \mathbb{C}^{N \times M}} \mathcal{L}(u, z, y) \quad (2.18)$$

This problem is called as the saddle point problem. The equality condition of the primal problem,  $\mathcal{F}^{-1}z = u$ , becomes unconstrained in the Lagrange dual problem.

When the primal problem is convex, Karush–Kuhn–Tucker (KKT) conditions are the sufficient conditions of primal and dual optimal points with zero duality gap. Although KKT conditions are necessary conditions for optimal solutions, they become sufficient and necessary conditions if the problems hold strong duality. For the general nonlinear optimization problem, KKT conditions are defined as follows.

$$\begin{aligned} 0 &\in \partial f(x^*) + \sum_k \mu_k \partial g_k(x^*) + \sum_l \nu_l \partial h_l(x^*) && \text{(Stationary)} \\ g_k(x^*) &\leq 0, \quad \text{for } \forall k && \text{(Primal feasibility)} \\ h_l(x^*) &= 0, \quad \text{for } \forall l && \text{(Dual feasibility)} \\ \mu_k &\geq 0, \quad \text{for } \forall k && \text{(Complementary slackness)} \\ \mu_k g_k(x^*) &= 0, \quad \text{for } \forall k \end{aligned} \quad (2.19)$$

, where  $x^*$  is a local optimum and  $\mu_k$  and  $\nu_l$  are KKT multipliers. Here, the general problem is defined as follows.

$$\min_{x \in \mathcal{X}} f(x), \quad \text{subject to } g_k(x) \leq 0, h_l(x) = 0 \quad (2.20)$$

, where  $f$  is an objective function,  $\mathcal{X}$  is a convex subset of  $\mathbb{R}^N$ , and  $g_k$  and  $h_l$  are inequality and equality constraint functions, respectively. All functions are  $\mathbb{R}^N \rightarrow \mathbb{R}$ . KKT approach is a generalized form of the method of Lagrange multipliers, allowing inequality constraints. For the phase problem that does not have inequality constraints, the stationary condition gives the following conditions.

$$\begin{aligned}
0 &\in \partial_u \mathcal{J}_S(u^*) - \operatorname{Re}[\partial_u \langle y, u \rangle(u^*)] = \partial_u \mathcal{J}_S(u^*) - \operatorname{Re}[y] \\
0 &\in \partial_z \mathcal{J}_T(z^*) + \operatorname{Re}[\partial_z \langle y, \mathcal{F}^{-1}z \rangle(z^*)] = \partial_z \mathcal{J}_T(z^*) + \operatorname{Re}[\partial_z \langle \mathcal{F}y, z \rangle(z^*)] \\
&= \partial_z \mathcal{J}_T(z^*) + \operatorname{Re}[\mathcal{F}y]
\end{aligned} \tag{2.21}$$

Unlike  $\mathcal{J}_T$ ,  $\mathcal{J}_S$  is safely treated as a lower semi-continuous extended real-valued convex function. Thus, it allows substitution with its Legendre–Fenchel transform as follows.

$$\begin{aligned}
\operatorname{Re}[y] &\in \partial_u \mathcal{J}_S(u^*) \\
\Leftrightarrow \operatorname{Re}\langle y, u \rangle - \mathcal{J}_S(u) &\geq \operatorname{Re}\langle y, v \rangle - \mathcal{J}_S(v), \quad \exists u \text{ for } \forall v \in \mathbb{C}^{N \times M} \\
\Leftrightarrow \operatorname{Re}\langle y, u \rangle - \mathcal{J}_S(u) &= \sup_{v \in \mathbb{C}^{N \times M}} \operatorname{Re}\langle y, v \rangle - \mathcal{J}_S(v) \\
\Leftrightarrow \mathcal{J}_S(u) &= -\mathcal{J}_S^*(y) + \operatorname{Re}\langle y, u \rangle
\end{aligned} \tag{2.22}$$

, where  $\mathcal{J}_S^*(u)$  is a Legendre–Fenchel transform of  $\mathcal{J}_S(u)$  and defined as  $\mathcal{J}_S^*(y) = \sup_{v \in \mathbb{C}^{N \times M}} \operatorname{Re}\langle y, v \rangle - \mathcal{J}_S(v)$  or equivalently  $\mathcal{J}_S^*(y) = -\inf_{v \in \mathbb{C}^{N \times M}} \mathcal{J}_S(v) - \operatorname{Re}\langle y, v \rangle$ . Using this conversion, the final expression of the dual problem is defined as follows.

$$\max_{y \in \mathbb{C}^{N \times M}} \min_{z \in \mathbb{C}^{N \times M}} [-\mathcal{J}_S^*(y) + \mathcal{J}_T(z) + \operatorname{Re}\langle y, \mathcal{F}^{-1}z \rangle] \tag{2.23}$$

## 2.5. Primal-dual algorithms

Primal-dual algorithms are widely used for convex optimization in imaging science [60]. Here, two representative algorithms, alternating direction method of multipliers (ADMM) and primal-dual hybrid gradient (PDHG), would be introduced for the case of the phase problem [61,62]. ADMM utilizes an augmented Lagrangian defined as follows [59,61].

$$\mathcal{L}_\rho(u, z, y) = \mathcal{J}_S(u) + \mathcal{J}_T(z) + \operatorname{Re}\langle y, \mathcal{F}^{-1}z - u \rangle + \frac{\rho}{2} \|\mathcal{F}^{-1}z - u\|_2^2 \tag{2.24}$$

, where  $\rho$  is a positive real parameter and  $\|\cdot\|_2$  is  $L^2$ -norm. Then, the algorithm is defined as follows.

$$\begin{aligned}
u^{(j+1)} &= \operatorname{argmin}_{u \in \mathbb{R}^{N \times M}} \mathcal{L}_\rho(u, z^{(j)}, y^{(j)}) \\
z^{(j+1)} &= \operatorname{argmin}_{z \in \mathbb{C}^{N \times M}} \mathcal{L}_\rho(u^{(j+1)}, z, y^{(j)}) \\
y^{(j+1)} &= y^{(j)} + \rho(\mathcal{F}^{-1}z - u)
\end{aligned} \tag{2.25}$$

ADMM can be written in a scaled form that is often more convenient. The last two terms in the augmented Lagrangian can be expressed as follows.

$$\begin{aligned} \operatorname{Re}\langle y, \mathcal{F}^{-1}z - u \rangle + \frac{\rho}{2} \|\mathcal{F}^{-1}z - u\|_2^2 &= \frac{\rho}{2} \left\| \mathcal{F}^{-1}z - u + \frac{1}{\rho}y \right\|_2^2 - \frac{1}{2\rho} \|y\|_2^2 \\ &= \frac{\rho}{2} \|\mathcal{F}^{-1}z - u + \tilde{y}\|_2^2 - \frac{\rho}{2} \|\tilde{y}\|_2^2 \end{aligned} \quad (2.26)$$

, where  $\tilde{y}$  is a scaled dual variable defined as  $\tilde{y} = (1/\rho)y$ . Thus, Eq. (2.25) can be simplified as follows.

$$\begin{aligned} u^{(j+1)} &= \underset{u \in \mathbb{R}^{N \times M}}{\operatorname{argmin}} \left[ \mathcal{J}_S(u) + \frac{\rho}{2} \|\mathcal{F}^{-1}z^{(j)} - u + \tilde{y}^{(j)}\|_2^2 \right] \\ z^{(j+1)} &= \underset{z \in \mathbb{C}^{N \times M}}{\operatorname{argmin}} \left[ \mathcal{J}_T(z) + \frac{\rho}{2} \|\mathcal{F}^{-1}z - u^{(j+1)} + \tilde{y}^{(j)}\|_2^2 \right] \\ \tilde{y}^{(j+1)} &= \tilde{y}^{(j)} + \mathcal{F}^{-1}z^{(j+1)} - u^{(j+1)} \end{aligned} \quad (2.27)$$

The first two step can be expressed by a proximal operator. The proximal operator is generally defined as follows.

$$\operatorname{prox}_{f,\lambda}(v) = \underset{x \in \mathcal{X}}{\operatorname{argmin}} \left[ f(x) + \frac{1}{2\lambda} \|x - v\|_2^2 \right] \quad (2.28)$$

Using this operator, Eq. (2.27) becomes as follows.

$$\begin{aligned} u^{(j+1)} &= \operatorname{prox}_{\mathcal{J}_S, 1/\rho} [\mathcal{F}^{-1}z^{(j)} + \tilde{y}^{(j)}] \\ z^{(j+1)} &= \operatorname{prox}_{\mathcal{J}_T, 1/\rho} [\mathcal{F}\{u^{(j+1)} - \tilde{y}^{(j)}\}] \\ \tilde{y}^{(j+1)} &= \tilde{y}^{(j)} + \mathcal{F}^{-1}z^{(j+1)} - u^{(j+1)} \end{aligned} \quad (2.29)$$

Note that ADMM can be interpreted as an application of Douglas–Rachford splitting.

Meanwhile, PDHG starts from the saddle point problem that is described for the case of the phase problem in the previous section [62]. Considering the saddle point problem presented in Eq. (2.23), PDHG is defined as follows.

$$\begin{aligned} y^{(j+1)} &= \operatorname{prox}_{\mathcal{J}_S^*, s} [y^{(j)} + s\mathcal{F}^{-1}\tilde{z}^{(j)}] \\ z^{(j+1)} &= \operatorname{prox}_{\mathcal{J}_T, t} [z^{(j)} - t\mathcal{F}y^{(j+1)}] \\ \tilde{z}^{(j+1)} &= z^{(j+1)} + \theta(z^{(j+1)} - z^{(j)}) \end{aligned} \quad (2.30)$$

, where  $\tilde{z}$  is a temporal primal variable initially set as  $\tilde{z}^{(0)} = z^{(0)}$  and  $s$ ,  $t$ , and  $\theta$  are real parameters satisfying  $s, t > 0$  and  $\theta \in [0,1]$ . Note that PDHG can also be interpreted by Douglas–Rachford splitting, and ADMM with a preconditioner defined as  $M = (1/s)\mathbb{I} - t\mathcal{F}^{-1}\mathcal{F}$  with  $0 < st < 1$  is equivalent with PDHG. As  $\mathcal{J}_S^*$  can be treated as a uniformly convex function of which the gradient is Lipschitz continuous, the convergence of the algorithm can be accelerated by modifying the parameters in Eq. (2.30) as follows.

$$\begin{aligned} y^{(j+1)} &= \text{prox}_{\mathcal{J}_S^*, s_j}[y^{(j)} + s_j \mathcal{F}^{-1} \tilde{z}^{(j)}] \\ z^{(j+1)} &= \text{prox}_{\mathcal{J}_T, t_j}[z^{(j)} - t_j \mathcal{F} y^{(j+1)}] \\ \theta_j &= 1/\sqrt{1 + 2\gamma t_j}, s_{j+1} = s_j/\theta_j, t_{j+1} = \theta_j t_j \\ \tilde{z}^{(j+1)} &= z^{(j+1)} + \theta_j(z^{(j+1)} - z^{(j)}) \end{aligned} \quad (2.31)$$

, where  $\gamma$  is a positive real parameter for updating the parameters and  $s$  and  $t$  are initially assigned values satisfying  $s_0 t_0 \leq 1$ . Both algorithms adopt proximal terms, thereby offer improved convergence and better handling of non-smooth objective functions.

## 2.6. Generalized proximal smoothing

Generalized proximal smoothing (GPS) is a phase retrieval algorithm proposed by Pham *et al.* in 2019, providing superior performance especially with noisy diffraction patterns [63]. GPS uses generalized Moreau–Yosida regularization defined as follows.

$$g_M(x) = \inf_{v \in \mathcal{X}} \left[ g(v) + \frac{1}{2} \|v - u\|_M^2 \right] \quad (2.32)$$

, where  $g$  is a lower semi-continuous extended real-valued function,  $M$  is a Hermitian positive-definite matrix satisfying  $M \in \mathbb{C}^N$ , and  $\mathcal{X}$  is a closed subset of  $\mathbb{C}^N$ . Using this regularization, the objective functions can be relaxed with certain Hermitian positive-definite matrices,  $G$  and  $H$ , modifying the saddle point problem in Eq. (2.23) as follows.

$$\max_{y \in \mathbb{C}^{N \times M}} \min_{z \in \mathbb{C}^{N \times M}} [-\mathcal{J}_{S,G}^*(y) + \mathcal{J}_{T,H}(z) + \text{Re}\langle y, \mathcal{F}^{-1}z \rangle] \quad (2.33)$$

As  $\mathcal{J}_{S,G}$  is still a lower semi-continuous extended real-valued convex function, it can

be expressed as follows.

$$\mathcal{J}_{\mathcal{S},G}(y) = \inf_{v \in \mathbb{C}^{N \times M}} \left[ \mathcal{J}_{\mathcal{S}}(v) + \frac{1}{2} \|v - y\|_{G^{-1}}^2 \right] = \left( \mathcal{J}_{\mathcal{S}} \square \frac{1}{2} \|\cdot\|_{G^{-1}}^2 \right)(y) \quad (2.34)$$

, where  $\square$  is an infimal convolution. Considering the Legendre–Fenchel transform of the infimal convolution,  $\mathcal{J}_{\mathcal{S},G}^*$  is defined as follows.

$$\mathcal{J}_{\mathcal{S},G}^*(y) = \left( \mathcal{J}_{\mathcal{S}} \square \frac{1}{2} \|\cdot\|_{G^{-1}}^2 \right)^*(y) = \mathcal{J}_{\mathcal{S}}^*(y) + \left( \frac{1}{2} \|\cdot\|_{G^{-1}}^2 \right)^*(y) \quad (2.35)$$

The first term is defined as follows.

$$\mathcal{J}_{\mathcal{S}}^*(y) = \sup_{v \in \mathbb{C}^{N \times M}} [\operatorname{Re}\langle y, v \rangle - \mathcal{J}_{\mathcal{S}}(v)] = \sup_{v \in \mathcal{S}} \operatorname{Re}\langle y, v \rangle = \mathcal{J}_{\mathcal{S}^*}(y) \quad (2.36)$$

, where  $\mathcal{S}^*$  is a set of matrices defined as follows.

$$\mathcal{S}^* = \{y \in \mathbb{C}^{N \times M} | y_i, \text{ if } i \in S \wedge \operatorname{Re}[y_i] \leq 0; \quad y_i = 0, \text{ otherwise}\} \quad (2.37)$$

The second term is defined as follows.

$$\left( \frac{1}{2} \|\cdot\|_{G^{-1}}^2 \right)^*(y) = \sup_{v \in \mathbb{C}^{N \times M}} \left[ \operatorname{Re}\langle y, v \rangle - \frac{1}{2} \|v\|_{G^{-1}}^2 \right] = \sup_{v \in \mathbb{C}^{N \times M}} \left[ \operatorname{Re}\langle y, v \rangle - \frac{1}{2} \langle v, G^{-1}v \rangle \right] \quad (2.38)$$

The first derivative condition for the supremum gives the following relation.

$$\partial_v \left[ \operatorname{Re}\langle y, v \rangle - \frac{1}{2} \langle v, G^{-1}v \rangle \right] = \operatorname{Re}[y - G^{-1}v] = 0 \quad (2.39)$$

Substituting by  $v = Gy$ , Eq. (2.38) becomes as follows.

$$\sup_{v \in \mathbb{C}^{N \times M}} \left[ \operatorname{Re}\langle y, Gy \rangle - \frac{1}{2} \langle Gy, G^{-1}Gy \rangle \right] = \|y\|_G^2 - \frac{1}{2} \|y\|_G^2 = \frac{1}{2} \|y\|_G^2 \quad (2.40)$$

Finally,  $\mathcal{J}_{\mathcal{S},G}^*$  becomes as follows.

$$\mathcal{J}_{\mathcal{S},G}^*(y) = \mathcal{J}_{\mathcal{S}^*}(y) + \frac{1}{2} \|y\|_G^2 \quad (2.41)$$

GPS is equivalent with PDHG for the abovementioned relaxed indicator functions, giving the following algorithm of which the order is slightly modified from Eq. (2.30). Note

that GPS sets  $\theta = 1$ .

$$\begin{aligned} z^{(j+1)} &= \text{prox}_{\mathcal{J}_{T,H},t}[z^{(j)} - t\mathcal{F}y^{(j)}] \\ y^{(j+1)} &= \text{prox}_{\mathcal{J}_{S,G}^*,s}[y^{(j)} + s\mathcal{F}^{-1}\{2z^{(j+1)} - z^{(j)}\}] \end{aligned} \quad (2.42)$$

GPS relaxes  $\mathcal{J}_{T,H}$  by simply assigning the constant to the matrix as  $H = \sigma\mathbb{I}$ , giving the least square terms as follows.

$$\begin{aligned} \mathcal{J}_{T,\sigma}(z) &= \inf_{v \in \mathbb{C}^{N \times M}} \left[ \mathcal{J}_T(v) + \frac{1}{2} \|v - z\|_{(1/\sigma)}^2 \right] = \inf_{v \in \mathcal{T}} \frac{1}{2\sigma} \|v - z\|_2^2 \\ &= \frac{1}{2\sigma} \|\text{proj}_{\mathcal{J}_T}[z] - z\|_2^2 = \frac{1}{2\sigma} \|b \odot e^{i \arg z} - z\|_2^2 = \frac{1}{2\sigma} \|b - |z|\|_2^2 \end{aligned} \quad (2.43)$$

Thus, the proximal operator in the first step of Eq. (2.42) can be conducted as follows.

$$\begin{aligned} \text{prox}_{\mathcal{J}_{T,\sigma},t}[z] &= \underset{v \in \mathbb{C}^{N \times M}}{\text{argmin}} \left[ \mathcal{J}_{T,\sigma}(v) + \frac{1}{2t} \|v - z\|^2 \right] \\ &= \underset{v \in \mathbb{C}^{N \times M}}{\text{argmin}} \left[ \frac{1}{2\sigma} \|b - |v|\|_2^2 + \frac{1}{2t} \|v - z\|^2 \right] \\ &= \frac{t}{\sigma + t} b \odot e^{i \arg z} + \frac{\sigma}{\sigma + t} z \end{aligned} \quad (2.44)$$

On the other hand, the proximal operator in the second step of Eq. (2.42) can be calculated as follows.

$$\begin{aligned} \text{prox}_{\mathcal{J}_{S,G}^*,s} y &= \underset{v \in \mathbb{C}^{N \times M}}{\text{argmin}} \left[ \mathcal{J}_{S^*}(y) + \frac{1}{2} \|y\|_G^2 + \frac{1}{2s} \|v - y\|^2 \right] \\ &= \underset{v \in S^*}{\text{argmin}} \left[ \frac{1}{2} \|y\|_G^2 + \frac{1}{2s} \|v - y\|^2 \right] \\ &= (\mathbb{I} + sG)^{-1} \text{proj}_{\mathcal{J}_{S^*}} y \end{aligned} \quad (2.45)$$

GPS provides two variants up to the choice of the matrix,  $G$ . One variant is GPS-R that uses the matrix defined as  $G = \gamma D^T D$ , where  $\gamma$  is a positive real parameter satisfying  $\gamma \ll 1$  and  $D$  is a discrete gradient operator. As  $(\mathbb{I} + s\gamma D^T D)^{-1}$  is roughly a kind of the Laplace smoothing, it can be expressed as a convolution of the heat kernel defined as  $\mathcal{G}_t(\mathbf{r}) = (1/4\pi t)e^{-r^2/4t}$ . Using the Fourier transform of  $\mathcal{G}_t(\mathbf{r})$  is defined as  $\mathcal{W}_t(Q) = e^{-tQ^2}$ , Eq. (2.45) becomes as follows.

$$(\mathbb{I} + s\gamma D^T D)^{-1} \text{proj}_{J_{S^*}}[y] \approx \mathcal{G}_{s\gamma} * \text{proj}_{J_{S^*}}[y] = \mathcal{F}^{-1}[\mathcal{W}_{s\gamma} \odot \mathcal{F}\{\text{proj}_{J_{S^*}}y\}] \quad (2.46)$$

Reminding the Gaussian kernel of OSS defined as  $W(Q) = e^{-Q^2/2\alpha^2}$ , the choice of  $\gamma$  is directly imported from OSS as  $\mathcal{W}_\gamma = W$ , thereby  $\gamma$  is defined as  $\gamma = 1/2\alpha^2$  with  $\alpha$  and its updating policy from OSS. Thus,  $\mathcal{W}_{s\gamma}$  can be obtained by  $\mathcal{W}_{s\gamma}(Q) = e^{-sQ^2/2\alpha^2}$ .

Another variant is GPS-F, and it uses the matrix defined as  $G = \gamma \text{diag}(r^2)$ , where  $r$  is a distance with respect to the center and  $\text{diag}$  denotes a diagonal matrix operator. Using this matrix, Eq. (2.45) becomes as follows.

$$\begin{aligned} [\mathbb{I} + s\gamma \text{diag}(r^2)]^{-1} \text{proj}_{J_{S^*}}[y] &= \text{diag}\left(\frac{1}{1 + s\gamma r^2}\right) \odot \text{proj}_{J_{S^*}}[y] \\ &\approx \text{diag}(e^{-s\gamma r^2}) \odot \text{proj}_{J_{S^*}}[y] \\ &= \mathcal{W}_{s\gamma/4\pi^2} \odot \text{proj}_{J_{S^*}}[y] \end{aligned} \quad (2.47)$$

Here, as the variables are discrete 2D data and can be mapped by integer coordinates,  $\mathbf{Q} \rightarrow \mathbf{r}$  can be simply converted by dividing  $2\pi$  to each  $Q$ , thereby giving  $\text{diag}(e^{-s\gamma r^2}) = \mathcal{W}_{s\gamma/4\pi^2}$ . The choice of  $\gamma$  is also directly imported from OSS like as GPS-R and  $\mathcal{W}_{s\gamma/4\pi^2}$  can be obtained by  $\mathcal{W}_{s\gamma/4\pi^2} = e^{-sQ^2/8\pi^2\alpha^2}$ .

The major difference of GPS-R and GPS-F is the space where Gaussian kernels are convolved. As their names state, GPS-R convolves the Gaussian kernel in the real space, while GPS-F convolves the kernel in the Fourier space. These variants should be properly chosen for better image reconstruction. In summary, GPS is equivalent with PDHG for the indicator functions relaxed by the generalized Moreau–Yosida regularization. It provides robust performance especially for data with strong noises, facilitating phase retrieval of photon-limited single-shot diffraction patterns that is essential for time-resolved imaging. In this regard, GPS has been played an important role in time-resolved CDI, which enables tracing ultrafast dynamics of various systems in nanoscale resolution [10,11].

### 3. Vortex beam

### 3.1. Introduction

Vortex beams, of which wavefronts have helical structures expressed by the Laguerre–Gaussian (LG) modes, have attracted research interests across multidisciplinary science due to their unique characteristics. In 1992, Allen *et al.* noticed that LG laser modes, of which wavefronts have an azimuthal dependence of  $e^{il\phi}$ , where  $l$  is an azimuthal mode index or topological charge, inhere an orbital angular momentum (OAM) of  $l\hbar$  [64]. He *et al.* observed transfer of OAM and subsequent rotations by trapped absorptive particles using LG beams in 1995 thereafter [65]. Similarly, Simpson *et al.* controlled both spin angular momentum (SAM) and OAM of the beam and observed mechanical rotations of the particles in 1997 [66]. After two decades, total angular momentum transfer to the valence electron of a trapped ion was experimentally observed by controlling both SAM and OAM of incident light, verifying the selection rule [67]. Besides such findings, applications of vortex beams have been actively developed in various fields for few decades [68].

The first observation of an X-ray vortex beam was achieved by Peele *et al.* in 2002 using a spiral phase plate [69]. However, as diffractive optical elements (DOEs) are known to be more efficient in the X-ray regime and have already been studied with computer-generated holograms, generation of X-ray vortex beams was also reported using binary DOEs including fork grating and spiral zone plate (SZP) [70,71]. In the X-ray imaging field, as such DOEs offer the radial Hilbert transform, an edge enhancement of images can be achieved methodologically by using SZPs [72,73]. Moreover, the resolution improvements were also reported for ptychography using vortex beams in the extreme ultraviolet regime [74,75]. These advantages have stimulated the use of SZPs for various X-ray imaging methods.

Another effect by the vortex beam is helical dichroism, which is sometimes referred as helicoidal or vortex dichroism. Unlike linear or circular dichroism, helical dichroism is a dichroism depend on topological charges of incident vortex beams not their polarization states, and it is expected to provide enhanced sensitivities to quadrupolar transitions and chirality of materials [76]. Recently, helical dichroism has been reported in various chiral systems such as chiral plasmonic nanostructures, enantiomers, magnetic vortices, and antiferromagnetic  $\mathbb{Z}2$  topological defects [77–80]. OAM has higher degree of freedom on its value compared to SAM,

which is limited to  $\pm\hbar$  corresponding to left and right circular polarization. In addition, though there have yet been only a few reports of helical dichroism in X-ray regime, strong helical dichroism has been theoretically predicted, thereby having great potentials [81–84]. In this chapter, light–matter interaction by vortex beam and subsequent helical dichroism would be introduced. Brief explanation on SZPs would also be given.

### 3.2. Vector potential of vortex beam

A vector potential of the vortex beam is described by LG modes, and it is crucial to understand the light–matter interaction by the vortex beam. From the Helmholtz equation with paraxial approximation as in Eq. (1.8), the beam can be described as follows in cylindrical coordinates [20,64,85].

$$\text{LG}_{pl}(r, \phi, z) = \sqrt{\frac{2p!}{\pi(p+|l|)!}} \frac{w_0}{w} \left(\frac{\sqrt{2}r}{w}\right)^{|l|} e^{-r^2/w^2} L_p^{|l|}\left(\frac{2r^2}{w^2}\right) \cdot e^{il\phi} e^{ikr^2z/2(z^2+z_R^2)} e^{-i(2p+|l|+1)\tan^{-1}(z/z_R)} \quad (3.1)$$

, where  $p$  and  $l$  are radial and azimuthal mode indices for the associated Laguerre polynomial,  $L_p^{|l|}$ , respectively,  $z$  is a coordinate from the beam center,  $z_R$  is the Rayleigh range given by  $z_R = \pi w_0^2/\lambda$ , and  $w$  is a radius of the Gaussian beam at  $1/e^2$  of its intensity defined as  $w(z) = w_0\sqrt{1+z^2/z_R^2}$  with a radius of the beam waist,  $w_0$ . Note that  $(2p+|l|+1)\tan^{-1}(z/z_R)$  is the Gouy phase. For the sake of simplicity, the coefficient  $\sqrt{2p!/\pi(p+|l|)!}$  would be ignored hereafter. Then, the vector potential of the vortex beam in the Lorenz gauge is expressed as follows.

$$\mathbf{A}^L(\mathbf{r}) = \boldsymbol{\varepsilon}_\Lambda \text{LG}_{pl}(\mathbf{r}) e^{ikz} \quad (3.2)$$

, where  $\boldsymbol{\varepsilon}_\Lambda$  denotes the polarization vector of a state,  $\Lambda$ .

When in-plane components of the wavevector is considered with a small angle of  $\theta_k = \tan^{-1}(k_\perp/k_z) \ll 1$  yet satisfying the paraxial approximation, the wavevector is defined as follows.

$$\mathbf{k} = k_{\perp} \cos \phi_k \hat{e}_x + k_{\perp} \sin \phi_k \hat{e}_y + k_z \hat{e}_z \quad (3.3)$$

, where  $\mathbf{k}_{\perp}$  and  $\phi_k$  are in-plane coordinate and corresponding azimuthal angle perpendicular to the propagating axis,  $z$ , respectively. Then, the vector potential can be expressed by Fourier-space components as follows. Note that this relation assumes superposition of plane waves at  $z = 0$ .

$$\mathbf{A}^L(r, \phi, z = 0) = \int d^2 \mathbf{k}_{\perp} \boldsymbol{\varepsilon}_{\Lambda} \Upsilon_{pl}(\mathbf{k}_{\perp}) e^{i \mathbf{k} \cdot \mathbf{r}} \quad (3.4)$$

, where  $\Upsilon_{pl}$  is a Fourier component of the vector potential and can be obtained as follows.

$$\begin{aligned} \Upsilon_{pl}(\mathbf{k}_{\perp}) &= \frac{1}{(2\pi)^2} \int d^2 \mathbf{r}_{\perp} L G_{pl}(r, \phi, z = 0) e^{-i \mathbf{k}_{\perp} \cdot \mathbf{r}_{\perp}} \\ &= \frac{1}{(2\pi)^2} \int d^2 \mathbf{r}_{\perp} \left( \frac{\sqrt{2} r_{\perp}}{w_0} \right)^{|l|} e^{-r_{\perp}^2/w_0^2} L_p^{|l|} \left( \frac{2r_{\perp}^2}{w_0^2} \right) e^{il\phi} e^{-ik_{\perp} r_{\perp} \cos(\phi - \phi_k)} \\ &= \frac{1}{(2\pi)^2} \int_0^{\infty} dr_{\perp} r_{\perp} \left( \frac{\sqrt{2} r_{\perp}}{w_0} \right)^{|l|} e^{-r_{\perp}^2/w_0^2} L_p^{|l|} \left( \frac{2r_{\perp}^2}{w_0^2} \right) \int_0^{2\pi} d\phi e^{il\phi} e^{-ik_{\perp} r_{\perp} \cos(\phi - \phi_k)} \end{aligned} \quad (3.5)$$

As the integral term about the azimuthal angle,  $\phi$ , in Eq. (3.5) is analogous with the integral representation of the Bessel function of the first kind,  $J_l$ , it can be expressed as follows.

$$\int_0^{2\pi} d\phi e^{il\phi} e^{-ik_{\perp} r_{\perp} \cos(\phi - \phi_k)} = 2\pi (-i)^l e^{il\phi_k} J_l(k_{\perp} r_{\perp}) \quad (3.6)$$

Here,  $(-i)^l$  and  $J_l(k_{\perp} r_{\perp})$  in Eq. (3.6) satisfies  $(-i)^{-|l|} J_{-|l|}(k_{\perp} r_{\perp}) = i^{|l|} (-1)^{|l|} J_{|l|}(k_{\perp} r_{\perp}) = (-i)^{|l|} J_{|l|}(k_{\perp} r_{\perp})$  for  $l < 0$ , thereby guaranteeing  $(-i)^l J_l(k_{\perp} r_{\perp}) \rightarrow (-i)^{|l|} J_{|l|}(k_{\perp} r_{\perp})$  for all  $l$ . Meanwhile, the associated Laguerre polynomial term is defined as follows.

$$L_p^{|l|} \left( \frac{2r_{\perp}^2}{w_0^2} \right) = \sum_{\beta=0}^p \frac{(-1)^{\beta}}{\beta!} \binom{p+|l|}{p-\beta} \left( \frac{2r_{\perp}^2}{w_0^2} \right)^{\beta} \quad (3.7)$$

, where  $\binom{\cdot}{\cdot}$  is the binomial coefficient. Then, Eq. (3.5) becomes as follows.

$$\begin{aligned} \Upsilon_{pl}(\mathbf{k}_\perp) &= \frac{(-i)^{|l|} w_0 e^{il\phi_k}}{2\sqrt{2}\pi} \sum_{\beta=0}^p \frac{(-1)^\beta}{\beta!} \binom{p+|l|}{p-\beta} \left(\frac{\sqrt{2}}{w_0}\right)^{2\beta+|l|+1} \\ &\quad \cdot \int_0^\infty dr_\perp r_\perp^{2\beta+|l|+1} e^{-r_\perp^2/w_0^2} J_{|l|}(k_\perp r_\perp) \end{aligned} \quad (3.8)$$

Substituting by  $u = r_\perp^2/w_0^2$ , the integral term in Eq. (3.8) can be simplified by the special identity between the associated Laguerre polynomial and the Bessel function of the first kind as follows [86].

$$\begin{aligned} &\int_0^\infty dr_\perp r_\perp^{2\beta+|l|+1} e^{-r_\perp^2/w_0^2} J_{|l|}(k_\perp r_\perp) \\ &= \frac{w_0^{2\beta+|l|+2}}{2} \int_0^\infty du u^{\beta+|l|/2} e^{-u} J_{|l|}\left(2\sqrt{u \frac{k_\perp^2 w_0^2}{4}}\right) \\ &= \frac{w_0^{2\beta+|l|+2}}{2} \beta! e^{-k_\perp^2 w_0^2/4} \left(\frac{k_\perp^2 w_0^2}{4}\right)^{|l|/2} L_\beta^{|l|}\left(\frac{k_\perp^2 w_0^2}{4}\right) \end{aligned} \quad (3.9)$$

Using this result, Eq. (3.8) finally becomes as follows.

$$\begin{aligned} \Upsilon_{pl}(\mathbf{k}_\perp) &= \frac{(-i\sqrt{2})^{|l|} w_0^2}{4\pi} \left(\frac{k_\perp^2 w_0^2}{4}\right)^{|l|/2} e^{-k_\perp^2 w_0^2/4} e^{il\phi_k} \sum_{\beta=0}^p (-2)^\beta \binom{p+|l|}{p-\beta} L_\beta^{|l|}\left(\frac{k_\perp^2 w_0^2}{4}\right) \\ &\equiv v_{pl}(k_\perp) e^{il\phi_k} \end{aligned} \quad (3.10)$$

, where  $v_{pl}(k_\perp)$  is a radial distribution of  $\Upsilon_{pl}$ .

When the polarization vector is not perpendicular to the wavevector, the divergence of the vector potential does not vanish, and consequent nonzero scalar potential makes the Lorenz gauge no longer more convenient than the Coulomb gauge. Using the small-angle approximation, the wavevector is defined as follows.

$$\begin{aligned} \mathbf{k} &= k \sin \theta_k \cos \phi_k \hat{e}_x + k \sin \theta_k \sin \phi_k \hat{e}_y + k \cos \theta_k \hat{e}_z \\ &\approx k \theta_k \cos \phi_k \hat{e}_x + k \theta_k \sin \phi_k \hat{e}_y + k \hat{e}_z \end{aligned} \quad (3.11)$$

The polarization vector is also defined as  $\boldsymbol{\varepsilon}_\Lambda = (-\Lambda/\sqrt{2})(\hat{e}_x + i\Lambda \hat{e}_y)$  with  $\Lambda = \pm 1$  corresponding to left and right circular polarization that give SAM of  $\pm \hbar$ , respectively [87].

Then, the polarization vector associated with the wavevector is given as follows.

$$\begin{aligned}
\boldsymbol{\varepsilon}_{k,\Lambda} &= \boldsymbol{\varepsilon}_{-\Lambda} e^{i\Lambda\phi_k} \sin^2\left(\frac{\theta_k}{2}\right) + \boldsymbol{\varepsilon}_\Lambda e^{-i\Lambda\phi_k} \cos^2\left(\frac{\theta_k}{2}\right) + \frac{\Lambda}{\sqrt{2}} \sin \theta_k \hat{e}_z \\
&= \frac{\Lambda}{\sqrt{2}} \left[ \left\{ e^{i\Lambda\phi_k} \sin^2\left(\frac{\theta_k}{2}\right) - e^{-i\Lambda\phi_k} \cos^2\left(\frac{\theta_k}{2}\right) \right\} \hat{e}_x \right. \\
&\quad \left. + \left\{ -i\Lambda e^{i\Lambda\phi_k} \sin^2\left(\frac{\theta_k}{2}\right) - i\Lambda e^{-i\Lambda\phi_k} \cos^2\left(\frac{\theta_k}{2}\right) \right\} \hat{e}_y + \sin \theta_k \hat{e}_z \right] \\
&= -\frac{\Lambda}{\sqrt{2}} \left[ (\cos \theta_k \cos \phi_k - i\Lambda \sin \phi_k) \hat{e}_x \right. \\
&\quad \left. + (\cos \theta_k \sin \phi_k + i\Lambda \cos \phi_k) \hat{e}_y - \sin \theta_k \hat{e}_z \right] \\
&\approx -\frac{\Lambda}{\sqrt{2}} \left[ (\cos \phi_k - i\Lambda \sin \phi_k) \hat{e}_x + (\sin \phi_k + i\Lambda \cos \phi_k) \hat{e}_y - \theta_k \hat{e}_z \right] \\
&= -\frac{\Lambda}{\sqrt{2}} \left[ e^{-i\Lambda\phi_k} (\hat{e}_x + i\Lambda \hat{e}_y) - \theta_k \hat{e}_z \right] = e^{-i\Lambda\phi_k} \boldsymbol{\varepsilon}_\Lambda + \frac{\Lambda}{\sqrt{2}} \theta_k \hat{e}_z
\end{aligned} \tag{3.12}$$

Thus, using Eq. (1.13) and Eq. (3.4) substituted by Eq. (3.10), the vector potential in the Coulomb gauge is defined as follows.

$$\begin{aligned}
\mathbf{A}^C(\mathbf{r}) &\approx \int d^2 \mathbf{k}_\perp \left[ \boldsymbol{\varepsilon}_\Lambda + \frac{\Lambda}{\sqrt{2}} \theta_k (\cos \phi_k + i\Lambda \sin \phi_k) \hat{e}_z \right] v_{pl}(k_\perp) e^{il\phi_k} \\
&= \int d^2 \mathbf{k}_\perp \left( \boldsymbol{\varepsilon}_\Lambda + \frac{\Lambda}{\sqrt{2}} \theta_k e^{i\Lambda\phi_k} \hat{e}_z \right) v_{pl}(k_\perp) e^{il\phi_k} \\
&= \int d^2 \mathbf{k}_\perp \boldsymbol{\varepsilon}_{k,\Lambda} v_{pl}(k_\perp) e^{i(l+\Lambda)\phi_k} e^{i\mathbf{k} \cdot \mathbf{r}}
\end{aligned} \tag{3.13}$$

The azimuthal term,  $e^{i(l+\Lambda)\phi_k}$ , has the integer coefficient of  $l + \Lambda$ , which eventually indicates the total angular momentum. Both vector potentials in the Lorenz and Coulomb gauges obviously bring identical physical observables, thereby the gauge can be chosen for the simplicity of calculation based on each situation.

### 3.3. Light-matter interaction with vortex beams and helical dichroism

When considering an absorption of a single photon characterized by  $\mathbf{k}$  and  $\Lambda$  by an atom, the matrix elements for the light-matter interaction are defined by the bra-ket notation with the

interaction Hamiltonian as in Eq. (1.29). Here, the interaction Hamiltonian is given as follows. Note that only leading terms,  $\mathbf{p} \cdot \mathbf{A}$  and  $\mathbf{A} \cdot \mathbf{p}$ , are considered. Note that the transversality condition is assumed, giving  $\mathbf{p} \cdot \mathbf{A} = \mathbf{A} \cdot \mathbf{p}$ .

$$H_{\text{int}} = -\frac{e}{mc} \mathbf{A}(\mathbf{r}, t) \cdot \mathbf{p} \quad (3.14)$$

Then, the transition matrix is given as follows.

$$\langle f | H_{\text{int}} | g \rangle = -\frac{e}{mc} \langle f; n_{k,\Lambda} - 1 | \mathbf{A} \cdot \mathbf{p} | g; n_{k,\Lambda} \rangle \quad (3.15)$$

Here, the vector potential is assumed to have the following formula at  $z = 0$  with the assumption of the dipole approximation,  $e^{ikz} \approx 1$ .

$$\mathbf{A}_{pl}(r, \phi, z = 0) = \epsilon_{\Lambda} a_{k,\Lambda} \sqrt{\frac{2p!}{\pi(p + |l|)!}} \left( \frac{\sqrt{2}r}{w_0} \right)^{|l|} e^{-r^2/w_0^2} L_p^{|l|} \left( \frac{2r^2}{w_0^2} \right) e^{il\phi} \quad (3.16)$$

For the sake of simplicity, the radial mode index is fixed by  $p = 0$  and the Gaussian term is ignored by the approximation,  $r^2/w_0^2 \ll 1 \rightarrow e^{-r^2/w_0^2} \approx 1$ , giving the following vector potential formula.

$$\mathbf{A}_l(r, \phi) = \epsilon_{\Lambda} a_{k,\Lambda} \sqrt{\frac{2}{\pi|l|!}} \left( \frac{\sqrt{2}r}{w_0} \right)^{|l|} e^{il\phi} \quad (3.17)$$

As the spherical coordinate system is more convenient to describe electron transitions, it is better to represent the vector potential in the spherical coordinates [81]. The spherical harmonics having  $e^{il\phi}$  term is given as follows.

$$Y_{|l|}^{\pm|l|} \left( \theta = \frac{\pi}{2}, \phi \right) = \frac{(\mp 1)^{|l|}}{2^{|l|}|l|!} \sqrt{\frac{(2|l| + 1)!}{4\pi}} e^{\pm i|l|\phi} \quad (3.18)$$

Then, the vector potential can be written as follows.

$$\begin{aligned}\mathbf{A}_{\pm|l|}(r, \phi) &= \boldsymbol{\varepsilon}_\Lambda a_{k,\Lambda} (\mp 1)^{|l|} 2 \sqrt{\frac{2|l|!}{(2|l|+1)!}} \left(\frac{2\sqrt{2}r}{w_0}\right)^{|l|} Y_{|l|}^{\pm|l|}(\phi) \\ &\equiv \boldsymbol{\varepsilon}_\Lambda a_{k,\Lambda} (\mp 1)^{|l|} A_{|l|} \frac{r_{\pm|l|}^{(|l|)}(r, \phi)}{w_0^{|l|}}\end{aligned}\quad (3.19)$$

, where  $A_{|l|}$  is the coefficient of the vector potential and  $r_q^{(m)}$  is a tensor defined as  $r_l^{(m)}(r, \phi) = \sqrt{4\pi/(2m+1)} r^m Y_m^l(\phi)$ . Substituting by  $\mathbf{r} \rightarrow \mathbf{R} + \mathbf{r}$ , where  $\mathbf{R}$  is the position of an atom and  $\mathbf{r}$  is now the position from the center of an atom, the transition matrix becomes as follows for  $l = \pm 1$ .

$$\begin{aligned}& -\frac{e}{mc} \langle f | \mathbf{A}_{\pm 1}(\mathbf{R} + \mathbf{r}) \cdot \mathbf{p} | g \rangle \\ & \approx \pm \frac{eA_1}{mcw_0} \langle f; n_{k,\Lambda} - 1 | a_{k,\Lambda} \left( R_{\pm 1}^{(1)} + r_{\pm 1}^{(1)} \right) \boldsymbol{\varepsilon}_\Lambda \cdot \mathbf{p} | g; n_{k,\Lambda} \rangle \\ & = \pm \frac{e\sqrt{n_{k,\Lambda}}A_1}{mcw_0} \langle f; n_{k,\Lambda} - 1 | \left( R_{\pm 1}^{(1)} + r_{\pm 1}^{(1)} \right) \boldsymbol{\varepsilon}_\Lambda \cdot \mathbf{p} | g; n_{k,\Lambda} - 1 \rangle \\ & = \pm \frac{e\sqrt{n_{k,\Lambda}}A_1}{mcw_0} \left[ \langle f | R_{\pm 1}^{(1)} \boldsymbol{\varepsilon}_\Lambda \cdot \mathbf{p} | g \rangle + \langle f | r_{\pm 1}^{(1)} \boldsymbol{\varepsilon}_\Lambda \cdot \mathbf{p} | g \rangle \right]\end{aligned}\quad (3.20)$$

Using the commutation relation as in Eq. (1.28), Eq. (3.20) becomes as follows.

$$\begin{aligned}& \pm \frac{ie\sqrt{n_{k,\Lambda}}A_1}{\hbar c w_0} \left[ \langle f | R_{\pm 1}^{(1)} \boldsymbol{\varepsilon}_\Lambda \cdot [H_0, \mathbf{r}] | g \rangle + \langle f | r_{\pm 1}^{(1)} \boldsymbol{\varepsilon}_\Lambda \cdot [H_0, \mathbf{r}] | g \rangle \right] \\ & = \pm \frac{ie\sqrt{n_{k,\Lambda}}\omega_{fg}A_1}{c w_0} \left[ \langle f | R_{\pm 1}^{(1)} \boldsymbol{\varepsilon}_\Lambda \cdot (H_0 \mathbf{r} - \mathbf{r} H_0) | g \rangle + \langle f | r_{\pm 1}^{(1)} \boldsymbol{\varepsilon}_\Lambda \cdot (H_0 \mathbf{r} - \mathbf{r} H_0) | g \rangle \right] \\ & = \pm \frac{ie\sqrt{n_{k,\Lambda}}\omega_{fg}A_1}{c w_0} \left[ R_{\pm 1}^{(1)} \langle f | \boldsymbol{\varepsilon}_\Lambda \cdot \mathbf{r} | g \rangle + \langle f | r_{\pm 1}^{(1)} \boldsymbol{\varepsilon}_\Lambda \cdot \mathbf{r} | g \rangle \right]\end{aligned}\quad (3.21)$$

, where  $\omega_{fg}$  is the frequency corresponding to the energy difference between the states,  $f$  and  $g$ , defined as  $\omega_{fg} = (E_f - E_g)/\hbar$ . Here,  $\boldsymbol{\varepsilon}_\Lambda \cdot \mathbf{r}$  also can be expressed by the spherical harmonics as follows.

$$\boldsymbol{\varepsilon}_\Lambda \cdot \mathbf{r} = -\frac{\Lambda}{\sqrt{2}} (\hat{e}_x + i\Lambda \hat{e}_y) \cdot \mathbf{r} = -\frac{\Lambda}{\sqrt{2}} r e^{i\Lambda\phi} = -\Lambda \sqrt{\frac{3}{8\pi}} r_\Lambda^{(1)} \quad (3.22)$$

This term indicates SAM of  $\Lambda\hbar$ . Thus, Eq. (3.21) becomes as follows.

$$\mp \frac{i\Lambda e\sqrt{n_{k,\Lambda}}\omega_{fg}A'_1}{cw_0} \left[ R_{\pm 1}^{(1)} \langle f | r_{\Lambda}^{(1)} | g \rangle + \langle f | r_{\pm 1}^{(1)} r_{\Lambda}^{(1)} | g \rangle \right] \quad (3.23)$$

, where  $A'_1$  is a new coefficient defined as  $\sqrt{3/8\pi}A_1$ . Here,  $r_{\pm 1}^{(1)}r_{\Lambda}^{(1)}$  can be calculated as follows.

$$r_{\pm 1}^{(1)}r_{\Lambda}^{(1)} = \sqrt{\frac{4\pi}{3}}rY_1^{\pm 1} \cdot \sqrt{\frac{4\pi}{3}}rY_1^{\Lambda} = \begin{cases} \sqrt{\frac{4\pi}{5}}r^2Y_2^0, & \text{if } \Lambda = \mp 1 \\ \sqrt{\frac{8\pi}{15}}r^2Y_2^{\pm 2}, & \text{otherwise} \end{cases} = c_{\Lambda \pm 1}r_{\Lambda \pm 1}^{(2)} \quad (3.24)$$

, where the coefficient  $c_{\Lambda \pm 1}$  is given by  $c_0 = 1$  and  $c_{\pm 2} = \sqrt{2/3}$ . This term indicates the total angular momentum of  $(\Lambda \pm 1)\hbar$ . Then, the transition matrix finally becomes as follows.

$$\langle f | H_{\text{int}} | g \rangle \approx \mp \frac{i\Lambda e\sqrt{n_{k,\Lambda}}\omega_{fg}A'_1}{cw_0} \left[ R_{\pm 1}^{(1)} \langle f | r_{\Lambda}^{(1)} | g \rangle + c_{\Lambda \pm 1} \langle f | r_{\Lambda \pm 1}^{(2)} | g \rangle \right] \quad (3.25)$$

As the complex conjugate of  $R_{\pm 1}^{(1)}$  gives  $R_{\pm 1}^{(1)*} = -R_{\mp 1}^{(1)}$ , the absorption probability is derived as follows.

$$\begin{aligned} & I_{\pm 1}(\mathbf{R}) \\ &= \sum_f |\langle f | H_{\text{int}} | g \rangle|^2 \approx \frac{e^2 A'^2}{c^2 w_0^2} \sum_f \omega_{fg}^2 \left| \sum_{\Lambda} \sqrt{n_{k,\Lambda}} [R_{\pm 1}^{(1)} \mathcal{M}_{1,\Lambda}^f + c_{\Lambda \pm 1} \mathcal{M}_{2,\Lambda \pm 1}^f] \right|^2 \\ &= \frac{e^2 A'^2}{c^2 w_0^2} \sum_{f,\Lambda',\Lambda} \sqrt{n_{k,\Lambda'} n_{k,\Lambda}} \omega_{fg}^2 \left[ -R_{\pm 1}^{(1)} R_{\mp 1}^{(1)} \mathcal{M}_{1,\Lambda'}^{f\dagger} \mathcal{M}_{1,\Lambda}^f - R_{\mp 1}^{(1)} c_{\Lambda \pm 1} \mathcal{M}_{1,\Lambda'}^{f\dagger} \mathcal{M}_{2,\Lambda \pm 1}^f \right. \\ &\quad \left. + R_{\pm 1}^{(1)} c_{\Lambda' \pm 1} \mathcal{M}_{2,\Lambda' \pm 1}^{f\dagger} \mathcal{M}_{1,\Lambda}^f + c_{\Lambda' \pm 1} c_{\Lambda \pm 1} \mathcal{M}_{2,\Lambda' \pm 1}^{f\dagger} \mathcal{M}_{2,\Lambda \pm 1}^f \right] \end{aligned} \quad (3.26)$$

, where the transition matrix is simply represented as  $\mathcal{M}_{ml}^f = \langle f | r_l^{(m)} | g \rangle$ . The first term is related to dipole transitions, the second and third term related to dipole-quadrupole interferences, and the last term related to quadrupole transitions. When the cross terms vanish, Eq. (3.26) is simplified as follows. Note that it is valid for systems with inversion symmetry.

$$I_{\pm 1}(\mathbf{R}) \approx \frac{e^2 A_1'^2}{c^2 w_0^2} \sum_{f,\Lambda} n_{\mathbf{k},\Lambda} \omega_{fg}^2 \left[ \frac{R^2}{2} |\mathcal{M}_{1,\Lambda}^f|^2 + c_{\Lambda \pm 1}^2 |\mathcal{M}_{2,\Lambda \pm 1}^f|^2 \right] \quad (3.27)$$

Integrating over all atomic positions, the absorption difference from the opposite sign of the OAM can be obtained. When the anisotropy defined as  $2(I_{+1} - I_{-1})/(I_{+1} + I_{-1})$  is nonzero, this is called helical dichroism.

### 3.4. Linear response theory with vortex beams and helical dichroism

For more explicit calculation for physical measurements, the calculation can be conducted based on the linear response theory. Considering a time-dependent perturbation, the Hamiltonian is defined as follows [88].

$$H = H_0 + H'(t) = H_0 + F(t)H_{\text{int}} \quad (3.28)$$

, where  $F$  is the time-dependence of the perturbation. The perturbed ground state,  $\Psi'_g$ , can be expressed using the interaction picture as follows.

$$\Psi'_g = \Psi_g + \sum_f c_f(t) e^{-i\omega_{fg} t} \Psi_f \quad (3.29)$$

, where  $\omega_{fg}$  is the frequency corresponding to the energy difference between the states,  $g$  and  $f$ , given by  $\omega_{fg} = (E_f - E_g)/\hbar$ . Here,  $c_f$  is a time-dependent coefficient, which can be obtained by the following formula.

$$c_f(t) = -\frac{i}{\hbar} \int_{-\infty}^t dt' \langle f | H_{\text{int}} | g \rangle F(t') e^{i\omega_{fg} t'} \quad (3.30)$$

For the linear response of  $H_{\text{int}}$ , the time-dependent fluctuation at a specific time,  $t$ , can be derived as follows.

$$\mathcal{D}(t) = \int_{-\infty}^t dt' \mathcal{K}(t - t') F(t') \quad (3.31)$$

, where  $\mathcal{K}$  is the nonlocal time-correlation function defined as follows. Note that  $\mathcal{K}$  is defined

only in the region where  $t' < t$ .

$$\begin{aligned}\mathcal{K}(t-t') &= -\frac{i}{\hbar} \sum_f \left[ \langle f | H_{\text{int}}(\mathbf{r}) | g \rangle^\dagger \langle f | H_{\text{int}}(\mathbf{r}') | g \rangle e^{-i\omega_{fg}(t-t')} \right. \\ &\quad \left. - \langle f | H_{\text{int}}(\mathbf{r}') | g \rangle^\dagger \langle f | H_{\text{int}}(\mathbf{r}) | g \rangle e^{i\omega_{fg}(t-t')} \right] \\ &= \frac{2}{\hbar} \text{Im} \sum_f \left[ \langle f | H_{\text{int}}(\mathbf{r}) | g \rangle^\dagger \langle f | H_{\text{int}}(\mathbf{r}') | g \rangle e^{-i\omega_{fg}(t-t')} \right]\end{aligned}\quad (3.32)$$

As it is often more convenient to express the formula by its Fourier transform, the Fourier transform of  $F$  is obtained by the following equation for the monochromatic beam with  $F(t) = e^{-i\omega_{fg}t}$ .

$$f(\omega) = \int_{-\infty}^{\infty} dt F(t) e^{i\omega t} = \int_{-\infty}^{\infty} dt e^{i(\omega - \omega_{fg})t} = 2\pi\delta(\omega - \omega_{fg}) \quad (3.33)$$

Then, the perturbation can be expressed as follows.

$$H'(t) = \frac{1}{2\pi} \int_{-\infty}^{\infty} d\omega f(\omega) \frac{1}{2} (H_{\text{int},\omega} e^{-i\omega t} + H_{\text{int},-\omega} e^{i\omega t}) \quad (3.34)$$

Here,  $\pm\omega$  in the subscript of  $H_{\text{int}}$  indicates each operator associated with  $e^{\mp i\omega t}$  to distinguish each term. Thus, the perturbation in the frequency domain is derived as follows.

$$H'(\omega) = \frac{1}{2} (H_{\text{int},\omega} e^{-i\omega t} + H_{\text{int},-\omega} e^{i\omega t}) \quad (3.35)$$

Starting from Eq. (3.30), the coefficient,  $c_f$ , can be obtained by the following equation with a convergence factor,  $e^{\Gamma t}$ .

$$\begin{aligned}c_f(t) &= -\frac{i}{\hbar} \lim_{\Gamma \rightarrow 0} \int_{-\infty}^t dt' \frac{1}{2\pi} \int_{-\infty}^{\infty} d\omega f(\omega) \langle f | H'(\omega) | g \rangle e^{i\omega_{fg}t'} e^{\Gamma t'} \\ &= -\frac{i}{\hbar} \lim_{\Gamma \rightarrow 0} \int_{-\infty}^t dt' \int_{-\infty}^{\infty} d\omega \delta(\omega - \omega_{fg}) \langle f | H'(\omega) | g \rangle e^{i\omega_{fg}t'} e^{\Gamma t'} \\ &= -\frac{i}{2\hbar} \lim_{\Gamma \rightarrow 0} \int_{-\infty}^t dt' \left[ \langle f | H_{\text{int},\omega} | g \rangle e^{-i(\omega - \omega_{fg} + i\Gamma)t'} + \langle f | H_{\text{int},-\omega} | g \rangle e^{i(\omega + \omega_{fg} - i\Gamma)t'} \right] \\ &= \frac{1}{2\hbar} \lim_{\Gamma \rightarrow 0} \left[ \frac{\langle f | H_{\text{int},\omega} | g \rangle}{\omega - \omega_{fg} + i\Gamma} e^{-i(\omega - \omega_{fg} + i\Gamma)t} - \frac{\langle f | H_{\text{int},-\omega} | g \rangle}{\omega + \omega_{fg} - i\Gamma} e^{i(\omega + \omega_{fg} - i\Gamma)t} \right]\end{aligned}\quad (3.36)$$

Similarly,  $\mathcal{D}$  can be expressed as follows.

$$\mathcal{D}(\omega) = \frac{1}{2} [\mathcal{P}(\omega)e^{-i\omega t} + \mathcal{P}(-\omega)e^{i\omega t}] \quad (3.37)$$

Starting from Eq. (3.31),  $\mathcal{D}$  can be obtained similarly by the following equation. Note that  $\text{Im}$  is ignored during the calculation.

$$\begin{aligned} \mathcal{D}(t) &= \lim_{\Gamma \rightarrow 0} \int_{-\infty}^t dt' \frac{1}{2\pi} \int_{-\infty}^{\infty} d\omega \frac{1}{2} [\mathcal{K}_{\omega}(t-t')f(\omega)e^{-i\omega t'} + (\omega \rightarrow -\omega)]e^{\Gamma t'} \\ &= \frac{1}{2} \lim_{\Gamma \rightarrow 0} \int_{-\infty}^t dt' \int_{-\infty}^{\infty} d\omega [\mathcal{K}_{\omega}(t-t')\delta(\omega - \omega_{fg})e^{-i\omega t'} + (\omega \rightarrow -\omega)]e^{\Gamma t'} \\ &= \frac{1}{2} \lim_{\Gamma \rightarrow 0} \mathcal{K}' \int_{-\infty}^t dt' [e^{-i\omega_{fg}t} e^{-i(\omega - \omega_{fg} + i\Gamma)t'} + (\omega \rightarrow -\omega)] \\ &= \frac{i}{2} \lim_{\Gamma \rightarrow 0} \mathcal{K}' \left[ \frac{e^{-i(\omega + i\Gamma)t}}{\omega - \omega_{fg} + i\Gamma} - \frac{e^{i(\omega - i\Gamma)t}}{\omega + \omega_{fg} - i\Gamma} \right] \end{aligned} \quad (3.38)$$

, where  $\mathcal{K}'$  is the time-independent term in  $\mathcal{K}$ . Thus, the coefficient in the frequency domain is given as follows.

$$\mathcal{P}(\omega) = \frac{2}{\hbar} \text{Im} \sum_f \frac{\langle f | H_{\text{int}}(\mathbf{r}) | g \rangle^\dagger \langle f | H_{\text{int}}(\mathbf{r}') | g \rangle}{\omega - \omega_{fg} + i\Gamma} \quad (3.39)$$

Using these relations, the absorption rate in the frequency domain is given by the following formula. Note that the time-dependence is neglected.

$$\begin{aligned} S(\omega) &= -\frac{1}{\hbar} \mathcal{D}(\omega) \\ &= -\frac{1}{\hbar^2} \text{Im} \sum_f \left[ \frac{\langle f | H_{\text{int}}(\mathbf{r}) | g \rangle^\dagger \langle f | H_{\text{int}}(\mathbf{r}') | g \rangle}{\omega - \omega_{fg} + i\Gamma} - \frac{\langle f | H_{\text{int}}(\mathbf{r}') | g \rangle^\dagger \langle f | H_{\text{int}}(\mathbf{r}) | g \rangle}{\omega + \omega_{fg} - i\Gamma} \right] \end{aligned} \quad (3.40)$$

This can be represented with the minimal-coupling interaction Hamiltonian defined as follows [89].

$$H_{\text{int}} = - \int d^3\mathbf{r} \left[ \mathbf{j}(\mathbf{r}) - \frac{e}{2mc^2} \sigma(\mathbf{r}) \mathbf{A}(\mathbf{r}) \right] \cdot \mathbf{A}(\mathbf{r}) \quad (3.41)$$

, where  $\mathbf{j}$  is the current density operator defined as  $\mathbf{j}(\mathbf{r}) = (-ie\hbar/2mc)[\psi^\dagger(\mathbf{r})(\nabla\psi)(\mathbf{r}) -$

$(\nabla\psi)^\dagger(\mathbf{r})\psi(\mathbf{r})]$  and  $\sigma$  is the charge density operator defined as  $\sigma(\mathbf{r}) = e\psi^\dagger(\mathbf{r})\psi(\mathbf{r})$ . Similarly,  $\mathbf{A} \cdot \mathbf{A}$  term would be also ignored hereafter. Using this representation, the absorption ratio can be obtained by the following formula [84].

$$S(\omega) = -\frac{1}{\hbar^2} \text{Im} \sum_f \int d^3\mathbf{r} \int d^3\mathbf{r}' \left[ \frac{\mathbf{j}_{gf}(\mathbf{r}) \cdot \mathbf{A}^*(\mathbf{r}) \mathbf{j}_{fg}(\mathbf{r}') \cdot \mathbf{A}(\mathbf{r}')}{\omega - \omega_{fg} + i\Gamma_{fg}} \right. \\ \left. - \frac{\mathbf{j}_{fg}(\mathbf{r}) \cdot \mathbf{A}^*(\mathbf{r}) \mathbf{j}_{gf}(\mathbf{r}') \cdot \mathbf{A}(\mathbf{r}')}{\omega - \omega_{gf} + i\Gamma_{gf}} \right] \quad (3.42)$$

For the spatial integral for  $\mathbf{r}$  and  $\mathbf{r}'$ , it is preferred to calculate under the Cartesian coordinate system. In this regard, the associated Laguerre polynomial in LG modes can be expanded by the Hermite polynomials as follows [90].

$$\left( \frac{\sqrt{2}r}{w_0} \right)^{|l|} L_p^{|l|} \left( \frac{2r^2}{w_0^2} \right) e^{\pm i|l|\phi} = \frac{(-1)^p}{2^{2p+|l|} p!} \sum_{u=0}^p \sum_{v=0}^{|l|} (\pm i)^v \binom{p}{u} \binom{|l|}{v} \\ \cdot H_{2u+|l|-v} \left( \frac{\sqrt{2}x}{w_0} \right) H_{2p-2u+v} \left( \frac{\sqrt{2}y}{w_0} \right) \quad (3.43)$$

, where  $H_n$  is the Hermite polynomial. For  $p = 0$  and  $l = \pm 1$ , it is given by the follow equation.

$$\frac{\sqrt{2}r}{w_0} L_0^1 \left( \frac{2r^2}{w_0^2} \right) e^{\pm i\phi} = \frac{1}{2} \left[ H_1 \left( \frac{\sqrt{2}x}{w_0} \right) H_0 \left( \frac{\sqrt{2}y}{w_0} \right) \pm i H_0 \left( \frac{\sqrt{2}x}{w_0} \right) H_1 \left( \frac{\sqrt{2}y}{w_0} \right) \right] \quad (3.44)$$

Then, the vector potential from Eq. (3.16) with  $e^{ikz}$  becomes as follows.

$$\mathbf{A}_{\pm 1}(x, y) = \boldsymbol{\epsilon}_\Lambda \sqrt{\frac{1}{2\pi}} e^{-(x^2+y^2)/w_0^2} \left[ H_1 \left( \frac{\sqrt{2}x}{w_0} \right) H_0 \left( \frac{\sqrt{2}y}{w_0} \right) \right. \\ \left. \pm i H_0 \left( \frac{\sqrt{2}x}{w_0} \right) H_1 \left( \frac{\sqrt{2}y}{w_0} \right) \right] e^{ikz} \quad (3.45)$$

Meanwhile, when assuming the real wave functions, the use of the Gaussian-type orbital, of which the wave function is defined as follows, might be considered [84].

$$\psi_i(\mathbf{r}; R, \alpha_i, a_i, b_i, c_i) = N_i(x - X_i)^{a_i} (y - Y_i)^{b_i} (z - Z_i)^{c_i} e^{-\alpha_i |\mathbf{r} - \mathbf{R}_i|^2} \quad (3.46)$$

, where  $N_i$  is a normalization constant,  $\alpha_i$  is the Gaussian exponent, and  $a_i$ ,  $b_i$ , and  $c_i$  are the integer superscripts for the Gaussian-type orbitals. As the multiplications and derivatives of the Gaussian-type orbitals are the Gaussian-type orbitals,  $\mathbf{j}_{mn}$  can be obtained by the following equation.

$$\mathbf{j}_{mn}(r) = -\frac{ie\hbar}{2mc} [\psi_m(\mathbf{r})(\nabla\psi_n)(\mathbf{r}) - (\nabla\psi_m)(\mathbf{r})\psi_n(\mathbf{r})] = \sum_i \hat{e}_i c_i \psi_i \quad (3.47)$$

, where  $C_i$  is the coefficient for each wave function. Using these representations, the numerical calculation of helical dichroism for the absorption by the atom can be easily accomplished.

### 3.5. Spiral zone plate (SZP)

The most straightforward method to generate a vortex beam is spatially assigning phase retardance from 0 to  $2\pi$  along the azimuthal direction to the wavefront of a plane-wave incidence. However, it is hard to assign the phase delay of  $2\pi$  in the X-ray regime and requires a considerably thick optical component that gives rise to a significant attenuation of the incident flux. In this regard, various DOEs have been proposed for the generation of the vortex beam, and the most common DOE for such purpose is SZP.

Zone plates, or equivalently Fresnel zone plates, are a kind of DOEs which consist of concentric circular diffraction gratings [27]. As their name suggests, each grating is called a zone. The beam is diffracted by an alternating configuration of opaque and transparent zones, providing the constructive interference at a focus. For the plane-wave incidence, the radii of the zone boundaries should be given as follows by the constructive interference condition at the focus, giving a path difference of  $\lambda/2$  for each zone boundary. Note that the number of the zone is counted for both opaque and transparent zones.

$$f^2 + r_n^2 = \left(f + \frac{n\lambda}{2}\right)^2 \Rightarrow r_n = \sqrt{n\lambda f + \left(\frac{n\lambda}{2}\right)^2} \approx \sqrt{n\lambda f} \quad (3.48)$$

, where  $f$  is the focal length of the zone plate and  $r_n$  is the radius of the  $n$ th zone. The second

term,  $(n\lambda/2)^2$ , which corrects the spherical aberration, can be ignored as  $n\lambda \ll f$  in the X-ray regime. Then, the outermost zone width can be derived as follows.

$$\Delta r_N = r_N - r_{N-1} = \sqrt{N\lambda f} - \sqrt{(N-1)\lambda f} = \sqrt{N\lambda f} \left( 1 - \sqrt{1 - \frac{1}{N}} \right) \approx \frac{1}{2} \sqrt{\frac{\lambda f}{N}} = \frac{\lambda f}{2r_N} \quad (3.49)$$

, where  $N$  is the total number of the zones and the approximation is valid for sufficiently large  $N$ .

$\Delta r_N$  is important as it is directly related to the resolution, or similarly the spot size. The resolution is defined as follows by the Rayleigh criterion with the small-angle approximation.

$$\text{NA} \approx \frac{r_N}{f} \approx \frac{\lambda}{2\Delta r_N} \Rightarrow d_R = \frac{0.61\lambda}{\text{NA}} \approx 1.22\Delta r_N \quad (3.50)$$

, where NA is the numerical aperture. For the resolution along the  $z$ -axis, the intensity distribution by a circular lens is defined as follows.

$$I(z) \propto \left| \text{sinc} \left( \frac{\pi \text{NA}^2}{2\lambda} z \right) \right|^2 \quad (3.51)$$

Considering the first minima,  $z = \pm 2\lambda/\text{NA}^2$ , and the Rayleigh criterion, the resolution along the  $z$ -axis can be derived as follows.

$$d_{R,z} = \frac{\lambda}{\text{NA}^2} \approx \frac{4(\Delta r_N)^2}{\lambda} \quad (3.52)$$

The depth of focus is obtained by  $\text{DOF} = 2d_{R,z}$ . The zone plates have high diffraction orders, specifically the odd orders, like as any other binary diffraction gratings. The parameters for the  $m$ th order focus are given by the following equations.

$$f^{(m)} = \frac{f}{m} \approx \frac{2r_N \Delta r_N}{\lambda}, \quad d_R^{(m)} \approx \frac{1.22 \Delta r_N}{m}, \quad d_{R,z}^{(m)} \approx \frac{4(\Delta r_N)^2}{m^2 \lambda} \quad (3.53)$$

The zone plates can be expressed by the transmittance function defined as follows.

$$T_0(\mathbf{r}) = P(\mathbf{r}) \exp\left(-\frac{i\pi r^2}{\lambda f}\right) \quad (3.54)$$

, where  $P$  is the magnitude function from an optical property of the materials. Here, the binary structure of the zone plates can be obtained from the phase term in Eq. (3.54) as follows.

$$T_0(\mathbf{r}) \propto \begin{cases} 1, & \text{if } (1 - 2m)\pi < -\pi r^2/\lambda f \leq (2 - 2m)\pi \\ 0, & \text{otherwise} \end{cases} \quad (3.55)$$

, where  $m$  is the index for the transparent zones. Note that the inversion of 0 and 1 in Eq. (3.55) also provides the valid zone plates but reversing the transparent and opaque zones. Here, the relation in Eq. (3.55) naturally gives the equivalent result in Eq. (3.48).

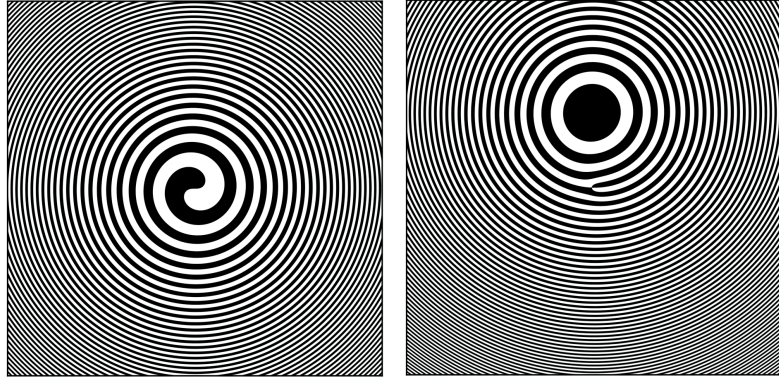


**Figure 3.1** · Example images of on-axis (left) and off-axis (right) SZPs for  $l = 1$ .

When the azimuthal phase term,  $e^{il\phi}$ , is added to Eq. (3.54), the transmittance function of SZPs can be easily obtained [91].

$$T_l(\mathbf{r}) = P(\mathbf{r}) \exp\left(-\frac{i\pi r^2}{\lambda f} + il\phi\right) \quad (3.56)$$

Similarly, this gives the following binary relation.

$$T_l(\mathbf{r}) \propto \begin{cases} 1, & \text{if } (3 - 2m)\pi < -\pi r^2/\lambda f + l\phi \leq (4 - 2m)\pi \\ 0, & \text{otherwise} \end{cases} \quad (3.57)$$

If there is a small off-axis angle,  $\alpha \ll 1$ , Eq. (3.48) becomes as follows.

$$\begin{aligned} \left(f + \frac{n\lambda}{2}\right)^2 &= (r_n \cos \phi - f \sin \alpha \cos \phi')^2 + (r_n \sin \phi - f \sin \alpha \sin \phi')^2 + f^2 \cos^2 \alpha \quad (3.58) \\ &= r_n^2 - 2r_n f \sin \alpha \cos(\phi - \phi') + f^2 \cos^2 \alpha \\ &\approx r_n^2 - 2r_n f \alpha \cos(\phi - \phi') + f^2 \end{aligned}$$

, where  $\phi'$  is the azimuthal angle that defines the tilting plane with the principal axis for the off-axis geometry. The additional term,  $-2r_n f \alpha r_n \cos(\phi - \phi')$ , corresponds to the phase term of  $(2\pi/\lambda)\alpha r \cos(\phi - \phi')$ , giving the following transmittance function.

$$T_l(\mathbf{r}) = P(\mathbf{r}) \exp\left(-\frac{i\pi r^2}{\lambda f} + il\phi + \frac{2i\pi}{\lambda}\alpha r \cos(\phi - \phi')\right) \quad (3.59)$$

This is the general transmittance function of the zone plate reflecting both topological charge and off-axis angle. Using this function, off-axis SZP patterns can be generated from half-period zones like as Eq. (3.55), and they are fabricated with high-Z elements like Au and W typically on Si-based membranes by lift-off or etching process. As  $\Delta r_N$  is directly involved in optical performance of the zone plates, high-resolution nanofabrication facility is required for nanoscale resolution, and the fabrication processes become much more difficult for the hard X-rays because of substantially high aspect ratios, interrupting the resolution below 10 nm [92,93].

### **III. Development of Experimental Techniques for CDI**

#### **4. Multidistance CDI**

##### **4.1. Introduction**

There are many functional materials with nanoscale structures, and these materials typically have sizes up to a few microns for their practical usages in macroscopic circumstances including physical adsorptions, catalytic reactions, ion transport, etc. Representatives for such materials include mesoporous materials, which have pores with diameters typically in the range of 2–50 nm, and they have been spotlighted due to their great potentials in various fields, such as catalyst, drug delivery, and energy storage, from their extremely high surface area to volume ratios [94–96]. In addition, synthesis of mesoporous materials represents significant advancements, even achieved nanoscale controls of their porous structures [97]. As structure and spatial distribution of pores are directly related to the functionality of the mesoporous materials, it is important to investigate their morphologies accurately and nondestructively. In this regard, CDI is a perfect solution for a nondestructive inspection of mesoporous particles, fully covering complicated nanoscale structures inside them. Although its competitor, the transmission electron microscopy, has realized 3D tomography of nanoparticles in atomic resolution, the size of particles is restricted by several tens of nanometers because of a low penetration power of an electron beam, limiting its use with larger particles [98,99].

In the CDI scheme, where a plane-wave incidence is assumed across a sample, X-ray diffraction patterns are invariant under translational movements of the sample, thereby CDI is advantageous for high-resolution imaging, where a vibration is one of the main concerns. A pixel resolution of CDI is defined by a wavelength of the incident beam and the maximum angle covered by a 2D pixelated detector like as a numerical aperture in the optical microscopy. Considering the limited size of the detector, the sample-to-detector distance (SDD) should be shortened to increase the resolution. However, as a large portion of the incident flux would be transmitted, the low- $Q$  components near the center of the diffraction pattern would be buried by the intense direct beam or a beam stop blocking such contribution from the detector. Such signals, especially the zeroth speckle, represent the overall shape of the sample and losing this information makes phase retrieval difficult [100,101]. As the divergence angle of the zeroth

speckle is given by  $1.22\lambda/d$  in terms of the Airy disk, where  $z$  is SDD and  $d$  is the sample width, this problem becomes aggravated for larger particles. Several approaches have been proposed to circumvent such problems by dark-field imaging, the Fourier transform of an optical microscope image, and deep-learning-based inpainting, but they have difficulties in practice [102–104]. Thus, the experiments are usually conducted with moderate resolution conditions, where SDD is sufficiently long. Here, we developed a new method, named multidistance CDI, that measures diffraction patterns at multiple SDDs to complement lacking low- $Q$  signals with a diffraction pattern obtained at a longer SDD, offering the best image resolution as diffraction signals allow [12]. In this chapter, multidistance CDI with a dedicated phase retrieval algorithm and experimental results on 3D tomography of a mesoporous SiO<sub>2</sub> nanoparticle would be introduced.

#### 4.2. Multidistance CDI and adaptive phase retrieval algorithm

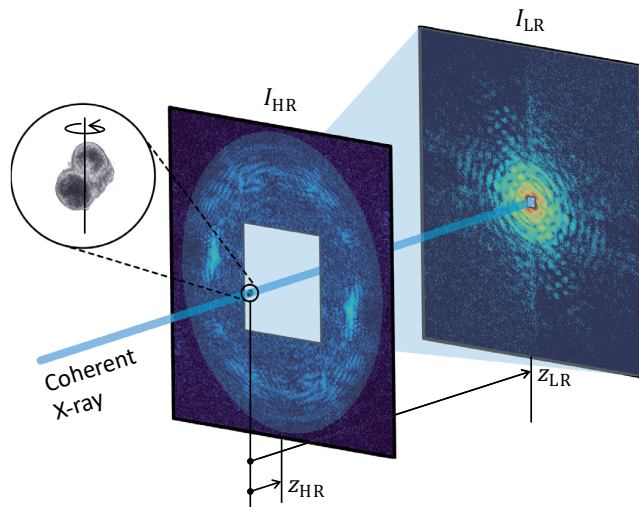


**Figure 4.1** · Schematic diagram of coherent X-ray tomography using multidistance CDI.  
Adapted from Ref. [12], American Chemical Society.

As mentioned above, a basic concept of multidistance CDI is straightforward, measuring diffraction patterns at different SDDs. It does not restrict the number of SDDs for the diffraction patterns, but the case of two SDDs,  $z_{\text{HR}}$  and  $z_{\text{LR}}$ , where HR and LR denote high and low resolution, respectively, is treated for the sake of simplicity. A similar approach has been

proposed, but it directly merges two patterns into a single diffraction pattern [105]. However, if the ratio of two SDDs, which is defined as  $\eta = z_{\text{LR}}/z_{\text{HR}}$ , is not an integer or the pixels of each pattern are not exactly matched, this direct merging method uses interpolation to assign values from the low-resolution pattern,  $I_{\text{LR}}$ , to unknown pixels of the high-resolution pattern,  $I_{\text{HR}}$ . Such interpolation gives significant errors to the low- $Q$  signals, thereby resulting in erroneous reconstruction results. On the contrary, multidistance CDI does not directly merge the measured patterns; instead, it sequentially uses both patterns as they are without any interpolation during the phase retrieval process.

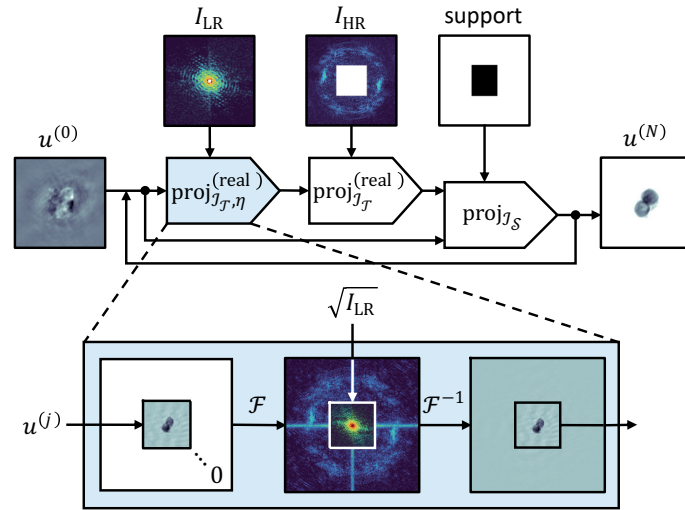


**Figure 4.2** · Schematic diagram of adaptive phase retrieval algorithm for multidistance CDI.  
Adapted from Ref. [12], American Chemical Society.

As the conventional algorithm cannot deal with multiple diffraction patterns with different oversampling ratios, an adaptive phase retrieval is newly introduced. A base diffraction should be  $I_{\text{HR}}$  for a high-resolution image, and the Fourier-space projection onto  $I_{\text{LR}}$  requires matching its oversampling ratio with  $I_{\text{HR}}$ . Also, it is preferred to priorly update low-resolution information, which reflects an overall shape of the sample, for a stable Fourier-space projection; the projection onto  $I_{\text{LR}}$  should be conducted prior to the projection onto  $I_{\text{HR}}$ . In this regard, the projection with respect to two diffraction patterns is defined as a sequence of projection operators onto  $I_{\text{LR}}$  and  $I_{\text{HR}}$  in order. For  $I_{\text{LR}}$ , the projection operator is defined as follows.

$$\text{proj}_{j_T, \eta}^{(\text{real})} u = \text{crop}_\eta \left[ \mathcal{F}^{-1} \left\{ \sqrt{\eta^2 I} \odot e^{i \arg \mathcal{F}(\text{pad}_\eta u)} \right\} \right] \quad (4.1)$$

, where  $\text{pad}_\eta$  is an operator that extends an input by  $\eta$  times along each dimension by padding zeroes to its boundaries and  $\text{crop}_\eta$  is an operator that reduces an input by  $\eta$  times along each dimension by cropping at its center. Note that the minimum error of the matched oversampling ratio is given as follows.

$$\frac{|\delta\sigma_{\text{LR}}|}{\sigma_{\text{LR}}} \leq \frac{1}{2\eta N_{\text{HR}}} \quad (4.2)$$

, where  $\sigma$  and  $N$  is oversampling ratio and number of pixels along a single dimension. Using this projection operator, the adaptive phase retrieval is given based on HIO as follows [4,47].

$$u^{(j+1)} = \text{proj}_{\mathcal{J}_S} \left[ \text{proj}_{\mathcal{J}_T}^{(\text{real})} \left\{ \text{proj}_{\mathcal{J}_T, \eta}^{(\text{real})} u^{(j)} \right\} \right] + \text{proj}_{\mathcal{J}_{S^c}} \left[ u^{(j)} - \beta \text{proj}_{\mathcal{J}_T}^{(\text{real})} \left\{ \text{proj}_{\mathcal{J}_T, \eta}^{(\text{real})} u^{(j)} \right\} \right] \quad (4.3)$$

, where  $\text{proj}_{\mathcal{J}_T}^{(\text{real})}$  and  $\text{proj}_{\mathcal{J}_T, \eta}^{(\text{real})}$  use  $I_{\text{HR}}$  and  $I_{\text{LR}}$  for the Fourier-space amplitude constraint, respectively. Moreover,  $R$ -factor is redefined as follows.

$$R_F^{(j)} = \frac{\sum_i \left| |\mathcal{F}u^{(j)}|_i - \sqrt{I_{\text{HR},i}} \right| + c \sum_i \left| |\mathcal{F}[\text{pad}_\eta u^{(j)}]|_i - \sqrt{\eta^2 I_{\text{LR},i}} \right|}{\sum_i \sqrt{I_{\text{HR},i}} + c \sum_i \sqrt{\eta^2 I_{\text{LR},i}}} \quad (4.4)$$

, where  $c$  is a weight parameter assigned to the contribution of  $I_{\text{LR}}$ , given by  $1/\eta^2$ .

To verify the proposed algorithm, numerical simulation was performed using the Mandrill image from USC-SIPI image database (<https://sipi.usc.edu/database>) to generate diffraction patterns by the Fourier transform. Oversampling ratios for diffraction patterns were set as 9 and 3 along each dimension for  $I_{\text{LR}}$  and  $I_{\text{HR}}$ , respectively. Diffraction patterns were scaled to have total diffracted intensities of  $10^8$  photons, and the Poisson noises were added for the noisy case. For phase retrieval, identical procedures were performed in both cases; 900 iterations of HIO with  $\beta = 0.9$  followed by 100 iterations of ER were conducted for total 128 initial random phases and the best 25% of resultant images were averaged to obtain a final image. For an evaluation of the reconstructed images, normalized root-mean-square error (NRMSE), structural similarity index measure (SSIM), and peak SNR (PSNR) were calculated with respect to the original test image [106]. These metrics are defined as follows.

$$\text{NRMSE}(u, u_{\text{ref}}) = \sqrt{\frac{\mu(u-u_{\text{ref}})^2}{\mu_{u_{\text{ref}}}^2}}, \quad (4.5)$$

$$\text{SSIM}(u, u_{\text{ref}}) = \frac{(2\mu_u\mu_{u_{\text{ref}}} + c_1)(2\sigma_{u,u_{\text{ref}}} + c_2)}{(\mu_u^2 + \mu_{u_{\text{ref}}}^2 + c_1)(\sigma_u^2 + \sigma_{u_{\text{ref}}}^2 + c_2)},$$

$$\text{PSNR}(u, u_{\text{ref}}) = 20 \log_{10} \frac{\max u_{\text{ref}}}{\sqrt{\mu(u-u_{\text{ref}})^2}}$$

, where  $u_{\text{ref}}$  is a reference image, here the ground-truth image,  $c_1$  and  $c_2$  is stabilizing variables, given by  $c_1 = (0.01 \max u_{\text{ref}})^2$  and  $c_2 = (0.03 \max u_{\text{ref}})^2$ , and  $\mu_u$ ,  $\sigma_u$ , and  $\sigma_{u,v}$  are mean, variance, and covariance of the images,  $u$  and  $v$ , respectively. Note that all operations are for values of the pixels in the images.

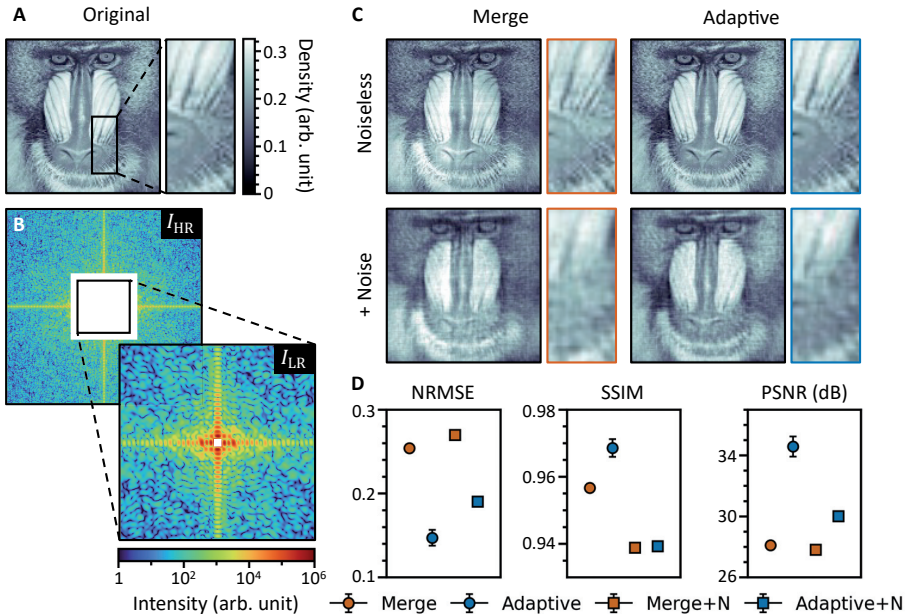


**Figure 4.3** · Numerical simulation for a comparison of direct merging method (Merge) and non-merging method with the adaptive algorithm (Adaptive). (A, B) The test image (A) and corresponding diffraction patterns (B) with different oversampling ratios are presented. (C, D)

Reconstructed images (C) and their image quality metrics (D) are also provided for both noiseless and noisy (+N) cases. Markers and whiskers indicate average and standard error of the metrics, respectively. Adapted from Ref. [12], American Chemical Society.

As a result, the proposed method showed significant improvements of image qualities compared to the direct merging method for both noiseless and noisy cases. The metrics also

represented the superiority of the adaptive algorithm, showing all metrics surpassing the direct merging method. It even showed higher PSNR for the noisy case compared to the noiseless case with the direct merging method. Considering that  $\eta$  was given as 3 and the integer  $\eta$  minimizes the interpolation error, the proposed method truly offered the best performance dealing with multiple diffraction patterns, outperforming the direct merging method. Thus, the adaptive phase retrieval algorithm with as-measured diffraction patterns was verified to reconstruct more accurate images than using the merged pattern.

#### 4.3. Multidistance coherent X-ray tomography of mesoporous SiO<sub>2</sub> nanoparticle

Using the proposed method, coherent X-ray tomography experiment was performed with a mesoporous SiO<sub>2</sub> nanoparticle at 9C beamline of Pohang Light Source-II (PLS-II) in Pohang Accelerator Laboratory (PAL). X-ray beam was generated by in-vacuum undulator and spectrally filtered by Si double-crystal monochromator. Both devices are tune to the photon energy of 6 keV. Then, the beam was focused into 15 μm (horizontal) × 7 μm (vertical) by a pair of Kirkpatrick–Baez mirrors located 3 m upstream from the sample, giving total flux of  $3.89 \times 10^8$  photons·s<sup>-1</sup>·μm<sup>-2</sup>. Beam paths were in vacuum and imaging chamber was purged by He gas. Diffraction patterns were measured by EIGER 2X 1M detector (DECTRIS Ltd.), of which the size of each pixel is 75 × 75 μm<sup>2</sup>, at 4.57 m and 1.57 m downstream from the sample, giving  $\eta = 2.91$ . For a tomographic scan, total 27 angles from  $-69.44^\circ$  to  $+69.44^\circ$  in an equal slope were assigned to each measurement [30]. The mesoporous SiO<sub>2</sub> nanoparticles were synthesized by spherical and hollow assembly-based particle engineering (Prof. Jinwoo Lee's group at KAIST) [97]. Then, the particles in a powder form were placed in ethanol, dispersed by sonication, and spread on a 30-nm-thick Si<sub>3</sub>N<sub>4</sub> membrane for the experiment.

As radiation dose gradually damages the sample, it is important to determine a secure total exposure time for the high-resolution imaging experiment. For this purpose, irradiation with an exposure time of 5 s was repeated to an identical particle and correlation coefficients between diffraction patterns from the first and subsequent exposures were calculated [107]. As a result, total exposure time of 300 s was set as a safe limit, retaining the correlation coefficient

above 90% of the initial value. Thus, the exposure times were set as 1 s for  $I_{LR}$  and 5 s for  $I_{HR}$ , giving total exposure time of 162 s, which is well below the limit. For the further validation, diffraction patterns were additionally measured at the initial angle after the main experiment and the correlation coefficient with the first exposure of the main experiment was calculated as 0.995; therefore, an influence of the radiation damage was negligible.

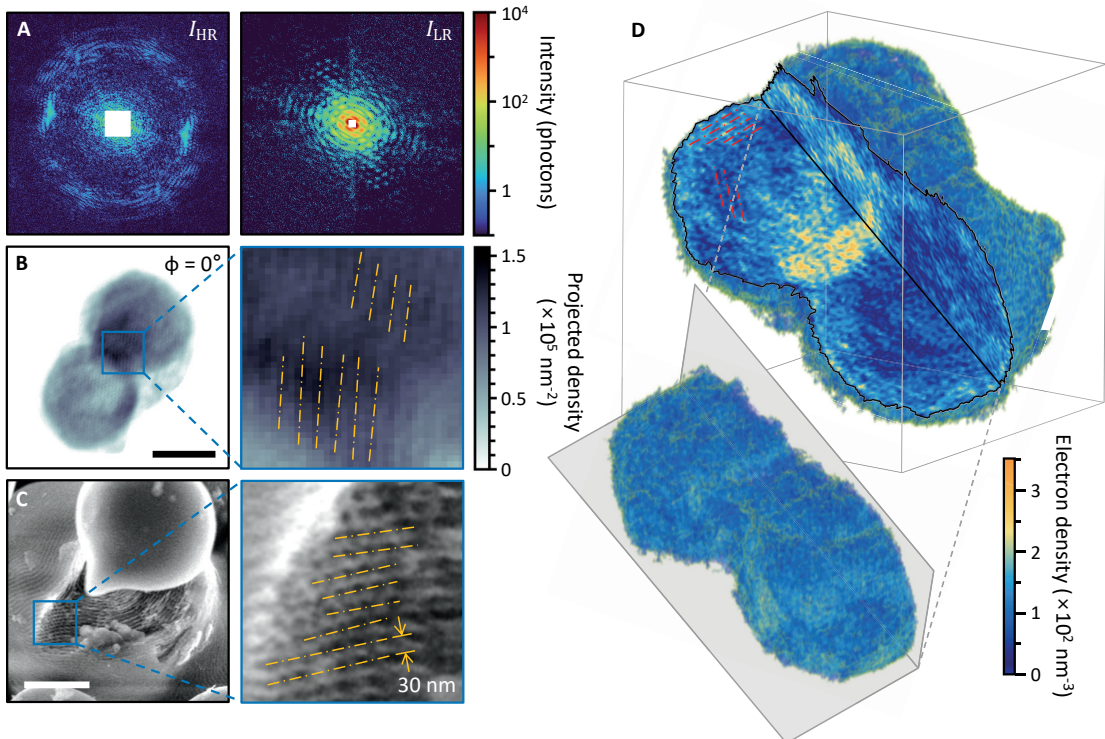


**Figure 4.4** · Multidistance coherent X-ray tomography of mesoporous  $\text{SiO}_2$  nanoparticle. (A, B) An example of diffraction patterns (A) and corresponding 2D projection image (B) are presented for the measurement at  $\phi = 0^\circ$ . (C) Scanning electron microscope (SEM) image is also given for the reference. Scale bars represent 500 nm. (D) 3D image reconstructed from the tomographic scan. Several shell-like periodic structures are indicated by dashed lines.

Adapted from Ref. [12], American Chemical Society.

All measured data subtracted background signals and were cropped into  $500 \times 500$  pixels [108]. After data processing, initial phase retrieval was conducted using the adaptive algorithm consist of 1,400 iterations of HIO with  $\beta = 0.9$  followed by 100 iterations of ER for total 64 initial random phases. Then, the support was updated by a tight boundary of an average of the best 12.5% resultant images and identical phase retrieval procedure was perform

with the updated support. The final image was obtained after repeating this process five times. All 2D reconstruction results showed PRTF well above the typical criterion, 0.5, across all spatial frequency region, giving the highest possible resolution of 8.65 nm defined from the solid angle covered by the detector for the case of  $I_{\text{HR}}$  [25].

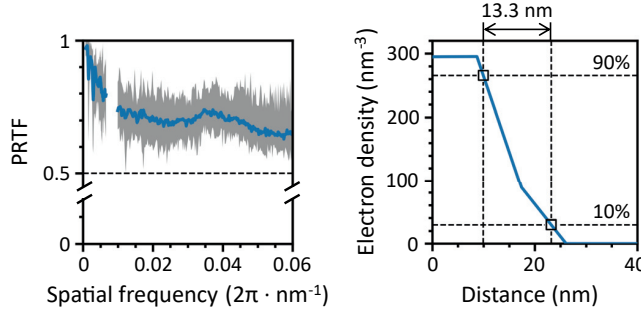


**Figure 4.5** · PRTF (left) and line profile (right) for the resolution estimation of 2D and 3D reconstructions, respectively. Gray region indicates PRTF range for all 2D reconstructions and 10%–90% criterion was applied for the 3D case. Adapted from Ref. [12], American Chemical Society.

3D tomographic reconstruction was achieved by the accurate real-space iterative reconstruction (RESIRE) algorithm [109]. For a position alignment of given 2D images, 20 iterations of RESIRE were conducted and the given images were aligned in a subpixel unit based on projection images from the reconstructed 3D image [110,111]. This process was repeated until the misalignment below 0.01 pixel. After the alignment, the Fourier-space projection was performed to the 3D image with the measured diffraction patterns. Then, 100 iterations of RESIRE were conducted for the final 3D image. As the tomographic scan was performed only at 27 angles, the FSC cannot be properly calculated; therefore, an effective 3D resolution was calculated by the 10%–90% criterion on a line profile passing a voxel with the greatest gradient value, giving the resolution of 13.3 nm. Such resolution was roughly four times higher than the resolution of previous reports on nondestructive 3D imaging of porous materials with the size up to few micrometers, outperforming the former imaging techniques [112,113]. The reconstructed 3D image was visualized using the open-source software, ParaView (<https://www.paraview.org>).

3D electron density distribution showed a good agreement with the electron

microscope image with periodic structures of which a regular interval of the pores was roughly 30 nm. An overall shape of the target nanoparticle was identified as an adjoining double sphere, which was from an incomplete separation during the spinodal decomposition. It also showed a higher density at an intersecting region of two spherical chunks. This was supposed to be occurred due to a substantial capillary pressure by the Marangoni flow that generates a rapid movement of fluidic block-copolymer/SiO<sub>2</sub> droplets during the spinodal decomposition [114,115].

#### 4.4. Quantitative analyses on porous structures

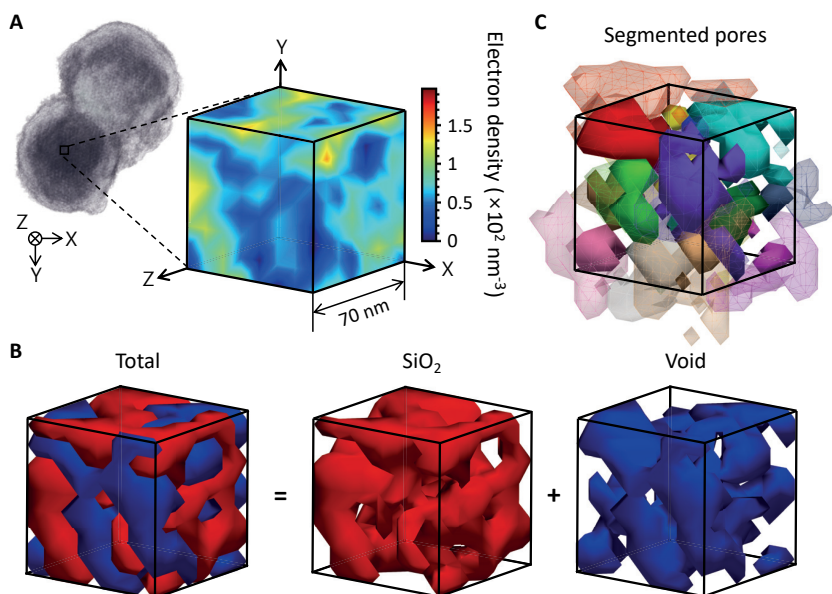


**Figure 4.6** · Pore structure extracted from the 3D image. (A–C) Examples of clustering (B) and segmentation (C) of 3D electron density distribution (A) are presented. Clustering is for a separation of a void region and segmentation is for an extraction of pores from the void region. Adapted from Ref. [12], American Chemical Society.

For further quantitative analyses on porous structures inside the nanoparticle, additional data processing procedures, clustering, segmentation, and skeletonization, were performed. The clustering was for a separation of void regions from the 3D electron density distribution. This was accomplished by using a plugin, trainable Weka segmentation, from the open-source software, ImageJ2 [116,117]. It used a machine learning technique, the random forest classifier,

based on mean and variance values of convolving cubic kernels with radii of 1 to 8 voxels. The extracted void regions occupied 32.2% of the total volume of which the value represented a porosity. This was a relatively low value compared to other mesoporous SiO<sub>2</sub> materials of which porosities are around 50% or higher [118]. Moreover, 99.6% of the total void voxels were interconnected, forming a highly interconnected complex structure like a network. Thus, a network-based analysis can provide additional information, especially for regional importance of the pore structure [119,120].

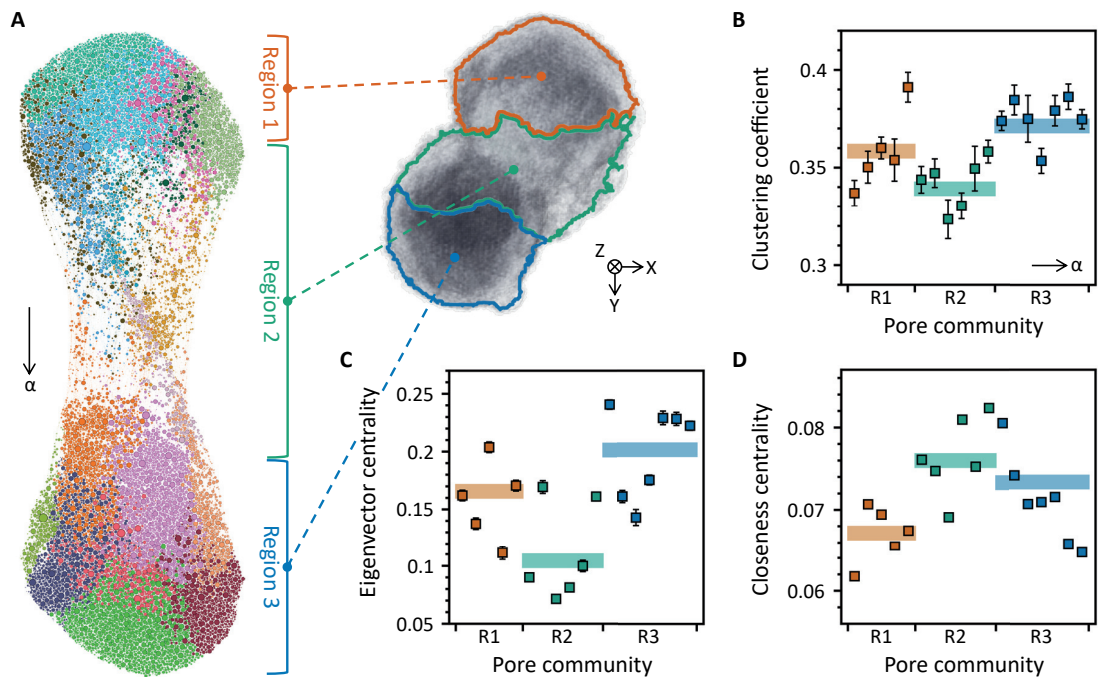


**Figure 4.7** Network-based analysis of the highly interconnected porous structure. (A) A pore network is visualized by assigning attractive and repulsive forces to connected and unconnected nodes, respectively. The size of each node represents its degree rank and the nodes with a same color represents a community. (B–D) Clustering coefficients (B), eigenvector centrality (C), and closeness centrality (D) for each pore community. Markers and whiskers indicate average and standard error of the metrics, respectively. Translucent lines indicate an average for each region. Adapted from Ref. [12], American Chemical Society.

A pore network was constructed by dividing the void regions into multiple pores. This was accomplished by using a segmentation algorithm, watershed, in the open-source library, scikit-image [121]. It gradually fills the region from local minima based on a distance map until

the region is fully filled to define segments. Here, the distance map was obtained by negatives of the number of void voxels in convolving cubic kernels with the size of  $3 \times 3 \times 3$  voxels. The segments, equivalently the pores, were identified to have a volume of  $1.65 \times 10^4 \text{ nm}^3$  on average. Then, the obtained segments and interconnections with their neighbors were treated as nodes and edges, respectively, constructing the pore network. Pore communities, which were groups of pores with strong interconnections, were also defined using a heuristic method with the modularity optimization [122]. The network was visualized using the open-source software, Gephi, with a built-in continuous graph layout algorithm, ForceAtlas2 [123,124]. It arranges the nodes by assigning attractive and repulsive forces to connected and unconnected nodes, respectively. The size and color of each node indicated its degree rank and community, respectively. Consequently, the network presented a similar shape with the sample but showing an elongation between two circular chunks. The nodes at both ends were concentrated while the nodes at an intermediate region were sparsely arranged. Accordingly, region 1 (R1) to region 3 (R3) were appointed along the long axis,  $\alpha$ , for a further regional classification.

For a quantitative analysis of the pore network, three metrics, clustering coefficients, eigenvector centrality, and closeness centrality, were calculated to investigate the importance of each node in the network based on the graph theory. The clustering coefficient, which represents a relevance of each node with its neighbors, was defined by a ratio of complete interconnections between neighboring nodes based on the Watts–Strogatz model [125]. The eigenvector centrality, which represents an influence of each node in the network, was defined by a nonnegative eigenvector of an adjacency matrix of the network. The closeness centrality, which represents a closeness of each node to other nodes, was defined by a reciprocal of the average shortest path to other nodes. As a result, the nodes in R1 and R3 showed higher clustering coefficients and eigenvector centralities but lower closeness centralities compare to the nodes in R2. These tendencies represented that the nodes in R1 and R3 were densely connected with the nodes in the same regions but not with the nodes in the other regions, while the nodes in R2 showed exactly opposite behaviors, acting like a bridge between the nodes in R1 and R3. They were also matched with the 3D image showing the channel-like porous structure in the intersecting high-density region unlike the shell-like structures in both ends.

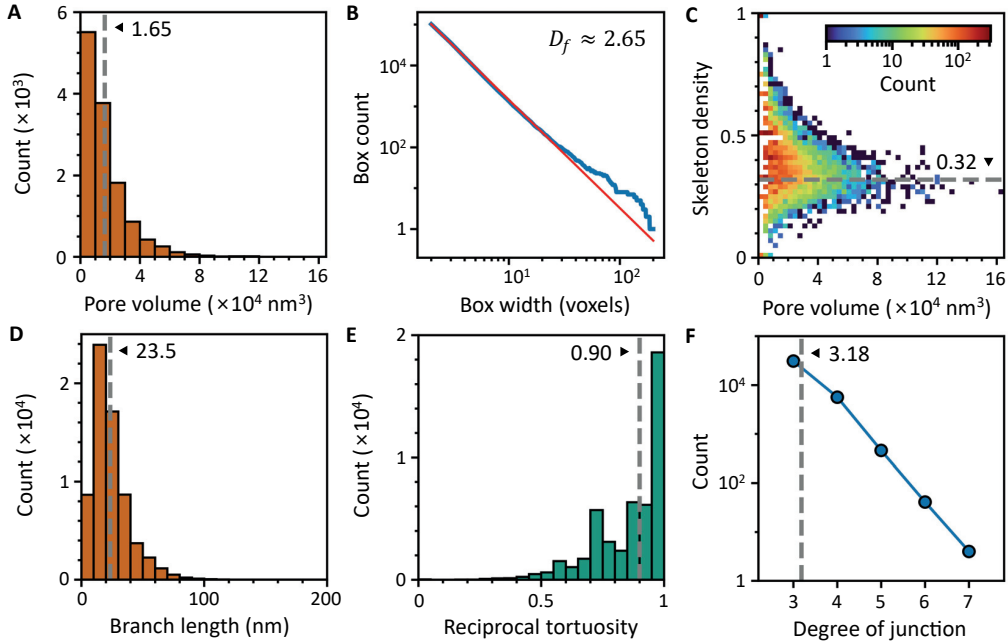


**Figure 4.8** · Quantitative analyses of the porous structure based on fractal theory and its skeletons. (A) A distribution of the pore volume is presented for reference. (B) A box width to box count graph is fitted by the power law and the exponent gives a surface fractal dimension of 2.65. Blue and red lines indicate actual and fitted data, respectively. (C–F) Distributions of pore volume to skeleton density (C), length and reciprocal tortuosity of branches (D and E, respectively), and degree of junctions (F) are also presented using skeletons of the porous structure. Adapted from Ref. [12], American Chemical Society.

Further quantitative analyses were conducted based on the fractal theory and skeletons of the porous structure. A surface fractal dimension, which represents a space efficiency, or similarly a roughness, of the porous structures with respect to their surface area, can be determined by the box counting method [126,127]. This method counted the number of overlapping components, equivalently boxes, of a regular 3D grid with the void regions while increasing widths of the grid. If the box count,  $N_{\text{box}}$ , well follows the power law, the structure can be described to have a fractality and the surface fractal dimension can be obtained by the following formula.

$$N_{\text{box}} = Aw_{\text{box}}^{-D_f} \quad (4.6)$$

, where  $A$  is an arbitrary coefficient,  $w_{\text{box}}$  is a width of the grid, and  $D_f$  is a surface fractal dimension. After the power-law fitting, the surface fractal dimension was obtained as 2.65 with

R-squared of 0.9999, thereby the porous structure was identified to have the fractality. The surface fractal dimension also means a surface complexity of the materials. The value of 2.65 was a relatively high value among the typical mesoporous materials mostly within the range from 2.2 to 2.8 [118]. In addition, using the calculated surface fractal dimension, the porosity can be obtained by the following equation based on a single-fractal pore model [128].

$$\varrho_f = 1 - \left( \frac{r_{\min}}{r_{\max}} \right)^{3-D_f} \approx 1 - \left( \frac{V_{\min}}{V_{\max}} \right)^{1-D_f/3} \quad (4.7)$$

, where  $r_{\min}$  and  $r_{\max}$  are the minimum and maximum radii of the pores, respectively, and  $r_{\min}/r_{\max}$  can be approximately obtained by  $(V_{\min}/V_{\max})^{1/3}$  with the minimum and maximum volumes,  $V_{\min}$  and  $V_{\max}$ , respectively. The fractal-based porosity was calculated as 33.0%, which is analogous with the ratio of void regions calculated as 32.2%.

Skeletons of the porous structure also offer a geometric information, especially about paths where adsorbates travel inside the nanoparticle [129]. To obtain the skeletons, the void regions were skeletonized by the 3D medial surface axis thinning algorithm [130]. It gradually thins the void regions with respect to their local medial surface axes. Then, the obtained skeletons were organized into a minimum spanning tree by using the open-source library, Skan, and all junctions with degrees of 1 or 2 were removed, eliminating the junctions at endpoints and merging single branches cut by the junctions [131]. A skeleton density, which is a ratio of skeleton voxels in the pores, was converged to 0.32 as the pore volume increased and a total length of the skeletons was  $1.56 \times 10^6$  nm. As the cross section of the skeletons occupied a single voxel, an effective radius of the pores can be obtained by the following equation, giving the value of 7.65 nm.

$$r_{\text{eff}} = \frac{d_{\text{res}}}{2\sqrt{\rho_{\text{skel}}}} \quad (4.8)$$

, where  $\rho_{\text{skel}}$  is the skeleton density and  $d_{\text{res}}$  is the voxel resolution. When assuming the cylindrical porous structure, the effective surface area and volume can be calculated as  $7.50 \times 10^7$  nm<sup>2</sup> and  $2.87 \times 10^8$  nm<sup>3</sup>, respectively, and the corresponding surface-to-volume ratio of 0.261 nm<sup>-1</sup> was identical to that of a sphere with a radius of 11.5 nm. In addition, ideal filling

capacities of spherical adsorbates with a radius of  $r_{\text{ads}}$  can be obtained based on the simple pore-filling model for several cases: total  $1.02 \times 10^5$  adsorbates with a filling ratio of 66.6% for a simple close packing with  $r_{\text{ads}} \approx r_{\text{eff}}$  and total  $1.67 \times 10^6$  adsorbates with a filling ratio of 53.6% and total  $9.47 \times 10^5$  adsorbates with a filling ratio of 49.4% for interdigitated triangular close packings with  $r_{\text{ads}} \approx r_{\text{eff}}/(1 + \sqrt{3})$  and  $r_{\text{ads}} \approx r_{\text{eff}}/(1 + \sqrt{7}/2)$ , respectively [132]. Here, the interdigitated triangular close packings are analogous to the star of David, but the triangles had intervals of  $r_{\text{ads}}$  and  $(3/2)r_{\text{ads}}$  along a height direction of the cylinder, respectively.

As the skeletons were organized into the minimum spanning tree, junctions and branches of the tree structure can give additional geometrical insights. The branches presented average length of 23.5 nm and average reciprocal tortuosity, or equivalently straightness, of 0.901, while an average degree of junctions was 3.18. Thus, when the adsorbates travel through the porous structure inside the sample, they passed the routes that break into 3.18 branches for every 23.5 nm of curved paths with the tortuosity of 1.11, on average. Moreover, a permeability can be calculated using the Kozeny–Carman equation based on the smooth capillary model defined as follows, giving the value of  $2.12 \text{ nm}^2$  [133].

$$k = \frac{1}{8} \tau^{-1} \varrho r_{\text{eff}}^2 \quad (4.9)$$

, where  $\varrho$  is the porosity and  $\tau$  is the tortuosity. An effective radius of a grain for the smooth grain packing model, equivalently with the smooth capillary model, can also be given as follows based on the fractal pore-space model, giving the value of 16.4 nm.

$$r_{\text{grain}} = r_{\text{eff}} \left( \frac{2}{3} \tau^{-1} \frac{\varrho}{1 - \varrho} \right)^{-1/(D_f - 1)} \quad (4.10)$$

Then, the permeability is defined as follows, representing an equivalent result with the smooth capillary model.

$$k = \frac{1}{8} \tau^{-1} \varrho r_{\text{grain}}^2 \left( \frac{2}{3} \tau^{-1} \frac{\varrho}{1 - \varrho} \right)^{2/(D_f - 1)} \quad (4.11)$$

#### **4.5. Conclusion**

Multidistance CDI with the adaptive phase retrieval algorithm has enabled nondestructive high-resolution X-ray imaging compatible with large particles that exhibit smaller sizes of the zeroth speckles. By overcoming the limitations of conventional CDI, multidistance CDI successfully realized a nanoscale tomography of mesoporous SiO<sub>2</sub> nanoparticles in the actual experiment, achieving the spatial resolutions of 8.65 nm and 13.3 nm in 2D and 3D, respectively. Especially, the 3D resolution of 13.3 nm was roughly four times better than the resolution from the previous reports on porous materials [112,113]. Based on the actual structural information of the mesoporous nanoparticle, various quantitative analyses including network, fractal, and skeletal analyses can be conducted after appropriate data processing procedures. Thus, multidistance CDI offers a maximal resolution among the X-ray imaging techniques while taking all advantages of CDI with the straightforward experimental setups, facilitating further applications on *in situ*, *in operando*, and element-specific imaging of various functional materials [134–138].

### **5. Off-axis vortex beam ptychography**

#### **5.1. Introduction**

Vortex beams, of which wavefronts exhibit azimuthal phase gradients, have been spotlighted due to their unique morphology and intrinsically defined OAM as previously described in Chapter 3. Their unique characteristics make them serve as functional probes resolving topologically distinct structures in various materials [77–80,139,140]. Additionally, their intrinsic OAM offer a mode selectivity in optical transitions, facilitating a quantum-mechanical control of materials in various fields [67,81,141,142]. In the X-ray regime, a generation of the vortex beams is typically achieved by SZPs. However, a flux of the vortex beam is restricted because of a limited transverse coherence length of the third-generation synchrotron facility that requires a slit configuration blocking an incoherent portion of an incident flux. Additionally, as SZP requires central beam stop (CBS) and OSA to discard direct transmissions, the flux loss

becomes significant. In this circumstance, an off-axis geometry can be applied to SZPs for circumventing the use of CBS, efficiently generating the focused vortex beam. Here, we verified the generation of the focused X-ray vortex beams by the off-axis SZPs numerically and experimentally in the hard X-ray regime and checked an effect of the off-axis vortex beam on the ptychographic reconstructions [13]. In this chapter, new findings related to the ptychography using off-axis X-ray vortex beam would be introduced.

## 5.2. Numerical simulation of vortex beam generation by off-axis SZPs

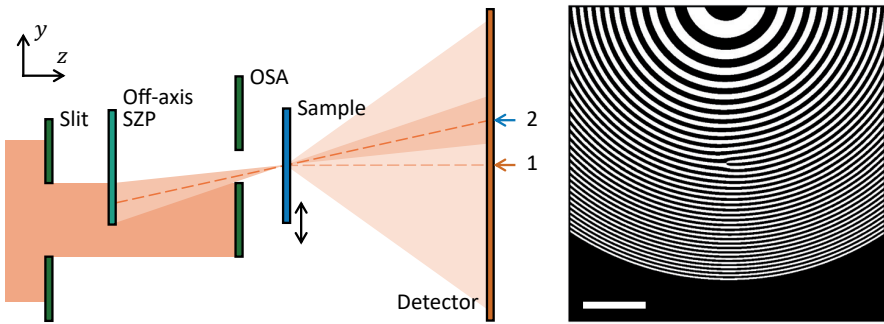


**Figure 5.1** · Schematic diagram of ptychography experiments using the off-axis SZP (left) and example of off-axis SZP patterns (right). Points marked as 1 and 2 indicates nominal diffraction center and beam center, respectively. The pattern is designed for  $l = 1$  and  $\alpha = 0.2$  mrad along  $y$ -axis. A scale bar represents 10  $\mu\text{m}$ . Adapted from Ref. [13], American Chemical Society.

Off-axis SZP patterns can be generated by binarizing the phase term of Eq. (3.59) by half-period intervals. For both numerical simulation and actual experiment, parameters of the off-axis SZPs were set as  $l = 1$ ,  $\alpha = 0.2$  mrad along  $y$ -axis, and  $f = 135$  mm at the photon energy of 6 keV. The generation of the vortex beam was numerically simulated by the Fresnel–Kirchoff integral using a convolution-based approach implemented in the open-source library LightPipes (<https://opticspy.github.io/lightpipes>). A size of the field for the simulation was  $100 \times 100 \mu\text{m}^2$  with a pixel resolution of 50 nm and plane-wave incidence partially illuminated the pattern by a rectangular area of  $30 \mu\text{m}$  (horizontal)  $\times$   $40 \mu\text{m}$  (vertical). The partial illumination reflected a slit configuration for discarding an incoherent portion of the incident flux in the experiment. Contributions of high foci were blocked by OSA with a hole diameter of 20  $\mu\text{m}$  positioned 50

mm upstream from the focal plane. A far-field diffraction pattern from the focal plane was generated by the Fourier transform.

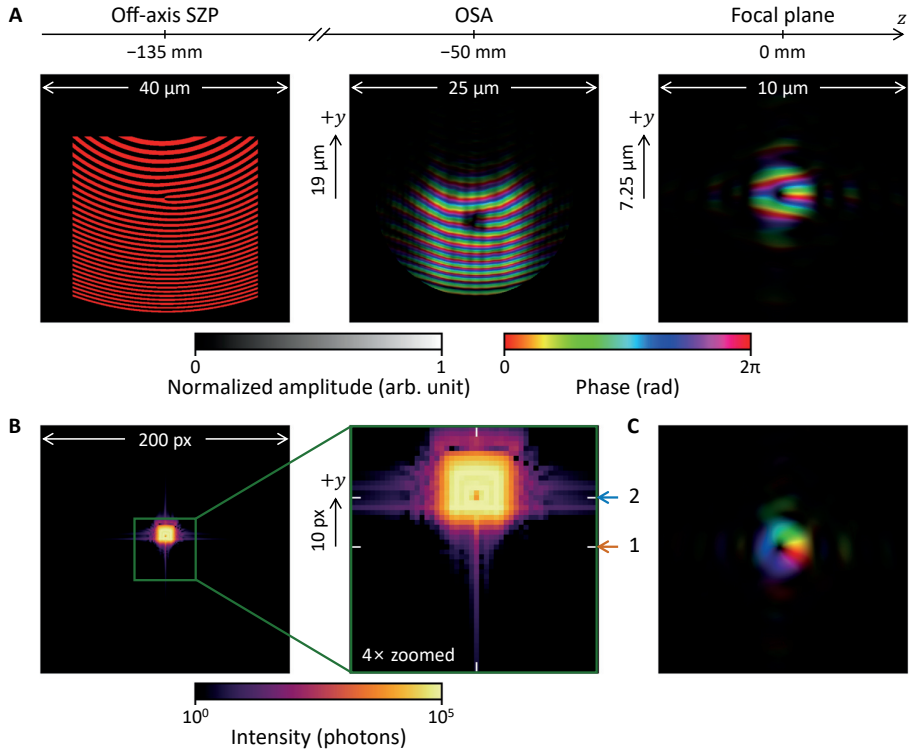


**Figure 5.2** · Numerical simulation of vortex beam generation by the partial illumination of off-axis SZPs. (A, B) Light propagation by the Fresnel–Kirchoff integral (A) and far-field diffraction pattern from the focal plane (B) are presented. The diffraction pattern clearly shows difference between nominal diffraction center and beam center marked as 1 and 2, respectively. (C) When the beam center is treated as a diffraction center, the inverse Fourier transform gives specific azimuthal phase gradients, removing a phase ramp along  $y$ -axis.

Adapted from Ref. [13], American Chemical Society.

The generation of the off-axis focused vortex beam was successfully confirmed by the numerical simulation of a light propagation from the partially illuminated off-axis SZP. The generated wavefront at the focal plane showed a circular shape with a singularity at its center, having inner and outer radii of 312 nm and 1036 nm at the half-maximum points in radial intensity distribution. In addition, it exhibited a linear phase ramp of  $2\pi\alpha y/\lambda$  from the off-axis geometry. The far-field diffraction pattern showed a separation of nominal diffraction center and beam center. When treating the beam center as a diffraction center, the inverse

Fourier transform of the pattern gave the wavefront without the phase ramp, clearly showing the counterclockwise rotation of the phase along the azimuthal direction that gave OAM of  $+\hbar$ . Such operation was equivalent to a Fourier-space shift of  $2\pi\alpha/\lambda$  along  $Q_y$ -direction and a real-space multiplication of  $e^{-2i\pi\alpha y/\lambda}$ , removing the phase term from the off-axis geometry. These shifted diffraction patterns would be called as center-corrected patterns hereafter.

### 5.3. Numerical experiments on off-axis vortex beam ptychography

Numerical experiments on ptychography of a weakly scattering object using the simulated beam were conducted to identify an influence of off-axis vortex beams in ptychographic reconstructions. The object exhibited contrasts of 10% and  $0.1\pi$  rad for its amplitude and phase, respectively, compared to the empty space. Far-field diffraction patterns were generated along a regular grid with an interval of 200 nm by the Fourier transform of element-wise product of probe and object functions of which a window size was set to possess a pixel resolution of 50 nm. Each diffraction pattern was scaled to have a total diffraction intensity of  $10^7$  photons and included Poisson and Gaussian noise with  $\sigma = 1/2.35482$  to reflect measurement noises.

Ptychographic reconstructions were conducted for both as-centered and center-corrected patterns using DM followed by least-squares maximum-likelihood (LSQ-ML) algorithm with geometry and position refinements implemented in the publicly available software package, PtychoShelves [38,143,144]. Specifically, 1,000 iterations of DM followed by 100 iterations of LSQ-ML were executed with a root-mean-square error as an error metric. However, as the reconstruction of as-centered diffraction patterns showed split probes and corresponding separated multiple objects modes; therefore, 10,000 iterations, instead of 1,000 iterations, of DM followed by 100 iterations of LSQ-ML were executed and a probe alignment was conducted to forcibly merge split probes into a single probe. After the probe alignment, identical reconstruction procedures as before were performed.

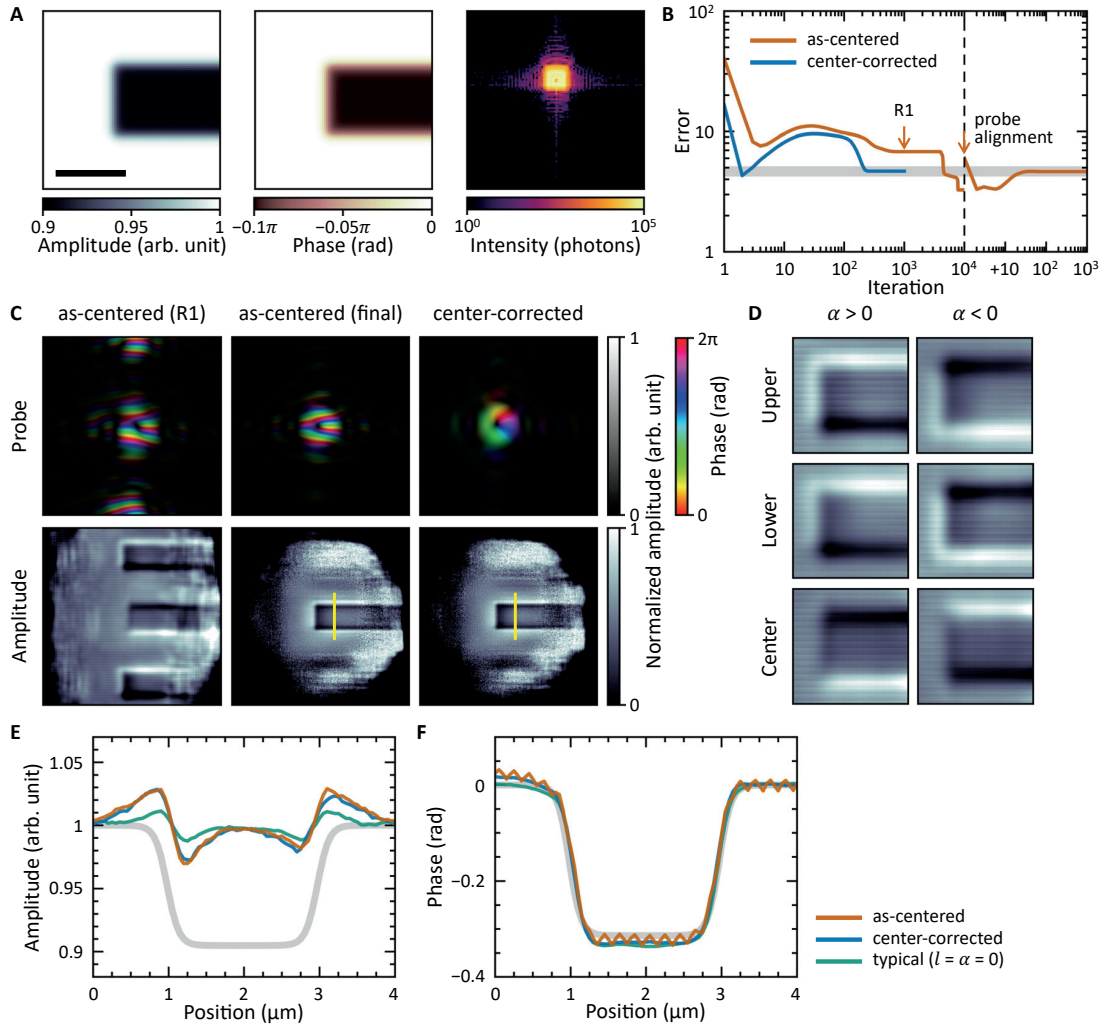


**Figure 5.3** · Numerical experiments on ptychography of a weakly scattering object using off-axis vortex beams. (A) Amplitude and phase of the object and example far-field diffraction pattern are presented. Scale bar represents 2 μm. (B) Evolutions of root-mean-square errors during ptychographic reconstructions are given. R1 represents an intermediate point right after 1,000 iterations. Probe alignment is conducted for as-centered diffraction patterns after 10,000 iterations followed by additional 10<sup>3</sup> iterations. (C) Reconstructed probe and amplitude of the object are presented. (D) Multiple object modes with distinct edge contrasts appear at R1 and the contrasts are inverted for opposite off-axis directions. (E, F) Line profiles of amplitude (E) and phase (F) of the object along yellow lines in (C). Adapted from Ref. [13], American Chemical Society.

Final reconstructed images showed enhanced edge responses like the first-order derivate of the Gaussian function in their amplitude, roughly three times stronger than that for

a case of a typical Gaussian beam with  $l = \alpha = 0$ . The phase of the resultant images well followed the ideal image, showing only 2% difference on a full width at half maximum (FWHM) of the edge gradient profile, while the case of the typical beam showed 3% difference. Both as-centered and center-corrected patterns gave similar results, but the as-centered case had difficulties to find proper images and a small oscillation appeared in the phase of the object. This oscillation was from the regular scanning intervals and such effect was rectified in the center corrected case during the refinement process [145]. Thus, regardless of the off-axis angles, the vortex beam with  $l = 1$  offered better imaging performance than the typical beam with  $l = 0$ , but the diffraction center correction was required for a stable reconstruction.

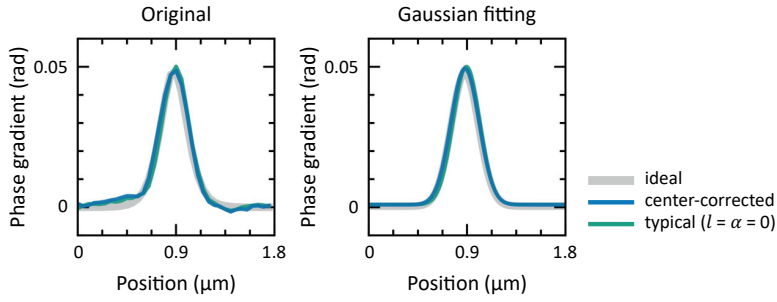


**Figure 5.4** Edge gradient profiles of the phase of the reconstructed object. Both original and Gaussian-fitted profiles are presented.

During the reconstruction of the as-centered patterns, split probes and corresponding multiple object modes appeared with edge contrasts in the amplitude of the objects. Unlike the abovementioned final images, the edge contrasts showed directionality; bright upper and dark lower edges appeared for the object modes located at upper and lower region of the reconstruction window, while dark upper and bright lower edges appeared for the object mode at the center. Interestingly, these directional edge contrasts inverted for the opposite off-axis angle,  $\alpha = -0.2$  mrad. This effect should be considered carefully even though the successful reconstruction did not have any dependency on off-axis angles, especially for strong noise conditions.

## 5.4. Synchrotron experiments on off-axis X-ray vortex beam ptychography

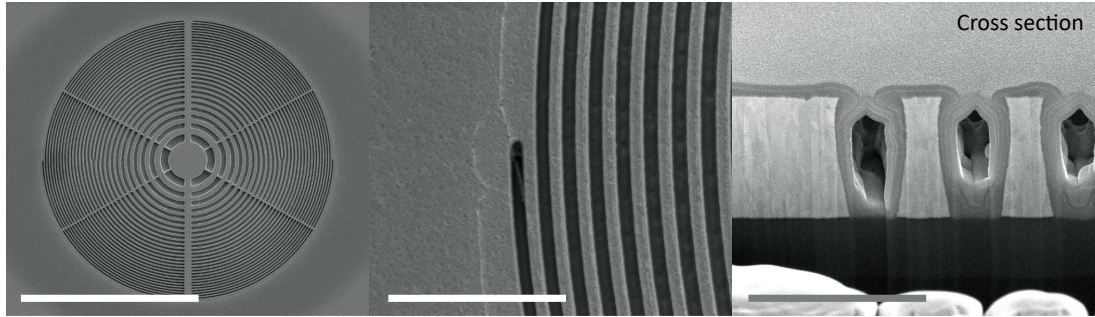


**Figure 5.5** · SEM images of fabricated off-axis SZP patterns. Scale bars represent 50  $\mu\text{m}$ , 5  $\mu\text{m}$ , and 1  $\mu\text{m}$  in order.

For actual experiments, the off-axis SZPs were produced with the help of fabrication service by National NanoFab Center (NNFC). The off-axis SZP patterns with parameters as described above were patterned with 1- $\mu\text{m}$ -thick W on 1- $\mu\text{m}$ -thick low-stress  $\text{Si}_3\text{N}_4$  membrane. First, the  $\text{Si}_3\text{N}_4$  membrane was chemically deposited on both sides of a p-type Si wafer. For a frontside patterning, 10-nm-thick Ti and 1- $\mu\text{m}$ -thick W were sequentially deposited by multi-target sputtering. Then, bottom anti-reflective coating (BARC) and photoresist were deposited after a deposition of a hard mask consist of amorphous carbon and SiON, facilitating an etching of the thick W layer. After the deposition, KrF lithography of the photoresist layer was conducted followed by dry etching of BARC and hard mask layers. Finally, the W layer was etched by  $\text{SF}_6$  in a metal etching system, TCP-9600PTX (Lam Research Corp.). For a backside opening, both reactive ion etching and wet etching by KOH were employed to remove Si in 1 mm  $\times$  1 mm behind the pattern, forming the membrane structure.

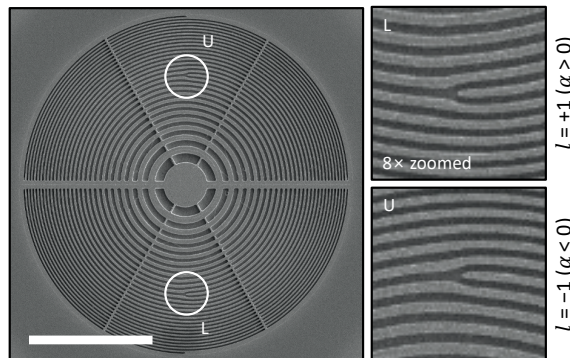


**Figure 5.6** · SEM image of the off-axis SZP patterns in the actual experimental geometry. Images zoomed at principal centers of each off-axis SZP pattern are also presented. A scale bar represents 30  $\mu\text{m}$ . Adapted from Ref. [13], American Chemical Society.

The experiments were performed at 9C beamline of PLS-II in PAL. X-ray beam was generated by in-vacuum undulator and spectrally filtered by Si double-crystal monochromator. Both devices were tuned to a photon energy of 6 keV. Generated monochromatic beam was cropped into a rectangular area of  $30 \mu\text{m}$  (horizontal)  $\times 40 \mu\text{m}$  (vertical) by two slit systems located at 3.8 m and 0.1 m upstream from the off-axis SZP, considering the nominal transverse coherence lengths of  $55 \mu\text{m}$  (horizontal) and  $62 \mu\text{m}$  (vertical). The nominal value was calculated by using Eq. (1.79), considering the undulator giving a source size of  $500 \mu\text{m}$  (horizontal)  $\times 50 \mu\text{m}$  (vertical) located at 30 m upstream from the imaging chamber and a horizontal white beam slit with a separation of  $30 \mu\text{m}$  located at 16 m upstream from the chamber. A circular aperture with a diameter of  $20 \mu\text{m}$  made of 50- $\mu\text{m}$ -thick W was positioned at 15 mm upstream from the sample, serving as OSA. Total intensity of the generated off-axis vortex beam was measured as  $2.16 \times 10^7 \text{ photons}\cdot\text{s}^{-1}$ . Diffraction patterns were measured by the photon-counting detector, EIGER 2X 1M detector (DECTRIS Ltd.), with SDD of 4.37 m and an exposure time of 0.5 s for each measurement. The patterns were cropped to have a pixel resolution of 50 nm, matching the resolution with the numerical simulation.

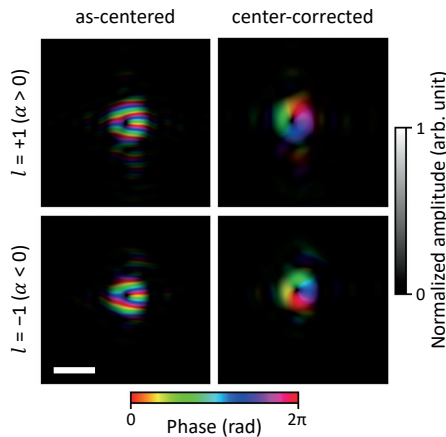


**Figure 5.7** · Recovered beam profile generated by the off-axis SZPs from ptychography experiments on the test target. A scale bar represents  $3 \mu\text{m}$ . Adapted from Ref. [13], American Chemical Society.

First, the experiments were performed on a test target made of 600-nm-thick W to confirm the generation of the vortex beams. Recovered beam profiles were analogous with the results from the numerical simulation; therefore, the fabricated off-axis SZPs were verified to

have designed performance. The reconstructed probes had inner and outer radii of 340 nm and 1130 nm, respectively, and these values were approximately 9% larger than those from the numerical simulation. The linear phase ramp was also eliminated by the center correction as expected.

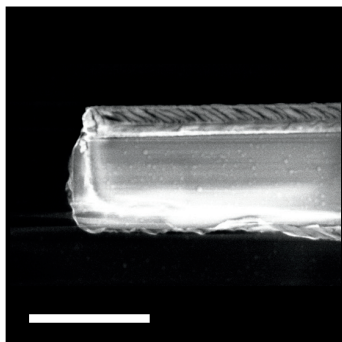


**Figure 5.8** · SEM image of the bar-shaped multilayer film. A scale bar represents 3  $\mu\text{m}$ .  
Adapted from Ref. [13], American Chemical Society.

After the verification of the manufactured off-axis SZPs, the experiments were performed on a bar-shaped multilayer film. The bar-shaped sample was fabricated by lift-off process for the multilayer film (Dr. Jun Woo Choi's group at KIST). Specifically, [Pt (3 nm)/Gd<sub>24</sub>Fe<sub>66</sub>Co<sub>10</sub> (8 nm)/MgO (1 nm)]<sub>20</sub> multilayer film was deposited on a 100-nm-thick Si<sub>3</sub>N<sub>4</sub> membrane and patterned by electron beam lithography followed by the lift-off process.

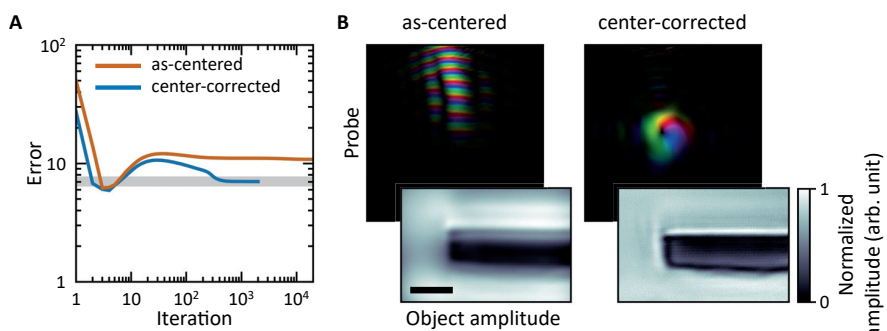


**Figure 5.9** · Reconstruction results of off-axis vortex beam ptychography on the bar-shaped multilayer film. (A) Evolutions of the errors during ptychographic reconstructions are given. (B) Reconstructed probes and amplitude of the objects are presented. A scale bar represents 3  $\mu\text{m}$ . Adapted from Ref. [13], American Chemical Society.

As the diffraction signals from the sample were weak, a ptychographic reconstruction

was failed to produce proper shapes of probe and object when using the as-centered patterns. On the other hand, the reconstruction using the center-corrected patterns showed appropriate images for both probe and object, representing the importance of the center correction when using off-axis beams. Thus, the probe functions obtained from the experiment on the test target were assigned as initial estimations to improve the quality of the images.

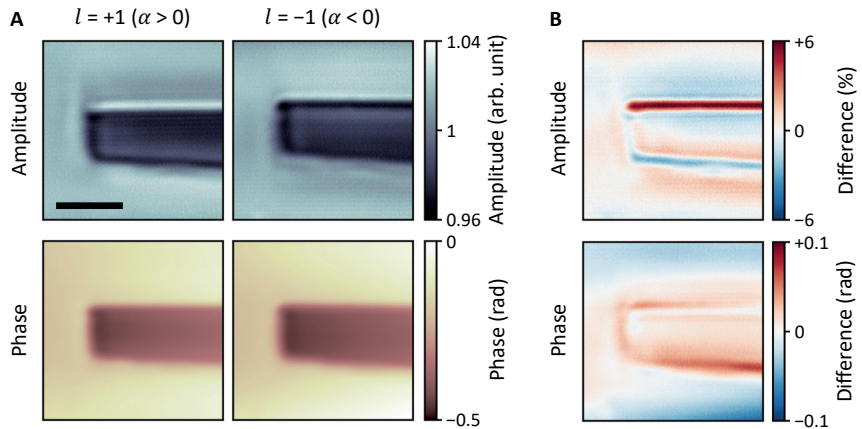


**Figure 5.10** · Final results of off-axis vortex beam ptychography on the bar-shaped multilayer film. (A, B) Reconstructed images (A) and differences for the case of opposite off-axis angles (B) are presented. (B) A scale bar represents 3  $\mu\text{m}$ . Adapted from Ref. [13], American Chemical Society.

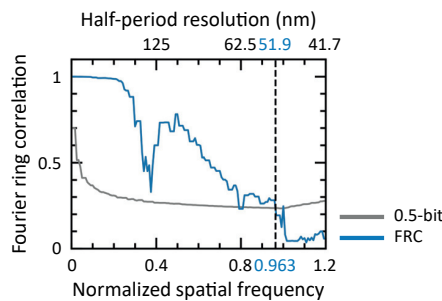


**Figure 5.11** · Resolution estimation of off-axis vortex beam ptychography by FRC with the 0.5-bit information threshold curve.

Resultant images showed directional edge responses, which exhibited an inversion for the opposite off-axis angle, in the amplitude of the objects like as the intermediate result for the case of as-centered patterns from the numerical simulation and their edge contrasts were approximately 5%. On the other hand, the phase of the objects was matched with the SEM

image of the sample. In addition, as values of the phase delay satisfied the following relation, a thickness of the sample can be derived.

$$\Delta\phi = -\frac{2\pi}{\lambda} \sum_i (1 - n_i) t_i \quad (5.1)$$

, where  $n_i$  and  $t_i$  are refractive index and thickness of the  $i$ th layer. Using the refractive indices from the literature, the thickness of the sample was calculated as  $226 \pm 7.3$  nm, compatible with the designed value of 240 nm [146]. Note that a thickness ratio of each layer was assumed to be equivalent to the designed ratio and the refractive index of  $\text{Gd}_{24}\text{Fe}_{66}\text{Co}_{10}$  layer was roughly given by a weighted average of composing elements by the composition ratios. Meanwhile, an effective resolution of the off-axis vortex beam ptychography was estimated by FRC with the 0.5-bit information threshold curve defined in Eq. (2.14) and Eq. (2.16), respectively, giving the value of 51.9 nm [57].

## 5.5. Conclusion

The generation of off-axis vortex beams and their influences on ptychography were successfully verified with weakly scattering objects by both numerical simulations and synchrotron experiments. The off-axis SZPs enabled efficient generations of the vortex beams by eliminating the use of CBS when transverse coherence lengths were limited. However, the linear phase ramp appeared due to the off-axis geometry, thereby correction of the diffraction center was introduced for a removal of such phase ramp and also stable ptychographic reconstructions. When dealing with the weakly scattering objects, off-axis vortex beam ptychography offered strong directional edge contrasts in amplitude of the reconstructed objects depending on the off-axis direction, while their phase properly exhibited the structure of the sample. Moreover, regardless of the off-axis angle, the vortex beam provided the improved resolution compared to the typical non-vortex beam. Thus, off-axis X-ray vortex beam ptychography would facilitate edge-sensitive imaging of weakly scattering samples while enabling an extraction of accurate structural information from the phase of reconstructed images. Considering the unique nature of the vortex beams, this can be extended by utilizing their

chirality sensitivity and transition selectivity [67,77–80].

## 6. Helical dichroism on ferroelectric topological defects

### 6.1. Introduction

Topological defects are topologically protected structures that remain stable under certain conditions and include domain walls, vortices, and quasiparticles like skyrmions [147,148]. Various kinds of topological defects are found in materials and often induce hidden properties that are not normally exhibited. Morphology of a topological defect can be defined by a winding number, and a sign of the winding number provide the most basic information such as directionality or handedness of its morphology. Identifying such information is crucial to understand physical properties from topological defects in materials systems.

Recently, helical dichroism, which is dichroism caused by OAM of light, has been reported in various chiral systems [77–80]. Since OAM of light is defined from a helical wavefront that has a constant phase gradient along azimuthal direction, it has high degrees of freedom corresponding to integer times of  $\hbar$  compared to SAM, which is limited to  $\pm\hbar$  from left and right circular polarization, respectively. In addition, it has been theoretically predicted that various systems exhibit strong helical dichroism in the hard X-ray regime [81]. Despite this prediction and advantages of hard X-rays in imaging science, experimental reports are limited. Thus, investigation of helical dichroism in the hard X-ray regime is necessary for a development of functional nanoprobes for such topological structures exhibited particularly in ferroelectric systems, but dichroism from these systems have been identified only as soft X-ray circular dichroism [149,150]. Here, we conducted an X-ray fluorescence spectroscopy experiment on an epitaxial thin film of a ferroelectric material using hard X-ray vortex beams and employed a physical model for an interpretation of measured signals. In this chapter, overall experimental details and results would be introduced with the physical model for helical dichroism. Note that this work is being prepared for publication and the data have not yet been fully analyzed.

### 6.2. Helical dichroism and ferroelectric structures of BiFeO<sub>3</sub>

Typical topological defects that appear in polarization structures of ferroelectric materials are ferroelectric domain walls, polar vortices, and polar skyrmions. In a case of domain walls, they show gradual rotations of polarization vectors along the axis interconnecting two different ferroelectric domains; therefore, they possess chirality that might raise dichroic events during scattering processes of photons. However, the polarization itself is not observable in E1–E1 scattering because an electric dipole has an odd parity, and signals are faint for E1–E2 interference in hard X-ray regime. Instead, a chiral arrangement of electric quadrupoles has an imaginary component, therefore circular dichroism can be observed [150,151]. In this regard, helical dichroism can replace circular dichroism with stronger sensitivity on topological defects in hard X-ray regime. A photon with the OAM gives additional values to the total angular momentum during a scattering process, triggering multipole transitions [67]. Meanwhile, nanoscale structural defects itself can directly assign OAM to lights, and this has been reported with dislocation singularities in single-crystal Si [152]. Thus, there are many routes to incur helical dichroism from topological structures.

For an investigation of helical dichroism, BiFeO<sub>3</sub> was selected as a target material. BiFeO<sub>3</sub> is a multiferroic material that shows both ferroelectricity and antiferromagnetism with critical temperatures higher than room temperature, and it exhibits stripe ferroelectric domains [153]. Its ferroelectric domain walls and rotation axes of consisting polarizations are well arranged along a same direction. Additionally, rotations of polarizations in each domain wall have also been reported to share an identical handedness, thereby having homochirality across the sample [149]. For this reason, BiFeO<sub>3</sub> is suitable for an identification of helical dichroism from topological defects.

Atomic configurations of single-crystal BiFeO<sub>3</sub> obviously show regular arrangements with slight atomic displacements of Bi or Fe cations toward pseudocubic vertices that correspond to the polarizations [154]. In addition, considering experimental parameters with the Bragg reflection condition, the model described in Section 3.4 is preferred to take account of 3D rotations of those configurations. Thus, starting from Eq. (3.42), an absorption rate in the frequency domain is modified as follows [84]. Note that only the first term that represents an electron excitation from  $g$  to  $f$  is considered for the sake of simplicity.

$$S_{\pm 1}^{fg}(\omega) = -\frac{1}{\hbar^2} \text{Im} \left[ \frac{\int d^3\mathbf{r} \mathcal{R}\mathbf{j}_{gf}(\mathcal{R}^{-1}\mathbf{r}) \cdot \mathbf{A}_{\pm 1}^*(\mathbf{r}) \int d^3\mathbf{r}' \mathcal{R}\mathbf{j}_{fg}(\mathcal{R}^{-1}\mathbf{r}') \cdot \mathbf{A}_{\pm 1}(\mathbf{r}')}{\omega - \omega_{fg} + i\Gamma_{fg}} \right] \quad (6.1)$$

, where  $\mathcal{R}$  is a rotation matrix for the Euler angles. When a polarization state of an incident beam is linear along  $x$ -axis, each integral term becomes as follows.

$$\begin{aligned} J_{10}^{mn} &= \sum_i \int d^3\mathbf{r} \mathcal{R}_x [\psi_m(\mathcal{R}^{-1}\mathbf{r}) \nabla \psi_n(\mathcal{R}^{-1}\mathbf{r})] \frac{2}{\sqrt{\pi}w_0} xe^{-\frac{x^2+y^2}{w_0^2}} e^{-ikz} \\ J_{01}^{mn} &= \sum_i \int d^3\mathbf{r} \mathcal{R}_x [\psi_m(\mathcal{R}^{-1}\mathbf{r}) \nabla \psi_n(\mathcal{R}^{-1}\mathbf{r})] \frac{2}{\sqrt{\pi}w_0} ye^{-\frac{x^2+y^2}{w_0^2}} e^{-ikz} \end{aligned} \quad (6.2)$$

, where  $i$  is an index for each atom,  $\mathcal{R}_x$  is a row vector from the rotation matrix corresponding to an  $x$ -axis component, subscripts indicate indices of the Hermite polynomial in order, and superscripts indicate final and initial states of electron transition in order. Using these terms, the absorption rate becomes as follows.

$$\begin{aligned} S_{\pm 1}^{fg}(\omega) &= \frac{e^2}{4m^2c^2} \text{Im} \left[ \frac{\{(J_{10}^{gf} \pm iJ_{01}^{gf}) - (J_{10}^{fg} \pm iJ_{01}^{fg})\}^* \{(J_{10}^{fg} \pm iJ_{01}^{fg}) - (J_{10}^{gf} \pm iJ_{01}^{gf})\}}{\omega - \omega_{fg} + i\Gamma_{fg}} \right] \\ &= -\frac{e^2}{4m^2c^2} \text{Im} \left[ \frac{|(J_{10}^{fg} - J_{10}^{gf}) \pm i(J_{01}^{fg} - J_{01}^{gf})|^2}{\omega - \omega_{fg} + i\Gamma_{fg}} \right] \\ &= \frac{e^2}{4m^2c^2} \frac{\Gamma_{fg}}{(\omega - \omega_{fg})^2 + \Gamma_{fg}^2} |(J_{10}^{fg} - J_{10}^{gf}) \pm i(J_{01}^{fg} - J_{01}^{gf})|^2 \end{aligned} \quad (6.3)$$

As wave functions are assumed to be the Gaussian-type orbitals, various basis sets such as STO-3G can be used [155]. For example, STO-3G is a minimal basis sets approximating the Slater-type orbitals each by linear combinations of three primitive Gaussian functions. Thus, as terms with the wave functions and their gradients are complicated, it is convenient to rearrange the coordinate by a substitution of  $\mathbf{r}' = \mathcal{R}^{-1}\mathbf{r} - \mathbf{R}_i$  with an atomic position,  $\mathbf{R}_i$ , for the  $i$ th atom. Then, Eq. (6.2) becomes as follows.

$$\begin{aligned}
J_{10}^{mn} &= \sum_i \int d^3 \mathbf{r}' \mathcal{R}_x [\psi_m(\mathbf{r}') \nabla \psi_n(\mathbf{r}')] \\
&\quad \cdot \frac{2}{\sqrt{\pi} w_0} \mathcal{R}_x(\mathbf{r}' + \mathbf{r}_a) e^{-\frac{[\mathcal{R}_x(\mathbf{r}' + \mathbf{r}_a)]^2 + [\mathcal{R}_y(\mathbf{r}' + \mathbf{r}_a)]^2}{w_0^2}} e^{-ik\mathcal{R}_z(\mathbf{r}' + \mathbf{r}_a)} \\
J_{01}^{mn} &= \sum_i \int d^3 \mathbf{r}' \mathcal{R}_x [\psi_m(\mathbf{r}') \nabla \psi_n(\mathbf{r}')] \\
&\quad \cdot \frac{2}{\sqrt{\pi} w_0} \mathcal{R}_y(\mathbf{r}' + \mathbf{r}_a) e^{-\frac{[\mathcal{R}_x(\mathbf{r}' + \mathbf{r}_a)]^2 + [\mathcal{R}_y(\mathbf{r}' + \mathbf{r}_a)]^2}{w_0^2}} e^{-ik\mathcal{R}_z(\mathbf{r}' + \mathbf{r}_a)}
\end{aligned} \tag{6.4}$$

Note that gradient operators are still with respect to  $\mathbf{r}$ . For  $s$ - and  $p$ -orbitals that contribute to major E1 transitions of Fe atoms, the primitive Gaussian function is defined as follows.

$$\begin{aligned}
\psi_s^{(i,j)}(\mathbf{r}') &= C_j e^{-\alpha_j |\mathbf{r}'|^2} \\
\psi_{p_x}^{(i,j)}(\mathbf{r}') &= C_j x' e^{-\alpha_j |\mathbf{r}'|^2}
\end{aligned} \tag{6.5}$$

, where  $j$  is an index of each composing primitive Gaussian function. Then, their partial derivates with respect to  $\mathbf{r}$  are given as follows.

$$\begin{aligned}
\partial_u \psi_s^{(i,j)}(\mathbf{r}') &= C_j \partial_u e^{-\alpha_j \{(\mathcal{R}_{xx}^{-1}x + \mathcal{R}_{xy}^{-1}y + \mathcal{R}_{xz}^{-1}z - X_i)^2 + (\mathcal{R}_{yx}^{-1}x + \dots)^2 + (\mathcal{R}_{zx}^{-1}x + \dots)^2\}} \\
&= -2C_j \alpha_j [\mathcal{R}_{xu}^{-1}(\mathcal{R}_x^{-1}\mathbf{r} - X_i) \\
&\quad + \mathcal{R}_{yu}^{-1}(\mathcal{R}_y^{-1}\mathbf{r} - Y_i) + \mathcal{R}_{zu}^{-1}(\mathcal{R}_z^{-1}\mathbf{r} - Z_i)] e^{-\alpha_j |\mathbf{r}'|^2} \\
&= -2C_j \alpha_j [\mathcal{R}_{ux}(\mathcal{R}_x^{-1}\mathbf{r} - X_i) \\
&\quad + \mathcal{R}_{uy}(\mathcal{R}_y^{-1}\mathbf{r} - Y_i) + \mathcal{R}_{uz}(\mathcal{R}_z^{-1}\mathbf{r} - Z_i)] e^{-\alpha_j |\mathbf{r}'|^2} \\
&= -2C_j \alpha_j \mathcal{R}_u \mathbf{r}' e^{-\alpha_j |\mathbf{r}'|^2} \\
\partial_u \psi_{p_v}^{(i,j)}(\mathbf{r}') &= C_j v' \left( \partial_u e^{-\alpha_j |\mathbf{r}'|^2} \right) + C_j [\partial_u (\mathcal{R}_{vx}^{-1}x + \mathcal{R}_{vy}^{-1}y + \mathcal{R}_{vz}^{-1}z - V_i)] e^{-\alpha_j |\mathbf{r}'|^2} \\
&= -2C_j \alpha_j v' \mathcal{R}_u \mathbf{r}' e^{-\alpha_j |\mathbf{r}'|^2} + C_j \mathcal{R}_{vu}^{-1} e^{-\alpha_j |\mathbf{r}'|^2} \\
&= -2C_j \alpha_j v' \mathcal{R}_u \mathbf{r}' e^{-\alpha_j |\mathbf{r}'|^2} + C_j \mathcal{R}_{uv} e^{-\alpha_j |\mathbf{r}'|^2} \\
&= -2C_j \alpha_j v' \mathcal{R}_u \mathbf{r}' e^{-\alpha_j |\mathbf{r}'|^2} + C_j \mathcal{R}_u \hat{\mathbf{e}}_{v'} e^{-\alpha_j |\mathbf{r}'|^2}
\end{aligned} \tag{6.6}$$

, where  $u$  and  $v$  are arbitrary coordinates. Gradients of the wave functions are finally derived as follows.

$$\begin{aligned}
\nabla \psi_s^{(i,j)}(\mathbf{r}') &= -2C_j \alpha_j \mathcal{R} \mathbf{r}' e^{-\alpha_j |\mathbf{r}'|^2} \\
\nabla \psi_{p_v}^{(i,j)}(\mathbf{r}') &= C_j (-2\alpha_j v' \mathcal{R} \mathbf{r}' + \mathcal{R} \hat{\mathbf{e}}_{v'}) e^{-\alpha_j |\mathbf{r}'|^2}
\end{aligned} \tag{6.7}$$

Using these relations, the absorption ratio can be calculated depend on topological charges of incident beams, thereby resulting in helical dichroism.

### 6.3. Synchrotron experiments on helical dichroism with BiFeO<sub>3</sub>

Experiments were performed at 9C beamline of PLS-II in PAL. X-ray beam was generated by in-vacuum undulator and spectrally filtered by Si double-crystal monochromator. Both devices were tuned for an energy scan from 7.110 keV to 7.145 keV, covering near *K*-edge of Fe. Then, the beam was cropped into 30 μm (horizontal) × 40 μm (vertical) rectangle by two slit systems located at 3.8 m and 0.1 m upstream from off-axis SZPs and illuminated the SZPs to generate vortex beams equivalently with our previous work [13]. A circular aperture with a diameter of 20 μm made of 50-μm-thick W was positioned at 15 mm upstream from the sample, serving as OSA. Total intensity of the beam was measured as  $2.16 \times 10^7$  photons·s<sup>-1</sup>. Diffraction patterns and fluorescence signals were simultaneously measured by photon-counting detector, EIGER 2X 1M detector, and silicon drift detector, SiriusSD (RaySpec, Ltd.). The photon-counting detector was mounted at the arm of a diffractometer, giving SDD of roughly 0.8 m, and the silicon drift detector was installed close to a sample and nearly perpendicular to the incident beam to maximally exclude an influence of scattered photons. Measurements were conducted under the Bragg reflection condition for pseudocubic (0 0 1) of BiFeO<sub>3</sub> with a small  $\theta$ -offset for the highest contrast of satellite signals from ferroelectric domains.

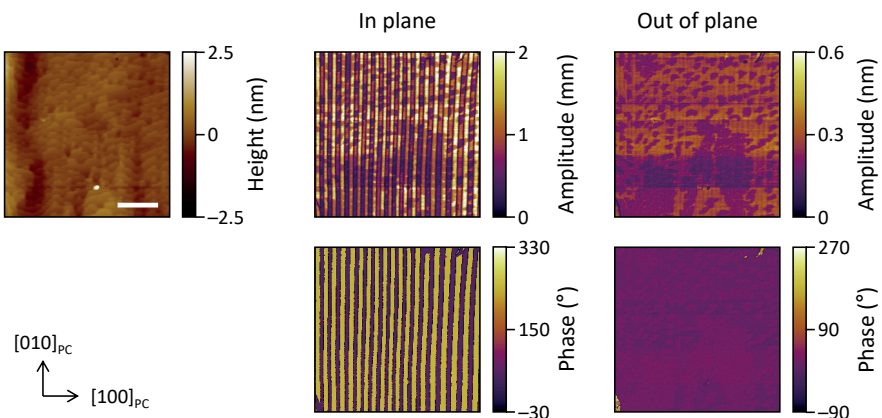


**Figure 6.1** PFM images of BiFeO<sub>3</sub> thin film. Coordinates are given based on pseudocubic

lattice. A scale bar represents 1  $\mu\text{m}$ .

Sample was epitaxially grown single-crystal BiFeO<sub>3</sub> thin film by pulsed laser decomposition (Prof. Chan-Ho Yang's group at KAIST). Specifically, the film was BiFeO<sub>3</sub> (120 nm)/SrRuO<sub>3</sub> (40 nm) deposited on orthorhombic [1 1 0]-oriented DyScO<sub>3</sub> substrate with a 20-nm-thick LaAlO<sub>3</sub> capping layer. Prior to the experiments, piezoresponse force microscopy (PFM) and X-ray diffraction (XRD) measurements were conducted to identify ferroelectric domain structures and lattice parameters, respectively. As a result, by PFM measurements, the sample was confirmed to have well-defined stripe ferroelectric domains that only contain in-plane variations across the domains. XRD measurements gave pseudocubic lattice parameters of 3.8475  $\text{\AA}$ , 4.0322  $\text{\AA}$ , and 3.9894  $\text{\AA}$  corresponding to  $a$ ,  $b$ , and  $c$ , respectively, extracted from  $\theta$ - $2\theta$ -scan curves near pseudocubic (0 0 3), (-1 0 3), and (0 1 3) Bragg peaks of BiFeO<sub>3</sub>.

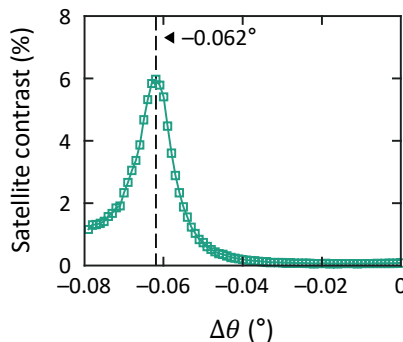


**Figure 6.2** Contrast changes of satellite peaks from ferroelectric domains with respect to a specular peak during  $\theta$ -rocking at a photon energy of 7.130 keV.

Before main experiments, the  $\theta$ -offset was determined from contrast changes of satellite signals from the ferroelectric domains with respect to specular signals during  $\theta$ -rocking. Here, the offset angle was negatively given due to an influence of the strong orthorhombic (1 1 0) Bragg peak of DyScO<sub>3</sub> substrate that appear at angle slightly higher than that of the pseudocubic (0 0 1) Bragg peak of BiFeO<sub>3</sub>. As a result, moving averages with  $5 \times 5$  kernel showed a smooth curve with the maximum value at the  $\theta$ -offset of -0.062°. As the value of -0.062° was identified at a photon energy of 7.130 keV, the offset angles were adjusted proportional to energy ratios. After deciding the  $\theta$ -offset, fluorescence signals and diffraction patterns were collected at a fixed sample position at different energies.

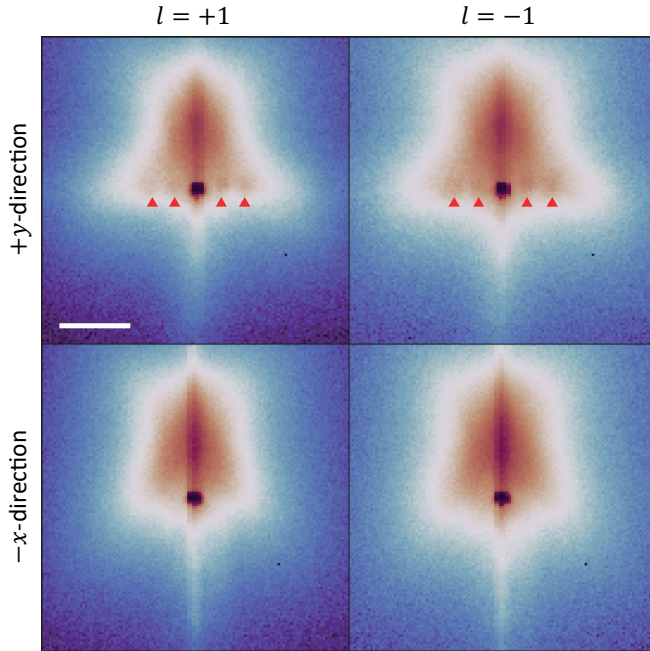


**Figure 6.3** Diffraction patterns measured near the pseudocubic (0 0 1) Bragg peak of BiFeO<sub>3</sub> with the  $\theta$ -offset of  $-0.062^\circ$  at a photon energy of 7.124 keV. They are measured with different OAMs and sample orientations. Satellite peaks from ferroelectric domains are marked by red triangles. A scale bar represents  $0.025 \text{ nm}^{-1}$ .

The sample was aligned based on the satellite peaks from its ferroelectric domains. As the domains were laid along the pseudocubic [0 1 0]-direction of BiFeO<sub>3</sub>, the coordinates were matched with the pseudocubic lattice of BiFeO<sub>3</sub>. After the sample alignment, the fluorescence signals were collected for sample orientations along  $+y$ - and  $-x$ -directions with photon energies from 7.110 keV to 7.145 keV. Energy steps were set as 1 eV for the range from 7.120 keV to 7.135 keV and 5 eV otherwise. The measured fluorescence spectra were fitted with the Voigt profile to extract intensities for Sc  $K\alpha$  and Fe  $K\alpha$  emission lines, and confidence intervals for the fitting were also identified with a confidence level of 95%. These signals would be related to an absorption of each atom. Then, as the signals of interest was for Fe atoms, extracted Fe  $K\alpha$  components were normalized by Sc  $K\alpha$  components, giving final X-ray absorption spectra. The absorption spectra showed a smooth curve with a rising edge from 7.120 keV to 7.127 keV and two post-edge peaks at 7.127 keV and 7.133 keV. The first peak was known to be caused by the ligand-to-metal charge transfer process, in which electrons in

O 2p-orbitals partially transfer to Fe 3d-orbitals, and the second peak came from dipole transitions from 1s- to 4p-orbitals of Fe cations [156].

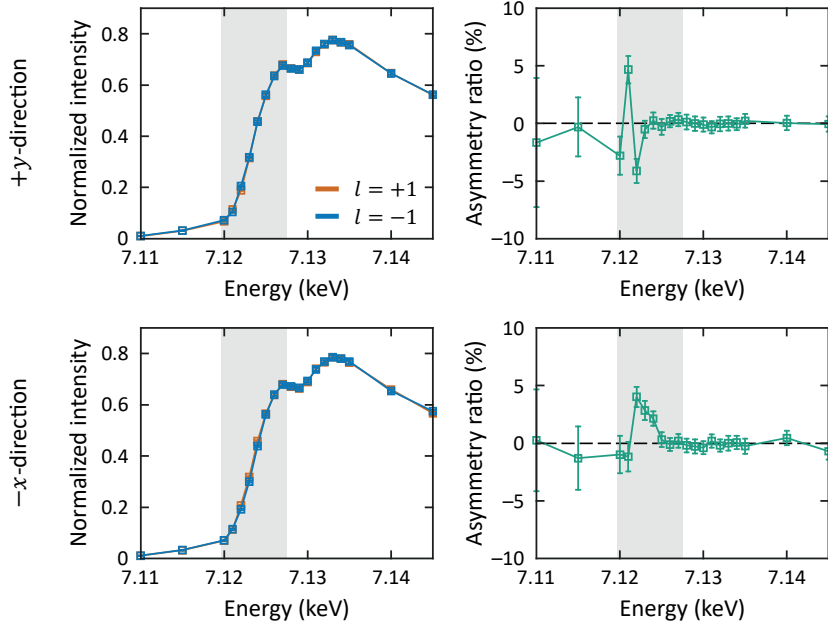


**Figure 6.4** · X-ray fluorescence signals (left) and their asymmetry ratios for helical dichroism (right) measured with different sample orientations. Rising edge regions are colored gray, and whiskers indicate propagated uncertainties from 95% confidence intervals for the Voigt-profile fitting of raw data, respectively.

Asymmetry ratios of the absorption spectra for helical dichroism were calculated as follows. Note that propagation of uncertainty was applied with 95% confidence intervals for the fitting.

$$AR_{HD}(\omega) = \frac{I_{+1}(\omega) - I_{-1}(\omega)}{I_{+1}(\omega) + I_{-1}(\omega)} \quad (6.8)$$

, where  $I$  is an absorption intensity and its subscript indicates a topological charge of an incident beam. The calculated asymmetry ratios showed clear helical dichroism depend on OAMs of the incident beam. They also exhibited different behaviors for different sample orientations, presenting roughly three peaks in total with different energies; the first one near 7.121 keV was a positive peak appeared only for +y-direction case, the second one near 7.122

keV was a negative peak for  $+y$ -direction case but positive for  $-x$ -direction case, and the last one near 7.124 keV was a positive peak appeared only for  $-x$ -direction case.

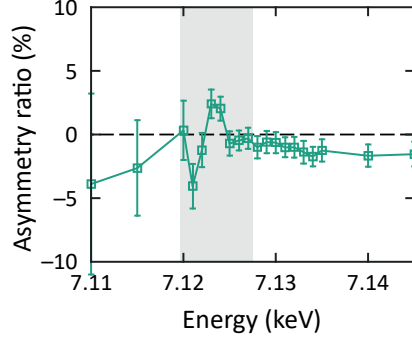


**Figure 6.5** Asymmetry ratios of X-ray fluorescence signals for linear dichroism. Rising edge regions are colored gray, and whiskers indicate propagated uncertainties from 95% confidence intervals for the Voigt-profile fitting of raw data, respectively.

As the X-ray beams were linearly polarized along the horizontal direction, the sample orientations along  $+y$ - and  $-x$ -directions gave polarization vectors along pseudocubic [1 0 0]- and [0 1 0]-directions of BiFeO<sub>3</sub>, respectively. The lattice parameters,  $a$  and  $b$ , were different as  $a < b$ ; therefore, the orbitals lied along  $y$ -axis have lower energies than those lied along  $x$ -axis. In this circumstance, linear dichroism would be raised depend on the sample orientations. Asymmetry ratios for linear dichroism can also be derived from the measured absorption signals as follows.

$$AR_{LD}(\omega) = 2 \frac{[I_{+1,+y}(\omega) + I_{-1,+y}(\omega)] - [I_{+1,-x}(\omega) + I_{-1,-x}(\omega)]}{I_{+1,+y}(\omega) + I_{-1,+y}(\omega) + I_{+1,-x}(\omega) + I_{-1,-x}(\omega)} \quad (6.9)$$

, where subscripts of  $S$  indicate topological charge and sample orientation in order. They showed two peaks with different signs in the rising edge region, where helical dichroism was observed. The negative peak represented orbitals lied along  $y$ -axis, while the positive peak represented orbitals lied along  $x$ -axis. These peaks appeared at different energies as expected; orbitals lied along  $y$ -axis for lower energy than those lied along  $x$ -axis. As linear dichroism shared same energy ranges with helical dichroism, it provided additional information including directionalities of the involved orbitals for an interpretation of helical dichroism.

With these experiments, an existence of helical dichroism for ferroelectric structures of BiFeO<sub>3</sub> was experimentally confirmed together with the directional information on contributing orbitals based on linear dichroism. In accordance with these observations, further analyses based on the physical model as described in Section 6.2 will be conducted to find relationships between helical dichroism and ferroelectric structures of BiFeO<sub>3</sub>, especially with the topological defects.

#### 6.4. Conclusion

The experimental observation of helical dichroism on ferroelectric structures was successfully accomplished with the epitaxial thin film of BiFeO<sub>3</sub> using hard X-ray vortex beams generated by off-axis SZPs. The physical model to analyze helical dichroism was also suggested for single-crystal ferroelectric materials with arbitrary orientations. Although theoretical analyses using this model are not conducted yet, the findings themselves sufficiently proved the existence of helical dichroism on ferroelectric structures whether it came from the topological defects or not. According to this discovery, helical dichroism together with linear dichroism would give structural information that might not be captured by ordinary imaging methods; therefore, a combination of such dichroic effects with X-ray diffraction imaging methods has a great potential for functional nanoimaging of ferroelectric materials.

Considering that the X-ray fluorescence yields were integrated values that are not spatially resolved, the imaging methods using helical dichroism would give higher contrasts on OAM-sensitive structures in ferroelectric materials. Recently, 3D tomography methods using hard X-ray ptychography with circular and linear dichroism have been successfully demonstrated, identifying magnetization vectors and crystal orientations of the materials, respectively, with nanoscale resolution in 3D [157,158]. As 3D Bragg ptychography provides information on atomic displacement fields that are crucial for ferroelectric materials, a combination with helical dichroism would offer a great opportunity to investigate OAM-sensitive structures in ferroelectric materials with an exceptional sensitivity on 3D arrangements of their polarizations [159].

## IV. Development of Deep-Learning Models for CDI

### 7. Diffraction pattern denoiser

#### 7.1. Introduction

A rapid development of computing devices and methodologies has opened a new avenue in various scientific areas with the help of machine-learning techniques [160–163]. As scientific research relies on analyses of experimental data, computational methods, which can efficiently and accurately extract meaningful information from the measured data, have been demanding. This becomes severe for imaging science because of relatively large size and noise vulnerability of image data. In this circumstance, deep-learning techniques with deep neural networks (DNNs) have recently showed a notable progress while reducing human inspection times in beam diagnosis, ultrafast photonics, and various microscopies including localization microscopy, scanning tunnelling microscopy, holography, and coherent imaging [164–167].

Convolutional neural networks (CNNs) are DNNs of which layers include convolution operations instead of element-wise linear operations [168,169]. Such operation offers an efficient calculation by convolving a small kernel with trainable parameters across the image data, while effectively reflecting local distributions of the data. Using these networks, phase retrievals of images measured with low photon counts, diffusive media, and holography have been successfully demonstrated, outperforming conventional algorithms with much faster processing times [170–172]. Despite such superior performance of CNNs in imaging science, DL techniques has not been actively developed with data in the  $k$ -space, or equivalently reciprocal space. Considering that scattering data, especially for the X-ray regime, are mapped in the  $k$ -space with respect to  $Q$ , interpretations of such data using DL approaches have been demanding. However, wide value range, strong noise, and partial loss have impeded applications of CNNs to the  $k$ -space data. Here, we proposed a  $k$ -space CNN to suppress noises in the noisy, partially damaged  $k$ -space data and investigated its positive impact on phase retrieval [14]. In this chapter, this DL-based approach would be introduced.

#### 7.2. $k$ -space convolutional neural network for denoising diffraction data

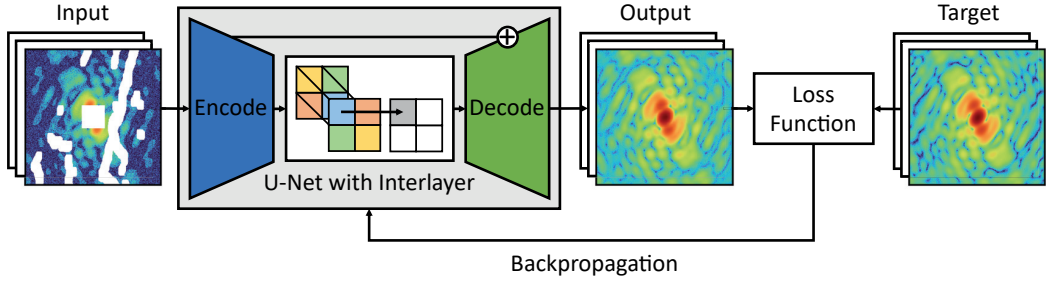


**Figure 7.1** · Schematic diagram of the  $k$ -space CNN for denoising noisy, partially damaged diffraction patterns. Adapted from Ref. [14], American Physical Society.

Layer no.	Structure	Output shape ( $C \times H \times W$ )
0	$\rightarrow x_0$	$1 \times 512 \times 512$
1	$PC(7, 2, 3) + BN + ReLU \rightarrow x_1$	$16 \times 256 \times 256$
2	$PC(5, 2, 2) + BN + ReLU \rightarrow x_2$	$32 \times 128 \times 128$
3	$PC(5, 2, 2) + BN + ReLU \rightarrow x_3$	$64 \times 64 \times 64$
4	$PC(3, 2, 1) + BN + ReLU \rightarrow x_4$	$128 \times 32 \times 32$
5	$PC(3, 2, 1) + BN + ReLU \rightarrow x_5$	$128 \times 16 \times 16$
6	$PC(3, 2, 1) + BN + ReLU \rightarrow x_6$	$128 \times 8 \times 8$
7	$PC(3, 2, 1) + BN + ReLU \rightarrow x_7$	$128 \times 4 \times 4$
8	$PC(3, 2, 1) + BN + ReLU \rightarrow x_8$	$128 \times 2 \times 2$
9	$(x_8, Rx_8) \rightarrow \text{Concatenate} + PC(1, 1, 0) + BN + ReLU \rightarrow x_9$	$128 \times 2 \times 2$
10	$(x_7, Ux_9) \rightarrow \text{Concatenate} + PC(3, 1, 1) + BN + LReLU \rightarrow x_{10}$	$128 \times 4 \times 4$
11	$(x_6, Ux_{10}) \rightarrow \text{Concatenate} + PC(3, 1, 1) + BN + LReLU \rightarrow x_{11}$	$128 \times 8 \times 8$
12	$(x_5, Ux_{11}) \rightarrow \text{Concatenate} + PC(3, 1, 1) + BN + LReLU \rightarrow x_{12}$	$128 \times 16 \times 16$
13	$(x_4, Ux_{12}) \rightarrow \text{Concatenate} + PC(3, 1, 1) + BN + LReLU \rightarrow x_{13}$	$128 \times 32 \times 32$
14	$(x_3, Ux_{13}) \rightarrow \text{Concatenate} + PC(3, 1, 1) + BN + LReLU \rightarrow x_{14}$	$64 \times 64 \times 64$
15	$(x_2, Ux_{14}) \rightarrow \text{Concatenate} + PC(3, 1, 1) + BN + LReLU \rightarrow x_{15}$	$32 \times 128 \times 128$
16	$(x_1, Ux_{15}) \rightarrow \text{Concatenate} + PC(3, 1, 1) + BN + LReLU \rightarrow x_{16}$	$16 \times 256 \times 256$
17	$(x_0, Ux_{16}) \rightarrow \text{Concatenate} + PC(3, 1, 1) \rightarrow x_{17}$	$1 \times 512 \times 512$

**Table 7.1** · Full description of layers composing the  $k$ -space CNN. The layers corresponding to encoder, interlayer, and decoder are colored in green, orange, and blue, respectively. All convolution operations are given with kernel size, stride, and padding parameters in parentheses and they are followed by batch normalization (BN) and activation functions, rectified linear unit (ReLU) and leaky ReLU (LReLU) for encoder and decoder, respectively, except for the last layer. Concatenation is performed along the channel axis and  $180^\circ$  rotation and nearest-neighbor upsampling operators are denoted by  $R$  and  $U$ , respectively.

The  $k$ -space CNN was designed to handle noisy, partially damaged diffraction patterns from single-pulse diffraction measurements using XFELs [173]. Noise and partial loss in the measured data were originated from limited photon counts in a single X-ray pulse, beam stop

configuration, detector chipset arrangement, and other unwanted contributions. As conventional methods have not been successfully overcome these obstacles, the proposed DL-based approach would offer an effective option dealing with such data. For this purpose, the network was designed based on U-Net, which have a symmetric encoder–decoder architecture with skipped connections between encoder and decoder [174]. Here, all convolution operations were replaced with partial convolutions (PCs), which correct an influence of missing values by multiplying a reciprocal ratio of valid values in convolving regions, and nearest-neighbor interpolation was applied for the skipped connections to match the dimensions. [175]. Additionally, as diffraction patterns of real-valued objects, which are typically assumed for CDI, show centrosymmetry by the Friedel's law, pointwise convolutions on values at centrosymmetric points were newly introduced and were employed between encoder and decoder layers of the network. Batch normalizations and activation functions were applied after the convolution operations except for the last layer, and rectified linear unit (ReLU) and leaky ReLU (LReLU) with a negative slope of 0.2 were used as the activation functions for encoder and decoder layers, respectively.

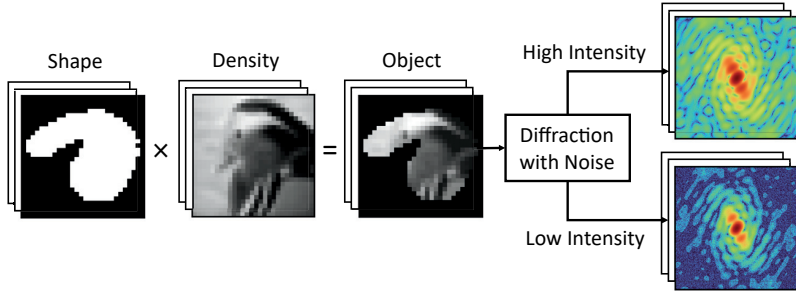


**Figure 7.2** · Schematic diagram of dataset generation for the  $k$ -space CNN.

Generation of datasets for training and test of the proposed  $k$ -space CNN was based on the Fourier transform of unbiased pseudorandom objects that are defined by products of two images, each randomly selected from publicly available image datasets, EMNIST and CIFAR-10 [176,177]. EMNIST is an image dataset of handwritten character digits, defining shapes of the pseudorandom objects, while CIFAR-10 is an image dataset of real-world objects, providing their internal density distribution. Then, the noisy diffraction patterns were generated by the following equation.

$$I = \text{Pois}\left(|\mathcal{F}u|^2 \frac{I_{\text{tot}}}{\sum_i |\mathcal{F}u|_i^2}\right) + \mathcal{N}(0, \sigma) \quad (7.1)$$

, where  $\text{Pois}(\lambda)$  generates random values from the Poisson distribution for  $\lambda$  events,  $\mathcal{N}(\mu, \sigma)$  generates random values from the Gaussian distribution with mean and standard deviation of  $\mu$  and  $\sigma$ , respectively, and  $I_{\text{tot}}$  is total diffraction intensity.  $I_{\text{tot}}$  were set as  $2 \times 10^6$  photons and  $2 \times 10^8$  photons for low- and high-intensity patterns, respectively, with  $\sigma = 0.25$ . Note that all operations were conducted for  $512 \times 512$  window, giving oversampling ratio of roughly between 20 and 40 along each dimension. The generated noisy diffraction patterns were randomly masked for each training epoch by irregular masks from NVIDIA irregular mask dataset with additional center masks reflecting CBS [175]. The irregular masks occluded 1% to 20% of the window and the center masks were defined as square masks with random radii from 1 to 64 pixels. Total 50,000 data were generated for training and 10,000 for test of the network.

For training the  $k$ -space CNN, a composite loss function was used for a backpropagation of the network, comparing outputs of the network, of which inputs were low-intensity diffraction patterns, with corresponding high-intensity patterns as references. The loss function consisted of mean absolute error (MAE),  $\mathcal{L}$ , MAE on masked regions,  $\mathcal{L}_{\text{mask}}$ , perceptual loss,  $\mathcal{L}_{\text{perc}}$ , style loss,  $\mathcal{L}_{\text{style}}$ , MAE between outputs and their  $180^\circ$  rotated images,  $\mathcal{L}_{\text{symm}}$ , and total variation loss,  $\mathcal{L}_{\text{tv}}$  [175,178,179]. Each function was defined as follows.

$$\begin{aligned} \mathcal{L}(u, v) &= \frac{1}{N} \sum_{i=1}^N |u_i - v_i|, & \mathcal{L}_{\text{mask}}(u, v) &= \frac{\sum_{M_i=0} |u_i - v_i|}{\sum_{M_i=0} 1} \\ \mathcal{L}_{\text{perc}}(u, v) &= \mathcal{L}(\Phi[u], \Phi[v]), & \mathcal{L}_{\text{style}}(u, v) &= \mathcal{L}(\text{Gr}[\Phi\{u\}], \text{Gr}[\Phi\{v\}]), \\ \mathcal{L}_{\text{symm}}(u) &= \mathcal{L}(u, \mathcal{R}_\pi u), & \mathcal{L}_{\text{tv}}(u) &= \mathcal{L}(u, \mathcal{D}_{1,x} u) + \mathcal{L}(u, \mathcal{D}_{1,y} u) \end{aligned} \quad (7.2)$$

, where  $u$  is an output image of the network,  $v$  is a reference image,  $\Phi[x]$  is high-level feature vectors from the outputs from first to third blocks of ImageNet-pretrained VGG-16 with an input image,  $x$ ,  $\text{Gr}[\Phi\{x\}]$  is the Gram matrix of the feature vectors,  $\mathcal{R}_\pi$  is a  $180^\circ$ -rotation operator and  $\mathcal{D}_1$  is a 1-pixel-deviation operators along the given axis of the image. Then, the final loss function was defined as follows.

$$\begin{aligned}\mathcal{L}_{\text{total}} = & (\mathcal{L} + 0.1\mathcal{L}^{\text{AC}}) + 5\mathcal{L}_{\text{mask}} + 0.05(\mathcal{L}_{\text{perc}} + 0.1\mathcal{L}_{\text{perc}}^{\text{AC}}) \\ & + 120(\mathcal{L}_{\text{style}} + 0.1\mathcal{L}_{\text{style}}^{\text{AC}}) + 0.1\mathcal{L}_{\text{symm}} + 0.1\mathcal{L}_{\text{tv}}\end{aligned}\quad (7.3)$$

, where  $\mathcal{L}^{\text{AC}}$  indicates the loss function on autocorrelations of corresponding real-space objects, which can be obtained by the inverse Fourier transform of the diffraction patterns. Note that the inputs of the network were log-scaled by  $\tilde{x}_0 = \ln [1 + \sqrt{\max(I, 0)}]$  and were normalized by  $x_0 = \tilde{x}_0 / \max(\tilde{x}_0)$ ; therefore, the inverse operations of these processes were required to obtain the autocorrelations. Using this composite loss function, network parameters were updated by AdamW optimizer with gradually decreasing learning rates from 0.01 to 0.00001 [180]. Denoising of diffraction patterns by the trained  $k$ -space CNN would be called as deep denoising hereafter.

### 7.3. Phase retrieval of simulated diffraction patterns with deep denoising

Application of deep denoising to phase retrieval was accomplished based on the conventional iterative projection algorithm, RAAR [49]. Starting from Eq. (2.8), the latter projection operator was executed with a modified Fourier-space amplitude constraint defined as follows.

$$\tilde{\mathcal{T}} = \{z \in \mathbb{C}^{N \times M} | |z| = \text{Denoise}[b]\} \quad (7.4)$$

, where  $\text{Denoise}[b]$  gives a denoised Fourier amplitude by deep denoising or the Gaussian smoothing. Deep denoising replaced the values in regions with the photon counts above 0.5 per pixel by output values of the  $k$ -space CNN with limited change ratios of  $\pm 20\%$  and suppressed the values in remaining regions by 20%. The Gaussian smoothing convolved the Gaussian kernel with  $\sigma = 1.5$  pixel. Then, the modified RAAR was defined as follows.

$$u^{(j+1)} = \frac{1}{2}\beta \left[ \text{refl}_{\mathcal{I}_S} \left\{ \text{refl}_{\mathcal{I}_T}^{(\text{real})} u^{(j)} \right\} + u^{(j)} \right] + (1 - \beta) \text{proj}_{\mathcal{I}_T}^{(\text{real})} u^{(j)} \quad (7.5)$$

Then, phase retrievals were accomplished with 3,000 iterations of the modified RAAR for total 500 initial random phases with linearly increasing  $\beta$  from 0.5 to 1 and the best results were selected based on  $R$ -factor. For phase retrievals on equal terms, fixed real-space supports were used and they were obtained by thresholding objects, which were reconstructed by GPS and the

shrink-wrap algorithm, by 1% of their maximum values followed by assigning 1-pixel margins at their boundaries [51,63].

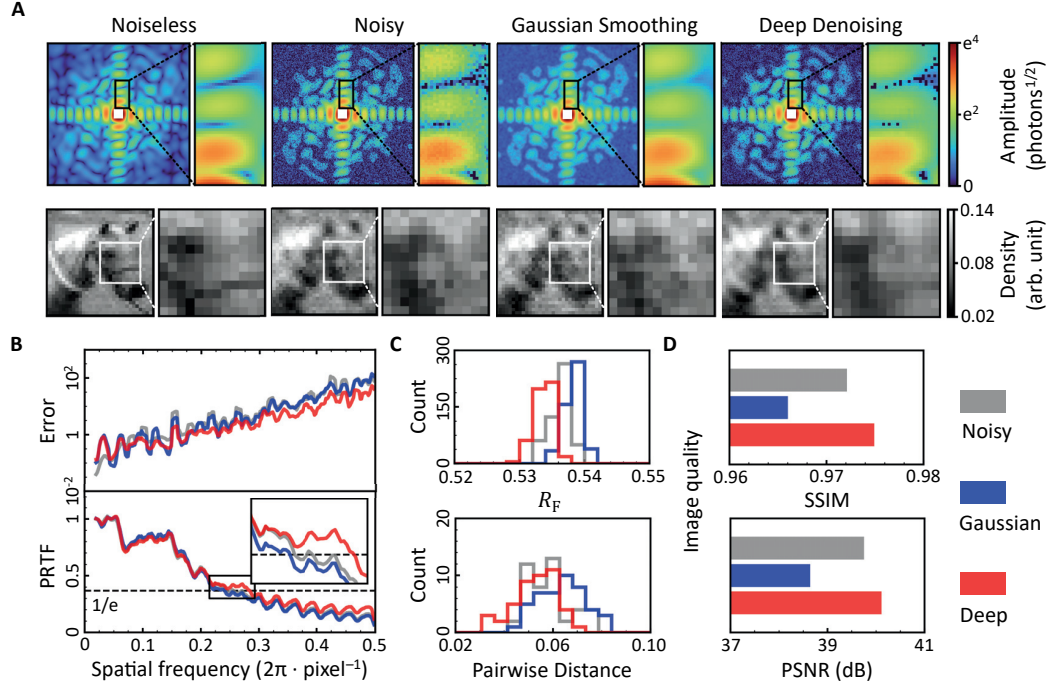


**Figure 7.3** · Phase retrieval of the simulated diffraction pattern with deep denoising. (A) Reconstructed images from the noisy diffraction pattern, the pattern with the Gaussian smoothing, and with deep denoising are presented. (B–D) Radial error (B, top), PRTF (B, bottom),  $R$ -factor (C, top), pairwise distance (C, bottom), SSIM (D, top), and PSNR (D, bottom) are calculated to evaluate reconstruction qualities. Adapted from Ref. [14], American Physical Society.

Reconstructed images from the noisy diffraction pattern, the pattern with the Gaussian smoothing, and with deep denoising showed significant differences. The result using deep denoising provided better agreements with the given diffraction pattern based on lower  $k$ -space error and higher PRTF compared to the other results, giving higher effective resolution based on  $1/e$  criterion [55]. In addition, convergence of phase retrieval was enhanced with lower  $R$ -factor and real-space pairwise distance. Note that the pairwise distance was defined as  $d_{\text{pair}}(u, u') = \sum_i |u - u'|_i / \sum_i |u + u'|_i$  and calculated for all possible pairs among the 10 best images. Moreover, an image quality was also improved with higher SSIM and PSNR.

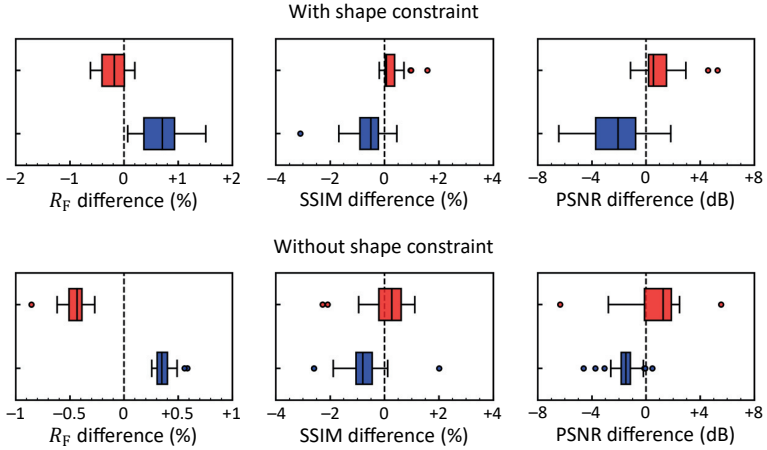


**Figure 7.4** Box and whisker plots to compare deep denoising and the Gaussian smoothing on phase retrieval. Differences of deep denoising (red) and the Gaussian smoothing (blue) on  $R$ -factor, SSIM, and PSNR of the reconstruction results are presented with respect to the case without applying the denoising method.

Investigation on change ratio statistics for  $R$ -factor, SSIM, and PSNR of reconstruction results by applying deep denoising and the Gaussian smoothing during phase retrievals was conducted for cases of the initial objects with and without assigning the shapes from EMNIST. As a result, deep denoising showed enhancements on all metrics by giving lower  $R$ -factor and higher SSIM and PSNR for both cases, while the Gaussian smoothing deteriorated the results. Thus, deep denoising improved phase retrieval in every way by providing noise-suppressed Fourier-space amplitude constraints, while the Gaussian smoothing showed even worse result than without applying the denoising method.

## 7.4. Phase retrieval of experimental data with deep denoising

Actual experiments were conducted to verify performance of deep denoising on experimental data. The experiments were performed at nanocrystallography and coherent imaging (NCI) beamline of PAL-XFEL in PAL [181]. Femtosecond X-ray pulses were generated by a self-amplified spontaneous emission (SASE) process tuned at a photon energy of 5 keV with an energy bandwidth of  $\Delta E/E \approx 5 \times 10^{-3}$ . Then, beams were focused into  $5 \mu\text{m}$  (horizontal)  $\times 7 \mu\text{m}$  (vertical) by a pair of Kirkpatrick–Baez mirrors located at 5 m upstream from the sample,

giving a total flux of  $8 \times 10^9$  photons· $\mu\text{m}^{-2}$  for a single pulse [107]. Single-pulse diffraction patterns were measured by a 1-megapixel multi-port charge-coupled device (MPCCD), of which the size of each pixel is  $50 \times 50 \mu\text{m}^2$ , at 1.6 m downstream from a sample position [182]. Samples were core–shell nanoparticles consisting of trisoctahedral (TOH) Au core and spherical TiO<sub>2</sub> shell. They were spread on 100-nm-thick Si<sub>3</sub>N<sub>4</sub> membranes and were mounted in an imaging chamber. The chamber and beam paths were kept under vacuum.

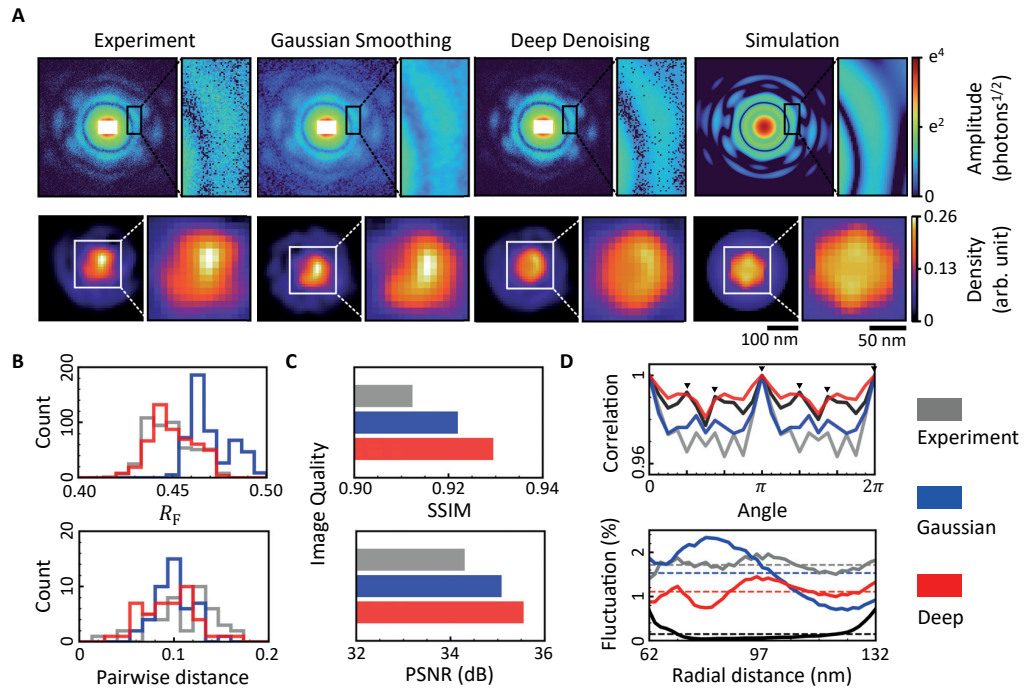


**Figure 7.5** · Phase retrieval of the single-pulse diffraction pattern from the core–shell nanoparticle with deep denoising. (A) Reconstructed images from the noisy diffraction pattern, the pattern with the Gaussian smoothing, and with deep denoising are presented. (B, C)  $R$ -factor (B, top), pairwise distance (B, bottom), SSIM (C, top), and PSNR (C, bottom) are calculated to evaluate reconstruction qualities. (D) Angular correlation and density fluctuation are also calculated for an additional evaluation. Adapted from Ref. [14], American Physical Society.

Reconstruction of experimental data with deep denoising showed significant improvements, giving lower pairwise distance and higher SSIM and PSNR. Unlike the results with simulated data, the Gaussian smoothing also showed a similar result, but inferior to deep denoising. While the Gaussian smoothing presented a considerably higher  $R$ -factor, deep denoising only presented a slight increment due to a gap between measured and denoised

diffraction patterns. Moreover, using an ideal structure with TOH core and spherical shell as a reference, angular correlation and density fluctuation were calculated for an additional performance evaluation. In comparison with the ideal structure, only deep denoising showed comparable angular correlation and the lowest density fluctuation in shell regions. Considering that phase retrievals of core–shell particles are challenging due to their structural heterogeneity and weak scattering signals from the shells, deep denoising succeeded to offer definite improvements in phase retrieval of actual noisy diffraction patterns from such complex particles.

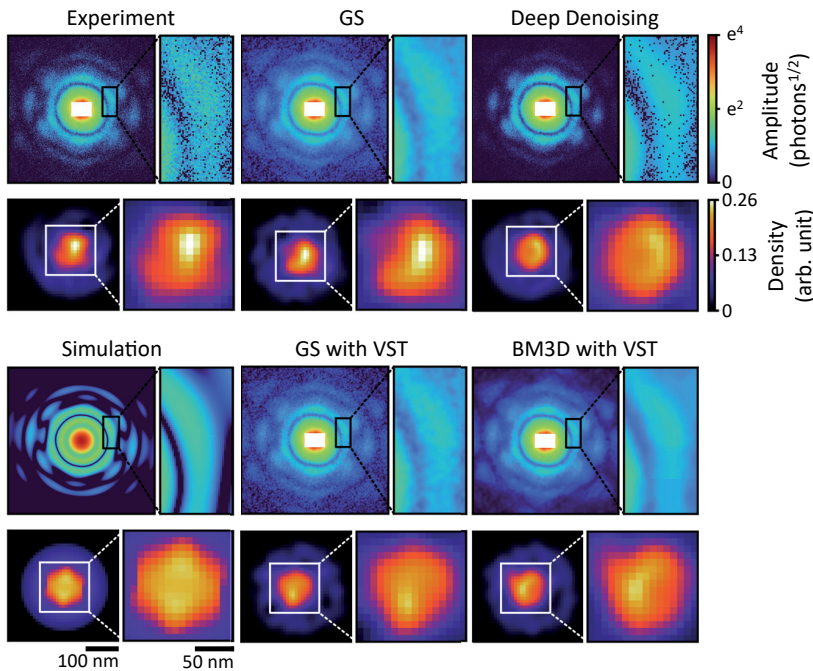


**Figure 7.6** · Denoising and phase retrieval of the single-pulse diffraction pattern from the core–shell nanoparticle by various denoising methods. The results using the Gaussian smoothing (GS), GS with VST, and BM3D with VST are presented to compare with deep denoising.

To supplement the comparison group, block-matching and 3D filtering (BM3D) algorithm and variance-stabilizing transformation (VST) were additionally confirmed [183]. BM3D is a conventional denoising algorithm based on an enhanced sparse representation, providing the highest level of denoising performance among non-DL algorithms. Meanwhile, as its name suggests, VST is a transformation that stabilize the variance of values from a certain distribution into a specific constant, typically 1. As the concerned noises were mixed Poisson–

Gaussian noises, a generalized Anscombe transformation was used as VST for the diffraction patterns before applying the denoising methods and it is defined as follows [184].

$$VST[I] = 2 \sqrt{\max\left(I + \sigma^2 + \frac{3}{8}, 0\right)} \quad (7.6)$$

Using this transformation, the Gaussian smoothing and BM3D were applied to the experimental data with VST and their influences on phase retrieval were additionally identified. Unfortunately, both methods did not show any meaningful improvements, falling behind deep denoising.

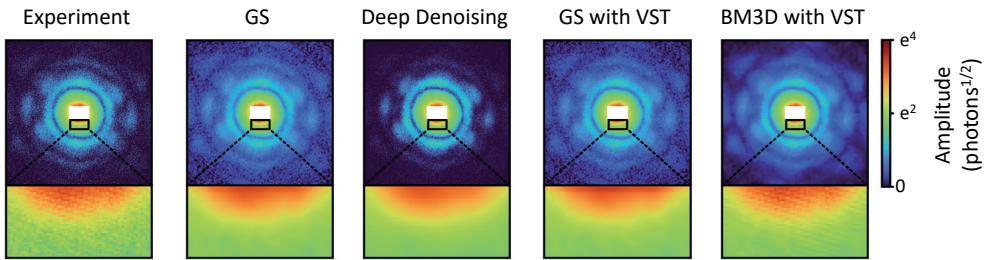


**Figure 7.7** Denoising results near the zeroth speckle by various denoising methods. The results using the Gaussian smoothing (GS), GS with VST, and BM3D with VST are presented to compare with deep denoising.

Unlike deep denoising, a comb pattern at the zeroth speckle remained in the pattern denoised by BM3D with VST and a rough border also remained in the pattern denoised by the Gaussian smoothing. These signals were a signature of multiple particles and were not desirable for single-particle imaging. As the  $k$ -space CNN was trained with the diffraction patterns from the single objects, deep denoising suppressed unwanted contributions from foreign particles, leading to accurate phase retrieval.

## 7.5. Application of deep denoising on preconditioning the phase problem

As deep denoising provides an adjusted Fourier-space amplitude constraint for phase retrieval, the operation of deep denoising can be treated as preconditioning by a matrix multiplication of a diagonal matrix to the constraint. Preconditioning is an application of a specific

transformation, preconditioner, that makes conditions of a certain problem more suitable to be solved by numerical methods. In this regard, a preconditioned version of PDHG can be applied to the phase problem in accordance with GPS, which is a kind of PDHG algorithms for phase retrieval [185]. The preconditioned version of GPS is simply defined as follows.

$$\begin{aligned} z^{(j+1)} &= \text{prox}_{J_{T,\sigma}}^{M_1}[z^{(j)} - M_1^{-1}\mathcal{F}y^{(j)}] \\ y^{(j+1)} &= \text{prox}_{J_{S,G}^*}^{M_2}[y^{(j)} + M_2^{-1}\mathcal{F}^{-1}\{2z^{(j+1)} - z^{(j)}\}] \end{aligned} \quad (7.6)$$

, where  $M_1$  and  $M_2$  are preconditioners satisfying that  $M_1$  and  $M_2$  are positive definite. Here, the proximal operator with the preconditioner is defined as follows.

$$\text{prox}_f^M(v) = \underset{x \in \mathcal{X}}{\operatorname{argmin}} \left[ f(x) + \frac{1}{2} \|x - v\|_M^2 \right] \quad (7.7)$$

When  $M_1 = t^{-1}\mathbb{I}$  and  $M_2 = s^{-1}\mathbb{I}$ , the preconditioned GPS reduces to the plain GPS. Here, for any positive-definite  $M_1$ , the optimal  $M_2$  is given as  $M_2 = \mathcal{F}^{-1}M_1^{-1}\mathcal{F}$  by Schur complement and the  $y$ -subproblem can be approximately solved by fixed iterations of proximal gradient descent method as follows [185].

$$\begin{aligned} y^{(j+1,0)} &= y^{(j)} \\ y^{(j+1,k+1)} &= \text{prox}_{J_{S,G},\eta}^{M_2}[y^{(j+1,k)} + \eta\mathcal{F}^{-1}\{2z^{(j+1)} - z^{(j)}\}] \\ y^{(j+1)} &= y^{(j+1,p)} \end{aligned} \quad (7.8)$$

, where  $p \geq 1$  and  $\eta$  is a proximal-gradient step size in range of 0 to  $2\lambda_{\min}(M_2)/\lambda_{\max}^2(M_2)$  with the minimum and maximum eigenvalues,  $\lambda_{\min}$  and  $\lambda_{\max}$ , respectively. As the Fourier transform is unitary and  $M_1$  is assumed as a diagonal matrix, the eigenvalue of  $M_2$  is equivalent with that of  $M_1$ . When only a single iteration with the maximum  $\eta$  is applied for an approximate solution of the  $y$ -subproblem, the preconditioned GPS becomes as follows.

$$\begin{aligned} z^{(j+1)} &= \text{prox}_{J_{T,\sigma}}^{M_1}[z^{(j)} - M_1^{-1}\mathcal{F}y^{(j)}] \\ y^{(j+1)} &= \text{prox}_{J_{S,G},\eta_{\max}}^{M_2}[y^{(j)} + \eta_{\max}\mathcal{F}^{-1}\{2z^{(j+1)} - z^{(j)}\}] \end{aligned} \quad (7.9)$$

, where  $\eta_{\max} = 2 \min(M_1^{-1}) / [\max(M_1^{-1})]^2 = 2[\min(M_1)]^2/\max(M_1)$ . While the second step in Eq. (7.9) is identical to the plain GPS, the first step can be calculated as follows.

$$\text{prox}_{\mathcal{J}_{T,\sigma}}^{M_1}[z] = (\mathbb{I} + \sigma M_1)^{-1} b \odot e^{i \arg z} + (\mathbb{I} + \sigma M_1)^{-1} M_1 z \quad (7.10)$$

The diagonal matrix defined from the change ratios by deep denoising is assigned to the preconditioner,  $M_1$ , with limiting its values as before. This algorithm would be called as deep-preconditioned GPS (dpGPS) hereafter. Note that  $\eta_{\max}$  was given as 0.8 for the limited change ratios of  $\pm 28\%$ .

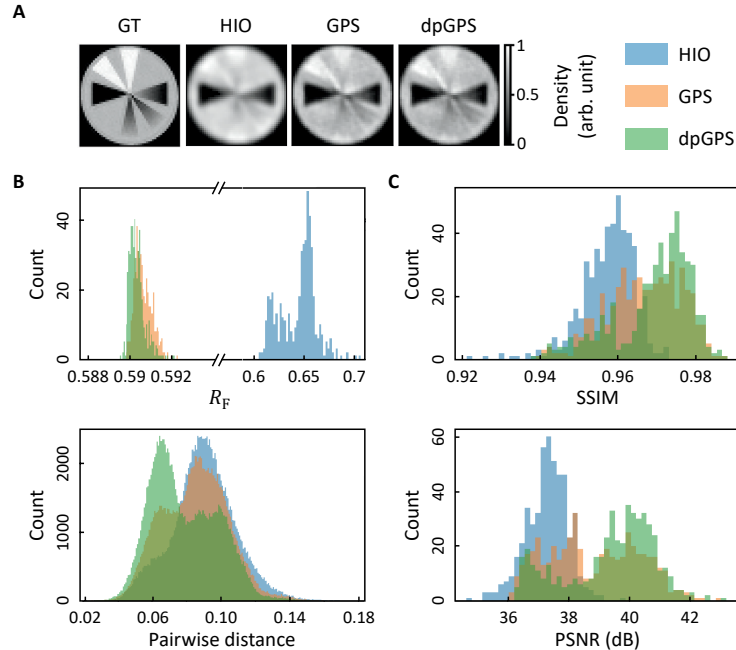


**Figure 7.8** · Reconstruction results by HIO, GPS, and dpGPS. (A) An average of the best 5 reconstructed images by each method is presented. (B, C)  $R$ -factor (B, top), pairwise distance (B, bottom), SSIM (C, top), and PSNR (C, bottom) are calculated to evaluate reconstruction qualities.

Phase retrieval performance of dpGPS was evaluated with a simulated diffraction pattern from a synthetic object. As a result, dpGPS outperformed the conventional algorithms, HIO and GPS, with lower  $R$ -factor and pairwise distance and higher SSIM and PSNR. Thus, deep denoising was verified to positively modify the conventional algorithms by providing data-specific preconditioners for phase retrieval.

## 7.6. Conclusion

Deep denoising based on the  $k$ -space CNN was demonstrated to improve phase retrieval of single-pulse diffraction patterns by properly suppressing the noise in such data. It outperformed conventional denoising methods with significantly better reconstructed images when applying to the phase retrieval algorithm. In addition, the employed data generation strategy maximally excluded physical biases with a sufficient randomness, showing positive effects on reconstructions of noisy single-object diffraction patterns. The use of partial convolutions also offered the stable handling of partially damaged data, which usually suffered from X-ray diffraction measurements. Since the development of XFEL has enabled time-resolved studies using X-rays that were not possible with the conventional synchrotron facilities, effective and efficient handling of strong noises from single-pulse measurements has been requested [8–11]. In this circumstance, the  $k$ -space CNN realized effective denoising of these noisy data solely in the  $k$ -space. As inference of DNNs can be immediately achieved with a help of graphics processing units (GPUs) after appropriate training procedures, it also realized rapid processing of massive diffraction data from XFEL experiments. Thus, the  $k$ -space CNN would be a robust platform dealing with the  $k$ -space data, which exhibit drastic deviation and partial loss with strong noises.

\* Source codes and trained parameters of the  $k$ -space CNN with modified phase retrieval algorithms are available at <https://github.com/sungyun98/PhaseRetrieval>.

## 8. Real-time phase retrieval

### 8.1. Introduction

The phase problem is a problem of losing phase information from physical measurements and it poses significant difficulties in various research modalities, especially crystallography and high-resolution imaging [186]. Extracting such information that might be hidden in interference patterns is crucial for interpretations of measured signals. While various methods have been proposed for effective phase retrievals, they often demand long processing time and are influenced by factors including noise, completeness of data, and other experimental constraints.

In this circumstance, DL-based approaches have shown meaningful progresses dealing with diffraction data by improving or replacing traditional iterative processes with faster and non-iterative operations accelerated by GPUs [169,187]. Thus, efforts on developing DL methods have been continued to facilitate tasks including denoising, classification, and phase retrieval, despite several difficulties incurred in the X-ray regime [14,104,188–197].

Recent advancements in brighter X-ray sources, such as XFELs, which generate ultrashort, extremely intense coherent X-ray pulses, have enabled observations of ultrafast phenomena including molecular bonding, transient material dynamics, and hidden material phases in nonequilibrium states [9,198–200]. CDI, which uses iterative methods to recover the phase information, have shown a considerable potential for determining nanoscale structures of individual specimens. However, diffraction signals, especially for single-pulse measurements using XFELs, typically suffer low SNR and partial data occlusion and these have hindered practical applications of DL in interpreting actual experimental data [173]. Here, we proposed a DNN to recover phase information from the imperfect, photon-limited diffraction patterns, realizing real-time reconstructions of real-space images for single-particle imaging experiments using XFELs [15]. In this chapter, architecture and training strategy of the proposed network and its application on simulated and experimental data would be introduced.

## 8.2. Deep neural network for phase retrieval of diffraction data

The DNN for phase retrieval was based on a residual neural network (ResNet) with the encoder–decoder architecture [201]. The network employed not only PCs but also depth-wise separable convolutions (DSCs) and fast Fourier convolutions (FFCs) to accomplish a real-time reconstruction of imperfect, photon-limited diffraction patterns [175,202,203]. Those convolution operations are designed to improve performance of DNNs for specific applications; PC enables a mask-aware operation by an equal allocation of valid values within convolving regions, DSC offers an efficient operation with typically ten times fewer parameters than the plain convolution while maintaining the performance, and FFC provides a global receptive field by using the convolution on the Fourier transform of an input. A ResNet-based DNN named LaMa has recently been proposed to have superior performance in image inpainting by

employing FFCs in the entire network, despite its straightforward architecture [204]. Adopting a concept of LaMa, DNN for phase retrieval was designed to have an architecture with two newly introduced operations, an encoder with weight-corrected PCs (WPCs) to properly deal with imperfect diffraction data and a two-stage decoder with an intermediate Fourier modulation to increase consistency with the measured diffraction patterns.

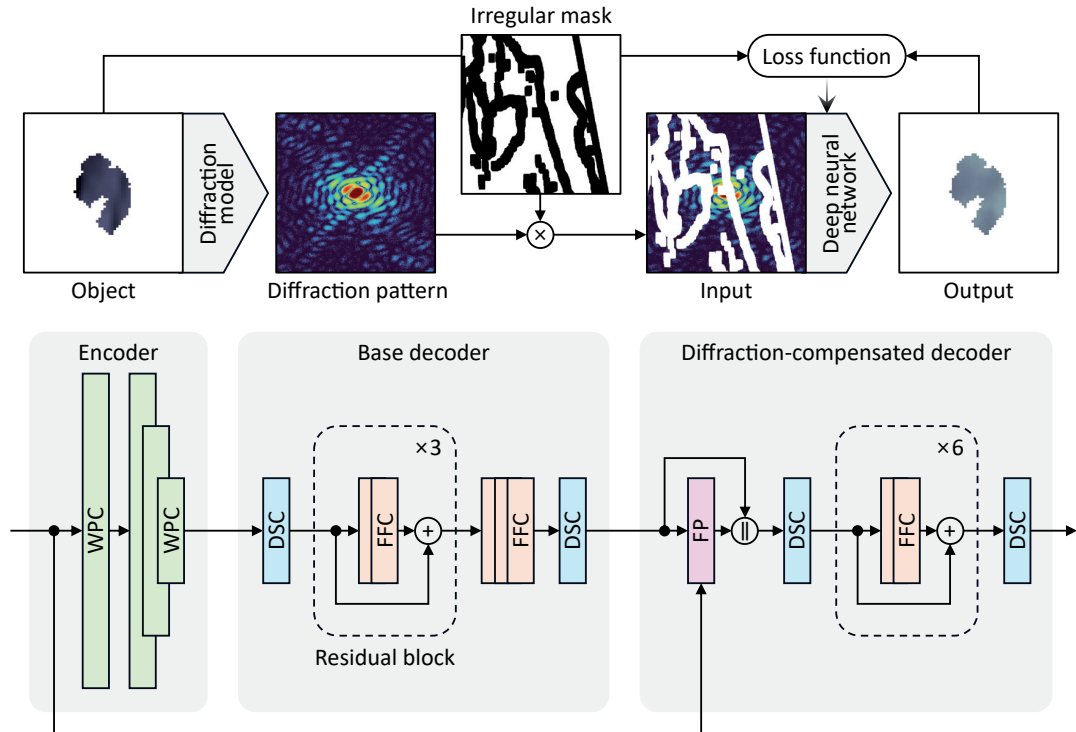


**Figure 8.1** · Schematic diagrams of dataset generation (top) and architecture (bottom) of the DNN for phase retrieval of imperfect, photon-limited diffraction patterns. Adapted from Ref. [15], Springer Nature Limited.

Layer no.	Structure	Output shape (C × H × W)
0		$1 \times 512 \times 512$
1	WPC(7, 1, 3) + BN + ReLU	$64 \times 512 \times 512$
2	WPC(3, 2, 1) + BN + ReLU	$128 \times 256 \times 256$
3	WPC(3, 2, 1) + BN + ReLU	$256 \times 128 \times 128$
4	WPC(3, 2, 1) + BN + ReLU	$512 \times 64 \times 64$
5	DSC(3, 1, 1) + BN + ReLU + Split	$(256 + 256) \times 64 \times 64$
6–11	FFC residual blocks $\times 3$ $(x_0, x'_0) \rightarrow \text{FFC}(3, 1, 1) + \text{BN} + \text{ReLU} \rightarrow (x_1, x'_1)$	$(256 + 256) \times 64 \times 64$

	$(x_1, x'_1) \rightarrow \text{FFC}(3, 1, 1) + \text{BN} + \text{ReLU} \rightarrow (x_2, x'_2)$ $\rightarrow (x_0 + x_2, x'_0 + x'_2)$	
12	FFC(3, 1, 1) + BN + ReLU	$(128 + 128) \times 64 \times 64$
13	FFC(3, 1, 1) + BN + ReLU	$(64 + 64) \times 64 \times 64$
14	FFC(3, 1, 1) + BN + ReLU	$(32 + 32) \times 64 \times 64$
15	Concatenate + DSC(3, 1, 1) + Sigmoid	$1 \times 64 \times 64$
16	$x_0 \rightarrow \text{Fourier projection} \rightarrow x_1$ $(x_0, x_1) \rightarrow \text{Concatenate} \rightarrow x_2$	$2 \times 64 \times 64$
17	DSC(3, 1, 1) + BN + ReLU + Split	$(32 + 32) \times 64 \times 64$
18–29	FFC residual blocks × 6	$(32 + 32) \times 64 \times 64$
30	Concatenate + DSC(3, 1, 1) + Sigmoid	$1 \times 64 \times 64$
Total trainable parameters: $1.52 \times 10^7$		

**Table 8.1** Full description of layers composing the DNN for phase retrieval. The layers corresponding to encoder, base decoder, and diffraction-compensated decoder are colored in green, orange, and blue, respectively. All convolution operations are given with kernel size, stride, and padding parameters in parentheses and they are followed by batch normalization (BN) and activation functions, ReLU, except for the last layers of decoders with the sigmoid functions. Concatenation and split are performed along the channel axis.

As diffraction intensities typically decrease by  $Q^{-4}$ , it is required to handle drastic deviations of the signals for an appropriate reconstruction of an imperfect data. In this case, a log scale can make them linear, but this is not sufficient for phase retrieval where an accurate Fourier-space information is important. Thus, while PC revises an output value by multiplying a reciprocal ratio of valid values in convolving regions, WPC assigns  $Q$ -dependent weights for this correction based on the Guinier–Porod model [175,205]. The Guinier–Porod model describes a radial intensity distribution of small-angle scattering signals from a sample with a specific shape. For a smooth sphere, it gives the following relations.

$$I(Q) = \begin{cases} G \exp\left(-\frac{R^2 Q^2}{5}\right), & \text{for } Q \leq Q_1 \\ G \exp\left(-\frac{R^2 Q_1^2}{5}\right) \left(\frac{Q_1}{Q}\right)^4, & \text{for } Q > Q_1 \end{cases} \quad (8.1)$$

, where  $G$  is the Guinier scale factor,  $R$  is a radius of the sphere, and  $Q_1$  is a boundary value between Guinier and Porod models, giving  $Q_1 = \sqrt{10}/R$ . As measured diffraction patterns are in a unit of pixels,  $R$  is given by  $\pi/\sigma$  with an oversampling ratio,  $\sigma$ . Then, with the weights set as the intensity values in Eq. (8.1), an operation of WPC is finally defined as follows.

$$x' = \begin{cases} K^T(x \odot M) \frac{\sum_i W_i}{\sum_i W_i M_i}, & \text{if } \sum_i W_i \neq 0 \\ 0, & \text{otherwise} \end{cases} \quad (8.2)$$

, where  $x$  is an input,  $M$  is a binary mask for valid data points,  $W$  is the  $Q$ -dependent weights. Note that this operation is executed for data points in convolving regions. After the encoder extracted feature vectors from input diffraction patterns with a help of WPCs, the two-stage decoder generated real-space images with a help of FFCs, which refer the Fourier-space information. A reason of the two-stage structure was that initial Fourier-space information might be faded out while passing deep layers of the network, even though residual structures suppress such effect. Thus, the Fourier modulation in the diffraction-compensated decoder forcibly recalled an initial Fourier-space information by concatenating an output of the base decoder and the output with a Fourier-space projection onto the measured data before feeding to its residual blocks, increasing the consistency with the measured diffraction data. These components worked together for a successful phase retrieval of imperfect, photon-limited diffraction patterns and this DL-based phase retrieval would be called as deep phase retrieval (DPR) hereafter.

Generation of datasets for training, validation, and test of the proposed network was conducted by a diffraction model with pseudorandom real-space objects. Shapes and internal densities of the objects were assigned by images randomly selected from publicly available image datasets, EMNIST and CIFAR-100 [176,177]. Specifically, EMNIST images were enlarged by maximum filters with random widths from 3 to 7 pixels and were modified by affine transforms with random angles from  $0^\circ$  to  $90^\circ$  and random scales from 0.8 to 1.5. Then, the images were cropped into  $64 \times 64$  squares, giving oversampling ratios approximately from 10 to 20 along each dimension for  $512 \times 512$  windows. CIFAR-100 images were cropped into rectangles covering random scales from 0.08 to 1 with random aspect ratios from 0.75 to 1.33, and they were resized into  $64 \times 64$  squares to match their size with EMNIST images. Then, the image pairs were combined to generate final pseudorandom objects. These objects maximally excluded any physical or human biases, leading to a general applicability of DPR.

The diffraction model took account of limited photon counts and transverse coherence,

reflecting factors of single-pulse measurements using XFELs. Note that the model assumed a typical CDI scheme that impose nonnegative real-valued objects, which is legitimate in X-ray diffractions of specimens with weak scattering and negligible absorption, and an influence of longitudinal coherence is naturally ignored [25,136]. Starting from basic diffraction patterns obtained by the Fourier transform of the objects, the transverse coherence was applied based on the Gaussian Schell model using Eq. (1.82) with random transverse coherence lengths from 180 to 220 pixels [31]. Then, the patterns were scaled to have total diffraction intensities randomly from  $10^6$  to  $10^7$  and mixed Poisson–Gaussian noises were added like as Eq. (7.1) with  $\sigma = 1/2.35482$ , which gave FWHM of 1 for the Gaussian distribution. Final diffraction patterns were occluded by random masks consisted of irregular masks and center masks. The irregular masks were from NVIDIA Irregular Mask Dataset and their occlusion ratios were limited up to 50% [175]. The center masks were generated with random radii from 8 to 32 pixels and positional deviations from -8 to 8 pixels along each dimension. Total 96,000 data were generated for training, 12,000 for validation, and 12,000 for test of the network. Note that multiple scattering was ignored by satisfying Eq. (1.53) [24]. If multiple scattering was not negligible, such effect should be considered using appropriate methods such as the multislice method [26].

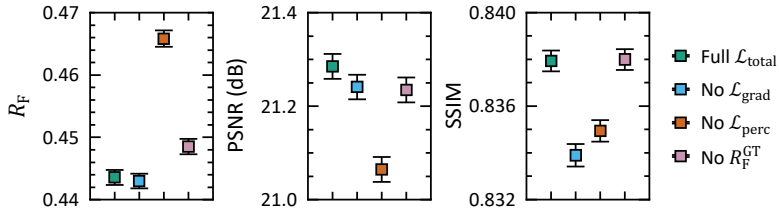


**Figure 8.2** · Ablation studies on loss function components.  $R$ -factor, PSNR, and SSIM are given in order.

A composite loss function was used for the training of the network. It was comprised by MAE and perceptual loss described in Eq. (7.2) with gradient loss and ground-truth  $R$ -factor defined as follows.

$$\mathcal{L}_{\text{grad}}(u, v) = \frac{\sum_{v_i \neq 0} \|\nabla u_i - \nabla v_i\|_1}{\sum_{v_i \neq 0} 1}, \quad R_F^{\text{GT}}(u, v) = \frac{\sum_i |\mathcal{F}u|_i - |\mathcal{F}v|_i}{\sum_i |\mathcal{F}v|_i} \quad (8.3)$$

Then, after an ablation study on each loss function component, the final loss function was defined as follows.

$$\mathcal{L}_{\text{total}} = \mathcal{L} + 10\mathcal{L}_{\text{grad}} + 0.1\mathcal{L}_{\text{perc}} + 0.01R_F^{\text{GT}} \quad (8.4)$$

Here, the perceptual loss used outputs of 4th and 5th blocks of ImageNet-pretrained VGG-19 [178]. Outputs of the network were scaled based on the input diffraction patterns, and they assigned additional weights for a calculation of the loss function to linearly reduce influences of weak or largely masked data during training procedures. These operations were defined as follows.

$$u_{\text{out}} = \sqrt{\frac{\sum_{M_i \neq 0} I_i}{\sum_{M_i \neq 0} |\mathcal{F}u|_i^2}} u, \quad u_{\text{loss}} = \sqrt{\frac{\sum_{M_i \neq 0} I_i}{\sum_{M_i \neq 0} |\mathcal{F}u|_i^2}} u_{\text{out}} \quad (8.5)$$

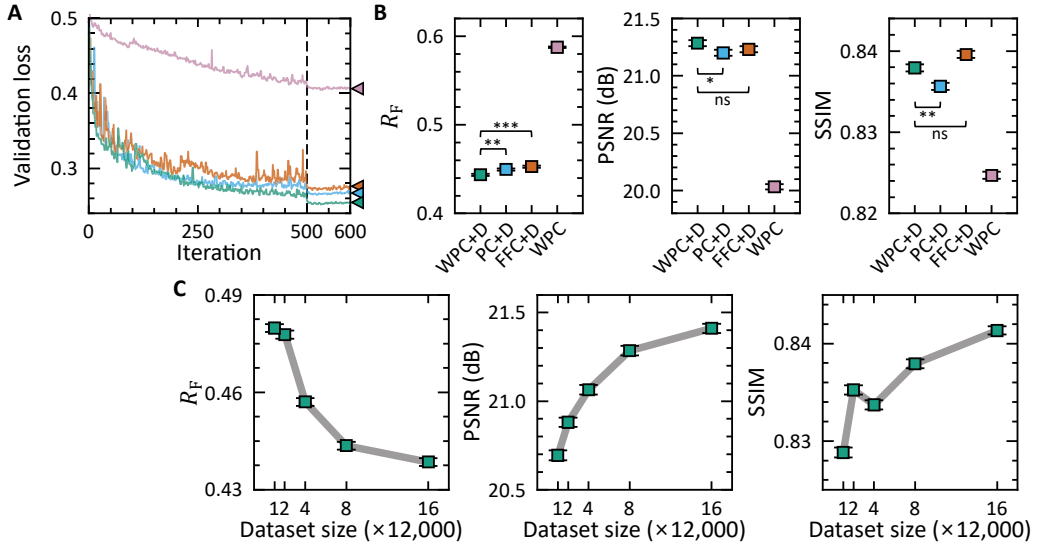


**Figure 8.3** · Training results of DPR with different conditions. (A, B) Evolution of validations loss (A) and evaluation metrics (B) are presented to verify the architecture of DPR. Cases of DPR (WPC+D), encoder based on PC (PC+D), encoder based on FFC (FFC+D), and without the diffraction-compensated decoder (WPC) are given for a comparison. Differences with DPR are verified by the Mann-Whitney U test (not indicated,  $p \leq 10^{-8}$ ;  $***10^{-8} < p \leq 0.001$ ;  $**0.001 < p \leq 0.01$ ; ns,  $p > 0.05$ ). (C) Changes of evaluation metrics with different sizes of training datasets.  $R$ -factor, PSNR, and SSIM are given as the evaluation metrics in order. Adapted from Ref. [15], Springer Nature Limited.

Using the generated dataset and loss function, the network was trained by the AdamW

optimizer with a weight decay of 0.0001, iterating over 500 epochs with a learning rate of 0.001 followed by 100 epochs with a learning rate of 0.0001 [180]. All training procedures were accomplished using twelve GeForce RTX 3090 GPUs (NVIDIA Corp.). After training the network, the architecture of DPR was verified by comparing with different architectures including DPR with a PC-based decoder, DPR with an FFC-based encoder, and DPR with a single-stage decoder without diffraction-compensated decoder. Evaluation metrics were *R*-factor, PSNR, and SSIM, and Mann–Whitney U test was performed on each metric to identify statical differences. As a result, the WPC-based encoder outperformed the other encoders with the lowest *R*-factor, while maintaining or surpassing PSNR and SSIM. In addition, even though the single-stage decoder had much more trainable parameters by doubling the residual blocks instead of the diffraction-compensated decoder, the two-stage decoder showed significantly better performance with 43% fewer trainable parameters. Thus, the architecture of DPR was demonstrated to have superior performance on effective and efficient handling of imperfect, photon-limited diffraction patterns.

An influence of the size of the training dataset was also identified by doubling the size of the dataset from 12,000 to 192,000 for the training procedure. Unsurprisingly, increasing the size led to enhance the performance, but the performance improvements were quickly saturated. This confirmed an adequacy of the size of the training dataset, but the saturation might imply a limitation of the used dataset generation policy. In this regard, the AdamWR optimizer with adaptive sharpness-aware minimization (ASAM) was employed in the training procedure to improve performance and general applicability of DPR, instead of the plain AdamW optimizer [180,206]. The AdamWR optimizer is equal to the AdamW optimizer but updating the learning rate by cosine annealing with warm restarts. The learning rates were limited between  $10^{-8}$  and 0.005, respectively, and the period of the cosine annealing was doubled at the end of the period starting with an initial period of 40. ASAM is a two-step optimization strategy to seek flat minima in optimization that mostly lead to lower generalization loss. Parameters of ASAM were set as  $\rho = 0.2$  and  $\eta = 0.01$ . Both methods were demonstrated to improve generalization performance.

### 8.3. Deep phase retrieval on simulated diffraction patterns

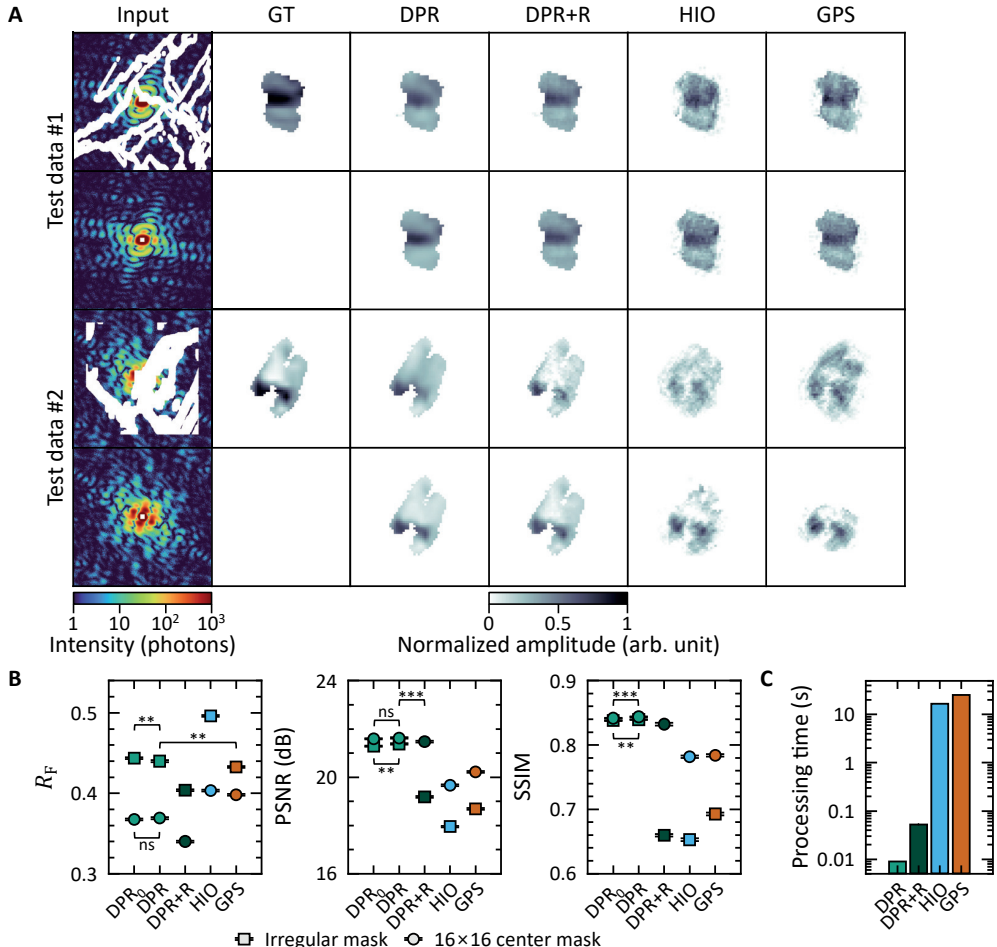


**Figure 8.4** Phase retrieval of the simulated diffraction patterns by DPR. (A, B) Examples (A) and evaluation metrics (B) of reconstructed images from the diffraction patterns with irregular masks or a  $16 \times 16$  center mask are presented to compare DPR trained by the AdamWR optimizer with ASAM with DPR trained by the AdamW optimizer ( $DPR_0$ ), DPR with the refinement (DPR+R), HIO, and GPS.  $R$ -factor, PSNR, and SSIM are given as the evaluation metrics in order. Differences with DPR are verified by the Mann-Whitney U test (not indicated,  $p \leq 10^{-8}$ ; \*\*\* $10^{-8} < p \leq 0.001$ ; \*\* $0.001 < p \leq 0.01$ ; ns,  $p > 0.05$ ). (C) Processing time is provided for each phase retrieval method. Adapted from Ref. [15], Springer Nature Limited.

Using the trained DPR, comparisons with conventional phase retrieval algorithms, HIO and GPS, were conducted to validate its excellence [4,63]. DPR trained by the AdamW optimizer and DPR with a refinement was also compared to check improvements from using the

AdamWR optimizer with ASAM. An execution of each conventional algorithm was accomplished as follows: for the case of HIO, 900 iterations of HIO were conducted with  $\beta = 0.9$  followed by 100 iterations of ER; for the case of GPS, 1000 iterations of GPS-R were conducted with  $t = 1$ ,  $s = 0.9$ ,  $\sigma$  increasing from 0.01 to 1 by a factor of 10 after 400 and 700 iterations, and  $\gamma = 1/2\alpha^2$  with  $\alpha$  decreasing from 1024 by 10% after every 100 iterations. Both algorithms started with 100 initial random phases and the shrink-wrap algorithm was employed to update real-space supports with  $\sigma$  decreasing from 3 pixels by 1% and a threshold of 20% of the maximum value after every 50 iterations [51]. Here, initial real-space supports were given as  $60 \times 60$  squares. Then, final images were obtained from averages of best 5 images based on *R*-factors. Meanwhile, the refinement for DPR was simply performed by 50 iterations of GPS-R with  $t = 1$ ,  $s = 0.9$ ,  $\sigma$  increasing from 0.1 to 1 after 20 iterations, and  $\gamma = 1/2\alpha^2$  with  $\alpha$  decreasing from 1024 by 20% after every 10 iterations. Here, real-space supports were fixed by thresholding the output of DPR at 1% of the 99th percentile value.

As expected, DPR gained a slight improvement on its performance when using the AdamWR optimizer with ASAM compared to that trained by the AdamW optimizer, especially for the case with irregular masks; therefore, the use of the AdamWR optimizer with ASAM was confirmed. Compared with HIO and GPS, DPR significantly outperformed with higher PSNR and SSIM. In addition, DPR showed only small difference on PSNR and SSIM for both cases with irregular masks and a  $16 \times 16$  center mask, indicating its robustness on masking shape and area. Despite its superior performance, it showed higher *R*-factors than GPS for the case with irregular masks. However, considering that *R*-factor was the measure based on the measured diffraction patterns that were buried by strong noises, significantly higher PSNR and SSIM from using DPR implied that it offered accurate reconstructions regardless of the noises in given diffraction signals. Otherwise, the conventional algorithms were directly projecting onto the measured data, naturally providing lower *R*-factors, but influences of the noises could not be sufficiently avoided. Even in this circumstance, DPR provided lower *R*-factors for the case with the center mask. When the refinement was additionally employed to DPR, *R*-factors became lower, even lower than the case of GPS, but with a sacrifice of PSNR and SSIM. Thus, if it was required to maximally minimize *R*-factors for certain situations, DPR with the refinement would offer the best results; otherwise, DPR would provide better real-space images.

DPR also offered dramatically reduced processing times compared to the conventional algorithms with a help of its efficient architecture. Its processing times were  $9.02 \pm 0.00215$  ms and  $52.2 \pm 2.45$  ms per a single diffraction pattern without and with the refinement, respectively, using one GeForce RTX 3090 GPU. This value was more than 1,000 times faster than phase retrieval using conventional algorithms, and 100 times faster even with refinement. Moreover, considering that the conventional algorithms demand to search rather tight real-space supports for successful reconstructions, DPR realized immediate reconstructions by eliminating such meticulous human inspections, thereby facilitating real-time phase retrievals in substance. The only thing required by DPR was properly feeding the measured diffraction data together with corresponding masks after unit conversion from analog-to-digital unit (ADU) to photon count, and these were typical predefined by the detector. Experiments using XFELs bring enormous amounts of data, and this becomes severe for MHz-repetition-rate XFELs, which have recently been developed for further scientific studies [207]. In this circumstance, a rapid processing of diffraction data is mandatory to afford such massive data, and DPR can be a very solution.

#### 8.4. Deep phase retrieval on experimental data

After the successful demonstration of DPR on the test dataset, applicability of DPR on experimental data was evaluated. For this purpose, actual imaging experiments were performed at the NCI beamline of PAL-XFEL in PAL [181]. Femtosecond X-ray pulses were generated by the SASE process tuned at a photon energy of 5 keV with an energy bandwidth of  $\Delta E/E \approx 5 \times 10^{-3}$ . Generated beams were focused into  $5 \mu\text{m}$  (horizontal)  $\times$   $7 \mu\text{m}$  (vertical) by a pair of Kirkpatrick–Baez mirrors located at 5 m upstream from the sample, giving a total flux of  $8 \times 10^9 \text{ photons} \cdot \mu\text{m}^{-2}$  for a single pulse [107]. Single-pulse diffraction patterns were measured by a 1-megapixel MPCCD, of which the size of each pixel is  $50 \times 50 \mu\text{m}^2$ , at 1.6 m downstream from a sample position [182]. This gave a pixel resolution of 15.5 nm for a  $512 \times 512$  window.

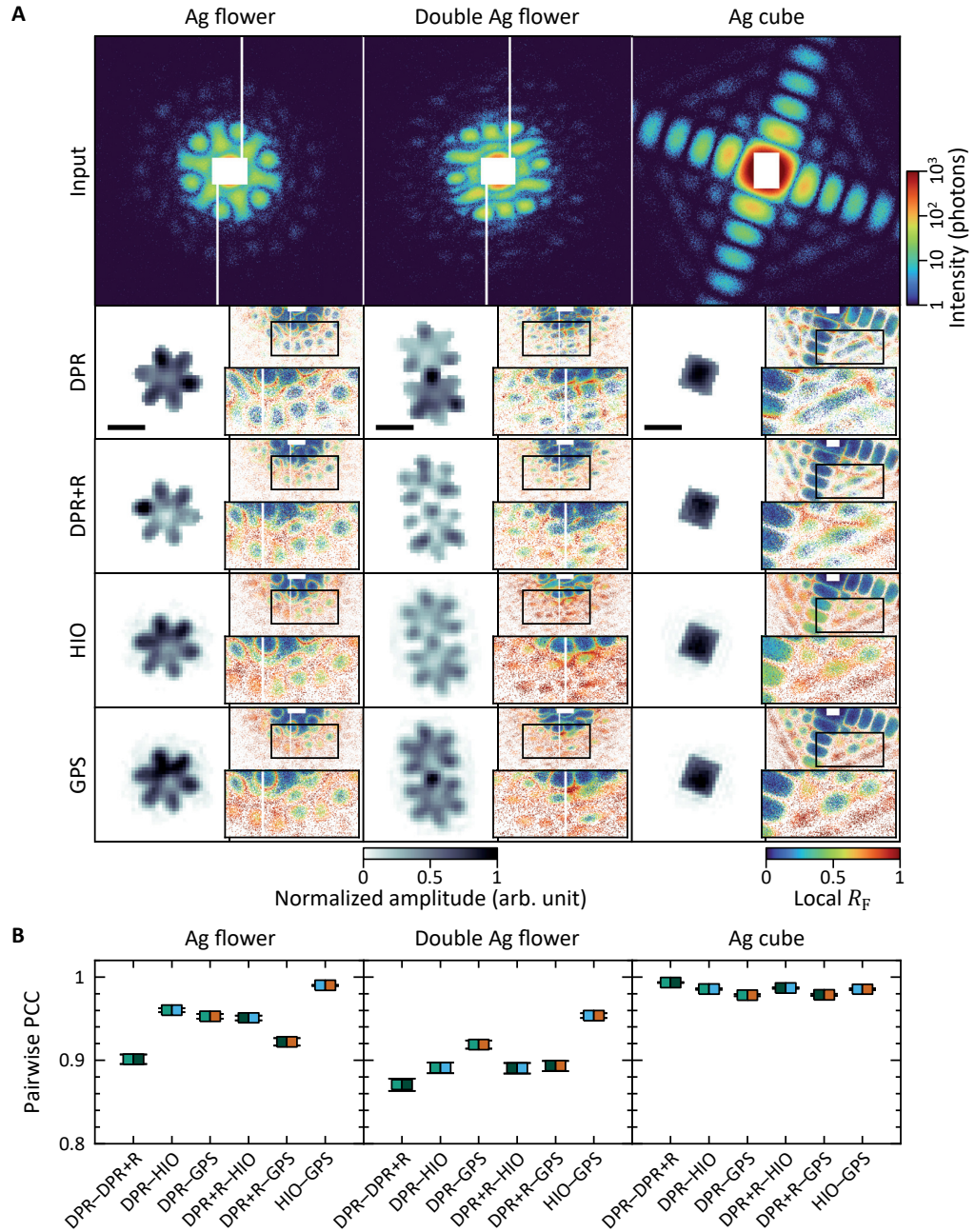


**Figure 8.5** Phase retrieval of single-pulse diffraction patterns from actual experiments at PAL-XFEL by DPR. (A) Diffraction patterns and reconstructed images are presented with local  $R$ -factors. Results from using DPR with the refinement (DPR+R) and conventional algorithms, HIO and GPS, are also presented for a comparison. (B) PCCs for all real-space image pairs are given for a reference. Adapted from Ref. [15], Springer Nature Limited.

For single-particle imaging, specimens were chosen as Ag nanoparticles having specific shapes of flower and cube with approximate widths of 250 nm and 150 nm, respectively, and they were spread on 100-nm-thick  $\text{Si}_3\text{N}_4$  membranes. The membranes with samples were mounted in an imaging chamber, and the chamber and beam paths were kept under vacuum. After single-pulse diffraction measurements, background signals were subtracted from measured diffraction patterns, and the unit of measured values was converted from ADU to photon count based on their distribution. Then, missing parts of the patterns were filled by values at centrosymmetric points based on the Friedel's law. Phase retrieval was conducted like as the case with the test dataset except for initial real-space supports that were given by  $30 \times 30$  squares for the conventional algorithms. As ground-truth real-space images cannot be given for the experimental data, the Pearson correlation coefficient (PCC) and local  $R$ -factor were employed instead of PSNR and SSIM. PCC, which is defined as  $\text{PCC}(u, v) = \sigma_{uv}/\sigma_u\sigma_v$ , represents a linear correlation between two images, and the local  $R$ -factor is an element-wise  $R$ -factor calculated for every data point with a photon count over 0.5, indicating regional Fourier-space conformities with measured diffraction patterns. Both metrics gave additional information related to real-space images.

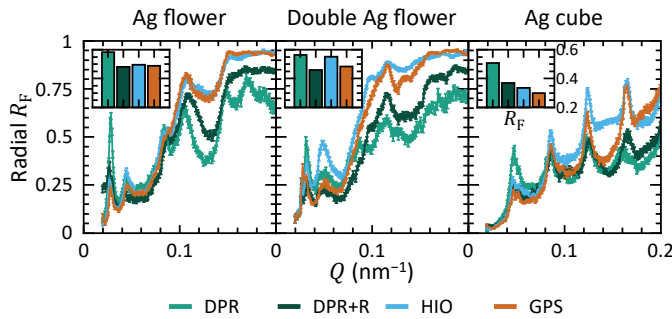


**Figure 8.6** Radial distributions of local  $R$ -factors from reconstructions of experimental data measured at PAL-XFEL. Results from using DPR, DPR with the refinement (DPR+R) and conventional algorithms, HIO and GPS, are presented.

Using the as-trained DPR without any fine-tuning procedures, DPR succeeded to directly reconstruct real-space images from the experimental data. The results showed strong positive linear correlations with results from using the conventional algorithms. Their shapes were considerably analogous with other results, while their internal densities slightly varied

upon the reconstruction methods. Considering that the internal density distributions were related to high- $Q$  signals in the Fourier space, the local  $R$ -factor could be used to verify their appropriateness, and DPR provided high-contrast images with significantly lower local  $R$ -factors at major speckle patterns away from a diffraction center compared to the conventional algorithms, representing its remarkable accuracy on such high frequency components. While the conventional algorithms were strongly influenced by dominant low- $Q$  signals near the diffraction center, DPR was not biased to such signals, properly reconstructing based on overall diffraction signals. In addition, DPR with the refinement provided real-space images that more followed the low- $Q$  signals than without the refinement, offering more balanced results.

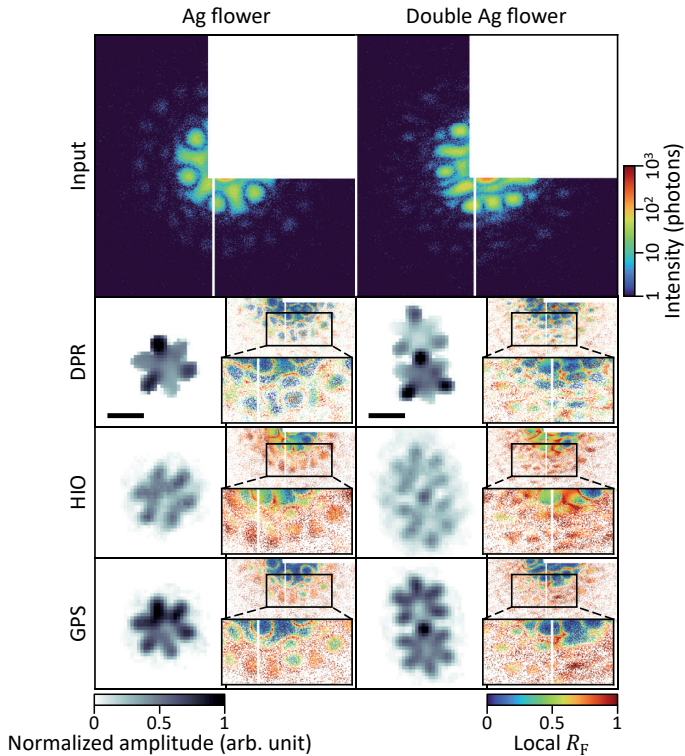


**Figure 8.7** · Phase retrieval of experimental data measured at PAL-XFEL by DPR without centrosymmetric filling. Results from using DPR with the refinement (DPR+R) and conventional algorithms, HIO and GPS, are also presented for a comparison.

DPR also offered stable phase retrievals regardless of occlusion areas. Thus, the robustness of DPR on strong noises and partial data loss from single-pulse diffraction measurements truly realized real-time phase retrievals for CDI experiments, handling massive

data acquisition of XFELS by minimizing both data processing and human inspections.

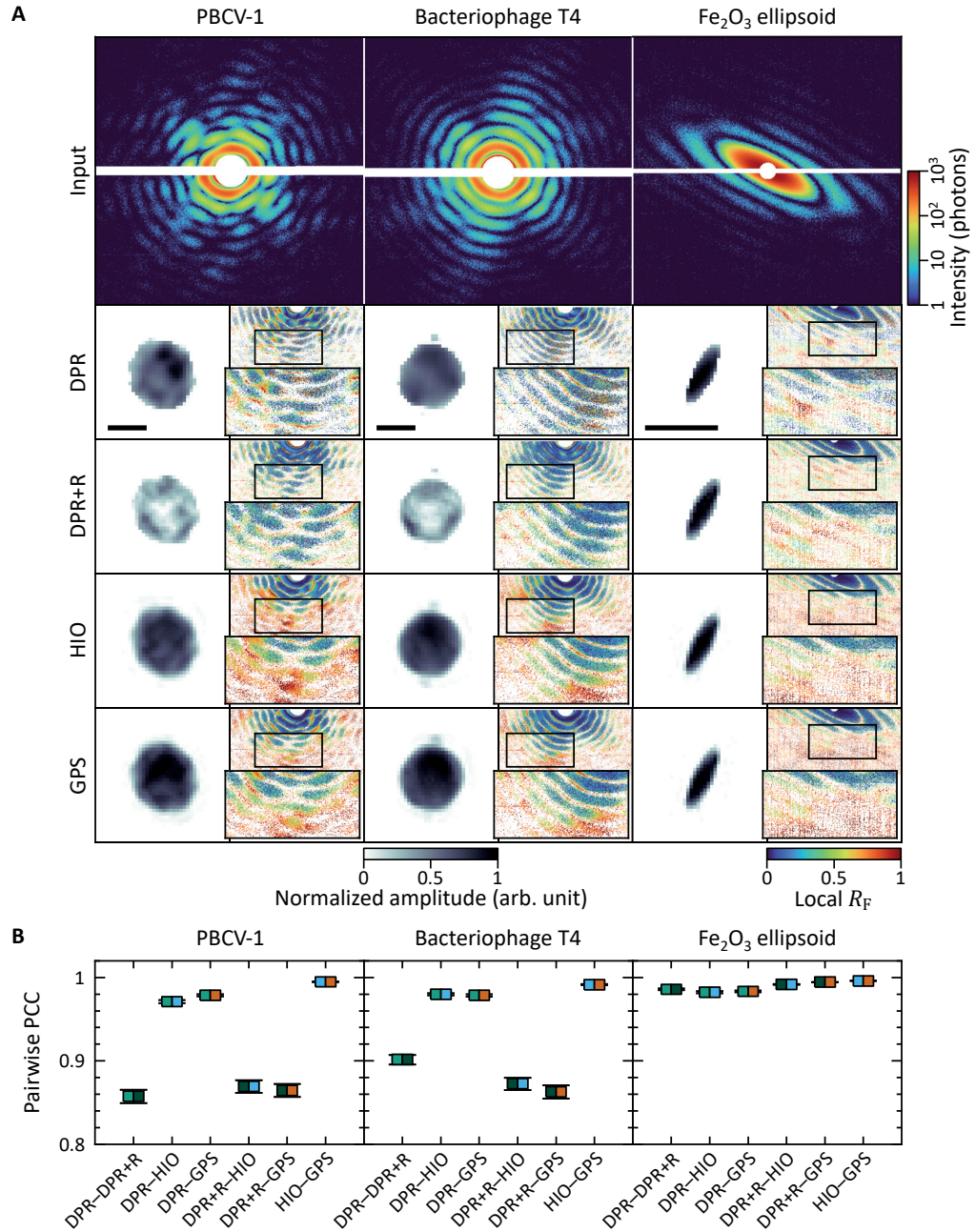


**Figure 8.8** Phase retrieval of single-pulse diffraction patterns from CXIDB by DPR. (A) Diffraction patterns and reconstructed images are presented with local  $R$ -factors. Results from using DPR with the refinement (DPR+R) and conventional algorithms, HIO and GPS, are also presented for a comparison. (B) PCCs for all real-space image pairs are given for a

reference. Adapted from Ref. [15], Springer Nature Limited.

As the data measured at PAL-XFEL only included diffraction patterns of Ag nanoparticles with identical experimental parameters, additional evaluation of DPR was performed with data from a public database, Coherent X-ray Imaging Data Bank (CXIDB), to verify its general applicability [208]. Among data deposited in CXIDB, three diffraction patterns of chlorovirus PBCV-1, bacteriophage T4, and  $\text{Fe}_2\text{O}_3$  ellipsoid nanoparticle in datasets from ID 10 to ID 14 were selected [209]. These data were obtained from X-ray pulses with a photon energy of 1.2 keV and were measured by 1-megapixel pnCCD, of which the size of each pixel is  $75 \times 75 \mu\text{m}^2$ , positioned at 0.738 m downstream from the sample [210]. This gave a pixel resolution of 19.9 nm for a  $512 \times 512$  window and 9.93 nm after  $2 \times 2$  binning. Note that the binning was conducted on the diffraction pattern of  $\text{Fe}_2\text{O}_3$  ellipsoid nanoparticle due to its small size.

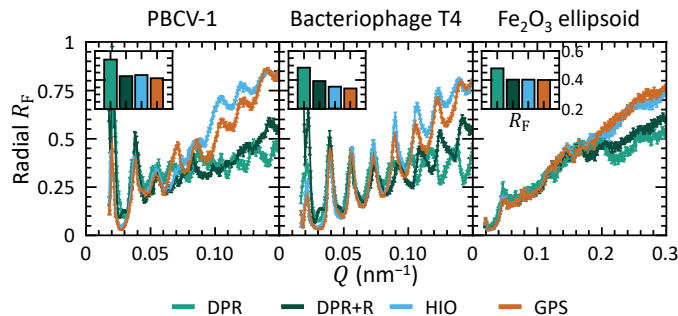


**Figure 8.9** · Radial distributions of local  $R$ -factors from reconstructions of experimental data from CXIDB. Results from using DPR, DPR with the refinement (DPR+R) and conventional algorithms, HIO and GPS, are presented.

Despite completely different sample types and experimental conditions, DPR showed consistent performance with the data from CXIDB like as with the data measured at PAL-XFEL. Resultant images from using DPR showed distinct shapes that had strong positive correlation, and their internal densities were clearer with well-matched high- $Q$  amplitudes in the Fourier space compared to those from the conventional algorithms. Thus, DPR was successfully verified its general applicability on various data from single-particle imaging experiments using XFELs.

## 8.5. Conclusion

With a help of dedicated architecture and training strategy, DPR was demonstrated to offer a generalized superior performance on phase retrievals of various imperfect, photon-limited diffraction patterns that typically obtained by single-pulse diffraction measurements with XFELs. It outperformed conventional algorithms regardless of strong noises and partial data loss, providing high-contrast real-space images with distinct shapes. While the conventional algorithms required tight real-space supports to be given for successful reconstructions, DPR eliminated such human-involved tasks, thereby enabling fully automatic real-time reconstructions. It also had potentials to cover extreme noise levels, complex-valued objects, and multiple scattering effects by modifying the model.

Leveraging the Guinier–Porod model to guide lost Fourier-space information, excellence of WPC emphasized an importance of appropriate processing of data that concerntheir characteristics. Although the WPC-based encoder occupied only 10% of total trainable parameters in DPR, it showed meaningful improvements in phase retrievals. Thus, a concept of WPC could be applied to various data, such as X-ray absorption or emission, by modifying convolution operations based on appropriate physical models to improve performance of CNNs when dealing with incomplete data. Thus, DPR can be a robust platform to handle various kinds of diffraction signals with high tolerance on noises and partial occlusions. Moreover, handling huge amounts of data has been demanding with the development of high-repetition-rate XFELs, thereby the importance of fast data processing becomes critical. In this circumstance, DPR is expected to play an important role in X-ray science with its accessibility.

\* Source codes and trained parameters of DPR are available at  
<https://github.com/sungyun98/DPR>.

## V. Summary

This thesis includes theoretical backgrounds and introductions of developed experimental techniques and DL models to improve conventional diffraction imaging methods. Since development and demonstration of CDI with phase retrieval algorithms, CDI has facilitated noninvasive imaging of various specimens in nanoscale resolutions using coherent X-rays. However, there are some restrictions mainly by experimental constraints, and overcoming such limitations require deep understanding of diffraction and phase problem.

Starting from a brief introduction on the electromagnetic wave equation, scattering of photons, quanta of electromagnetic radiation fields, was described to comprehend the light-matter interactions in the manner of the quantum mechanics, followed by the Lippmann–Schwinger equation with the first-order Born approximation that consequently corresponds to the case of typical X-ray diffraction imaging schemes. Additionally, the Fresnel–Kirchoff diffraction formula was explained to understand diffraction phenomena in the optical point of view. After giving overall remarks on diffraction of electromagnetic waves, the convenient geometric configurations for elastic scattering, the Ewald sphere, was introduced with the Bragg’s law, giving further insights into 3D reciprocal-space mapping. Then, as the coherence is an important keyword for diffraction imaging, being directly related to its resolution, derivations of its quantitative expressions, longitudinal and transverse coherence lengths, were given. Lastly, two diffraction imaging methods, CDI and ptychography, were briefly introduced with advantages and disadvantages of each method.

Another key component of CDI is phase retrievals, which are computational procedures to recover the lost phase information of measured diffraction intensities. With a help of numerical algorithms instead of image-forming optics, CDI is not constrained by a resolving power of such optical components, giving diffraction-limited performance in principle. In this regard, overall reviews on representative iterative phase retrieval algorithms were provided with metrics for estimating effective resolutions of reconstructed real-space images. Moreover, the Lagrange dual formulation of the phase problem and related primal-dual algorithms were also introduced, followed by the foundation of GPS, giving better understanding of the phase problem and convex optimization.

This thesis also dealt with the theory of vortex beams. Due to their unique wavefront structures and inherent OAMs, vortex beams have been spotlighted for various research fields. They have been reported to improve the resolution of diffraction imaging methods such as ptychography, and selective transitions by means of controlling total angular momenta. Especially, helical dichroism, which is a dichroism for topological charges of the vortex beams, has recently demonstrated to have a sensitivity on various chiral systems. Thus, light–matter interaction with vortex beams and corresponding helical dichroism were theoretically described. A basic principle of SZPs was also given as a representative of the X-ray optics for the generation of vortex beams.

Based on these background knowledges, experimental techniques to enhance performance and functionality of diffraction imaging methods were introduced. The first method is multidistance CDI. When investigating large samples, a finite size of a detector limits an image resolution as sufficiently long SDD is required for a reciprocal-space sampling small enough to capture the zeroth speckle signals, of which the sizes are inversely proportional to the sizes of the samples. These signals reflect overall shapes of the samples, thereby play an important role in phase retrieval. In this circumstance, the multidistance CDI employed measurements of diffraction patterns at multiple distances, separately obtaining low- and high-resolution information from long- and short-SDD measurements, respectively. Adaptive phase retrieval algorithm was also developed for phase retrieval of multiple diffraction patterns with different reciprocal-space samplings. Using this method, 3D tomography of a mesoporous nanoparticle was successfully conducted, giving effective resolutions of 8.7 nm in 2D and 13.3 nm in 3D. Considering that total exposure times were limited to minimize deformation of the sample by radiations, these values were in the highest level compared to the state-of-art results using X-rays, and roughly four times better than those from previous nondestructive imaging of porous materials. Thus, the multidistance CDI enables high-resolution imaging of the large samples without sacrificing the resolutions, while taking all advantages of CDI.

Other methods are off-axis vortex beam ptychography and helical dichroism on ferroelectric topological defects, and they both employed the vortex beams. The off-axis vortex beam ptychography were demonstrated to enhance edge responses in amplitude of

reconstructed objects by three times and improve accuracy in their phase by 1 percentage point from numerical experiments with weakly scattering objects. These effects came from the unique wavefront structures of the vortex beams. In addition, as a linear phase ramp from the off-axis geometry makes phase retrieval difficult, correction of a diffraction center was suggested and verified its utility. In actual experiments, edge contrasts exhibited directionality, showing inversion of the contrast in a case of an opposite off-axis direction, while acquiring accurate phase of the sample. Thus, the off-axis vortex beam ptychography offers edge-enhanced, phase-sensitive imaging of weakly scattering samples.

Meanwhile, the topological defects have attracted research interests due to their characteristic morphologies and potentials on inducing hidden properties of materials. In this regard, helical dichroism that has been reported to have remarkable sensitivities to chiral structures would be a promising tool to identify their structural information. Thus, helical dichroism on the ferroelectric topological defects was investigated with an epitaxial thin film of BiFeO<sub>3</sub>, which exhibited well-defined stripe ferroelectric domains along its pseudocubic [0 1 0]-direction. As a result, an existence of helical dichroism from the ferroelectric structures were experimentally demonstrated with differences by the sample orientations. Directional information on orbital configurations was also obtained by extracting linear dichroism from the measured data. Although further analyses are required to interpret the results, the physical model was also suggested for single-crystal ferroelectric materials with arbitrary orientations. Thus, these findings help guiding potential applications on functional imaging of ferroelectric materials, and especially, a combination of helical dichroism with Bragg ptychography, which can identify atomic displacement fields, is expected to facilitate investigation of OAM-sensitive structures with an exceptional sensitivity in a nanoscale resolution as a potential application.

Furthermore, DL models were also developed to deal with noisy, imperfect diffraction patterns from single-pulse measurements using XFELs. Since developments of XFELs, time-resolved studies have been realized in the X-ray regime. However, intense, but limited intensities of X-ray pulses lead to strong noise and partial occlusion by a use of beam stops. In addition, diffraction signals drastically decrease with increasing momentum transfer magnitudes, and these characteristics make diffraction data difficult to be handled. In this

circumstance, DL models for denoising and real-time phase retrieval were proposed, and their performances were validated for both simulated and experimental data. DNN architectures of the models were based on CNNs in encoder–decoder structures with several new operations; the network for denoising employed skipped connections between all layers of encoder and decoder and with an interlayer of pointwise convolution on the centrosymmetric points, and the network for real-time phase retrieval employed WPC-based encoder and two-stage decoder with FFC-based residual blocks and intermediate Fourier modulation. Both models adopted to use pseudorandom objects from a combination of preexisting datasets to generate noise-buried, partially damaged diffraction patterns, maximally excluding physical biases for general applicability. A major difference between two models dealing with diffraction patterns was that the denoising model log-scaled the input data, while the real-time phase retrieval model introduced WPCs for encoding layers, assigning positional weights based on the Guinier–Porod model. After appropriate training procedures, both models showed significant improvements compared to the conventional methods; the denoising model was verified to enhance the conventional phase retrieval algorithm by applying denoised diffraction patterns as Fourier-space constraints or preconditioners, and the real-time phase retrieval model was demonstrated to realize 1,000 times faster phase retrieval while providing much better results compared to the conventional algorithms. Considering overflowing massive datasets from experiments using XFELs, these DL models will serve as a solid platform for a rapid data processing of diffraction data.

In conclusion, this thesis contributes to the development of functional nanoimaging using coherent X-rays, focusing on experimental techniques and DL methods for a reinforcement of CDI and ptychography. Diffraction imaging has been a great tool for an investigation of nanoscale structures inside various samples, but recently, it has been requested to enhance performance and functionality due to rising of emerging materials with complicated properties to be analyzed. In this situation, the contents of this thesis will assist future research applications that uses diffraction imaging methods.

## Summary in Korean

본 학위논문은 기존의 회절 이미징 기법을 향상하기 위해 개발한 실험적 기법과 DL 모델의 이론적 배경과 소개를 담고 있습니다. 위상 복원 알고리즘을 포함한 CDI 의 개발과 검증 이후, CDI 는 결맞는 엑스선을 활용하여 나노 수준의 해상도로 다양한 시료의 비파괴적 이미징을 가능하게 하였습니다. 하지만 주로 실험적 제약조건으로 인한 몇 가지 제한이 있었고, 이러한 한계를 극복하기 위해서는 회절과 위상 문제에 대한 깊은 이해도가 필요합니다.

전자기 파동 방정식에 대한 간략한 소개를 시작으로, 양자역학적 관점에서 빛-물질 상호작용을 이해하기 위해 전자기 복사장의 양자인 광자의 산란을 설명하고, 결과적으로 일반적인 엑스선 회절 이미징 방식에 대응하는 1 차 본 근사법을 적용한 리프먼-슈윙거 방정식에 관해 설명했습니다. 또한, 광학적 관점에서 회절 현상을 이해하기 위해 프레넬-키르히호프 회절 공식에 관해서도 설명했습니다. 전자기파의 회절에 대한 전반적인 설명 이후, 탄성 산란을 설명하기 위한 편리한 기하학적 구조인 에발트 구를 브래그 법칙과 함께 소개하여 3 차원 역격자공간 매핑에 대한 추가적인 통찰을 제공했습니다. 그다음으로는 회절 이미징의 해상도에 직접적으로 관련된, 회절 이미징에서의 중요한 키워드인 결맞음의 양적 표현으로서 종방향 및 횡방향 결맞음 길이도 제공되었습니다. 마지막으로, CDI 와 타이코그래피의 두 가지 회절 이미징 기법에 대해 각각의 장단점을 간략하게 소개했습니다.

CDI 의 또 다른 핵심 구성요소는, 측정된 회절 강도로부터 손실된 위상 정보를 복원하는 계산적 과정인 위상 복원입니다. CDI 는 이미지를 형성하는 광학 장치 대신 수치 알고리즘을 사용하여 광학 장치에 의해 분해능에 제약을 받지 않기 때문에 회절 한계 성능을 원론적으로 제공합니다. 이와 관련하여 대표적인 반복 위상 복원 알고리즘에 대한 전반적인 검토와 함께 재구성된 실공간 이미지의 유효 해상도를 추정하기 위한 지표를 제공했습니다. 또한, 위상 문제의 라그랑주 쌍대화와 이와 관련된 원시-쌍대 알고리즘도 GPS 의 기초와 함께 소개되어 위상 문제와 볼록 최적화에 대한 이해를 높였습니다.

본 학위논문은 소용돌이 빔의 이론도 다루었습니다. 소용돌이 빔은 독특한 파면 구조와 내재된 OAM 으로 인해 다양한 연구 분야에서 주목받고 있습니다. 이러한 빔은 타이코그래피와 같은 회절 이미징 기법의 해상도를 향상하고, 총 각운동량을 제어하여 선택적 전이를 구현하는 것으로 보고되었습니다. 특히, 소용돌이 빔의 위상 전하에 대한 이색성이 나선형 이색성은 최근 다양한 카이랄 시스템에 대한 감도가 있음이 입증되었습니다. 따라서 소용돌이 빔에 대한 빛-물질 상호작용과 그에 따른 나선형 이색성을 이론적으로 설명하였습니다. 또한, 소용돌이 빔 생성을 위한 대표적인 엑스선 광학 장치로써 SZP 의 기본 원리에 대해서도 제공되었습니다.

이러한 배경지식을 바탕으로 회절 이미징 방법의 성능과 기능을 향상하기 위한 실험 기법을 소개했습니다. 첫 번째 방법은 다중거리 CDI 입니다. 큰 시료에 대해서 조사할 때,

검출기의 한정된 크기는, 시료의 크기에 반비례하는 크기의 0 차 스펙클 신호를 수집할 수 있을 정도로 작은 역격자공간 샘플링을 위해 충분히 긴 SDD 가 필요하므로, 이미지의 해상도가 제한됩니다. 이러한 신호는 시료의 전체적인 형태를 반영하기 때문에 위상 복원에서 중요한 역할을 합니다. 이러한 상황에서 다중거리 CDI 는 여러 거리에서 회절 패턴을 측정하여 길고 짧은 SDD 의 측정에서 각각 저해상도 및 고해상도 정보를 개별적으로 수집했습니다. 또한, 서로 다른 역격자공간 샘플링의 회절 패턴에 대한 위상 복원을 위해 적응형 위상 복원 알고리즘도 개발했습니다. 이 방법을 사용하여 메조다공성 나노 입자의 3 차원 단층 이미징을 성공적으로 수행하였고, 2 차원에서 8.7 nm, 3 차원에서 13.3nm 의 유효 해상도를 제공했습니다. 방사선에 의한 시료의 변형을 최소화하기 위해 총 노출 시간을 제한했다는 점을 고려하면, 이 수치는 엑스선을 이용한 최신 결과와 비교했을 때 최고 수준이며, 기존 다공성 물질에 대한 비파괴 이미징보다 약 4 배가량 향상된 결과입니다. 따라서 다중거리 CDI 는 CDI 의 모든 장점을 활용할 수 있는 동시에 큰 시료에 대해서도 해상도의 저하 없이 고해상도 이미징을 가능하게 하였습니다.

다른 방법으로는 축외 소용돌이 빔 타이코그래피와 강유전성 위상 결합에서의 나선 이색성이 있으며, 두 가지 방법 모두 소용돌이 빔을 사용했습니다. 축외 소용돌이 빔 타이코그래피는 약하게 산란하는 물체에 대하여 재구성된 물체의 진폭에서는 모서리 반응을 3 배 향상시키고, 위상에서는 정확도를 1 퍼센트포인트 향상하는 것이 수치 실험을 통해 입증되었습니다. 또한, 축외 기하학적 구조에서 온 선형 위상 경사가 위상 복원을 어렵게 만들기 때문에 회절 중심의 보정을 제안하였고, 그 유용성을 검증했습니다. 실제 실험에서는 시료의 정확한 위상 정보를 얻음과 동시에 모서리 대비에서 축외 방향을 따라 뒤집히는 방향성이 나타남을 확인했습니다. 따라서 축외 소용돌이 빔 타이코그래피는 약하게 산란하는 시료의 모서리 강화 및 위상 감지 이미징을 제공하였습니다.

한편, 위상 결합은 그 특징적인 형태와 물질의 숨겨진 특성을 유도할 수 있는 가능성으로 인해 연구자들의 관심을 끌고 있습니다. 이와 관련하여 카이랄 구조에 대한 감도가 매우 높은 것으로 보고된 나선 이색성은 위상 결합의 구조 정보를 파악할 수 있는 유망한 도구가 될 수 있을 것입니다. 따라서 강유전성 위상 결합에 대한 나선형 이색성을 유사 입방 [0 1 0] 방향을 따라 잘 정의된 줄무늬 강유전성 구역 구조를 보이는  $\text{BiFeO}_3$  에피택시 박막 시료에서 조사했습니다. 그 결과, 시료의 방향에 따라 차이를 보이는 나선 이색성이 강유전성 구조에서 나타남을 실험적으로 입증하였습니다. 또한, 측정한 데이터로부터 선형 이색성을 추출하여 오비탈 구성에 대한 방향 정보를 얻을 수 있었습니다. 결과를 해석하기 위해서는 추가적인 분석이 필요하지만, 임의의 방향에서의 단결정 강유전성 물질에 대한 물리적 모델도 제안하였습니다. 따라서 이러한 연구 결과는 강유전성 물질의 기능성 이미징에 대한 잠재적인 응용에 대해 도움을 줄 것이며, 특히 나선형 이색성과 원자 변위장을 파악할 수 있는 브래그 타이코그래피를 조합하면 OAM 에 민감한 구조를 뛰어난 감도와 함께 나노 수준의 해상도로 조사하는 것이 가능하게 될 것으로 기대됩니다.

이뿐만 아니라, XFEL 을 사용한 단일 펄스 측정에서 발생하는 잡음이 많고 불완전한 회절 패턴을 처리하기 위해 DL 모델도 개발하였습니다. XFEL 이 개발된 이후 엑스선 영역에서 시분해 연구가 가능하게 되었습니다. 그러나 강하지만 제한된 강도의 엑스선 펄스는 강한 잡음과 빔 스톱의 사용으로 인한 부분적인 가림을 야기했습니다. 또한, 회절 신호는 운동량 전달 크기가 증가함에 따라 급격히 감소하고, 이러한 특성은 회절 데이터를 다루기 힘들게 했습니다. 이러한 상황에서 잡음 제거 및 실시간 위상 복원을 위한 DL 모델을 제안하였고, 모의 데이터와 실험 데이터 모두에 대해 성능을 검증했습니다. 이 모델들의 심층 신경망 구조는 인코더-디코더 구조의 CNN 과 몇 가지 새로운 연산을 기반으로 합니다. 잡음 제거를 위한 신경망은 모든 인코더와 디코더 층에 생략 연결을 사용하였고, 이와 함께 중심 대칭점에 대한 점 단위 합성곱 중간층을 사용했습니다. 실시간 위상 복원을 위한 신경망은 WPC 기반 인코더와 FFC 기반 잔차 블록과 중간 푸리에 변조를 사용하는 2 단 디코더를 사용했습니다. 두 모델 모두 일반적인 적용 가능성을 위해 물리적 편향을 최대한 배제하면서 잡음이 섞인 부분적으로 손상된 회절 패턴을 생성하기 위해 이미 존재하는 데이터 세트를 조합한 의사 난수 물체를 사용하도록 채택하였습니다. 회절 패턴을 다루는 두 모델의 가장 큰 차이점은 잡음 제거 모델의 경우 입력 데이터를 로그 스케일링했지만, 실시간 위상 검색 모델은 기니에-포로드 모델을 기반으로 위치 가중치를 할당하는 WPC 를 인코더 층에 도입했다는 점입니다. 적절한 훈련 과정을 거친 후 두 모델은 기존 방법들에 비해 크게 향상된 성능을 보였는데, 잡음 제거 모델은 잡음이 제거된 회절 패턴을 푸리에 공간 제약조건으로 사용하거나 선조건자로써 적용하면 기존 위상 복원 알고리즘을 향상하는 것이 검증되었으며, 실시간 위상 복원 모델은 기존 알고리즘에 비해 훨씬 우수한 결과를 제공하면서 1,000 배 빠른 위상 복원을 구현함이 입증되었습니다. XFEL 을 사용한 실험에서 넘쳐흐르는 방대한 데이터 세트를 고려할 때, 이러한 DL 모델은 회절 데이터의 신속한 처리를 위한 단단한 플랫폼으로서 역할을 할 수 있을 것입니다.

끝으로, 본 학위논문은 CDI 와 타이코그래피의 강화를 위한 실험적 기법과 DL 방법론을 중심으로 결맞는 엑스선을 이용한 기능성 나노이미징의 발전에 기여합니다. 회절 이미징은 다양한 시료의 내부에 존재하는 나노 수준의 구조를 조사하는데 훌륭한 도구지만, 최근 복잡한 특성을 가진 새로운 소재들이 등장하면서 이를 분석하기 위해 성능과 기능을 강화하는 것이 요구되고 있습니다. 이러한 상황에서 본 논문의 내용은 향후 회절 이미징 기법을 사용한 연구 활용에 도움이 될 것입니다.

## References

- [1] D. Sayre and H. N. Chapman, *Acta Cryst. A* **51**, 237 (1995).
- [2] R. P. Millane, *J. Opt. Soc. Am. A* **7**, 394 (1990).
- [3] R. W. Gerchberg and W. O. Saxton, *Optik* **35**, 237 (1972).
- [4] J. R. Fienup, *Appl. Opt.* **21**, 2758 (1982).
- [5] J. Miao, P. Charalambous, J. Kirz, and D. Sayre, *Nature* **400**, 342 (1999).
- [6] J. Miao, T. Ishikawa, I. K. Robinson, and M. M. Murnane, *Science* **348**, 530 (2015).
- [7] J. Miao, *Nature* **637**, 281 (2025).
- [8] Y. Ihm *et al.*, *Nat. Commun.* **10**, 1 (2019).
- [9] C. Jung *et al.*, *Sci. Adv.* **7**, eabj8552 (2021).
- [10] J. Shin *et al.*, *Nano Lett.* **23**, 1481 (2023).
- [11] J. Hwang *et al.*, *Sci. Adv.* **10**, eadl6409 (2024).
- [12] S. Y. Lee *et al.*, *ACS Nano* **17**, 22488 (2023).
- [13] S. Y. Lee, E. Park, S. Kim, E. Jo, S. Y. Lee, J. W. Choi, and C. Song, *ACS Photonics* **11**, 3804 (2024).
- [14] S. Y. Lee, D. H. Cho, C. Jung, D. Sung, D. Nam, S. Kim, and C. Song, *Phys. Rev. Res.* **3**, 043066 (2021).
- [15] S. Y. Lee, D. H. Cho, C. Jung, D. Sung, D. Nam, S. Kim, and C. Song, *npj Comput. Mater.* **11**, 68 (2025).
- [16] R. Neutze, R. Wouts, D. van der Spoel, E. Weckert, and J. Hajdu, *Nature* **406**, 752 (2000).
- [17] H. N. Chapman *et al.*, *Nature* **470**, 73 (2011).
- [18] T. Young, *Philos. Trans. R. Soc.* **94**, 1 (1804).
- [19] L. W. Davis, *Phys. Rev. A* **19**, 1177 (1979).
- [20] A. A. Peshkov, D. Seipt, A. Surzhykov, and S. Fritzsche, *Phys. Rev. A* **96**, 023407 (2017).
- [21] J. J. Sakurai, *Advanced Quantum Mechanics* (Pearson Education, 1967).
- [22] J. J. Sakurai, *Modern Quantum Mechanics* (Addison-Wesley, 1994), Revised edn.
- [23] M. Born and E. Wolf, *Principles of Optics* (Cambridge University Press, 1999), 7th edn.
- [24] F. Natterer, *Inverse Probl.* **20**, 447 (2004).
- [25] H. N. Chapman *et al.*, *J. Opt. Soc. Am. A* **23**, 1179 (2006).
- [26] J. M. Cowley and A. F. Moodie, *Acta Cryst.* **10**, 609 (1957).
- [27] C. Jacobsen, *X-ray Microscopy* (Cambridge University Press, 2019).
- [28] E. Maire and P. J. Withers, *Int. Mater. Rev.* **59**, 1 (2014).
- [29] K. S. Raines, S. Salha, R. L. Sandberg, H. Jiang, J. A. Rodríguez, B. P. Fahimian, H. C. Kapteyn, J. Du, and J. Miao, *Nature* **463**, 214 (2010).
- [30] J. Miao, F. Förster, and O. Levi, *Phys. Rev. B* **72**, 052103 (2005).
- [31] H. Lee *et al.*, *J. Synchrotron Radiat.* **27**, 17 (2020).
- [32] V. De Andrade *et al.*, *Adv. Mater.* **33**, 2008653 (2021).
- [33] R. H. T. Bates, *Comput. Vis. Graph. Image Process.* **25**, 205 (1984).
- [34] W. Hoppe, *Acta Cryst. A* **25**, 495 (1969).
- [35] J. M. Rodenburg and R. H. T. Bates, *Philos. Trans. R. Soc. A* **339**, 521 (1992).

- [36] J. M. Rodenburg, A. C. Hurst, A. G. Cullis, B. R. Dobson, F. Pfeiffer, O. Bunk, C. David, K. Jefimovs, and I. Johnson, Phys. Rev. Lett. **98**, 034801 (2007).
- [37] P. Thibault, M. Dierolf, A. Menzel, O. Bunk, C. David, and F. Pfeiffer, Science **321**, 379 (2008).
- [38] P. Thibault, M. Dierolf, O. Bunk, A. Menzel, and F. Pfeiffer, Ultramicroscopy **109**, 338 (2009).
- [39] P. Thibault and M. Guizar-Sicairos, New J. Phys. **14**, 63004 (2012).
- [40] J. Miao, T. Ishikawa, E. H. Anderson, and K. O. Hodgson, Phys. Rev. B **67**, 174104 (2003).
- [41] T. B. Edo, D. J. Batey, A. M. Maiden, C. Rau, U. Wagner, Z. D. Pešić, T. A. Waigh, and J. M. Rodenburg, Phys. Rev. A **87**, 053850 (2013).
- [42] J. Miao, D. Sayre, and H. N. Chapman, J. Opt. Soc. Am. A **15**, 1662 (1998).
- [43] J. R. Fienup, Opt. Lett. **3**, 27 (1978).
- [44] R. H. T. Bates, Optik **61**, 247 (1982).
- [45] R. H. T. Bates, Comput. Vis. Graph. Image Process. **25**, 205 (1984).
- [46] J. R. Fienup, J. Opt. Soc. Am. A **4**, 118 (1987).
- [47] S. Marchesini, Rev. Sci. Instrum. **78**, 011301 (2007).
- [48] V. Elser, J. Opt. Soc. Am. A **20**, 40 (2003).
- [49] D. R. Luke, Inverse Probl. **21**, 37 (2004).
- [50] J. S. Wu, U. Weierstall, J. C. H. Spence, and C. T. Koch, Opt. Lett. **29**, 2737 (2004).
- [51] S. Marchesini, H. He, H. N. Chapman, S. P. Hau-Riege, A. Noy, M. R. Howells, U. Weierstall, and J. C. H. Spence, Phys. Rev. B **68**, 140101 (2003).
- [52] C.-C. Chen, J. Miao, C. W. Wang, and T. K. Lee, Phys. Rev. B **76**, 064113 (2007).
- [53] J. A. Rodriguez, R. Xu, C.-C. Chen, Y. Zou, and J. Miao, J. Appl. Crystallogr. **46**, 312 (2013).
- [54] D. Shapiro *et al.*, Proc. Natl. Acad. Sci. **102**, 15343 (2005).
- [55] H. N. Chapman *et al.*, Nat. Phys. **2**, 839 (2006).
- [56] T. Latychevskaia, Appl. Opt. **57**, 7187 (2018).
- [57] M. van Heel and M. Schatz, J. Struct. Biol. **151**, 250 (2005).
- [58] P. B. Rosenthal and R. Henderson, J. Mol. Biol. **333**, 721 (2003).
- [59] 모두를 위한 컨벡스 최적화, <https://convex-optimization-for-all.github.io>.
- [60] E. Esser, X. Zhang, and T. F. Chan, SIAM J. Imaging Sci. **3**, 1015 (2010).
- [61] S. Boyd, N. Parikh, E. Chu, B. Peleato, and J. Eckstein, Found. Trends Mach. Learn. **3**, 1 (2011).
- [62] A. Chambolle and T. Pock, J. Math. Imaging Vis. **40**, 120 (2011).
- [63] M. Pham, P. Yin, A. Rana, S. Osher, and J. Miao, Opt. Express **27**, 2792 (2019).
- [64] L. Allen, M. W. Beijersbergen, R. J. C. Spreeuw, and J. P. Woerdman, Phys. Rev. A **45**, 8185 (1992).
- [65] H. He, M. E. J. Friese, N. R. Heckenberg, and H. Rubinsztein-Dunlop, Phys. Rev. Lett. **75**, 826 (1995).
- [66] N. B. Simpson, K. Dholakia, L. Allen, and M. J. Padgett, Opt. Lett. **22**, 52 (1997).
- [67] C. T. Schmiegelow, J. Schulz, H. Kaufmann, T. Ruster, U. G. Poschinger, and F. Schmidt-Kaler, Nat. Commun. **7**, 12998 (2016).
- [68] Y. Shen, X. Wang, Z. Xie, C. Min, X. Fu, Q. Liu, M. Gong, and X. Yuan, Light: Sci. Appl. **8**, 90 (2019).

- [69] A. G. Peele *et al.*, Opt. Lett. **27**, 1752 (2002).
- [70] N. R. Heckenberg, R. McDuff, C. P. Smith, and A. G. White, Opt. Lett. **17**, 221 (1992).
- [71] D. Cojoc, B. Kaulich, A. Carpentiero, S. Cabrini, L. Businaro, and E. Di Fabrizio, Microelectron. Eng. **83**, 1360 (2006).
- [72] J. A. Davis, D. E. McNamara, D. M. Cottrell, and J. Campos, Opt. Lett. **25**, 99 (2000).
- [73] A. Sakdinawat and Y. Liu, Opt. Lett. **32**, 2635 (2007).
- [74] B. Wang, N. J. Brooks, P. Johnsen, N. W. Jenkins, Y. Esashi, I. Binnie, M. Tanksalvala, H. C. Kapteyn, and M. M. Murnane, Optica **10**, 1245 (2023).
- [75] M. Pancaldi *et al.*, Optica **11**, 403 (2024).
- [76] K. A. Forbes and D. L. Andrews, J. Phys.: Photonics **3**, 022007 (2021).
- [77] J. Ni *et al.*, ACS Nano **15**, 2893 (2021).
- [78] J. R. Rouxel *et al.*, Nat. Photonics **16**, 570 (2022).
- [79] M. Fanciulli *et al.*, Phys. Rev. Lett. **128**, 077401 (2022).
- [80] M. R. McCarter *et al.*, Phys. Rev. B **107**, L060407 (2023).
- [81] M. van Veenendaal and I. McNulty, Phys. Rev. Lett. **98**, 157401 (2007).
- [82] A. S. Rury, Phys. Rev. A **87**, 043408 (2013).
- [83] M. van Veenendaal, Phys. Rev. B **92**, 245116 (2015).
- [84] L. Ye, J. R. Rouxel, S. Asban, B. Rösner, and S. Mukamel, J. Chem. Theory Comput. **15**, 4180 (2019).
- [85] A. M. Yao and M. J. Padgett, Adv. Opt. Photonics **3**, 161 (2011).
- [86] G. Szegő, *Orthogonal Polynomials* (American Mathematical Society, 1975), 4th edn.
- [87] U. D. Jentschura and V. G. Serbo, Phys. Rev. Lett. **106**, 013001 (2011).
- [88] R. McWeeny, *Methods of Molecular Quantum Mechanics* (Academic Press, 1992), 2nd edn.
- [89] S. Tanaka, V. Chernyak, and S. Mukamel, Phys. Rev. A **63**, 063405 (2001).
- [90] I. Kimel and L. R. Elias, IEEE J. Quantum Electron. **29**, 2562 (1993).
- [91] Z. Jaroszewicz and A. Kołodziejczyk, Opt. Commun. **102**, 391 (1993).
- [92] C. Chang and A. Sakdinawat, Nat. Commun. **5**, 4243 (2014).
- [93] K. Li, M. J. Wojcik, R. Divan, L. E. Ocola, B. Shi, D. Rosenmann, and C. Jacobsen, J. Vac. Sci. Technol. B **35** (2017).
- [94] C. Perego and R. Millini, Chem. Soc. Rev. **42**, 3956 (2013).
- [95] M. Manzano and M. Vallet-Regí, Adv. Funct. Mater. **30**, 1902634 (2020).
- [96] W. Li, J. Liu, and D. Zhao, Nat. Rev. Mater. **1**, 16023 (2016).
- [97] J. Hwang, S. Kim, U. Wiesner, and J. Lee, Adv. Mater. **30**, 1801127 (2018).
- [98] M. C. Scott, C.-C. Chen, M. Mecklenburg, C. Zhu, R. Xu, P. Ercius, U. Dahmen, B. C. Regan, and J. Miao, Nature **483**, 444 (2012).
- [99] J. Miao, P. Ercius, and S. J. L. Billinge, Science **353**, aaf2157 (2016).
- [100] F. Zhang, B. Chen, G. R. Morrison, J. Vila-Comamala, M. Guizar-Sicairos, and I. K. Robinson, Nat. Commun. **7**, 13367 (2016).
- [101] J. Miao, Y. Nishino, Y. Kohmura, B. Johnson, C. Song, S. H. Risbud, and T. Ishikawa, Phys. Rev. Lett. **95**, 085503 (2005).
- [102] A. V. Martin *et al.*, Opt. Express **20**, 13501 (2012).
- [103] J. Miao, P. Charalambous, J. Kirz, and D. Sayre, Nature **400**, 342 (1999).
- [104] A. Bellisario, F. R. N. C. Maia, and T. Ekeberg, J. Appl. Crystallogr. **55**, 122 (2022).
- [105] Y. Sekiguchi, T. Oroguchi, Y. Takayama, and M. Nakasako, J. Synchrotron Radiat. **21**,

- 600 (2014).
- [106] W. Zhou, A. C. Bovik, H. R. Sheikh, and E. P. Simoncelli, IEEE Trans. Image Process. **13**, 600 (2004).
- [107] D. H. Cho *et al.*, ACS Nano **15**, 4066 (2021).
- [108] R. Xu *et al.*, J. Synchrotron Radiat. **18**, 293 (2011).
- [109] M. Pham, Y. Yuan, A. Rana, S. Osher, and J. Miao, Sci. Rep. **13**, 5624 (2023).
- [110] M. Guizar-Sicairos, S. T. Thurman, and J. R. Fienup, Opt. Lett. **33**, 156 (2008).
- [111] M. Odstrčil, M. Holler, J. Raabe, and M. Guizar-Sicairos, Opt. Express **27**, 36637 (2019).
- [112] J. Ihli, L. Bloch, F. Krumeich, K. Wakonig, M. Holler, M. Guizar-Sicairos, T. Weber, J. C. da Silva, and J. A. van Bokhoven, Angew. Chem., Int. Ed. **59**, 17266 (2020).
- [113] S. Weber *et al.*, Adv. Sci. **9**, 2105432 (2022).
- [114] E. Nowak, Z. Xie, N. M. Kovalchuk, O. K. Matar, and M. J. H. Simmons, Soft Matter **13**, 4616 (2017).
- [115] N. M. Kovalchuk, J. Chowdhury, Z. Schofield, D. Vigolo, and M. J. H. Simmons, Chem. Eng. Res. Des. **132**, 881 (2018).
- [116] I. Arganda-Carreras, V. Kaynig, C. Rueden, K. W. Eliceiri, J. Schindelin, A. Cardona, and H. Sebastian Seung, Bioinformatics **33**, 2424 (2017).
- [117] C. T. Rueden, J. Schindelin, M. C. Hiner, B. E. DeZonia, A. E. Walter, E. T. Arena, and K. W. Eliceiri, BMC Bioinf. **18**, 529 (2017).
- [118] D. M. Butts *et al.*, MRS Energy Sustain. **7**, E39, E39 (2020).
- [119] B. Gackiewicz, K. Lamorski, C. Ślawiński, S.-Y. Hsu, and L.-C. Chang, Sci. Rep. **11**, 5859 (2021).
- [120] D. A. Vecchio, S. H. Mahler, M. D. Hammig, and N. A. Kotov, ACS Nano **15**, 12847 (2021).
- [121] S. Van der Walt, J. L. Schönberger, J. Nunez-Iglesias, F. Boulogne, J. D. Warner, N. Yager, E. Gouillart, and T. Yu, PeerJ **2**, e453 (2014).
- [122] V. D. Blondel, J.-L. Guillaume, R. Lambiotte, and E. Lefebvre, J. Stat. Mech.: Theory Exp. **2008**, P10008 (2008).
- [123] M. Bastian, S. Heymann, and M. Jacomy, in *Proceedings of the 3rd International AAAI Conference on Weblogs and Social Media* (PKP Publishing Services Network, 2009), pp. 361.
- [124] M. Jacomy, T. Venturini, S. Heymann, and M. Bastian, PLoS One **9**, e98679 (2014).
- [125] D. J. Watts and S. H. Strogatz, Nature **393**, 440 (1998).
- [126] Z. Chen, D. Pan, B. Zhao, G. Ding, Z. Jiao, M. Wu, C.-H. Shek, L. C. M. Wu, and J. K. L. Lai, ACS Nano **4**, 1202 (2010).
- [127] J. Wang *et al.*, ACS Nano **12**, 635 (2018).
- [128] A. G. Hunt and G. W. Gee, Adv. Water Resour. **25**, 129 (2002).
- [129] M. J. Skaug, L. Wang, Y. Ding, and D. K. Schwartz, ACS Nano **9**, 2148 (2015).
- [130] T. C. Lee, R. L. Kashyap, and C. N. Chu, CVGIP: Graph. Models Image Process. **56**, 462 (1994).
- [131] J. Nunez-Iglesias, A. J. Blanch, O. Looker, M. W. Dixon, and L. Tilley, PeerJ **6**, e4312 (2018).
- [132] M. Miyahara, A. Vinu, and K. Ariga, Mater. Sci. Eng. C **27**, 232 (2007).
- [133] H. Pape, C. Clauser, and J. Iffland, Pure Appl. Geophys. **157**, 603 (2000).

- [134] Y. H. Lo, L. Zhao, M. Gallagher-Jones, A. Rana, J. J. Lodico, W. Xiao, B. C. Regan, and J. Miao, *Nat. Commun.* **9**, 1826 (2018).
- [135] A. Ulvestad, A. Singer, J. N. Clark, H. M. Cho, J. W. Kim, R. Harder, J. Maser, Y. S. Meng, and O. G. Shpyrko, *Science* **348**, 1344 (2015).
- [136] C. Song *et al.*, *Phys. Rev. Lett.* **100**, 025504 (2008).
- [137] A. Michelson, B. Minevich, H. Emamy, X. Huang, Y. S. Chu, H. Yan, and O. Gang, *Science* **376**, 203 (2022).
- [138] J. Deng *et al.*, *Sci. Adv.* **4**, eaau4548 (2018).
- [139] I. V. A. K. Reddy, A. Baev, E. P. Furlani, P. N. Prasad, and J. W. Haus, *ACS Photonics* **5**, 734 (2018).
- [140] Y. Cao *et al.*, *ACS Photonics* **10**, 1873 (2023).
- [141] T. Arikawa *et al.*, *Sci. Adv.* **6**, 1977 (2020).
- [142] S. Reich, N. S. Mueller, and M. Bubula, *ACS Photonics* **7**, 1537 (2020).
- [143] M. Odstrčil, A. Menzel, and M. Guizar-Sicairos, *Opt. Express* **26**, 3108 (2018).
- [144] K. Wakonig *et al.*, *J. Appl. Crystallogr.* **53**, 574 (2020).
- [145] X. Huang, H. Yan, R. Harder, Y. Hwu, I. K. Robinson, and Y. S. Chu, *Opt. Express* **22**, 12634 (2014).
- [146] B. L. Henke, E. M. Gullikson, and J. C. Davis, *At. Data Nucl. Data Tables* **54**, 181 (1993).
- [147] N. D. Mermin, *Rev. Mod. Phys.* **51**, 591 (1979).
- [148] J. M. Kosterlitz, *Rev. Mod. Phys.* **89**, 040501 (2017).
- [149] J. Y. Chauleau *et al.*, *Nat. Mater.* **19**, 386 (2020).
- [150] K. T. Kim *et al.*, *Nat. Commun.* **13**, 1769 (2022).
- [151] K. T. Kim, J. Y. Kee, M. R. McCarter, G. van der Laan, V. A. Stoica, J. W. Freeland, R. Ramesh, S. Y. Park, and D. R. Lee, *Phys. Rev. B* **106**, 035116 (2022).
- [152] Y. Takahashi, A. Suzuki, S. Furutaku, K. Yamauchi, Y. Kohmura, and T. Ishikawa, *Phys. Rev. B* **87**, 121201 (2013).
- [153] Y.-H. Chu, Q. He, C.-H. Yang, P. Yu, L. W. Martin, P. Shafer, and R. Ramesh, *Nano Lett.* **9**, 1726 (2009).
- [154] J.-G. Park, M. D. Le, J. Jeong, and S. Lee, *J. Phys.: Condens. Matter* **26**, 433202 (2014).
- [155] W. J. Hehre, R. F. Stewart, and J. A. Pople, *J. Chem. Phys.* **51**, 2657 (1969).
- [156] D. Lee, M. G. Kim, S. Ryu, H. M. Jang, and S. G. Lee, *Appl. Phys. Lett.* **86**, 222903 (2005).
- [157] C. Donnelly, M. Guizar-Sicairos, V. Scagnoli, S. Gliga, M. Holler, J. Raabe, and L. J. Heyderman, *Nature* **547**, 328 (2017).
- [158] A. Apseros, V. Scagnoli, M. Holler, M. Guizar-Sicairos, Z. Gao, C. Appel, L. J. Heyderman, C. Donnelly, and J. Ihli, *Nature* **636**, 354 (2024).
- [159] P. Li, N. W. Phillips, S. Leake, M. Allain, F. Hofmann, and V. Chamard, *Nat. Commun.* **12**, 7059 (2021).
- [160] P. Mehta, M. Bukov, C. H. Wang, A. G. R. Day, C. Richardson, C. K. Fisher, and D. J. Schwab, *Phys. Rep.* **810**, 1 (2019).
- [161] G. E. Karniadakis, I. G. Kevrekidis, L. Lu, P. Perdikaris, S. Wang, and L. Yang, *Nat. Rev. Phys.* **3**, 422 (2021).
- [162] G. Carleo, I. Cirac, K. Cranmer, L. Daudet, M. Schuld, N. Tishby, L. Vogt-Maranto, and L. Zdeborová, *Rev. Mod. Phys.* **91**, 045002 (2019).

- [163] K. T. Butler, D. W. Davies, H. Cartwright, O. Isayev, and A. Walsh, *Nature* **559**, 547 (2018).
- [164] A. Sanchez-Gonzalez *et al.*, *Nat. Commun.* **8**, 1 (2017).
- [165] G. Genty, L. Salmela, J. M. Dudley, D. Brunner, A. Kokhanovskiy, S. Koltsev, and S. K. Turitsyn, *Nat. Photonics* **15**, 91 (2021).
- [166] T. Kim, S. Moon, and K. Xu, *Nat. Commun.* **10**, 1 (2019).
- [167] Y. Rivenson, Y. Wu, and A. Ozcan, *Light: Science and Applications* **8**, 2047 (2019).
- [168] A. Krizhevsky, I. Sutskever, and G. E. Hinton, in *Advances in Neural Information Processing Systems* (NeurIPS, 2012), pp. 1097.
- [169] Y. LeCun, Y. Bengio, and G. Hinton, *Nature* **521**, 436 (2015).
- [170] A. Goy, K. Arthur, S. Li, and G. Barbastathis, *Phys. Rev. Lett.* **121**, 243902 (2018).
- [171] S. Li, M. Deng, J. Lee, A. Sinha, and G. Barbastathis, *Optica* **5**, 803 (2018).
- [172] Y. Rivenson, Y. Zhang, H. Günaydin, D. Teng, and A. Ozcan, *Light: Science and Applications* **7**, 17141 (2018).
- [173] J. Miao, R. L. Sandberg, and C. Song, *IEEE J. Sel. Top. Quantum Electron.* **18**, 399 (2012).
- [174] O. Ronneberger, P. Fischer, and T. Brox, in *Proceedings of the International Conference on Medical Image Computing and Computer-Assisted Intervention* (Springer, 2015), pp. 234.
- [175] G. Liu, F. A. Reda, K. J. Shih, T.-C. Wang, A. Tao, and B. Catanzaro, in *Proceedings of the European Conference on Computer Vision* (Springer, 2018), pp. 85.
- [176] G. Cohen, S. Afshar, J. Tapson, and A. v. Schaik, in *Proceedings of the International Joint Conference on Neural Networks* (IEEE, 2017), pp. 2921.
- [177] A. Krizhevsky and G. Hinton, *Learning multiple layers of features from tiny images* (University of Toronto, 2009).
- [178] J. Johnson, A. Alahi, and L. Fei-Fei, in *Proceedings of the European Conference on Computer Vision* (Springer, 2016), pp. 694.
- [179] L. Gatys, A. Ecker, and M. Bethge, *J. Vis.* **16**, 326 (2016).
- [180] I. Loshchilov and F. Hutter, arXiv:1711.05101 (2017).
- [181] D. Sung *et al.*, *Appl. Sci.* **11**, 5082 (2021).
- [182] T. Kameshima *et al.*, *Rev. Sci. Instrum.* **85**, 033110 (2014).
- [183] K. Dabov, A. Foi, V. Katkovnik, and K. Egiazarian, *IEEE Trans. Image Process.* **16**, 2080 (2007).
- [184] M. Makitalo and A. Foi, *IEEE Trans. Image Process.* **20**, 99 (2011).
- [185] Y. Liu, Y. Xu, and W. Yin, *J. Sci. Comput.* **86**, 21 (2021).
- [186] Y. Shechtman, Y. C. Eldar, O. Cohen, H. N. Chapman, J. Miao, and M. Segev, *IEEE Signal Process. Mag.* **32**, 87 (2015).
- [187] R. Harder, *IUCrJ* **8**, 1 (2021).
- [188] Z. Zhou *et al.*, *npj Comput. Mater.* **9**, 58 (2023).
- [189] J. Oppliger *et al.*, *Nat. Mach. Intell.* **6**, 180 (2024).
- [190] J. E. Salgado, S. Lerman, Z. Du, C. Xu, and N. Abdolrahim, *npj Comput. Mater.* **9**, 214 (2023).
- [191] K. Mallayya, J. Straquadine, M. J. Krogstad, M. D. Bachmann, A. G. Singh, R. Osborn, S. Rosenkranz, I. R. Fisher, and E.-A. Kim, *Nat. Phys.* **20**, 822 (2024).
- [192] C. Metzler, P. Schniter, A. Veeraraghavan, and R. Baraniuk, in *Proceedings of the 35th*

- International Conference on Machine Learning* (PMLR, 2018), pp. 3501.
- [193] M. J. Cherukara, Y. S. G. Nashed, and R. J. Harder, *Sci. Rep.* **8**, 16520 (2018).
- [194] L. Wu, S. Yoo, A. F. Suzana, T. A. Assefa, J. Diao, R. J. Harder, W. Cha, and I. K. Robinson, *npj Comput. Mater.* **7**, 175 (2021).
- [195] Y. Yao, H. Chan, S. Sankaranarayanan, P. Balaprakash, R. J. Harder, and M. J. Cherukara, *npj Comput. Mater.* **8**, 124 (2022).
- [196] A. Bellisario and T. Ekeberg, *Mach. Learn.: Sci. Technol.* **5**, 045022 (2024).
- [197] T.-S. Vu *et al.*, *npj Comput. Mater.* **11**, 66 (2025).
- [198] K. H. Kim *et al.*, *Nature* **518**, 385 (2015).
- [199] J. N. Clark *et al.*, *Science* **341**, 56 (2013).
- [200] A. S. Johnson *et al.*, *Nat. Phys.* **19**, 215 (2023).
- [201] K. He, X. Zhang, S. Ren, and J. Sun, in *Proceedings of the IEEE Conference on Computer Vision and Pattern Recognition* (IEEE, 2016), pp. 770.
- [202] F. Chollet, in *Proceedings of the IEEE Conference on Computer Vision and Pattern Recognition* (IEEE, 2017), pp. 1251.
- [203] L. Chi, B. Jiang, and Y. Mu, in *Advances in Neural Information Processing Systems* (NeurIPS, 2020), pp. 4479.
- [204] R. Suvorov *et al.*, in *Proceedings of the IEEE/CVF Winter Conference on Applications of Computer Vision* (IEEE, 2022), pp. 2149.
- [205] B. Hammouda, *J. Appl. Crystallogr.* **43**, 716 (2010).
- [206] J. Kwon, J. Kim, H. Park, and I. K. Choi, in *Proceedings of the 38th International Conference on Machine Learning* (PMLR, 2021), pp. 5905.
- [207] E. Sobolev *et al.*, *Commun. Phys.* **3**, 97 (2020).
- [208] F. R. N. C. Maia, *Nat. Methods* **9**, 854 (2012).
- [209] S. Kassemeyer *et al.*, *Opt. Express* **20**, 4149 (2012).
- [210] L. Strüder *et al.*, *Nucl. Instrum. Methods Phys. Res. A* **614**, 483 (2010).

## Acknowledgements

2019년 학부 연구 참여부터 시작한 결맞는 회절 이미징에 대한 여정이 학위 과정을 마무리하며 잠깐 멈추게 되었습니다. 6년이 넘는 긴 시간 동안 많은 분께 배우고 도움을 받았습니다. 가르침과 도움을 주신 모든 분께 감사의 인사를 드립니다.

가장 먼저 송창용 교수님께 감사합니다. 그동안 연구를 하면서 실수하기도 하고, 실험에 실패하기도 하는 등 우여곡절이 많았지만, 교수님께서 주신 가르침과 조언, 그리고 지속적인 관심과 지지 덕분에 계속해서 연구를 이어갈 수 있었습니다.

처음 연구실에 들어왔을 때 여러 가지를 알려주신 성대호 선배님, 정철호 선배님, 이희민 선배님, 그리고 제 사수로서 이끌어 주신 조도형 선배님께 감사합니다. 처음이라는 것은 항상 설렘과 어색함을 함께 가져오는 것 같습니다. 선배님들의 친절한 설명과 따뜻한 말씀 덕분에 연구실에 빠르게 적응할 수 있었습니다.

학위 기간 가장 많이 대화를 나누고, 여러 가지를 가르쳐 주셨던 신재용 선배님과 황준하 선배님께 감사합니다. 제가 학위 기간 진행한 모든 연구가 성공적으로 마무리될 수 있었던 것에는 두 분의 도움이 컸고, 두 분과의 추억이 가장 기억에 많이 남을 것 같습니다.

소극적인 연구실 사람들을 이끌어 주신 은영이 누나와 재밌는 이야기를 종종 해주시는 승필이 형, 그리고 연구실 후배인 신우와 정찬이에게 감사합니다. 여러분 덕분에 학위 기간을 즐겁게 보낼 수 있었습니다. 그리고 새로 들어온 근필 씨와 성국 씨의 건승을 기원합니다.

PLS-II 9C 빔라인의 이수용 박사님과 함다슬 선생님께 감사합니다. 매번 새로운 실험 장치를 설계해 와서 빔라인에 설치하기 위해 매번 고생했던 것 같습니다. 그럴 때마다 항상 조언과 도움을 주신 덕분에 실험을 해낼 수 있었습니다. 그리고 PAL-XFEL NCI 빔라인의 세심하게 신경 써주시고 쟁겨주신 남대웅 박사님과 매 실험 DAQ에 도움을 주신 김상수 박사님께도 감사합니다.

가속기 실험은 혼자서는 할 수 없는 실험입니다. 많은 분께 크고 작은 도움을 받아서 연구를 계속할 수 있었습니다. 시료를 제공해 주신 KIST의 최준우 박사님, KAIST의 이진우 교수님과 양찬호 교수님께 감사합니다. 1년 동안 함께 지내면서 여러 가지를 가르쳐 주신 김국태 박사님과 딥러닝과 관련하여 많은 도움을 준 재창이에게 감사합니다. 이 외에도 도움을 주신 여러 관계자분께도 이 기회를 빌려 감사의 인사를 드립니다.

마지막으로 학위 기간 저를 지지해 주신 부모님께 감사합니다. 모두가 주신 은혜를 기억하면서 앞으로의 미래를 그려 나가도록 하겠습니다.

본 학위논문 내용에 관하여 학술·교육 목적으로 사용할 모든 권리를 포항공대에 위임함.

# Curriculum Vitae

---

## Basic Information

Name: Sung Yun Lee  
Contact: [sungyun98@postech.ac.kr](mailto:sungyun98@postech.ac.kr)  
Homepage: <https://sungyun98.github.io/>  
Languages: Korean, English  
Python (PyTorch), MATLAB, C/C++, LabVIEW

---

## Education

**Ph. D.** 03/2020–08/2025  
Department of Physics, Pohang University of Science and Technology  
Thesis: *Development of functional coherent X-ray nanoimaging with deep-learning methods*  
Supervisor: Prof. Changyong Song

**B. Sc.** 03/2016–02/2020  
Department of Physics, Pohang University of Science and Technology & Minor in Department of Electrical Engineering (*Magna cum laude*)  
Thesis: *A Comprehensive Evaluation of the Process of Copying a Complex Figure in Early- and Late-Onset Alzheimer Disease*  
Supervisor: Prof. Changyong Song & Prof. Jee Hyun Choi (KIST, Republic of Korea)

---

## Experiences

**Participating Researcher (as a graduate student)** 03/2020–08/2025  
Femtosecond X-ray Diffraction & Imaging Laboratory, Department of Physics, Pohang University of Science and Technology (Supervisor: Prof. Changyong Song)  

- Time-resolved multiplexing X-ray measurement (small-angle X-ray scattering + wide-angle X-ray scattering + X-ray emission spectroscopy) @ PAL-XFEL
- Time-resolved coherent X-ray diffraction imaging @ PAL-XFEL
- Time-resolved X-ray diffraction @ PAL-XFEL
- X-ray Bragg ptychography @ ESRF
- X-ray ptychography + X-ray fluorescence @ PLS-II  
(with circularly polarized beam by diamond phase retarder and vortex beam by spiral zone plate)

- Coherent X-ray diffraction imaging @ PLS-II
- Scanning transmission X-ray microscopy @ PLS-II  
(with circularly polarized beam by elliptically polarizing undulator)

**Teaching Assistant**

09/2020–12/2021

Department of Physics, Pohang University of Science and Technology

- PHYS199: Freshman Research Participation 09/2021–12/2021
- PHYS103: General Physics Laboratory I 03/2021–06/2021
- PHYS250: Physics Laboratory I 09/2020–12/2020

**Undergraduate Researcher**

03/2019–02/2020

Femtosecond X-ray Diffraction & Imaging Laboratory, Department of Physics, Pohang University of Science and Technology (Principal investigator: Prof. Changyong Song)

**Student Mentoring Program Mentor**

03/2018–12/2019

Pohang University of Science and Technology

- CSED101: Programming & Problem Solving 09/2019–12/2019
- CSED101: Programming & Problem Solving 09/2018–12/2018
- PHYS101: General Physics I 03/2018–06/2018

**Intern**

06/2019–08/2019

Machine Learning Team, Columbus Center, Netmarble Corp.

**Research Trainee**

06/2018–08/2018

Convergence Research Center for Diagnosis, Treatment and Care System of Dementia, Brain Science Institute, KIST (Principal investigator: Prof. Jee Hyun Choi)

**Intern**

06/2017–08/2017

Accelerator PnA Team, Accelerator Business Division, Dawonsys Co., Ltd.

**The 13th University Student Knowledge Volunteering KOSAF Camp Mentor**

08/2016

Jeonggok Middle School (Topic: Tessellation & Four-color theorem)

**Honors & Awards**

**POSTECHIAN Fellowship – Innovation**

2024

Pohang University of Science and Technology

**Graduate Student Excellent Paper Award**

2024

KOSUA

**Graduate Student Excellent Paper Award**

2023

Department of Physics, Pohang University of Science and Technology

**Best Poster Award**

2023

The 35th Synchrotron Radiation Users' Workshop, KOSUA

**Best Poster Award**

2023

The 3rd PAL-XFEL Users' Meeting, KOSUA

**Best Poster Award**

2022

The 34th Synchrotron Radiation Users' Workshop, KOSUA

**Graduate Student Excellent Teaching Assistant Award**

2020

Department of Physics, Pohang University of Science and Technology

**BK21 First Paper Award**

2020

Department of Physics, Pohang University of Science and Technology

**Best Bachelor's Thesis Award**

2019

Department of Physics, Pohang University of Science and Technology

**Presidential Science Scholarship**

2016

Ministry of Science, ICT, and Future Planning

---

**Patents**

- [1] Apparatus and Method of Processing Image Copying Test for Evaluating Cognitive Impairment, and Computer Readable Recording Medium  
Registration #1023380710000, Republic of Korea 12/09/2021
- [2] METHOD FOR GAME DATA PROCESSING  
Registration #1023339410000, Republic of Korea 11/29/2021
- 

**Publications** (†: co-first author, \*: corresponding author)

- [1] Seung-Phil Heo, Choongjae Won, Heemin Lee, Hanbyul Kim, Eunyoung Park, Sung Yun Lee, Junha Hwang, Hyeonggi Choi, Sang-Youn Park, Byungjune Lee, Woo-Suk Noh, Hoyoung Jang, Jae-Hoon Park, Dongbin Shin\*, and Changyong Song\*, *Frustrated phonon with charge density wave in vanadium Kagome metal*, Nature Communications **16**, 4861 (2025).
- [2] Sung Yun Lee, Do Hyung Cho, Chulho Jung, Daeho Sung, Daewoong Nam, Sangsoo Kim, and Changyong Song\*, *Deep-learning real-time phase retrieval of imperfect diffraction patterns from X-ray free-electron lasers*, npj Computational Materials **11**, 68 (2025).
- [3] Jangwoo Kim†, HyoJung Hyun†, Seonghan Kim, Sun Min Hwang, Myong-Jin Kim, Dogeun Jang, Kyung Sook Kim, Jaeyong Shin, Sejin Kim, Junha Hwang, Sung Yun Lee, Eunyoung Park,

- Sangsoo Kim, Intae Eom, Changyong Song and Daewoong Nam\*, *Development of the Nanobeam X-ray Experiments instrument at PAL-XFEL*, Journal of Synchrotron Radiation **32**(2), 466–473 (2025).
- [4] Sung Yun Lee, Eunyoung Park, Sinwoo Kim, Euije Jo, Su Yong Lee, Jun Woo Choi, and Changyong Song\*, *Off-Axis X-Ray Vortex Beam Ptychography*, ACS Photonics **11**(9), 3804–3810 (2024).
- [5] Junha Hwang†, Yungok Ihm†, Daewoong Nam, Jaeyong Shin, Eunyoung Park, Sung Yun Lee, Heemin Lee, Seung-Phil Heo, Sangsoo Kim, Je Young Ahn, Ji Hoon Shim, Minseok Kim, Intae Eom, Do Young Noh, and Changyong Song\*, *Inverted nucleation for photoinduced nonequilibrium melting*, Science Advances **10**(18), eadl6409 (2024).
- [6] Junha Hwang, Sejin Kim, Sung Yun Lee, Eunyoung Park, Jaeyong Shin, Jae Hyuk Lee, Myong-jin Kim, Seonghan Kim, Sang-Youn Park, Dogeun Jang, Intae Eom, Sangsoo Kim, Changyong Song, Kyung Sook Kim\*, and Daewoong Nam\*, *Development of the multiplex imaging chamber at PAL-XFEL*, Journal of Synchrotron Radiation **31**(3), 469–477 (2024).
- [7] Sung Yun Lee†, Do Hyung Cho†, Sung Chan Song†, Jaeyong Shin, Junha Hwang, Eunyoung Park, Su Yong Lee, Seongseop Kim, Jinwoo Lee, and Changyong Song\*, *Nanoscale Three-Dimensional Network Structure of a Mesoporous Particle Unveiled via Adaptive Multidistance Coherent X-ray Tomography*, ACS Nano **17**(22), 22488–22498 (2023).
- [8] Sung Yun Lee, Do Hyung Cho, Chulho Jung, Daeho Sung, Daewoong Nam, Sangsoo Kim, and Changyong Song\*, *Denoising low-intensity diffraction signals using k-space deep learning: Applications to phase recovery*, Physical Review Research **3**(4), 043066 (2021).
- [9] Do Hyung Cho†, Zhou Shen†, Yungok Ihm, Dae Han Wi, Chulho Jung, Daewoong Nam, Sangsoo Kim, Sang-Youn Park, Kyung Sook Kim, Daeho Sung, Heemin Lee, Jae-Yong Shin, Junha Hwang, Sung Yun Lee, Su Yong Lee, Sang Woo Han, Do Young Noh, N. Duane Loh\*, and Changyong Song\*, *High-Throughput 3D Ensemble Characterization of Individual Core-Shell Nanoparticles with X-ray Free Electron Laser Single-Particle Imaging*, ACS Nano **15**(3), 4066–4076 (2021).
- [10] Ko Woon Kim†, Sung Yun Lee†, Jongdoo Choi, Juhee Chin, Byung Hwa Lee, Duk L. Na\*, and Jee Hyun Choi\*, *A Comprehensive Evaluation of the Process of Copying a Complex Figure in Early- and Late-Onset Alzheimer Disease: A Quantitative Analysis of Digital Pen Data*, Journal of Medical Internet Research **22**(8), e18136 (2020).
- [11] Sungyun Lee\*, Sunghun Kim, Inhae Seok, and Mincheol Kim, *Detecting Abuser Group in MMORPG by using Ranking System based on Game Transaction Network*, in Proceeding of the Korea Software Congress, **46**(2), 584–586 (2019).

## Presentations

- |     |   |      |
|-----|---|------|
| [1] | The 36th Synchrotron Radiation Users' Workshop, KOSUA (Poster)<br><i>Off-axis X-ray vortex beam ptychography</i>  | 2024 |
| [2] | APS March Meeting 2024, American Physical Society (Oral)<br><i>Nanoscale X-ray Tomography of Mesoporous Particle Improved via Adaptive Multidistance Coherent Diffraction Imaging</i>       | 2024 |
| [3] | The 35th Synchrotron Radiation Users' Workshop, KOSUA (Poster)<br><i>Network analysis of pore structure inside mesoporous particle revealed by multi-distance coherent X-ray tomography</i> | 2023 |

- [4] 2023 KPS Fall Meeting, Korean Physical Society (Poster) 2023  
*Nanoscale three-dimensional network structure of a mesoporous particle unveiled via adaptive multi-distance coherent X-ray tomography*
- [5] The 3rd PAL-XFEL Users' Meeting, KOSUA (Poster) 2023  
*Deep-Learning-Based Denoiser for Phase Recovery of Single-Shot Diffraction Signals via X-ray Free Electron Laser*
- [6] The 34th Synchrotron Radiation Users' Workshop, KOSUA (Poster) 2022  
*Multi-distance Coherent Diffraction Imaging for Super-resolution X-ray Microscopy*
- [7] 2021 KPS Fall Meeting, Korean Physical Society (Poster) 2021  
*Deep-Learning-Based Denoiser for Phase Recovery of Single-Shot Diffraction Patterns Using XFEL*
- [8] The 32nd Synchrotron Radiation Users' Workshop, KOSUA (Poster) 2020  
*Low Intensity Phase Retrieval Enhanced by Deep Neural Network*
- [9] Korea Software Congress 2019, KIISE (Poster) 2019  
*Detecting Abuser Group in MMORPG by using Ranking System based on Game Transaction Network*

